

An Efficient Approach To Producing One-Hundred Percent Synthesis Of Borides

A Major Qualifying Project

Submitted to the Faculty of

Worcester Polytechnic Institute

in partial fulfillment of the requirements for the

Degree in Bachelor of Science

in

Mechanical Engineering

By

Edwin Boby Joseph

Brian-Marcio Montenegro

Sanjeet Shankar Pawar

Date: April 27, 2023

Sponsoring Organization: Saint Gobain

Northborough, MA

Project Advisors:

Professor Yu Zhong, Advisor

This report represents the work of WPI undergraduate students submitted to the faculty as evidence of a degree requirement. WPI routinely publishes these reports on its website without editorial or peer review. For more information about the project's program at WPI, see <http://www.wpi.edu/Academics/Projects>.

Abstract

Borides are versatile materials with excellent properties, including high melting points, corrosion resistance, and hardness. These properties make them ideal for specialty applications like wear-resistant coatings and non-ferrous foundry. Due to their exceptional properties, Saint-Gobain's businesses, such as abrasives and refractories, show significant interest in using borides. The primary goal of this project is to screen oxide-based electrolytes for boride synthesis with the molten oxides electrolysis (MOE) process using thermodynamic modeling. The project's secondary objective is to exhibit boride synthesis and identify boride deposition. Our focus lies on AlMgB_{14} and ZrB_2 borides. We conducted thermodynamic simulations with manganese oxide to learn how to determine the optimum operating temperature and other essential parameters. Afterward, we translated our findings into boride synthesis for two boride compounds, aiming to synthesize them efficiently in a low-cost and low-temperature environment.

Acknowledgments

The authors of this paper would like to offer their sincere gratitude to Saint Gobain of Northborough, Massachusetts, and in particular, Mr. Charles Bateman and Mr. Bradley Nakanishi, our distinguished supporters. We appreciate our sponsors' kind assistance and support and the priceless opportunity to participate in this project. Additionally, we would like to thank Professor Yu Zhong of the Mechanical and Materials Engineering Department, our project advisor, for his constant support and direction.

We especially want to thank Mr. Jize Zhang, a Ph.D. candidate, who helped us by liaising between the team and Professor Zhong. His first-hand knowledge, wise counsel, and help setting up our meetings were crucial to accomplishing our project. Additionally, we would like to extend our sincere gratitude to Mr. Rui Wang, a Ph.D. student who served as our mentor for this project. His excellent advice and knowledge of FactSage computations significantly impacted how well our project turned out.

We would like to express our sincere appreciation to our sponsors, our advisor, and our mentors for their help and direction. Without their assistance, we would not have been able to complete this job, and we sincerely appreciate everything they did.

Authorship

<u>Sections & Subsections</u>	<u>Author</u>	<u>Editor</u>
Abstract	Edwin	<i>Sanjeet, Edwin</i>
Acknowledgments	Edwin	<i>Edwin</i>
Executive Summary	Edwin	<i>Edwin</i>
1.0 Introduction	Edwin, Brian	
1.1 Molten Oxide Electrolysis	Edwin, Brian	<i>Edwin</i>
1.2 Borides	Edwin, Brian	<i>Edwin</i>
1.3 Synthesis Of Borides	Edwin	<i>Edwin</i>
1.4 Project Objectives	Edwin	<i>Edwin</i>
2.0 Broader Impacts	Edwin	
2.1 Engineering Ethics	Edwin	<i>Edwin</i>
2.2 Societal Impact	Edwin	<i>Edwin</i>
2.3 Environmental & Sustainability Impact Environmental & Sustainability Impact	Edwin	<i>Edwin</i>
3.0 Background	Edwin	
3.1 Extractive Metallurgy Techniques	Edwin	<i>Edwin</i>
3.2 Molten Oxide Electrolysis	Edwin	<i>Edwin</i>
3.3 Manganese Molten Oxide Electrolysis	Edwin	<i>Edwin</i>

3.4 Boron Reduction	Edwin	<i>Edwin</i>
3.5 Boron Synthesis	Edwin	<i>Edwin</i>
3.6 Calculation Parameters	Edwin	<i>Edwin</i>
4.0 Methodology	Edwin, Sanjeet	
4.1 The Action Items	Edwin	<i>Edwin, Sanjeet</i>
4.2 Completion Of The Action Items	Edwin, Sanjeet	<i>Edwin, Sanjeet</i>
5.0 Results & Analysis	Edwin, Sanjeet	
5.1 Aluminum Magnesium Boride	Edwin, Sanjeet	<i>Edwin</i>
5.2 Zirconium Diboride	Edwin	<i>Edwin</i>
6.0 Conclusion	Edwin	<i>Edwin</i>
6.1 Aluminum Magnesium Boride	Edwin	<i>Edwin</i>
6.2 Zirconium Diboride	Edwin	<i>Edwin</i>
7.0 A New Approach Proposed	Edwin	
7.1 Introducing A Hydrogen Flux	Edwin	<i>Edwin</i>
7.2 Pairing Molten Oxide Electrolysis With A Hydrogen Flux To Produce Aluminum Magnesium Boride	Edwin	<i>Edwin</i>
8.0 Future Recommendations	Brian	
8.1 General Recommendations	Brian	<i>Edwin</i>

8.2 Specific Recommendations	Brian	<i>Edwin</i>
------------------------------	-------	--------------

Executive Summary

Introduction

This report is divided into two sections: molten oxide electrolysis (MOE) process and borides synthesis. The MOE process, which uses a molten salt electrolyte to create oxygen and metals, is an efficient method for extracting metals, particularly those with high melting temperatures. MOE techniques provide several advantages over traditional pyrometallurgical and hydrometallurgical processes, including lower energy consumption, fewer environmental impact and dangers, and higher metal purity. One of the most important advantages of MOE is the increased purity of the metal generated. MOE could potentially be used to recycle metal-containing waste materials.

The research also looks at the role of FactSage, a widely used computational tool that aids in the calculation of different thermodynamic and kinetic parameters that are important for understanding the MOE process. FactSage has made a substantial contribution to the knowledge of MOE by giving accurate and dependable data on a variety of parameters such as activity coefficients, Gibbs free energy, enthalpy, and entropy. This information is critical for forecasting the behavior of molten salts, oxides, and metals under various conditions, as well as building optimum MOE processes.

Borides, which have found great utility in a variety of applications due to their unusual chemical properties, are the report's second topic. Zirconium diboride (ZrB_2), a common boride, is used in high-temperature electrodes, thermowell tubes, and thermal protection systems for space re-entry vehicles. Borides are also utilized to manufacture neutron absorption materials, wear-resistant coatings, and molten metal crucibles. Saint Gobain, a multinational materials and

technology firm, has a strong presence in borides, particularly ZrB_2 . Finally, the research emphasizes the importance of borides in many industries as well as their potential for future technological applications.

Broader Impacts

This technical report's broader effect portion investigates the prospective applications of metal borides with a high modulus of elasticity (borides MOE) and their impact on engineering ethics, society, and the environment. Borides have good mechanical properties, making them useful for a wide range of technological applications, including cutting tools, bearings, and medical implants. However, because of the considerable energy and resource requirements for their manufacturing, the possible environmental impact, and the necessity for safety precautions to prevent exposure to toxic materials, their use poses ethical considerations.

Using MOE to synthesize borides have a broader societal influence since their application in electronics, renewable energy, and medical implants can improve device performance, reduce electronic waste, and encourage long-term growth. Borides produced from the MOE have the potential to improve energy efficiency and reduce greenhouse gas emissions, for example, by use in solar and thermoelectric applications, according to the literature. Boride-based coatings in vehicle engines have the potential to minimize friction, wear, and fuel consumption, hence contributing to a more environmentally friendly transportation system.

Background

The intent of this section of our engineering report is to present an overview of extractive metallurgy techniques, with a focus on molten oxide electrolysis (MOE) as a promising alternative to existing methods. Mineral processing, hydrometallurgy, pyrometallurgy, and electrometallurgy are among the extractive metallurgy methods included in the paper. MOE is an electrometallurgical process that refines and produces a metal-containing solution using electrolysis. This technology is easier and more environmentally benign than prior approaches, but it is expensive and necessitates the use of rare anode materials.

This section also investigates the boron reduction method, which entails extracting boron from a chemical and reducing it to elemental boron. The four primary methods for reducing boron compounds to elemental boron, as well as the environmental impact of borate processing, are reviewed. The report suggests MOE as an alternate method for producing boron compounds with low environmental impact.

In addition, the Background section looks into two boride synthesis methods: carbothermic reduction and MOE. Carbothermic reduction is a one-step process that uses carbon as a reducing agent, although it can introduce impurities and produce lower-purity products. MOE, on the other hand, produces borides with high purity and stoichiometry but requires more exact control of the electrolysis conditions and is more expensive.

Finally, this section addresses the project's computations, highlighting the importance of pseudo-binary and isothermal sections, nominal cathode-to-anode distance, and ohmic drop in achieving optimal reactor performance. The study admits that the challenging computations necessitated extensive investigation and contact with Saint-Gobain.

Methodology

This report's Methodology section covers the processes used to test for the commercial use of manufacturing borides by molten oxide electrolysis (MOE). Research and evaluation of literature, construction of phase diagrams, analysis of fugacity and viscosity trends, investigation of mass and energy balances, and determination of efficiencies and potentials were all developed as action items. The initial step was to create a pseudo-binary phase diagram and isothermal sections of the reaction products and reactants in order to identify the electrolyte solution parameters required to form the borides.

The methodology includes step-by-step instructions for doing various computations, such as building the fugacity and viscosity trends of the compositions of interest using FactSage, a computational tool. These calculations were then utilized to determine the focus composition and the operating temperature for the MOE reaction. FactSage and formulae were used to compute the overall reaction energy and potential, and the Nernst equation was used to get the Gibbs energy and potential.

The section also looks into the reaction's mass balance and energy balance. A procedure for determining the mass balance was created, and fugacity rates were calculated to produce the mass balance formula. The energy balance was investigated using two methods: looking at the reaction as a whole and looking at it at distinct stages. Finally, the technique goes over how to compute the nominal cathode-to-anode distance, faradaic efficiency, and energy efficiency for the MOE reaction. Overall, the approach provides a clear and precise explanation of the actions required to finish the project.

Results & Analysis

This section of the technical report focuses on the results and analysis of the molten oxide electrolysis technique used to produce aluminum magnesium boride (AlMgB_{14}) and zirconium diboride (ZrB_2). The aluminum magnesium boride production findings and analyses were thoroughly detailed. To identify the appropriate temperature range of operation, we produced a pseudo-binary phase diagram and two isothermal sections. Composition 4 at 1600 °C was judged to be the required composition for the electrolyte based on the fugacity and viscosity trends. FactSage was used to calculate the overall reaction energy and potential, and the energy value was determined to be 6247.1702 kJ at an operating temperature of 1600 °C. We computed the mass and energy balances to investigate the trend of losing the intended product as well as the quantity of energy required and extracted from the reaction. We also estimated the nominal cathode-to-anode distance for the electrolytic cell, as well as the reaction, faradaic, and energy efficiency efficiencies. Finally, the analysis determined that the molten oxide electrolysis technique used to produce aluminum magnesium boride is endothermic.

The following investigation sought to assess the possibility of generating zirconium diboride via the MOE method by creating a series of isothermal sections at various temperatures. The findings revealed that the mole fraction of zirconium remained low, and increasing the temperature did not produce the anticipated outcomes. This discovery implies that more study and development are required to synthesize zirconium diboride via MOE.

Conclusion

The paper discusses the findings and analysis of molten oxide electrolysis (MOE) attempts to create aluminum magnesium boride (AlMgB_{14}) and zirconium diboride. According to the report, pure AlMgB_{14} cannot be created via MOE, and alternative methods of producing AlMgB_{14} must be studied. The operating temperature range of 1400 °C to 1600 °C was discovered to reduce the flow rate, which must be accounted for in the mass balance calculation. In order to boost aluminum magnesium boride production, the airflow rate into the system must be reduced. As a result, more testing is required to determine the optimal cathode-to-anode distance for AlMgB_{14} MOE. The report finds that MOE's commercial production of AlMgB_{14} is not feasible, but the findings provide useful insights and direction for future research to increase process efficiency and optimize AlMgB_{14} production.

The report concludes that MOE is not a viable strategy for producing zirconium diboride due to zirconium's very low solubility in the electrolyte. The pseudo-binary and ternary phase diagrams supported this finding, demonstrating that if the percentage of ZrO_2 in the electrolyte combination was less than 20%, only slag liquid could develop. The mole fraction of zirconium in the slag-liquid zone remained low even at 2200 °C, indicating that increasing the operating temperature would not produce a feasible and environmentally sound technique for manufacturing zirconium diboride via MOE. Another reason for the infeasibility of this production process for ZrB_2 , was that the zirconium portion of the electrolyte– ZrO_2 –has an extremely high melting temperature. By mixing this compound with B_2O_3 to form the desired electrolyte, only a very limited amount of ZrO_2 could dissolve in the liquid.

As a result, it is suggested that other approaches for commercializing zirconium diboride manufacturing be researched. The paper examines the results and factual information given in a

scientific and professional manner, providing insights into the difficulties encountered in attempting to develop these materials through MOE and proposing recommendations for future research.

A New Approach Proposed

Following the conclusion regarding aluminum magnesium boride, our group investigated the possibility of a revolutionary method of producing this boride by molten oxide electrolysis. This study looked into the feasibility of injecting a hydrogen flux into the molten oxide electrolysis reaction.

Future Recommendations

This engineering technical report includes future recommendations as well as general and particular recommendations for the Molten Oxide Electrolysis (MOE) project. The general recommendations include reading knowledge, role separation, and experimentation with FactSage. A literature review was recommended to improve information about MOE and FactSage, with sources including scholarly peer-reviewed articles, published books, video tutorials, patents, and more. The position separation was proposed to allow the team to share experience and information, with different responsibilities flipping as needed. Experimenting with FactSage was encouraged in order to learn and comprehend the program's various features and modules, particularly the Equilib module, which was heavily used throughout the research.

The precise advice centered on comprehending the MOE process and the primary applications of FactSage. The Equilib module was recommended as the initial step in becoming acquainted with FactSage. It supports multiphase and multicomponent calculations and has access to solution and compound databases. The viscosity and phase diagram modules were also presented, as well as tips for understanding their applications and features. The recommendations in this report are intended to help future groups navigate FactSage and the MOE process in order to minimize difficulties and improve project outcomes.

Table Of Contents

Abstract	3
Acknowledgments	4
Authorship	5
Executive Summary	8
Introduction	8
Broader Impacts	9
Background	10
Methodology	11
Results & Analysis	12
Conclusion	13
A New Approach Proposed	14
Future Recommendations	14
Table Of Contents	16
List Of Figures	20
List Of Tables	25
1.0 Introduction	30
1.1 Molten Oxide Electrolysis	30
1.1.0 The MOE Process & Its Applications	30
1.1.1 MOE Process Through Fact Sage	31
1.2 Borides	32
1.2.0 Application Of Boron & Borides	32
1.2.1 Saint Gobain’s Work With Borides	33
1.2.2 Saint Gobain’s Interest In Boride Extraction Through The MOE Process	34
1.3 Synthesis Of Borides	35
1.3.0 Silicothermic Reactions	35
1.3.1 Carbothermic Reduction	36
1.3.2 Boride Molten Oxide Electrolysis	36
1.4 Project Objectives	37
2.0 Broader Impacts	38
2.1 Engineering Ethics	38
2.2 Societal Impact	39
2.3 Environmental & Sustainability Impact	40
3.0 Background	41
3.1 Extractive Metallurgy Techniques	41
3.1.0 Mineral Processing	41
3.1.1 Hydrometallurgy	42

3.1.2 Pyrometallurgy	42
3.1.3 Electrometallurgy	42
3.2 Molten Oxide Electrolysis	43
3.2.0 MOE & The Applications	43
3.2.1 Benefits Vs. Drawbacks	44
3.2.2 Future Outlook Of Molten Oxide Electrolysis	45
3.3 Manganese Molten Oxide Electrolysis	45
3.3.0 The Properties Of Manganese	45
3.3.1 The Applications Of Manganese	46
3.3.2 Brockris' Papers	47
3.3.3 Winard's Paper	48
3.3.4 Manganese MOE Post Winard	50
3.4 Boron Reduction	51
3.4.0 Isolating Boron From A Compound	51
3.4.1 Boron Reduction Methods	52
3.4.2 Environmental Impact Of Borate Processing	53
3.5 Borides Synthesis	53
3.5.0 Aluminum Magnesium Boride	53
3.5.1 Zirconium DiBoride	54
3.5.2 Boride Synthesis Research	56
3.5.3 Silicothermic Reaction	60
3.5.4 Carbothermic Reduction	61
3.5.5 Boride Synthesis Through Molten Oxide Electrolysis	62
3.5.6 Carbothermic Reduction Vs. Molten Oxide Electrolysis,	63
3.6 Calculation Parameters	64
3.6.0 Desired Calculation Research	65
3.6.1 Pseudo Binary & Ternary Phase Diagrams	65
3.6.2 Nominal Cathode-To-Anode Distance	66
3.6.3 Faradaic Efficiency	70
3.6.4 Energy Efficiency	71
4.0 Methodology	72
4.1 The Action Items	72
4.2 Action Item Completion	74
4.2.0 Research & Literature Review	74
4.2.1 Constructing A Pseudo-Binary Phase Diagram & Ternary Phase Diagram	75
4.2.2 Constructing The Fugacity Trend Of The Seven Compositions	77
4.2.3 Constructing The Viscosity Trend Of The Seven Compositions	82
4.2.4 Deciding The Operation Temperature & Electrolyte Composition	83

4.2.5 Calculating The Overall Reaction Energy & Potential	84
4.2.6 Calculating The Half-Cell Reaction Energies & Potentials	88
4.2.7 Investigating The Mass Balance Of The Reaction	92
4.2.8 Investigating The Energy Balance Of The Reaction	95
4.2.9 Calculating The Nominal Cathode-To-Anode Distance Of The Electrolytic Cell	99
4.2.10 Investigating The Faradaic & Energy Efficiency Of The Reaction	103
4.2.11 Endothermic Or Exothermic	107
5.0 Results & Analysis	109
5.1 Aluminum Magnesium Boride	109
5.1.0 Pseudo-Binary Phase Diagram	109
5.1.1 Isothermal Section	111
5.1.2 Vapor Pressure Trend Of The Seven Compositions	114
5.1.3 Viscosity Trend Of The Seven Compositions	118
5.1.4 Deciding The Desired Composition & Operating Temperature	120
5.1.5 Overall Reaction Energy & Potential	121
5.1.6 Half-Cell Reaction Energy & Potential	126
5.1.7 Mass Balance	131
5.1.8 Energy Balance	133
5.1.9 Nominal Cathode-To-Anode Distance	138
5.1.10 Faradaic Efficiency	141
5.1.11 Energy Efficiency	144
5.1.12 Endothermic Or Exothermic	145
5.2 Zirconium Diboride	146
5.2.0 Pseudo Binary Phase Diagram	146
5.2.1 Isothermal Section	147
6.0 Conclusions	152
6.1 Aluminum Magnesium Boride	152
6.2 Zirconium DiBoride	153
7.0 A New Approach Proposed	155
7.1 Introducing A Hydrogen Flux	155
7.1.0 The Benefits Of Introducing A Hydrogen Flux Into A Molten Oxide Electrolysis Reaction	155
7.1.1 The Ramifications Of Introducing A Hydrogen Flux Into A MOE Reaction	156
7.2 Pairing Molten Oxide Electrolysis With A Hydrogen Flux To Produce Aluminum Magnesium Boride	158
7.2.0 Calculating The Individual Moles Of The Elements & Moles Of Oxygen Gas	158
7.2.1 Calculating The Moles Of The Individual Products Of The Reaction & Oxygen Partial Pressures For Different Amounts Of Oxygen Gas Present	160
7.2.2 Calculating The Mole Fractions Of The Individual Products Of The Reaction For	

Different Amounts Of Oxygen Gas Present	164
7.2.3 Mapping Out The Hydrogen Flux	166
7.2.4 Deciding Where To Begin MOE After Flux Is Introduced Into Reaction	171
7.2.5 How Much Energy Is Saved With The Introduction Of Our Hydrogen Flux	175
8.0 Future Recommendations	180
8.1 General Recommendations	180
8.1.0 Literature Knowledge	180
8.1.1 Division of Roles	181
8.1.2 Experimenting With FactSage	182
8.2 Specific Recommendations	183
8.2.0 Equilibrium Module	183
8.2.1 Utilize Online Tutorials and Forums	186
8.2.2 Directed Experimentation	188
References	189
Appendix A: Manganese MOE	197
Figures	197
Tables	203
Appendix B: Aluminum Magnesium Boride MOE	211
Figures	211
Tables	225
Appendix C: Zirconium Diboride MOE	241
Figures	241
Appendix D: Miscellaneous	245
Figures	245

List Of Figures

Figure 1: A diagram of an electrolytic cell. Point 1 is the position of the anode. Point 2 is where the anode is electrically connected. Point 3 is the graphite anode. Points 4 and 8 are the tanks in which the water is cooled. Point 5 is a graphite anode in the shape of a cylinder. Point 6 is the location of the cover that holds over the graphite cylinder. Point 7 is a refractory removable plug (there are 2). Points 9 and 10 are refractory lining (9 is concrete, and 10 is manganese). Point 11 is the external metal-based sheath of the system. Point 12 is the cathode (Winard et al., 1977).

Figure 2: A process, shown by a flowchart, in which boron is isolated from a compound (Nakanishi & Murphy, 2015).

Figure 3: The invention of the mechanism responsible for housing and helping conduct the efficient and pure production of metal borides through fused salt electrolysis (Sindebad).

Figure 4: A summarized flowchart of the generalized process taken to ensure the completion of this project.

Figure 5: A base isothermal section, which we graphed, of MnO, SiO₂, and Al₂O₃

Figure 6: Liquidus projection we constructed of MnO, SiO₂, and Al₂O₃

Figure 7: Fugacity Trend Of All Seven Compositions Of MnO-SiO₂-Al₂O₃ Graphed Out In A Temperature Vs. Fugacity Graph

Figure 8: Focused Fugacity Trend Of All Seven Compositions Of MnO-SiO₂-Al₂O₃ Graphed Out In A Temperature Vs. Fugacity Graph. The Dotted Line Shows The Fugacity Value Of 10⁻³ atm.

Figure 9: The Overall Reaction Energy Trend Graph from 1100 to 1300 °C. This graph is displayed as Temperature (in degrees Celsius) versus the change in Gibbs Energy (J).

Figure 10: The Overall Reaction Potential Trend Graph from 1100 to 1300 °C. This graph is displayed as Temperature (in degrees Celsius) versus the Voltage Requirement (V).

Figure 11: The Overall Reaction, Cathodic Reaction, and Anodic Reaction Energy Functions for the Manganese reaction graph vs. Temperature.

Figure 12: The Overall Reaction, Cathodic Reaction, and Anodic Reaction Potential Functions for the Manganese reaction vs. Temperature.

Figure 13: An illustration of what is occurring in the electrolytic cell. On the left-hand side, it shows 1 mole of solid-phase MnO being inserted into the cell alongside air at a rate of 1 liter/minute. Inside the cell (the t-shaped figure) is where the reactions occur, where ultimately, Manganese would subside to the bottom of the cell, and oxygen gas would be produced and rise to the top. All of the gasses, including oxygen gas, leave the system through the outlet shown on the right-hand side of the figure.

Figure 14: The total Mass Balance of Mn graphed in terms of Fugacity rate (atm/min) vs. time (min). The graph is mapped out over a full day in terms of minutes.

Figure 15: The total Energy Balance of Mn graphed in terms of enthalpy (kJ) vs. temperature (K).

Figure 16: The Energy Balances of Mn graphed in terms of enthalpy (kJ) vs. temperature (K). This shows the enthalpy changes at each stage of the reaction, as well as that for the total reaction.

Figure 17: The Pseudo-Binary Phase Diagram Between AlMgB_{14} and O_2 from a temperature range of 1000 °C to 4000 °C. The 23 most significant resulting compositions are shown and labeled with a key.

Figure 18: The Pseudo-Binary Phase Diagram Between AlMgB_{14} and O_2 from a temperature range of 1200°C to 1600°C .

Figure 19: The Isothermal Section between B_2O_3 , MgO , and Al_2O_3 at 1440°C . The seven compositions we examine are the purple “x’s” in the Slag-liquid region.

Figure 20: The Isothermal Section between B_2O_3 , MgO , and Al_2O_3 at 1600°C . The purple “x’s” labeled one through seven are the same seven compositions consistent with the same region of 1440°C .

Figure 21: The Fugacity Trend of B_2O_3 from 900 to 2000°C . This graph is displayed as Temperature (in degrees Celsius) versus the Base-10 Log of Fugacity in (atm).

Figure 22: The “focused” Graph of the Fugacity Trend of B_2O_3 from 1200 to 16000°C . This graph is displayed as Temperature (in degrees Celsius) versus the Base-10 Log of Fugacity in (atm).

Figure 23: Graph of viscosity vs. temperature of selected compositions from 900 to 2000°C

Figure 24: Graph of viscosity vs. temperature of selected compositions from 1200 to 1600°C

Figure 25: The Overall Reaction Energy Trend Graph from 1200 to 16000°C . This graph is displayed as Temperature (in degrees Celsius) versus the change in Gibbs Energy (J).

Figure 26: The Overall Reaction Potential Trend Graph from 1200 to 1600°C . This graph is displayed as Temperature (in degrees Celsius) versus the Voltage Requirement (V).

Figure 27: The Graph of the Overall Reaction, Cathodic Reaction, and Anodic Reaction Energy Functions for the AlMgB_{14} reaction.

Figure 28: The Graph of the Overall Reaction, Cathodic Reaction, and Anodic Reaction Potential Functions for the AlMgB_{14} reaction.

Figure 29: The total Mass Balance of AlMgB_{14} , graphed in terms of Fugacity rate (atm/min) vs. time (min). The graph is mapped out over a full day in terms of minutes.

Figure 30: The partial Mass Balance of AlMgB_{14} , graphed in terms of Fugacity rate (atm/min) vs. time (min). The graph is mapped out over a full day in terms of minutes. This graph only contains the trend of magnesium and aluminum.

Figure 31: The total Energy Balance of AlMgB_{14} , graphed in terms of enthalpy (kJ) vs. temperature (K).

Figure 32: The Energy Balances of AlMgB_{14} , graphed in terms of enthalpy (kJ) vs. temperature (K). This shows the enthalpy changes at each stage of the reaction, as well as that for the total reaction.

Figure 33: The Pseudo-Binary Phase Diagram Between ZrB_2 and O_2 from a temperature range of 200 °C to 4000 °C.

Figure 34: The Isothermal Section between Zr, B, and O_2 at 1200 °C.

Figure 35: The Isothermal Section between Zr, B, and O_2 at 1500 °C.

Figure 36: The Isothermal Section between Zr, B, and O_2 at 2200 °C.

Figure 37: The Mole Fraction Data from Table 35 graphed out in a Mole Fraction Of Oxygen Vs. Mole Fraction Of Products relation.

Figure 38: Illustration of the Reaction System with the Introduction of Hydrogen Gas (the brown arrow) entering the reaction.

Figure 39: The data from Table 38 graphed out in a Hydrogen Percent vs. Base-10 Log Of Partial Pressure distribution.

Figure 40: The graph of the accumulated data from the reaction products, oxygen partial pressure, and percent of hydrogen gas introduced.

Figure 41: The graph from Figure 40 with labels of where the hydrogen gas influx would begin and end and where the MOE reaction would begin and end.

Figure 42: The regular features that come within the Equilib module of FactSage.

Figure 43: The regular features that come within the Equilib module of FactSage (cont.).

Figure 44: Mathematical tree delineating the flowchart of FactSage computation.

Figure 45: A bullet list of calculations the company Saint Gobain takes interest in Manganese in regards to MOE.

List Of Tables

Table 1: Melting point and mole fractions of MnO, SiO₂, and Al₂O₃

Table 2: Vapor Pressure/Fugacity Of Seven Compounds Of MnO-SiO₂-Al₂O₃ Displaying Largest-Fugacity Compound (Manganese) From 1100°C To 1300°C

Table 3: Raw data of the viscosity of selected compositions at a range of temperatures from the Mn MOE reaction.

Table 4: The Overall Reaction Energy, with a temperature range from 1100°C To 1300°C and the corresponding change in Gibbs Energy for each temperature. The difference in Gibbs Energy of the desired Operating Temperature is highlighted at the bottom of the table.

Table 5: The Voltage Requirement is split into two tables. The first table shows the Nernst Equation and its rearranged form to calculate the voltage requirement of the electrolytic cell at the operating temperature. The second table shows the change in Gibbs Energy at 1260 °C, the number of moles or electrons transferred as 2, and the Faraday's constant, all used to calculate the voltage requirement.

Table 6: The calculations made to obtain the Overall Reaction Energy and Potential formulas for the Manganese reaction.

Table 7: The calculations made to obtain the Cathodic Reaction Energy and Potential formulas for the Manganese reaction.

Table 8: The calculations made to obtain the Anodic Reaction Energy and Potential formulas for the Manganese reaction.

Table 9: The calculations made to obtain the Fugacity rates of Manganese over time for the Mass Balance of Mn.

Table 10: The calculations made to obtain the Energy Balance formula through the Gibbs Energy calculation in calculating the formula of Entropy Change for Mn MOE.

Table 11: The calculations made to obtain the Energy Balance formulas through the Gibbs Energy calculation in calculating the formula of Entropy Change. These formulas are the formulas generated of the measured energy balance at each stage of the total reaction. This is for the Mn MOE reaction.

Table 12: The calculation process to obtain the Nominal Cathode-To-Anode Distance for the electrolytic cell containing the Mn MOE reaction.

Table 13: The calculation process to obtain the Actual Produced Mass of Mn. This was done assuming the reaction occurred at a 90% faradaic efficiency.

Table 14: The calculation process to obtain the Energy Efficiency of Mn. This was done assuming the reaction occurred at a 90% faradaic efficiency.

Table 15: Vapor Pressure/Fugacity Of Seven Compounds Of MgO-B₂O₃-Al₂O₃ Displaying Largest-Fugacity Compound (B₂O₃) From 900°C To 2000°C.

Table 16: Raw data of the viscosity of selected compositions at various temperatures.

Table 17: The Overall Reaction Energy, with a temperature range from 1200°C To 1600°C and the corresponding change in Gibbs Energy for each temperature. The difference in Gibbs Energy of the desired Operating Temperature is highlighted at the bottom of the table.

Table 18: The Voltage Requirement is split into two tables. The first table shows the Nernst Equation and its rearranged form to calculate the voltage requirement of the electrolytic cell at the operating temperature. The second table shows the change in Gibbs Energy at 1600 °C, the number of moles or electrons transferred as 47, and the Faraday's constant, all used to calculate the voltage requirement.

Table 19: The calculations made to obtain the Overall Reaction Energy and Potential formulas for the AlMgB_{14} reaction.

Table 20: The calculations made to obtain the Cathodic Reaction Energy and Potential formulas for the AlMgB_{14} reaction.

Table 21: The calculations made to obtain the Anodic Reaction Energy and Potential formulas for the AlMgB_{14} reaction.

Table 22: The calculations made to obtain the Fugacity rate of Boron, Magnesium, and Aluminum over time for the Mass Balance calculation of AlMgB_{14} .

Table 23: The Results Window from FactSage's Reaction Module for the Total Reaction.

Table 24: The calculations made to obtain the Energy Balance formula through the Gibbs Energy calculation in calculating the formula of Entropy Change for AlMgB_{14} MOE.

Table 25: The Results Window from FactSage's Reaction Module for the Reactants heating up.

Table 26: The Results Window from FactSage's Reaction Module for the Reaction after the reactants were heated up.

Table 27: The calculations made to obtain the Energy Balance formulas through the Gibbs Energy calculation in calculating the formula of Entropy Change. These formulas are the formulas generated of the measured energy balance at each stage of the total reaction. This is for the AlMgB_{14} MOE reaction.

Table 28: The calculation process to obtain the Nominal Cathode-To-Anode Distance for the electrolytic cell containing the AlMgB_{14} MOE reaction.

Table 29: The calculation process to obtain the Actual Produced Mass of AlMgB_{14} . This was done assuming that the reaction occurs at 90% faradaic efficiency.

Table 30: The calculation process to obtain the Energy Efficiency of AlMgB_{14} . This was done assuming that the reaction occurs at 90% faradaic efficiency.

Table 31: The calculation made to obtain individual amounts of moles for the elements of AlMgB_{14} .

Table 32: The menu window to the FactSage calculations for oxygen partial pressure, moles of Slag #1, moles of Slag #2, total moles of AlB_2 , total moles of MgB_2 total moles of Al_2O_3 , total moles of MgB_7 , total moles of AlB_{12} , total moles of B, and total moles of AlMgB_{14} for each specific mole-amount of O_2 . Each of the constraints selected is shown in this table.

Table 33: The results window of the FactSage calculations for oxygen partial pressure, moles of Slag #1, moles of Slag #2, total moles of AlB_2 , total moles of MgB_2 total moles of Al_2O_3 , total moles of MgB_7 , total moles of AlB_{12} , total moles of B, and total moles of AlMgB_{14} for each specific mole-amount of O_2 . This particular example is for when we had 0.2157 moles of O_2 .

Table 34: The FactSage calculations for oxygen partial pressure, moles of Slag #1, moles of Slag #2, total moles of AlB_2 , total moles of MgB_2 , total moles of Al_2O_3 , total moles of MgB_7 , total moles of AlB_{12} , total moles of B, and total moles of AlMgB_{14} for each specific mole-amount of O_2 .

Table 35: The calculations for the mole fractions of the products— AlB_2 , MgB_2 , Al_2O_3 , MgB_7 , AlB_{12} , B, AlMgB_{14} , and the Slag-Liquid—for each specific mole fraction of O_2 .

Table 36: The menu window to the FactSage calculations for determining the moles of Hydrogen Gas that will satisfy the Oxygen Partial Pressure conditions of our unchanged reaction.

Table 37: The results window of the FactSage calculations for determining the moles of Hydrogen Gas that will satisfy the Oxygen Partial Pressure conditions of our unchanged reaction.

This range of percent of Argon goes from 80% to 100%. This particular example is for when we had 96% of Argon.

Table 38: The tabulation of the results window of the FactSage calculations for determining the moles of Hydrogen Gas that will satisfy the Oxygen Partial Pressure conditions of our unchanged reaction. This range of percent of Argon goes from 80% to 100%. In this table, we presented the percent of Argon (/100) and the corresponding percent of Hydrogen Gas (/100), alongside the oxygen partial pressure for each particular instance and the Base-10 logarithmic calculation of that pressure.

Table 39: The tabulation of the combination of our previous results from Table 33 and Table 37. This table shows the range of our oxygen partial pressure when we alter the oxygen gas's mole fraction (disregarding H₂) in base-10 logarithmic form. It also shows the hydrogen percentage from 0 to 20% and the corresponding oxygen partial pressure (regarding H₂) in base-10 logarithmic format.

Table 40: The tabulation for the mole fraction O₂ required to obtain the maximum yield of AlMgB₁₄.

Table 41: The calculation for the moles O₂ at the three points of interest that would assist in attaining the amount of energy saved.

Table 42: The calculation for the amount of energy saved.

1.0 Introduction

1.1 Molten Oxide Electrolysis

1.1.0 The MOE Process & Its Applications

Molten Oxide Electrolysis (MOE) has been shown to be efficient for the extraction of metals, particularly those with high melting points. In the MOE process, oxygen and metals are produced by electrifying a metal oxide in a molten salt electrolyte (Wei et al., 2019). This method provides more benefits, including lower energy consumption, environmental impact and risks, and higher metal purity than traditional pyrometallurgical and hydrometallurgical processes.

Numerous studies have emphasized the promise of MOE as a sustainable approach to producing metal. A study showed how to employ MOE to extract titanium and other reactive metals, highlighting this method's effectiveness (Li et al., 2017). The application of MOE to the sustainable extraction of metals has been recognized for its potential to lower carbon emissions and increase the metals industry's sustainability and application (Morita et al., 2020).

The low energy consumption of MOE over conventional techniques is one of its main advantages. MOE uses less energy to heat its metals because it runs at lower operating temperatures than pyrometallurgical operations (Wei et al., 2019). Additionally, using renewable energy sources to generate electricity helps MOE reduce its carbon footprint (Morita et al., 2020).

The improved purity of the metal produced is another crucial benefit of MOE. Compared to the 99.7% purity of titanium that can be produced using the Kroll method, MOE can do it with

a purity of up to 99.99% (Li et al., 2017). This is so that impurities in the reducing agents used in pyrometallurgical operations will not contaminate MOE's lower operating temperatures.

MOE's potential uses are manufacturing challenging high-purity metals (Li et al., 2017), using a cutting-edge extraction method in which acclaimed metals such as aluminum, titanium, and zirconium were successfully produced (Wei et al., 2019).

By selectively removing various metals from their oxides, MOE can create metal alloys in addition to high-purity metals (Li et al., 2017). The capacity to produce high-performance alloys with exact compositions significantly impacts the metallurgical sector. In as much, the MOE process allows the metals to be directly sent to a metallurgical ladle without reheating.

MOE could also be used to recycle waste products containing metal. Industrial waste, such as old catalysts and electronic trash, has been treated with MOE to recover metals (Morita et al., 2020). This method lessens trash disposal's environmental impact while recovering valuable materials.

1.1.1 MOE Process Through Fact Sage

This report will explore the fundamental principles of MOE and its various applications. We will also examine the role of FactSage, a software that assists in calculating various thermodynamic and kinetic parameters critical for understanding the MOE process. FactSage is a widely used computational tool that can predict phase equilibria, thermodynamic properties, and phase diagrams for complex systems involving multiple phases and components.

FactSage enables user manipulation to hypothesize what will occur in a given reaction. The use of FactSage has dramatically contributed to the understanding of MOE by providing accurate and reliable data on various parameters such as activity coefficients, Gibbs free energy,

enthalpy, and entropy. This data is essential for predicting the behavior of molten salts, oxides, and metals under different conditions and for designing optimized MOE processes.

Several studies have utilized FactSage to investigate various aspects of MOE, such as the effect of temperature, composition, and electrolyte properties on the electrochemical behavior and the production efficiency of different metals. In addition, FactSage has been used to optimize the design of MOE cells and to predict the formation of undesirable byproducts during the process.

This report aims to provide a comprehensive overview of the MOE process and its potential applications. Using FactSage, we can better understand MOE's complex thermodynamic and kinetic phenomena and optimize efficient and sustainable metal extraction.

1.2 Borides

1.2.0 Application Of Boron & Borides

Boron and its derivatives have found significant use in various applications due to their unique chemical properties (Nakanishi & Murphy, 2015). Boron is a versatile element used in various technological applications because it has metalloid and semiconductor qualities. High-purity boron was first obtained in 1892 by reacting boric oxide with magnesium (Nakanishi & Murphy, 2015). In contrast to the natural world, boron is found in compounds containing oxygen. Due to their numerous applications, boron-related chemicals and materials have since been in great demand. The reinforcement of glass and filaments on tungsten wires is one such instance.

Today's industries use zirconium diboride (ZrB_2), a widely used boride, in various ways. (Government of India Department of Atomic Research). It is frequently utilized in high-temperature electrodes, thermowell tubes, and space re-entry vehicle thermal protection systems. ZrB_2 makes materials for neutron absorption, wear-resistant coatings, and molten metal crucibles. According to the Government of India Department of Atomic Research, this material is desired for its high hardness, wear resistance, melting point, and thermal conductivity. Saint Gobain, a global materials and technology company, is heavily involved in borides, particularly zirconium diboride, because of its exceptional qualities and applications. As a result, we are searching for an efficient and affordable way to produce these borides.

1.2.1 Saint Gobain's Work With Borides

Borides have high melting points, hardness, and excellent thermal and electrical conductivity, promising them for various high-temperature applications. Saint Gobain has recently conducted several research projects on boride materials. In this report, we will discuss some of the recent projects conducted by Saint Gobain related to borides.

One recent study conducted by Saint Gobain on borides was documented under the title: "Boride-based ceramics: Synthesis, properties and applications" (Chaput, 2019).

This review article overviews the synthesis, properties, and applications, including ZrB_2 , HfB_2 , and TiB_2 . The authors discuss various synthesis methods, such as powder metallurgy and chemical vapor deposition, and the resulting properties of the materials, such as hardness, thermal conductivity, and electrical conductivity (Chaput, 2019). The review also highlights potential applications of boride-based ceramics, such as in armor, cutting tools, and electronic devices.

In another recent study by Saint Gobain on borides, the authors synthesized ZrB_2 using spark plasma sintering and investigated the resulting mechanical properties of the material (Kanitkar et al., 2021). The authors found that the ZrB_2 had high hardness, excellent wear resistance, and good fracture toughness, making it promising for use in cutting tools and wear-resistant coatings.

Saint Gobain has also researched the use of boride coatings for corrosion protection. In one recent study on this topic, the authors coated carbon steel with TiB_2 using magnetron sputtering and studied the corrosion behavior of the coated material in chloride and sulfate solutions (Li et al., 2020). The authors found that the TiB_2 coating provided excellent corrosion protection, reducing the corrosion rate by up to 85% compared to uncoated carbon steel. The authors suggest that the TiB_2 coating could be used in various applications, such as chemical and petrochemical industries (Li et al., 2020).

In another study, the authors investigated using molten oxide electrolysis to produce ZrB_2 from ZrO_2 and B_2O_3 precursors (Miroshnichenko et al., 2021). The experiments were conducted using a laboratory-scale MOE cell, and the effect of various parameters such as temperature, current density, and electrolyte composition on the production efficiency and purity of ZrB_2 was studied. The authors found that MOE could successfully produce ZrB_2 with high purity and yield, and the process parameters could be optimized for efficient and cost-effective production (Miroshnichenko et al., 2021).

1.2.2 Saint Gobain's Interest In Boride Extraction Through The MOE Process

Great melting temperatures, hardness, and excellent thermal and electrical conductivity characterize the class of materials known as borides. There are numerous possible uses for

borides in sectors like electronics, aircraft, and defense. An international manufacturer of materials and technology called Saint Gobain has expressed interest in employing molten oxide electrolysis to remove borides.

Saint Gobain has concentrated on producing zirconium diboride by utilizing MOE. ZrB_2 has outstanding thermal and mechanical applications. The traditional processes for making ZrB_2 are costly and time-consuming. MOE offers a potential response to these problems.

With the help of laboratory-scale trials, Saint Gobain has already achieved considerable strides in this field by successfully producing ZrB_2 utilizing MOE. The company attempts to scale up the procedure and improve product application specifications.

Overall, molten oxide electrolysis has a wide range of possible applications, and Saint Gobain's interest in boride extraction using this method demonstrates how it has the power to alter the field of materials science and engineering completely.

1.3 Synthesis Of Borides

1.3.0 Silicothermic Reactions

Due to their affordability and accessibility, silicothermic reactions have been the primary method for producing magnesium metal. However, it has several drawbacks, including high energy needs, emissions, and waste creation. Despite this, it is still employed because it can generate magnesium of high purity and can be done at relatively low temperatures. More sustainable techniques are being sought, such as carbothermic reduction, which uses carbon instead of silicon as the reducing agent (Svendsen & Westlund, 2021).

1.3.1 Carbothermic Reduction

Carbothermic reductions are one-step reduction processes that produce metal and carbon monoxide gas by using carbon as a reducing agent. Comparing carbothermic operations to silicothermic processes, the former requires less energy, emits fewer pollutants, and generates less waste (Svendsen & Westlund, 2021). An illustration of a carbothermic reaction is the employment of zirconium diboride in combination with boron carbide and carbon. Carbothermic methods offer benefits in generating high-purity products with less energy use and more application flexibility. However, to further increase the sustainability of metal production. One such technology is boride synthesis by molten oxide electrolysis (Bhabha Atomic Research Centre).

1.3.2 Boride Molten Oxide Electrolysis

Scientists are interested in a novel method called the molten oxide electrolysis (MOE) method for synthesizing borides. It can produce high-purity borides with controlled stoichiometry and form at lower temperatures and less energy. Numerous borides, including zirconium, titanium, and hafnium diborides, can be made using MOE, and recent research into this possibility has produced encouraging findings with high yields and low energy consumption (Kjlsseth et al., 2019). Despite difficulties, including high equipment costs and a lack of suitable electrolytes, researchers continue optimizing the process parameters for different borides, including producing nanostructured borides with distinct properties and applications (Gupta et al., 2019).

1.4 Project Objectives

This project aimed to find a commercial method of producing borides through molten oxide electrolysis. Zirconium DiBoride (ZrB_2) and Aluminum Magnesium Boride ($AlMgB_{14}$) Using FactSage, a database that simulates thermodynamic modeling and small-scale reactions, characteristics of these electrolyte-based reactions were explored. With these FactSage calculations, literature reviews, self-done calculations, and data collection and organization, commercial methods were explored for these borides.

2.0 Broader Impacts

2.1 Engineering Ethics

Metal borides with high modulus of elasticity, often known as borides MOE, have demonstrated good mechanical qualities that make them desirable for various technical applications. These materials suit hostile settings because of their high hardness, melting points, and wear and corrosion resistance. The broader influence of borides MOE is crucial since they present chances for creating cutting-edge materials with enhanced functionality and durability. In the automotive, aerospace, and manufacturing industries, borides MOE may improve the performance of cutting tools, bearings, and other high-stress applications (Wang et al., 2020).

The use of borides MOE offers many potentials, but it is vital to consider the moral ramifications of doing so. Engineers are expected to follow engineering ethics by considering how their actions may affect society, the environment, and future generations. For instance, because borides MOE demand a lot of energy and resources to produce, their use may raise concerns about their sustainability. Another study found that the synthesis of borides MOE frequently includes high-temperature processes that take up much energy and produce many greenhouse emissions (Zhang et al., 2017).

According to a third study, using borides MOE in industrial applications necessitates carefully evaluating their possible effects on people and the environment and putting the necessary safety precautions to guard against exposure to dangerous materials (Abdelrahman et al., 2021).

2.2 Societal Impact

Metal borides with high modulus of elasticity, often known as borides MOE, have a wider influence than engineering and manufacturing because they can significantly improve societal conditions. According to one study, borides MOE have been studied for use in medical implants due to their excellent biocompatibility, high strength, and resilience to wear (Gao et al., 2020). The quality of life for people and communities worldwide could be enhanced by using borides MOE in various applications, such as medical implants, electronics, and renewable energy systems.

Borides MOE has been researched for its possible use in photovoltaic and thermoelectric applications in renewable energy. For instance, a recent study showed that boride-based thermoelectric materials could considerably boost the effectiveness of thermoelectric generators, which turn waste heat into energy (Huda et al., 2019). Utilizing such materials might help create a future with fewer greenhouse gas emissions and more sustainable energy sources.

Additionally, using borides MOE in electronics has the potential to enhance device performance and lessen the adverse environmental effects of electronic waste. A study on boride-based materials found that these materials can potentially increase electronic devices' mechanical strength and thermal conductivity, resulting in more effective and long-lasting gadgets (Wang et al., 2018). Due to their exceptional wear- and corrosion resistance, using these materials in electronics may also help reduce the quantity of electronic waste produced.

2.3 Environmental & Sustainability Impact

Molten oxide electrolysis of borides has the potential to have an enormous positive environmental impact and promote sustainable growth. These materials have numerous potential uses in various industries, including construction, transportation, and renewable energy. Boride MOE use can lessen the environmental impact, promote energy efficiency, and increase the toughness and lifetime of buildings and products.

Borides MOE has been researched for photovoltaic and thermoelectric applications in renewable energy. A 2019 study found that the efficiency of thermoelectric generators, which turn waste heat into energy, might be significantly increased using boride-based thermoelectric materials (Huda et al., 2019). Utilizing such materials might help create a future with fewer greenhouse gas emissions and more sustainable energy sources. Borides MOE could also increase solar cells' performance and toughness, resulting in a longer lifespan and less waste.

According to another 2019 study, boride-based coatings have been developed for automotive engines, reducing friction, wear, and fuel consumption (Lee et al., 2019). These coatings could reduce emissions and contribute to a more sustainable transportation system. Furthermore, using borides MOE in transportation can reduce environmental impact and improve energy efficiency.

Using borides MOE in building and infrastructure can also boost a structure's durability and longevity, lowering the environmental effect of maintaining or replacing it. The development of boride-based coatings for steel structures has improved corrosion resistance and lengthened longevity, according to a more recent study in 2021 (Wang et al., 2021). Furthermore, adding borides MOE to concrete can boost its strength and toughness, lowering the frequency of repairs and replacements.

3.0 Background

To ensure the completion of this project, much research and literature review had to be conducted to gain a greater understanding of the project's overall scope.

3.1 Extractive Metallurgy Techniques

Extractive metallurgy is a branch concerned with extracting metals from natural mineral sources (Evans, 2003). Mineral processing, hydrometallurgy, pyrometallurgy, and electrometallurgy are the primary ore extraction methods in extractive metallurgy.

3.1.0 Mineral Processing

Mineral processing is a technique for dissolving mineral structures using physical forces such as crushing, grinding, sieving, and other procedures. (Wills & Finch, 2016). The mining industry uses the method to extract base metals, precious metals, and rare earth elements. The ore is crushed into tiny fragments to liberate the valuable minerals, then ground to reduce particle size. The minerals are then separated using physical techniques such as gravity separation, magnetic separation, or froth flotation. The final product is the concentrate, which includes the desired metal.

3.1.1 Hydrometallurgy

Hydrometallurgy is the extraction of metals from ore using aqueous liquids (Wills & Finch, 2016). The ore is crushed into tiny pieces before leaching with an acid or alkali solution. The metal ions are removed from the leach solution via solvent extraction, ion exchange, or precipitation. This method is commonly used in mineral extraction to extract copper, zinc, nickel, cobalt, and gold.

3.1.2 Pyrometallurgy

Pyrometallurgy is a method that uses high temperatures to enable chemical reactions that separate the required elements (Wills & Finch, 2016). This technique extracts iron, copper, lead, zinc, and tin metals. The procedure entails heating the ore in a furnace to temps above the melting point of the metal. As it melts, the metal separates from the gangue elements. The contaminants are eliminated using chemical processes like oxidation, reduction, or slagging. The final product is metal in its purest state.

3.1.3 Electrometallurgy

The process of electrometallurgy uses electrolysis to extract pure metals from a solution (Paul et al., 2020). The metal is dissolved in an electrolyte, and an electric charge is passed through the solution. The impurities are eliminated as sludge or gas, while the pure metal is deposited on the cathode. The cathode reduces metal ions, while the anode oxidizes anions. This method is extensively used to purify copper, nickel, and zinc.

3.2 Molten Oxide Electrolysis

3.2.0 MOE & The Applications

An electrometallurgical technique called molten oxide electrolysis (MOE) enables metal production in a liquid state from an oxide supply of raw material (Urquhart, 2020). In this process, metal is extracted using electrometallurgy, which uses electrolysis to refine and produce a solution containing metals. Compared to conventional extractive metallurgy methods, molten oxide electrolysis provided a streamlined procedure and reduced energy consumption. (Urquhart, 2020). This promising approach to steel production offers lower carbon emissions and the ability to produce carbon-free metals, making it an ideal technology for sustainable production.

Molten oxide electrolysis is a promising route for the steelmaking process. In contrast to other techniques, this one emits fewer carbon emissions, yields pure metals (devoid of carbon), and fosters oxygen for planetary exploration (Urquhart, 2020). However, until recent years, the MOE process never proved suitable for commercial uses because it utilized only anodes made of expensive or consumable materials. Since the anode material employed in this electrometallurgy process is resistant to total consumption in the oxidation reaction, it is possible to synthesize metal without using carbon (Urquhart, 2020). In light of this characteristic, MOE is a perfect technology for green metal manufacturing that lowers carbon emissions—yet another advantage of this developing procedure.

3.2.1 Benefits Vs. Drawbacks

Metals are extracted from their oxides using an electrolytic cell with a molten oxide electrolyte. Allanore described molten oxide electrolysis as a viable extractive metallurgy approach that simplifies the process and uses much less energy than traditional methods (Allanore et al., 2013). MOE is also seen to be a potential alternative for producing carbon-free metals and oxygen for space exploration.

When molten oxide electrolysis is compared to traditional extractive metallurgy processes, it is clear how much simpler the process is and how much less energy is consumed. This is one of the reasons why this strategy appears to be promising (Urquhart, 2020). Furthermore, MOE is a liquid-state direct metal manufacturing technique, which is particularly advantageous in manufacturing various metals.

However, several drawbacks to this electrometallurgy approach must be considered. The technique is expensive because it requires only consumable anode materials or extremely expensive and rare anodes (Urquhart, 2020). Second, obtaining resources can be difficult, mainly when producing iron, which demands a high temperature of 1600 degrees Celsius, at which most metals wear away (Urquhart, 2020).

To circumvent these constraints, Donald Sadoway of MIT advocated utilizing chromium anode alloys, which have been demonstrated to perform well in the MOE process (Urquhart, 2020). One approach uses inert anodes of titanium diboride (TiB₂) or cermet materials (Allanore et al., 2013). Because these anodes are not used throughout the process, it is possible to utilize a more cost-effective and environmentally beneficial option. Another field of research is the development of novel molten electrolytes with enhanced ionic conductivity and lower melting

points (Allanore et al., 2013). This could reduce the amount of energy required for the process, making it more appropriate for large-scale applications.

Despite ongoing research and development, MOE must still be considered the best practice (Allanore et al., 2013). MOE may become a more widely employed form of extractive metallurgy in the future as technology progresses. Despite the challenges, MOE is a highly researched and sought-after technology with extensive applications in various industries.

3.2.2 Future Outlook Of Molten Oxide Electrolysis

Unlike conventional steel manufacturing, which relies on fossil fuels, molten oxide electrolysis is more environmentally friendly (Boston Metal, 2023). Soon, molten oxide electrolysis can outperform all other extractive metallurgy processes. This process has the potential for substantial growth in the steel-making business in the coming years, with commercial iron-alloy plants expected to begin operations in 2023 and steel demonstration and testing plants slated for 2024 to 2025. MOE steelmaking is anticipated to be safe and commercially viable from 2025 to 2030.

3.3 Manganese Molten Oxide Electrolysis

3.3.0 The Properties Of Manganese

John Gottlieb Gahn, a Swedish chemist, found manganese in 1774. This transition metal can be found in the Earth's crust, oceans, and atmosphere. It is an essential trace element for all

life forms, including humans, engaged in various biological processes. It has the chemical symbol Mn and the atomic number 25 (Royal Society of Chemistry).

According to the Royal Society of Chemistry, Manganese has a melting point of 1246 degrees Celsius and a boiling point of 2061 degrees Celsius, rendering it a solid at room temperature. It has a density of 7.3 g/cm^3 , larger than iron. Manganese is a silvery-colored, rigid, brittle metal with high corrosion resistance. Additionally, it functions very well as a heat and energy conductor. The element can reside in several oxidation states, the most prevalent of which are +2, +3, +4, +6, and +7 (Royal Society of Chemistry).

Besides its physical and chemical properties, manganese has various applications in various disciplines.

3.3.1 The Applications Of Manganese

Due to its fragility, manganese is rarely used as a pure metal. However, it is widely used in alloys, with steel being its leading utility. According to the Royal Society of Chemistry, steel contains about 1% manganese, which improves its strength, workability, and wear resistance. Manganese steel alloy, which contains 13% Mn, is robust and is used for train tracks, safes, construction, gun barrels, and prison bars. Furthermore, a 1.5% Mn aluminum-manganese alloy is utilized to manufacture beverage cans to increase wear resilience to corrosion. Also, manganese can create extremely magnetic alloys with copper, antimony, and aluminum (Royal Society of Chemistry).

Manganese compounds are used in a variety of sectors. In contrast to manganese sulfate, manganese (IV) oxide is a catalyst and rubber ingredient. Manganese (II) oxide is potent in quantitative analysis, fertilizer production, and ceramics manufacturing.

Steel manufacturing is one of the most prominent uses for manganese. However, traditional steel manufacturing consumes a lot of energy and emits greenhouse gasses. To address this, a group of researchers created the manganese molten oxide electrolysis process, which has the potential to reduce energy consumption and greenhouse gas emissions significantly.

3.3.2 Bockris' Papers

Bockris' articles reported successful Mn production via electrolysis of MnO-SiO_2 (Allanore, 2014). This discovery has significant consequences for producing manganese and its alloys, providing a more energy-efficient and environmentally friendly alternative to traditional methods. Bockris also proposed a polarization-based carbothermic reduction of manganese ions by the carbon anode. This method can reduce energy consumption and production expenses, making it an appealing option for the manganese market.

Furthermore, Bockris' study has paved the way for future investigations into manganese and its alloy's electrochemical production. Researchers have since expanded on Bockris' work, investigating the use of different electrolyte systems, electrode materials, and operating conditions to increase the efficiency and yield of manganese production (Allanore, 2014).

The study by Bockris certainly helped the manganese industry grow and encouraged additional investigation in this area by other researchers. Bockris' papers helped lay the groundwork for many later studies, including Winard's.

3.3.3 Winard's Paper

The Winard paper details a successful Molten Oxide Electrolysis experiment in Manganese production patented in the United States and Europe in 1966 (Allanore, 2014). Winard did not use molten fluorides but used CaO-MgO-Al₂O₃-SiO₂ as a supporting electrolyte to facilitate the MnO reaction. The experiment resulted in a compelling performance of the carbon anode, which reduced carbon (0.4%) while increasing iron (2%) and silicon (11%), respectively, in the ferromanganese metal.

According to Winard and colleagues (Winard et al., 1977), in molten salt electrolysis for low carbon manganese, increasing the molten oxide ratio $(\text{CaO} + \text{MgO})/(\text{SiO}_2 + \text{Al}_2\text{O}_3)$ to greater than 0.75 with electrolysis between 1350 and 1450 °C yields a massive metal containing 94% Mn, 1% Si, and >0.5% C. However, the energy consumption for this procedure is excessive, and it was predicted that purified Mn would be more practical because of this. In order to control factory wear and generate heat to melt the charge, the type of electrolyte was freely selected, and the Mn content was maintained constant. Because pure MnO is expensive, brief research was initiated to test this.

The original selection of electrolyte mixtures was based on their melting points, and the most promising ones were then assessed for their conductivity and viscosities. The primary electrolytes selected were CaO-MgO-Al₂O₃ (Type I), CaO-MgO-SiO₂-Al₂O₃ (Type II), and Type III, created by partly replacing SiO₂ with Al₂O₃ in the Type II mixture. (Winard et al., 1977).

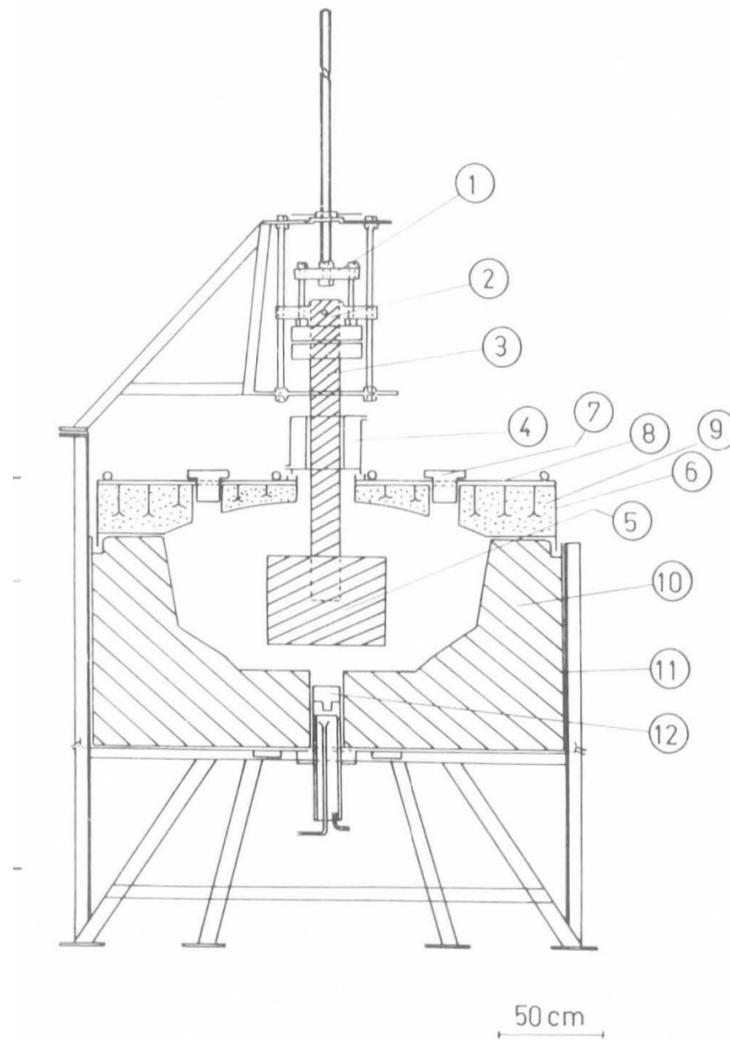


Figure 1: A diagram of an electrolytic cell. Point 1 is the position of the anode. Point 2 is where the anode is electrically connected. Point 3 is the graphite anode. Points 4 and 8 are the tanks in which the water is cooled. Point 5 is a graphite anode in the shape of a cylinder. Point 6 is the location of the cover that holds over the graphite cylinder. Point 7 is a refractory removable plug (there are 2). Points 9 and 10 are refractory lining (9 is concrete, and 10 is manganese). Point 11 is the external metal-based sheath of the system. Point 12 is the cathode (Winard et al., 1977).

The electrolytic cell, shown in Figure 1, included an anode, a ten cm-diameter graphite anode, a cooling tank for the water, a cylinder-shaped graphite anode (40 cm in diameter at 2400 A and 55 cm at 4800 A), a cover for the graphite cylinder, a steel sheath on this cover, two removable refractory plugs, and a refractory lining. (concrete and manganese). The objective was

to gather the information required for extrapolations to an industrial size rather than to collect data on specific energy consumption. To prevent refractory wear and the manipulation of the electrolyte composition during the experiment, experiments at 2400A required that the cell be purposefully constructed too large. (between 36 and 60 hours). The furnace was closed after the tests because the current efficiency was over 82%. The metal's ultimate chemical examination was representative. Computer simulations demonstrated that this particular setup could reach current efficiencies of 90%. (Winard et al., 1977).

These findings led to the industrialization of a plant in Belgium (Winard et al., 1977) and further research and applications soon.

3.3.4 Manganese MOE Post Winard

Interest in manganese molten oxide electrolysis was revived in 1995 following the release of Winard's experiment in 1977, which used a capacity of 50 kA and achieved 100% recovery of manganese with just 0.1% carbon (Allanore, 2014). Researchers investigated the direct current of the electric furnace that produced ferromanganese and validated the efficiency of the molten oxide electrolysis method for manganese extraction (Allanore, 2014).

3.4 Boron Reduction

3.4.0 Isolating Boron From A Compound

Due to the expense, separating boron from a compound can be difficult. However, there are several ways to create a high-purity boron complex. Sodium borates react with aqueous ammonium chloride to produce ammonium pentaborate, producing boric oxide from sodium borate minerals without creating a high-purity boric acid (Nakanishi & Murphy, 2015). The ammonia and water are then removed through heating.

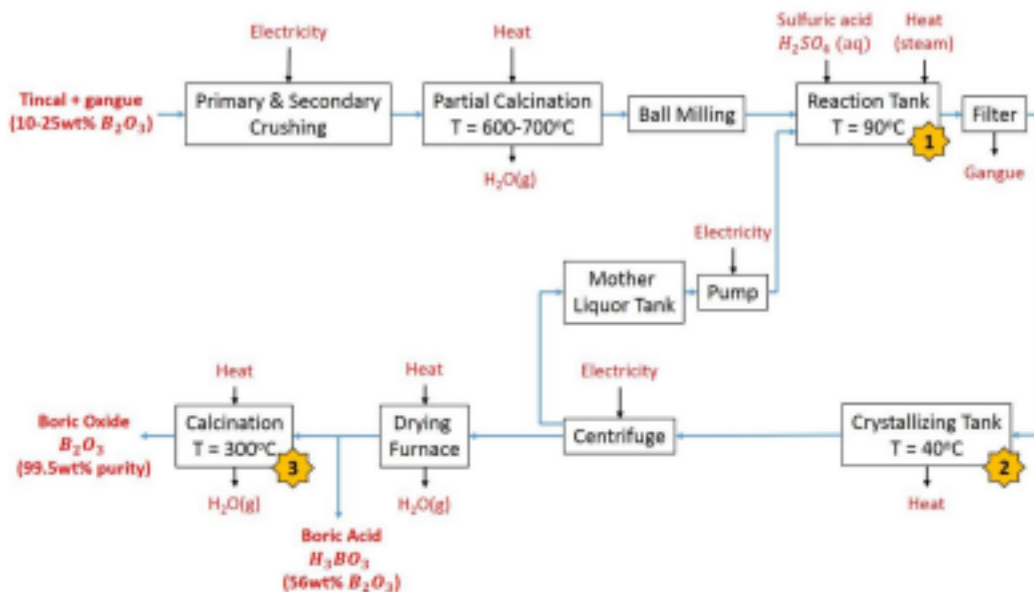


Figure 2: A process, shown by a flow chart, in which boron is isolated from a compound (Nakanishi & Murphy, 2015).

The next stage is to heat a mixture of sodium borate and sulfuric acid to 750 degrees Celsius, at which point the specific gravities of the boric oxide and sodium sulfate will cause them to separate (Nakanishi & Murphy, 2015). The finished product has a purity level of 99.5 weight percent after the crystallized boric acid solidifies.

This is one of many approaches. Boron isolation can be accomplished in four ways.

3.4.1 Boron Reduction Methods

According to Nakanishi and Murphy's research, four primary techniques for reducing boron compounds to elemental boron have been developed with different degrees of success (Nakanishi & Murphy, 2015). The first technique uses aluminum or magnesium to reduce borate oxide via metallothermic reduction, producing a 90–95 percent weight that can be a problematic purified end product. The second technique, electrolytic reduction of boron compounds, yields a 95-weight percent pure end product. The third technique is to reduce boron halides with hydrogen, yielding a 99 wt% pure product (Nakanishi & Murphy, 2015). Finally, the fourth technique involves the thermal decomposition of boron halides or hydrides, which produces a product with a purity of 99.9999 wt%.

The processes mentioned earlier produce solid boron in crystalline or amorphous form, depending on the process temperature and reaction rate. However, the high fusion temperature of elemental boron, compared to the fusion and boiling temperatures of boron compounds, poses significant challenges for increasing the scale and purity of production. As a result, there is now less commercial use for elemental boron. Using exceedingly low vapor pressure, vacuum distillation can remove impurity metals and boron suboxides.

Concerns have been made about the environmental effect of the borate processing industry due to the release of borates and other substances into the environment.

3.4.2 Environmental Impact Of Borate Processing

Borate manufacturing has severe environmental consequences. The manufacturing steps that contribute to these consequences include mining, the creation of steam, the movement of minerals, drying, and packing and shipping. These actions harm the environment by polluting the air and water, degrading the land, and emitting greenhouse gasses. The major contributor to environmental hazards in borate processing is using coal as the dryer's heat source (Nakanishi & Murphy, 2015).

Molten oxide electrolysis is one alternative method for producing boron compounds with minimal environmental impact. Borides are isolated using electrolysis of a molten oxide electrolyte in this procedure.

3.5 Borides Synthesis

3.5.0 Aluminum Magnesium Boride

Aluminum Magnesium Boride, with the molecular formula $AlMgB_{14}$, is a powdered ternary boron alloy made of aluminum (Al), magnesium (Mg), and boron (B) (Trunnano). With a Mohs hardness of 9, it is a robust and dense material that is an excellent option for applications that require high wear and abrasion resistance (American Elements, 2017). Moreover, due to its exceptional thermal conductivity, aluminum magnesium boride is an excellent material for high-temperature applications.

Typically grayish-black in appearance, AlMgB_{14} powder comes in a variety of particle sizes, from one to five microns to 45 to 53 microns (Trunnano). Because of this substance's outstanding chemical stability, it is resistant to oxidation, corrosion, and erosion even at high temperatures (American Elements, 2017). These characteristics make aluminum magnesium boride an excellent material for use in harsh chemical environments.

Numerous commercial uses for aluminum magnesium boron include cutting and grinding tools, wear-resistant coatings, advanced ceramics, and composites (American Elements, 2017). The substance is also employed in producing gas turbine motor turbine blades and as an additive in high-performance lubricants (Trunnano).

Due to its distinct physical and chemical characteristics, AlMgB_{14} is interesting for study purposes and practical applications. Researchers, for example, have examined its potential as a superconductor due to its high electrical conductivity and low resistivity (American Elements, 2017). AlMgB_{14} has also been investigated as a high-temperature heat sink material due to its good thermal conductivity and high melting point.

3.5.1 Zirconium DiBoride

Zirconium diboride (ZrB_2) is a ceramic substance with a hexagonal crystal structure (hP3) (Bhabha Atomic Research Centre). Due to its high melting point of 3246 °C and density of 6.08 g/cm³, it is an excellent material for high-temperature uses like thermowell tubes and thermal protection systems (Bhabha Atomic Research Centre). ZrB_2 has a molecular mass of 112.85 g/mol and is insoluble in water, most acids and alkalis, and aqueous solutions.

Zirconium diboride has a high in-plane lattice constant of 3.168 Å and a resistivity of 4.6 $\mu\Omega\cdot\text{cm}$, making it a hard and wear-resistant substance (Bhabha Atomic Research Centre).

Because of these characteristics, it is an excellent substance for use as a wear-resistant coating and in the manufacture of molten metal crucibles. The nuclear business can also use it as a neutron absorber thanks to its neutron absorption properties.

Due to its exceptional physical and chemical properties, zirconium diboride has various uses. It is a high-temperature electrode producing electronic parts and a wear-resistant coating involving cutting tools and high-speed machining. ZrB_2 is also used in aircraft engines as a thermal barrier material and a neutron absorber in nuclear reactors (Bhabha Atomic Research Centre).

Numerous studies have been conducted recently on the production of zirconium diboride. The following subsection contains a presentation of some of these studies.

3.5.2 Boride Synthesis Research

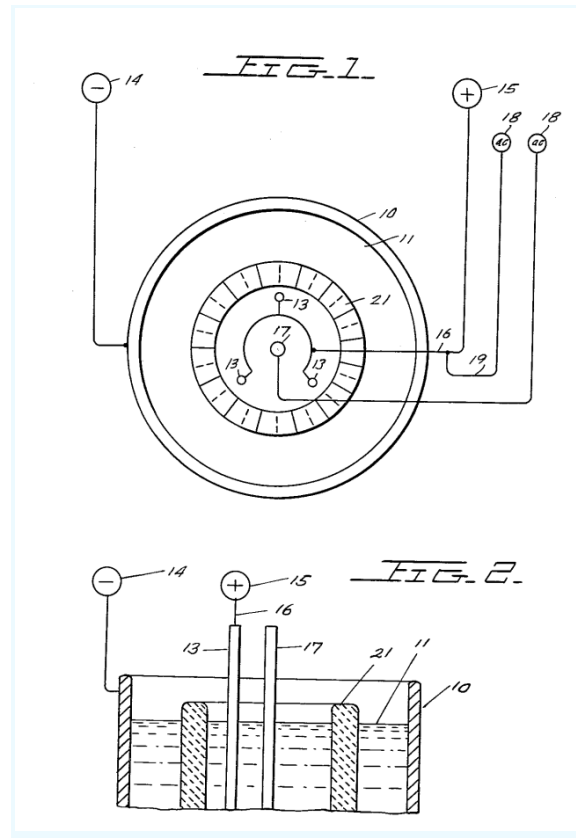


Figure 3: The invention of the mechanism responsible for housing and helping conduct the efficient and pure production of metal borides through fused salt electrolysis (Sindebad).

The subject of the invention, U.S. Patent 2741587, is the efficient and pure production of metal borides using fused salt electrolysis (Sindebad). *Figure 3* shows the device constructed to hold and conduct the reaction. By increasing the yield and purity of the boride particles created, the researchers hoped to reduce the production of defective borides. The scientists discovered that to accomplish this, the metal compound (metal oxide) needed to efficiently make the desired metal boride must be present in sufficient quantities in the fused salt bath. Due to unsettling side reactions, which produced defective borides, limiting the yield and making the procedure

ineffective, the researchers had trouble creating zirconium boride (Sindebad). To solve this issue, the researchers discovered that the electrolysis procedure should be performed under certain critical conditions. The scientists found it possible to make refractory metal borides using a fused salt solution. Nonetheless, they discovered that a barrier arrangement considerably increased the efficiency of the electrolysis process, resulting in higher-purity metal boride particles that were significantly free of metal oxide nuclei. The desired borides' efficiency yield was raised by 50% (Sindebad). The researchers adjusted the heat supplied during the electrolysis to maintain the desired bath temperature between 1000 and 1200 °C. The desired metal borides were produced satisfactorily by electrolysis with a cathode current density of about seven to twelve amps per square inch (Sindebad). The discoveries made by the researchers have implications for materials science and commercial applications because they enabled highly effective and pure metal boride production through fused salt electrolysis. Industrial uses that call for metal borides, like high-temperature ceramics, cutting tools, and wear-resistant coatings, may use this procedure (Sindebad). Similarly, the Norton Company's invention, "Electrolytic extraction of pure metal from its carbide," concentrates on the electrolytic production of pure metal. (Norton Company).

Patent Specification 164,170 outlines an invention relating to the production of pure boron (Norton Company). Boron carbide and electrode materials are used in an electrolytic procedure to obtain pure boron. The researchers investigated the procedure to operate at low temperatures for convenience and economic sustainability. The patent discusses the process's practical uses and entry into the business world. The experts discovered that the experiment could be successfully conducted with 40 mol of KCl and 60 mol of LiCl at 350 °C (Norton Company). There were, however, various methods for removing the boron from the salt. The researchers suggested three techniques: a spout-like substance was cast into ingots, salt was

dissolved in water, and salt was dissolved in an organic solvent. Producing pure boron using this electrolytic method allowed the manufacturing of borosilicate glasses, semiconductors, and ceramics, among other products with numerous commercial uses. Low-temperature operation of the process has been optimized, which made it economical and ecologically friendly (Norton Company). Malyshev and his colleagues also investigated the high-temperature electrochemical synthesis of molybdenum, tungsten, and chromium borides from halide-oxide melts, an electrolytic extraction method of pure boron from boron carbide. (Malyshev et al., 2009).

A group of researchers sought to explore the high-temperature electrolytic synthesis of molybdenum, tungsten, and chromium borides from halide-oxide melts in their article, "High Temperature Electrochemical Synthesis Of Molybdenum, Tungsten, And Chromium Borides From Halide-Oxide Melts" (Malyshev et al., 2009). One of the crucial procedures in the experiment was the separation of boron and oxides at the cathode, which was used as an electrode material to promote current and voltage movement during the electrolytic process. To make chromium borides, the researchers used a melt $\text{NaCl-Na}_3\text{AlF}_6\text{-B}_2\text{O}_3\text{-K}_2\text{CrO}_4$ with Ni or W cathodes (Malyshev et al., 2009). They changed the experiment parameters, such as the temperature, which was found to be between 1173 and 1223 K, and the current density, which was set to 1.0 to 1.8 A/cm², to create a variety of products such as CrB, CrB₄, Cr₂B, and Cr₂O₃. The experiment showed that, at high temperatures, the process parameters significantly impacted the final products of the synthesis above the eutectic phase. The researchers concluded that the technique they developed for synthesizing molybdenum, tungsten, and chromium borides could produce these materials in the future (Malyshev et al., 2009). The study also revealed the need for additional investigation into the best temperature and current density choices for manufacturing high-quality borides. In a similar study, Nelson P. Nies investigated the

electrolysis of fused salts to produce boron, a crucial subject for additional research in the area (Nies, 1960).

The author Nies describes the methods for preparing and extracting boron using salt baths in his 1960 publication "Preparation of Boron by Fused Salt Electrolysis." The primary goal of this paper was to identify an effective method for extracting boron from the mixture. Nies experimented with various salt baths to determine the most efficient method of boron extraction. One of the salt baths utilized was $KCl-K_2O-B_2O_2$; different KF and B_2O_2 were examined to establish the proper melting temperature. It was discovered that some concentrations of KF and B_2O_2 did not melt at the proper temperature, disrupting the composition's chemical equilibrium (Nies, 1960). To prevent such chemical imbalances, non-fluoride baths were also employed. As a result, the first run had the most substantial total boron extraction of any of the tests, at 96% (Nies, 1960). The trials revealed that choosing the proper bath composition is critical for obtaining maximum boron extraction. The results of this study have become very useful to academics and businesses looking to extract boron economically and effectively.

In summary, the four studies covered in this paper have significantly advanced the boride synthesis science. The "Electrolytic extraction of pure metal from its carbide" discovery by Norton Company and the U.S. Patent 2741587 have made it possible to produce metal borides by fused salt electrolysis effectively and purely. The synthesis of higher-purity metal boride particles with much fewer metal oxide nuclei has been achieved thanks to identifying crucial conditions and barrier configurations during the electrolysis process. This has ramifications for materials research and practical applications. Additionally, borosilicate glasses, semiconductors, and ceramics can now be produced thanks to the electrolytic manufacture of pure boron and boron carbide. Future investigations into boride synthesis will benefit from Malyshev et al.'s

high-temperature electrochemical synthesis of molybdenum, tungsten, and chromium borides from halide-oxide melts. The scientists discovered these materials might be produced someday using their invented method. Nevertheless, more investigation is required to find the ideal temperature and current density for producing high-quality borides. The following subsections examine various boride synthesis processes, such as the silicothermic reaction, carbothermal reduction, and molten oxide electrolysis.

3.5.3 Silicothermic Reaction

For many years, silicothermic reactions have been the main process for generating magnesium metal. In this procedure, magnesium metal is created in two steps by the reaction of silicon and carbon. In order to create magnesium metal, carbon must first be converted into silicon, which then interacts with magnesium oxide (Svendsen & Westlund, 2021). It is relatively inexpensive because the necessary raw materials are easily accessible. The technique, nevertheless, has some serious downsides, such as high energy needs, high emissions, and large trash production (Svendsen & Westlund, 2021).

With a range of 35 to 70 kWh/kg, the silicothermic processes have relatively high energy requirements. This is because the reaction necessitates the energy-consuming conversion of carbon to silicon. Also, the process produces considerable emissions, releasing 25 to 40 t CO₂/t Mg (Svendsen & Westlund, 2021). This is because the procedure necessitates high temperatures, and the reaction generates a sizable amount of carbon dioxide. Additionally, waste is produced at a rate of four to six t/t of magnesium, which might severely affect the environment.

Despite these disadvantages, silicothermic processes are still common for making magnesium metal. One explanation is that it is possible to produce high-purity magnesium,

which is necessary for some industrial purposes (Svendsen & Westlund, 2021). Furthermore, the reaction can be carried out at comparatively low temperatures, lowering energy expenses. This is especially relevant given that magnesium metal manufacturing is an energy-intensive process with significant environmental consequences.

Efforts are being undertaken in search of more sustainable methods of generating magnesium metal. One such technique is carbothermic reduction, which substitutes carbon for silicon as the reducing agent.

3.5.4 Carbothermic Reduction

Carbothermic reductions are a reduction reaction in which carbon is used as a reducing agent to generate a metal and carbon monoxide gas. Unlike silicothermic reactions, which are two-step processes with high energy demands and emissions, carbothermic reactions are one-step processes with low energy demands and emissions. It has been discovered that carbothermic processes can produce magnesium metal with emissions of 4 to 15 t CO₂/t Mg and energy requirements of just 15 to 25 kWh/kg, with waste products produced at a significantly lower rate of less than 1 t/t Mg (Svendsen & Westlund, 2021).

Using zirconium diboride with boron carbide and carbon is one illustration of a carbothermic reaction. According to the Bhabha Atomic Research Centre, this reaction is $2\text{ZrB}_2 + 4\text{CO} = 2\text{ZrO}_2 + \text{B}_4\text{C} + 3\text{C}$. Powdered zirconium diboride is created via the carbothermal reduction of zirconium dioxide with boron carbide and carbon (Bhabha Atomic Research Centre).

In the synthesis of metals like magnesium, carbothermic reactions have been found to offer several advantages over silicothermic processes. Due to the lack of impurities introduced

by the silicon utilized in silicothermic reactions, carbothermic processes have the potential to produce products with higher purity while also requiring less energy and emitting fewer pollutants.\ (Svendsen & Westlund, 2021). Moreover, a range of metals and alloys can be produced using carbothermic reactions, which are more versatile and flexible than conventional processes (Bhabha Atomic Research Centre).

In conclusion, due to their reduced energy needs, lower emissions, the possibility for higher purity products, and flexibility in application, carbothermic reductions are a promising alternative to silicothermic reactions for the synthesis of metals such as magnesium. However, to further increase the effectiveness and sustainability of metal production, researchers are now looking at other cutting-edge strategies. One such strategy is boride synthesis by molten oxide electrolysis (Svendsen & Westlund, 2021).

3.5.5 Boride Synthesis Through Molten Oxide Electrolysis

Boride synthesis by molten oxide electrolysis is a new technology that has piqued the interest of scientists. By applying an electric current, metal oxides are reduced in a molten salt electrolyte during the high-temperature electrochemical process known as "molten oxide electrolysis." Recently, scientists have investigated the possibility of MOE for the synthesis of certain borides, such as zirconium, titanium, and hafnium diborides. (Gupta et.al, 2019).

Zirconium diboride (ZrB_2) is made by converting zirconia (ZrO_2) into a molten calcium chloride electrolyte, which is an example of how MOE is used for boride synthesis (Kjlseth et al., 2019). Zirconia is converted to zirconium metal, which combines with boron oxide to generate ZrB_2 . The technique yielded encouraging results, with high yields and minimal energy use.

The ability of MOE to synthesize high-purity borides with regulated stoichiometry and shape is one of its advantages for boride synthesis (Gupta et al., 2019). MOE can also function at lower temperatures than other technologies, leading to decreased energy usage and a lower environmental effect. The technique still confronts the high cost of the necessary equipment, the scarcity of appropriate electrolytes, and the difficulty in managing the process parameters (Kjlsseth et al., 2019).

The future of boride synthesis using MOE looks promising as researchers continue investigating and refining process parameters for various borides. The use of MOE to create nanostructured borides, which can have distinctive characteristics and uses, is one intriguing breakthrough (Gupta et al., 2019).

3.5.6 Carbothermic Reduction Vs. Molten Oxide Electrolysis.

Two processes for manufacturing borides are carbothermic reduction and molten oxide electrolysis. Carbothermic reduction is a simple and low-cost technique that includes reducing the metal oxide with carbon to produce new metal and carbon dioxide gas. The procedure is energy-efficient, using between 15 and 25 kWh/kg (Svendsen & Westlund, 2021). However, the process emits considerable amounts of CO₂, releasing 4 to 15 t CO₂/t Mg, making it environmentally unfavorable (Svendsen & Westlund, 2021). The purity of the resultant borides may also be impaired due to contaminants in the starting materials.

On the other hand, the synthesis of borides by MOE is a trickier procedure that uses molten oxides as an electrolyte to reduce metal ions and boron oxide to generate borides. The technique necessitates precise control of the electrolysis conditions, which results in component advantages over carbothermic reduction. For example, molten oxide electrolysis creates borides

with high purity and exact stoichiometry (Sridhar et al., 2015). With fewer pollutants and trash, the process is also more environmentally friendly.

A wide variety of borides, including some that are challenging or impossible to synthesize using other techniques, can be produced using MOE (Sridhar et al., 2015). This approach enables the inclusion of dopants and the fabrication of composite materials, opening up new avenues for boride-based materials with superior characteristics. Furthermore, MOE has been utilized successfully to make borides with desirable qualities such as hardness and wear resistance, making it a potential approach for creating advanced boride materials (Sridhar et al., 2015).

In conclusion, there are two distinct ways to make borides. Carbothermic reduction is a straightforward and inexpensive process, but it generates many pollutants and degrades the purity of the resultant borides. In contrast, MOE is a more intricate process with numerous benefits over carbothermic reduction, including high purity and accurate stoichiometry of the borides and less waste and emissions. A promising technique for creating sophisticated boride materials, MOE can synthesize many borides with desirable characteristics.

3.6 Calculation Parameters

Some calculations were complex for our group, so further research and meetings with Saint Gobain were required to resolve these difficulties.

3.6.0 Desired Calculation Research

To continue and pursue some calculations during the project, some research and literature had to be conducted. Pseudo Binary Phase Diagrams, Nominal Cathode-To-Anode Distance, and Faradaic Efficiency were among the four results components that required extensive research and understanding.

3.6.1 Pseudo Binary & Ternary Phase Diagrams

Phase diagrams depict the relationship between a system's composition, temperature, and pressure, showing which phase or phases are present (Porter et al., 2009). Pseudo-binary phase diagrams and ternary phase diagrams are two types of phase diagrams that are frequently employed.

Phase diagrams of the pseudo-binary variety display the interaction between two parts of a binary system. They frequently illustrate how two metallic element alloys or solid solutions behave (Smith, 2004). In a pseudo-binary phase diagram, one element's composition is stable while the other element's composition changes. On the graph, various regions correspond to the phases in the system. Each area where a particular phase is stable corresponds to a distinct combination of temperature, pressure, and composition.

A type of phase diagram that depicts the interaction between three components in a ternary system is a ternary phase diagram. They frequently illustrate how alloys or solid solutions containing three metallic elements behave (Porter et al., 2009). A point on the graph represents each component's makeup in a ternary phase diagram. On the graph, various regions

correspond to the phases in the system. Each area where a particular phase or combination of phases is stable correlates to a different combination of temperature, pressure, and composition.

Understanding the various regions that are visible on the graph and the various phases that those regions represent is necessary to read a phase diagram. The conditions at which a phase transition occurs are represented by lines dividing the various regions on the graph representing the conditions at which a phase transition occurs. For instance, the boundary between the solid solution of copper and nickel in a copper-nickel alloy and the two-phase mixture of copper and nickel represents the conditions under which the two phases coexist in equilibrium. The graph's line can calculate the temperature and material composition at which a phase transition occurs.

3.6.2 Nominal Cathode-To-Anode Distance

The nominal cathode-to-anode distance is the distance between the anode and electrode that allows the reaction. In order to calculate this distance, the Voltage Balance of the reaction must be considered and analyzed.

After meeting with Mr. Bradley Nakanishi, he imparted the following knowledge to our group to help us comprehend voltage balance. Voltage balance is a critical component of the operation of electrochemical reactors and a significant factor for electrochemical engineers. The engineer can then consider scaling, operational, and other design factors that affect reactor performance based on a direct comparison of reactor performance with that of other electrochemical reactors. Through the Nernst equation, the voltage balance and total energy balance are tightly connected. The performance of the reactor can be directly observed by installing inexpensive sensors to monitor voltage dips along the current flow channel inside and

outside the reactor while it is operating. Minimizing voltage drops to increase reactor efficiency is one of the critical goals of the electrochemical engineer, and the voltage balance aids in identifying the "lowest hanging fruit." Anode voltage drop, cathode voltage drop, external voltage drop, and minimum operating voltage are frequently considered while calculating a voltage balance—a crucial step in achieving optimal voltage balancing and reactor performance.

The first step to calculating the nominal cathode-to-anode distance from analyzing the voltage balance of a reaction yields the minimum operating voltage. Here are the steps:

1. **Step One:** Dictate the Overall Reaction and the Operation Temperature
2. **Step Two:** Split the Overall Reaction into Anodic and Cathodic Reactions and determine the Number of Transferred Electrons
3. **Step Three:** Using Thermodynamic Simulator (i.e., FactSage), calculate the Overall thermodynamic properties (i.e., Gibbs Energy, Enthalpy Change, and Entropy Change)

a. *Note:* Entropy Change can be calculated via this formula: $\Delta S = \frac{(\Delta H - \Delta G)}{T}$

4. **Step Four:** Use Nernst Equation to calculate the Minimal Operating Voltage

a. *Note:* Minimal Operating Voltage can be calculated via this formula:

$$V_{min} = \frac{\Delta G}{n * F}$$

i. *Note:* Where n is the number of electrons transferred in the reaction

ii. *Note:* F is Faraday's Constant

The second step is to calculate the ohmic drop of the reaction. The operation of an electrochemical reactor depends critically on the IR drop, also known as the ohmic drop. It indicates the voltage drop across the electrolyte caused by current flow and is derived from Ohm's equation ($V = IR$). Due to irreversible processes, this voltage drop causes heat to be released into the reactor. The Ohmic drop balances thermal losses (sinks) during operation to

keep it running steadily. Endothermic reactions, cell wall losses, tapping (recovery of reactor product or waste), and other elements are examples of thermal sinks. The anode-cathode distance (ACD, or space between the anode and the cathode) R or the cell current " I " can be adjusted to control the IR-drop, which is crucial for optimum reactor performance. The nominal cathode-to-anode distance is an essential factor for optimal voltage balance and IR-drop management since, in most cases, cells operate at constant current, leaving R as the only free parameter. Here are the steps to calculate the ohmic drop:

5. **Step Five:** Calculate the Heat Lost from the Electrolysis Reaction

- a. **Note:** Heat Lost from the Electrolysis Reaction can be calculated via this formula:

$$\Delta Q = \Delta S * T$$

- i. ΔS is the entropy change, which was found in Step Three, and T is the
Operation Temperature

6. **Step Six:** Calculate the Potential of the Heat Lost from the Reaction

- a. **Note:** The Potential of this Heat Lost from the Electrolysis Reaction can be

calculated via this formula: $V_r = \frac{\Delta Q}{n * F}$

7. **Step Seven:** Calculate the Potential when introducing the Ore-feedstock at 25 °C

- a. **Note:** The Potential generated when introducing the ore-feedstock at 25 °C can

be calculated via this formula: $V_{feed} = \frac{\Delta H}{n * F}$

- b. **Note:** We must know the enthalpy change of the ore-feedstock, which is solid, at
the temperature of 25 °C

8. **Step Eight:** Determine the Voltage from other losses, which we can assume to be zero

9. **Step Nine:** Calculate the Ohmic Drop

a. **Note:** The Ohmic Drop can be calculated via this formula:

$$V_{IR} = V_r + V_{feed} + V_{other}$$

The final step is to calculate the nominal cathode-to-anode distance. This can be done by analyzing this distance's relation to the electrolyte's resistance in the reaction. This relation can be constructed into the following formula $R = \frac{\rho * D_{ac}}{Area}$. R is the resistance of the electrolyte, ρ (rho) is the resistivity of the electrolyte, D_{ac} is the nominal cathode-to-anode distance, and Area is the area between the anode and cathode. We can compare this resistance to the ohmic drop through the relationship between voltage, current, and resistance, or formulaically put $V_{IR} = I * R$. We can substitute the formula of resistance stated above into this formula. However, we still do not know the current (I) even with thermodynamic simulation. So we must also consider the following formula of current $I = j * Area$ —where j is the current density. We can substitute both current and resistance to the ohmic drop formula to help in solving for the nominal cathode-to-anode distance, as shown below:

$$V_{IR} = I * R = (j * Area) * \left(\frac{\rho * D_{ac}}{Area}\right) = j * \rho * D_{ac}$$

Now that we have the Ohmic Drop, we need to find the Current Density and Resistivity. Based on actual electrolysis reactions that have been conducted we can assume the values of these missing variables. We can assume the current density for the electrolysis reaction to be $2 \frac{A}{cm^2}$, which is the current density at the cathode for the aluminum electrolysis. The reactions that we are investigating are similar to that of this aluminum reaction: $Al_{(s)}^{3+} + 3e^- \rightarrow Al_{(l)}$. We can also assume the value of our resistivity to be $1 \text{ ohm} * \text{cm}$, which is typical for molten salts.

Knowing that we can solve for our nominal cathode-to-anode distance, in the following final step:

10. Step Ten: Rearrange the above revised Ohmic Drop formula, isolating Nominal Cathode-To-Anode Distance to one side, then solve

$$a. \text{ Note: The formula will look as follows: } D_{ac} = \frac{V_{IR}}{j * \rho} = \frac{V_{IR}}{2 \frac{A}{cm^2} * (1 \text{ ohm} * cm)}$$

3.6.3 Faradaic Efficiency

Mister Bradley Nakanishi from Saint Gobain also educated us about Faradaic Efficiency, explaining the following information about this efficiency value.

Faradaic efficiency is a crucial factor in the design and operation of electrochemical reactors. When a specific amount of charge is transported through the reactor, it is an empirically measured quantity that indicates the proportion of the actual mass produced to the theoretical mass. The formula for faradaic efficiency, $\eta_f = \frac{m}{m_o} * 100\%$, m is the theoretical mass produced by the reaction and m_o denotes the mass produced.

According to Faraday's law, the theoretical mass is given by the equation $m = \frac{M * Q}{n * F}$; the variables in this equation are M , n , F , and Q , which stand for the molecular weight, the number of moles of electrons per mole of product, the Faraday constant, and the amount of charge that is transported during electrolysis, respectively. Contemporary aluminum electrolysis cells function with a 90% faradaic efficiency, so we can assume our faradaic efficiency to be 90% based on the similarities of the reactions that we investigated.

Calculations from the nominal cathode-to-anode distance can determine faradaic efficiency by adjusting the distance to decrease the ohmic drop and raise the cell's efficiency. Electrochemical engineers can maximize the efficiency of their design and operations by using faradaic efficiency to calculate a process' overall energy efficiency. In conclusion, improving nominal cathode-to-anode distance can help boost efficiency and total energy efficiency. Faradaic efficiency is vital to the operation of electrochemical reactors.

3.6.4 Energy Efficiency

Energy efficiency was the last unidentified mathematical factor mentioned by Mister Bradley Nakanishi of Saint Gobain.

Energy efficiency is a crucial consideration in the design of electrochemical reactors since it compares the reactor's minimum theoretical energy consumption to the actual energy used, multiplied by its faradaic efficiency. Power or energy can be used to represent a reactor's energy efficiency. The energy efficiency equation is defined by $\eta_E = \frac{E_o}{E} * \eta_f$, where E_o is the reactor's theoretical potential consumption and E is the actual potential used. The energy efficiency of the reactor declines as actual energy or power increases. Therefore, increasing energy efficiency is crucial for lowering operational costs and reducing adverse environmental effects. The cathode-to-anode distance and cell voltage must be optimized while also maintaining high faradaic efficiency by electrochemical engineers in order to do this.

4.0 Methodology

4.1 The Action Items

To ensure the successful comprehension of MOE and the completion of this project, various information relating to thermodynamics, chemistry, literature, and the like were gathered, and deadlines were involved. To best navigate organizing those milestones and communicating achieving deadlines, action items were created to clarify the path to completion. The Methodology section describes the processes we took to test for a commercial application of producing borides through molten oxide electrolysis. This was done by completing the following action items we set along the way.

- 1. Action Item One:** Research & Literature Review On Extractive Metallurgy Methods, Silicothermic Reaction & Carbothermal Reduction, Molten Oxide Electrolysis, Manganese Molten Oxide Electrolysis, FactSage, Zirconium DiBoride, Aluminum Magnesium Boride, Past Boride Synthesis Patents & Experiments, Boride Synthesis Through Molten Oxide Electrolysis, & Several Calculations Required By Saint Gobain
- 2. Action Item Two:** Constructing Pseudo-Binary Phase Diagrams Of The Reaction Products & Ternary Phase Diagrams Of The Reactants For AlMgB_{14} & ZrB_2 MOE
- 3. Action Item Three:** Constructing The Fugacity & Viscosity Trend Of The Seven Compositions Derived From Action Item Two
- 4. Action Item Three:** Constructing The Viscosity Trend Of The Seven Compositions Derived From Action Item Two
- 5. Action Item Four:** Deciding The Operation Temperature & Electrolyte Composition Through Analysis Of Fugacity & Viscosity Trend Of Action Items Three & Four

6. **Action Item Five:** Calculating The Overall Reaction Energy & Potential
7. **Action Item Six:** Calculating The Half-Cell Reaction Energies & Potential From Data Gathered In Action Item Six
8. **Action Item Seven:** Investigating The Mass Balance Of The Reaction
9. **Action Item Eight:** Investigating The Energy Balance Of The Reaction
10. **Action Item Nine:** Calculating The Nominal Cathode-To-Anode Distance For The Reaction's Electrolytic Cell
11. **Action Item Ten:** Investigating The Faradaic Efficiency & Energy Efficiency Of The Reaction
12. **Action Item Eleven:** Determining Whether The Reaction Is Endothermic Or Exothermic

Below is a flowchart figure demonstrating the complete process of our action items and overall project.

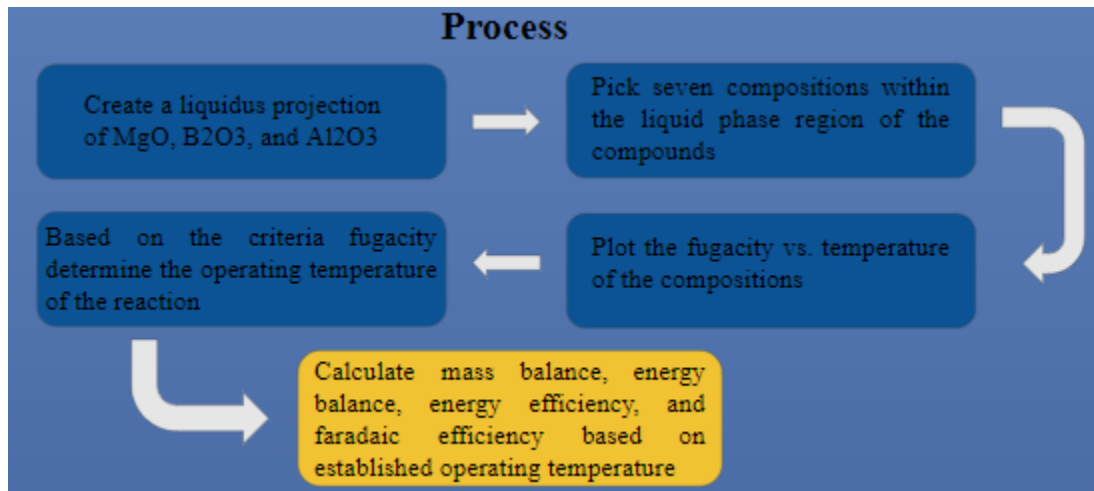


Figure 4: A summarized flowchart of the generalized process taken to ensure the completion of this project

4.2 Action Item Completion

This section focuses on the initial literature review and research as well as the necessary steps to complete and gather this project's results. To best illustrate the process of these results, subsections 4.2.1 to 4.2.11 will feature the steps taken for the test calculations. These test calculations were all of the same calculations required for this project. However, they were done to produce Manganese through the molten oxide electrolysis process. These subsections will be used and translated into producing aluminum magnesium boride and zirconium diboride, as shown in section 5.0 *Results & Analysis*.

4.2.0 Research & Literature Review

The action item was completed successfully. First, we conducted extensive literature evaluations on the primary extractive metallurgy procedures used to generate pure metals: silicothermal reaction and carbothermal reduction, molten oxide electrolysis, and pure manganese production via molten oxide electrolysis. The Winard paper was one significant source that was thoroughly investigated and analyzed. Professor Zhong and Saint Gobain gave us critical research sources, such as the Winard study. Still, we had to uncover many others through databases and journal articles. We extrapolated and evaluated the data before presenting our findings to our mentors and advisor.

Molten oxide electrolysis, manganese molten oxide electrolysis, and zirconium diboride were also investigated. In addition, we reviewed existing boride synthesis experiments and patents, notably aluminum magnesium boride and earlier boride synthesis methods. We also investigated boride production using molten oxide electrolysis.

We then worked hard to become "experts" in all FactSage computations and procedures. This started with us completing two lengthy lectures by Professor Zhong via the FactSage platform. We were expected to finish two degrees of difficulty for this training: basic and advanced. To begin the beginner-level training, our group completed various exercises to become acquainted with the haptics of the various databases and capabilities provided by FactSage. Next, we learned about FactSage's advanced capabilities and became well-equipped to calculate our outcomes.

Because some calculations were foreign to our group, we completed this action item's final stage: investigating many of these computations. We maintained a professional and cohesive approach throughout this process to ensure the success of the action item.

Section 3.0 Background, above, contains the information gathered from this activity.

4.2.1 Constructing A Pseudo-Binary Phase Diagram & Ternary Phase Diagram

To conduct the various calculations needed to evaluate the feasibility of synthesizing borides, a selection of electrolyte compositions needed to be determined. These compositions were vital as they allowed for the properties (i.e., temperature range, viscosity, vapor pressure, etc.) of the electrolyte solution required to produce the borides to be established. The first step of this process involved generating a ternary phase diagram of the three constituent compounds of the boride using the "phase diagram" module of FactSage. Using a three-point matrix, the graph represents a different combination of phases that are in equilibrium under a specific set of conditions. As the electrolyte solution is a liquid, compositions within the liquid phase region of the graph were selected. The initial trials investigating MOE using manganese illustrated the process below.

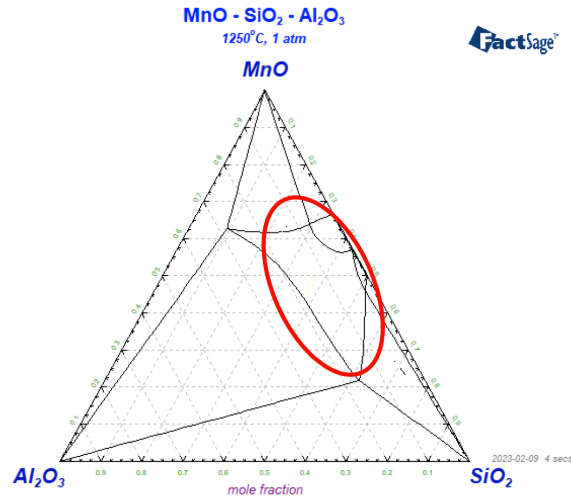


Figure 5: A base isothermal section, which we graphed, of MnO, SiO₂, and Al₂O₃

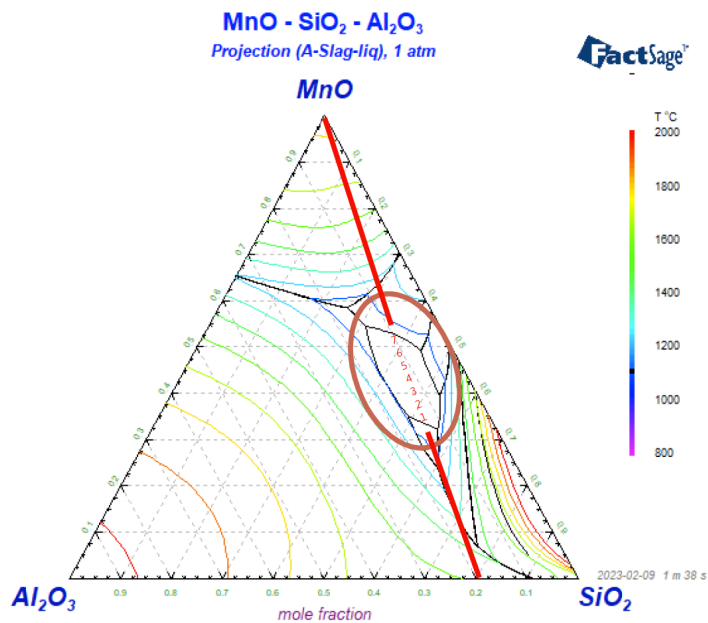


Figure 6: Liquidus projection we constructed of MnO, SiO₂, and Al₂O₃

The red circle in *Figure 5* highlights the region where the compounds are in a liquid phase at 1250 degrees. Seven compositions are selected within this region. Their precise location is shown as the red numbers one to seven in *Figure 6*. The compositions are located on a diagonal axis which intercepts MnO. This was intentionally done as it represents how the design of the

electrolyte slightly varies along this axis during the MOE process. As the reaction takes place, manganese is produced, so it has to be replaced by adding MnO to keep the response stable, thus moving the equilibrium of the reaction along the red axis. FactSage provides each composition's mole fractions and melting temperatures, resulting in the data below.

	Temperature	MnO	Al ₂ O ₃	SiO ₂
1	1154.74	0.345767	0.177504	0.476729
2	1163.3	0.378524	0.161125	0.46035
3	1174.49	0.403093	0.158733	0.438175
4	1179.57	0.43858	0.148408	0.413012
5	1179.34	0.468607	0.140813	0.390579
6	1175.43	0.493176	0.135948	0.370877
7	1159.2	0.528663	0.128096	0.343241

Table 1: Melting point and mole fractions of MnO, SiO₂, and Al₂O₃

The values shown in *Table One* allow for further calculations to be conducted on the electrolyte. The composition selection process was to be repeated identically for zirconium diboride (ZrB₂) and aluminum magnesium boride (AlMgB₁₄), however, this time a pseudo-binary phase diagram was introduced for both borides. This influenced the following calculations for both of these borides.

4.2.2 Constructing The Fugacity Trend Of The Seven Compositions

Once the seven compositions are determined, we transitioned to the subsequent calculations, plotting the fugacity trend to determine a feasible composition and operating temperature. To calculate the fugacity trend, FactSage must be used. Here were the steps to collecting all the data of the vapor pressure trend across a temperature range across all compositions:

1. Open up FactSage and navigate to the “Equilib” program
2. Once opened, select the appropriate databases that house the desired elements/compounds
 - a. In the case of extracting Manganese, the three compounds to select for the electrolyte are MnO, SiO₂, and Al₂O₃
3. Input the desired mole fractions of each compound of the first composition and click “Next.”
 - a. Make sure “Initial Conditions” is not selected.
4. In the next step, go to the “Units” tab and change the temperature units to °C and the amount units to mol.
5. Select “Ideal Gas” and “Solids” for the product, and make sure to select the “SlagA” solution as “Immiscible.”
6. It will be highlighted in yellow with an “I” next to it
7. Go down to the “Temperature/Pressure/Enthalpy” table and change the temperature to a range, making the pressure 1 atm and leaving the enthalpy blank
 - a. In this reaction, the temperature range must be from 1100 to 1300°C
 - b. This setup can be done by first entering 1100 °C as the minimum temperature, then 1300 °C as the maximum temperature, then an increment to calculate the fugacities in between
8. Once all is settled, click “Calculate,” and the “Results” window will appear, displaying the fugacities of each reaction occurring during the overall reaction at each temperature in the range

9. Since our focus is only on extracting Mn, we must only concern ourselves with the fugacity of Mn
10. Tabulate all of the fugacities across the temperature range for that composition, then repeat the above steps for the remaining compositions
11. Once all is tabulated, use a spreadsheet to graph the fugacity trend of each of the compositions

This process was conducted in a similar fashion for Aluminum Magnesium Boride and Zirconium Diboride.

VAPOR PRESSURE OF ALL POTENTIAL COMPOUNDS												
Composition	Electrolyte Compound Mole Fraction MnO: 0.XXXX SiO ₂ : 0.XXXX Al ₂ O ₃ : 0.XXXX	Temperature (1100 to 1300 oC)										
		1100	1120	1140	1160	1180	1200	1220	1240	1260	1280	1300
Vapor Pressure or Fugacity (atm) of Manganese												
1	0.345767 0.476729 0.117504	3.37E-11	5.98E-11	1.04E-10	1.31E-04	2.06E-04	2.76E-04	3.68E-04	4.86E-04	6.36E-04	8.27E-04	1.07E-03
2	0.378534 0.46035 0.161125	3.37E-11	5.98E-11	1.04E-10	1.23E-04	2.00E-04	3.15E-04	4.18E-04	5.50E-04	7.18E-04	9.31E-04	1.20E-03
3	0.403093 0.438175 0.158733	3.69E-11	6.54E-11	1.14E-10	1.95E-10	2.00E-04	3.71E-04	4.94E-04	6.54E-04	8.55E-04	1.11E-03	1.42E-03
4	0.43858 0.413012 0.148408	1.64E-10	2.15E-04	2.96E-04	3.90E-04	4.39E-04	4.48E-04	5.96E-04	7.83E-04	1.03E-03	1.33E-03	1.72E-03
5	0.468607 0.390579 0.140813	1.64E-10	2.15E-04	2.96E-04	3.99E-04	4.57E-04	5.33E-04	7.05E-04	9.27E-04	1.21E-03	1.57E-03	2.02E-03
6	0.493176 0.370877 0.135948	1.64E-10	2.15E-04	2.96E-04	3.99E-04	4.64E-04	6.19E-04	8.18E-04	1.07E-03	1.40E-03	1.81E-03	2.32E-03
7	0.538663 0.343241 0.128096	1.64E-10	2.15E-04	2.96E-04	4.04E-04	5.45E-04	7.30E-04	9.70E-04	1.28E-03	1.67E-03	2.17E-03	2.79E-03

Table 2: Vapor Pressure/Fugacity Of Seven Compounds Of MnO-SiO₂-Al₂O₃ Displaying Largest-Fugacity Compound (Manganese) From 1100°C To 1300°C

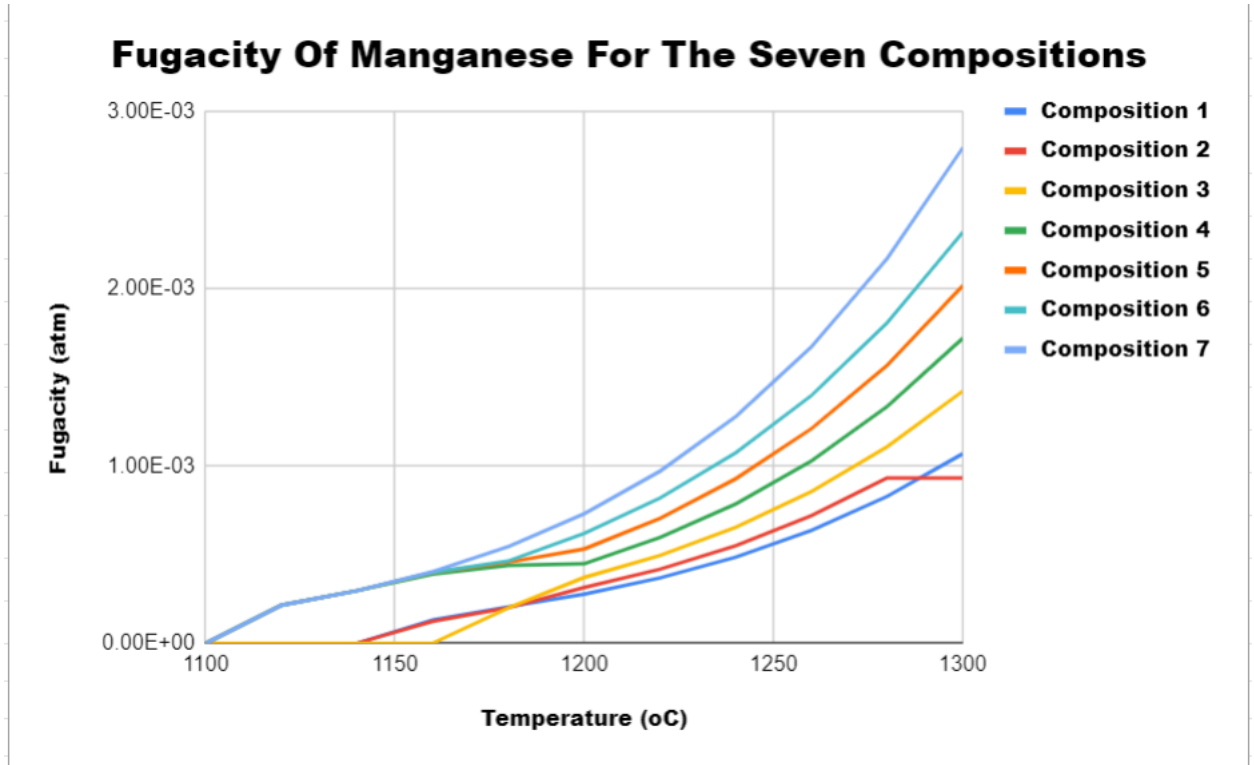


Figure 7: Fugacity Trend Of All Seven Compositions Of $MnO-SiO_2-Al_2O_3$ Graphed Out In A Temperature Vs. Fugacity Graph

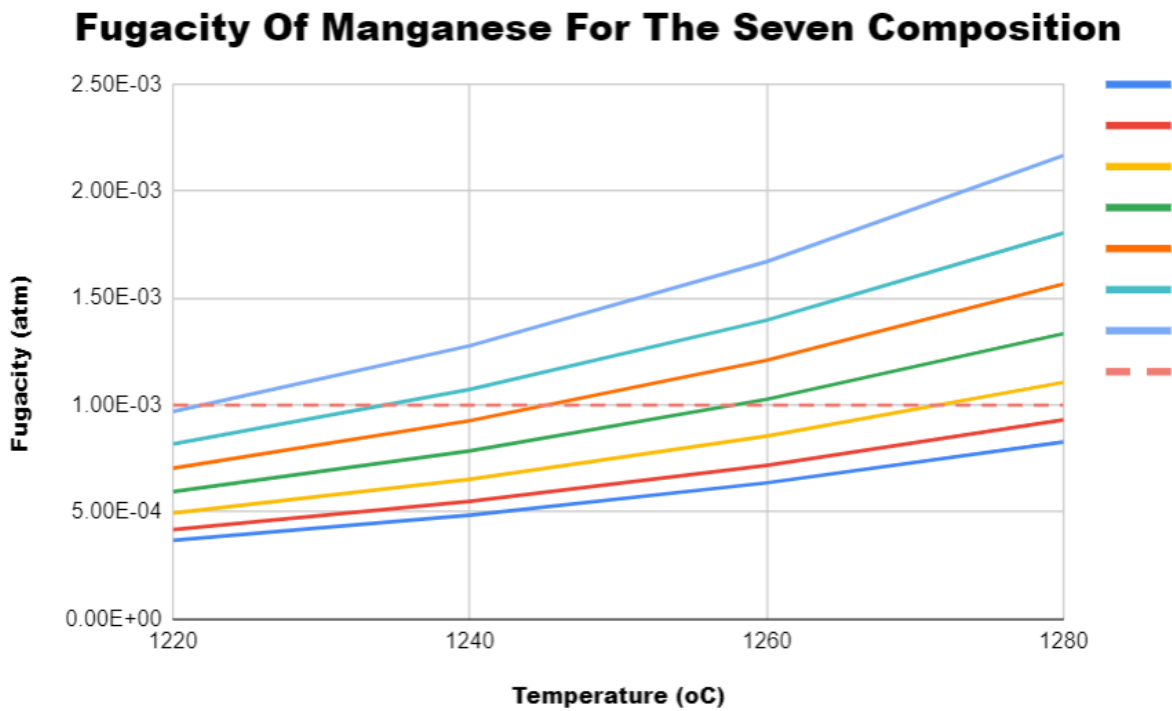


Figure 8: Focused Fugacity Trend Of All Seven Compositions Of MnO-SiO₂-Al₂O₃ Graphed Out In A Temperature Vs. Fugacity Graph. The Dotted Line Shows The Fugacity Value Of 10⁻³ atm.

Table 2 shows how the vapor pressures should be tabulated and organized. A figure, such as Figure 7, had to be made to show the fugacity trend of all seven compositions. Since the temperature range was too great, a second graph must be made that is more focused at a specific temperature range, mainly a range that provides fugacity below or around 10⁻³ atmospheres, for optimal reactions. Figure 7 is an example of this same graph. We then moved on to viscosity.

4.2.3 Constructing The Viscosity Trend Of The Seven Compositions

The following steps were carried out to calculate the viscosity trend of the seven compositions in *subsection 4.2.1*:

1. Open FactSage and navigate to the *Viscosity* module.
2. Input the required temperatures under the temperature column.
 - a. For the calculation of AlMgB₁₄ a temperature range of 900 to 2000 °C at 100 °C intervals was used.
3. Input the mol fractions of compositions 1 into their respective sections (i.e. B₂O₃, MgO, Al₂O₃). Make sure to enter the mol fractions across the entire temperature range.
4. Press calculate and record the resulting viscosity of the composition at each temperature level in an excel spreadsheet.
5. Repeat steps 3 to 4 for remaining compositions 2 through 7.
6. Use an excel spreadsheet to plot a viscosity vs. temperature graph of all seven compositions. Table 3 below shows the data set used to graph the viscosity vs. temperature graphs.

Temp.	1	2	3	4	5	6	7
900	106.325	107.403	110.805	114.718	119.345	125.454	131.331
1000	40.933	41.323	42.591	44.042	45.78	48.115	50.572
1100	18.114	18.278	18.824	19.444	20.194	21.214	22.346
1200	8.957	9.034	9.297	9.594	9.956	10.452	11.022
1300	4.845	4.885	5.024	5.18	5.372	5.634	5.944
1400	2.821	2.844	2.923	3.011	3.12	3.27	3.45
1500	1.746	1.76	1.808	1.861	1.927	2.018	2.128
1600	1.138	1.147	1.178	1.211	1.253	1.312	1.382
1700	0.774	0.781	0.801	0.823	0.852	0.89	0.938
1800	0.547	0.551	0.566	0.581	0.601	0.628	0.661
1900	0.399	0.402	0.413	0.423	0.437	0.457	0.481
2000	0.299	0.302	0.309	0.317	0.328	0.342	0.359

Table 3: Raw data of the viscosity of selected compositions at a range of temperatures from the Mn MOE reaction.

This process was conducted similarly to understand the viscosity trend of the selected compositions of AlMgB_{14} and ZrB_2 .

4.2.4 Deciding The Operation Temperature & Electrolyte Composition

From the results calculated in the previous calculation in regards to the fugacity and viscosity trends of the seven compositions, we can conclude our composition of focus. We can also conclude the temperature for operating our MOE reaction. From our test calculations in the department of manganese, we concluded our operating temperature to be 1260 °C and our optimized electrolyte composition to be Composition 4. These decisions were derived from the analysis of the fugacity trend graph and viscosity trend graph. From the fugacity trend, we focused on the area in which the fugacity would reach our criterion of 10^{-3} atmospheres. The most optimal composition and temperature in that regard were Composition 4 and 1260 °C, respectively. From the viscosity trend we could understand the relationship between the

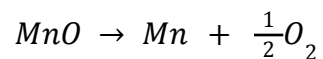
molecular makeup of the composition and its viscosity. Composition 1 had the lowest viscosity, with each succeeding composition having an increasingly greater viscosity. As the rate of reaction is inversely proportional to the viscosity, compositions with a lower viscosity (i.e. compositions 1-4) should be selected to maximize the efficiency of the reaction.

Similar steps were taken for optimizing the best electrolyte composition and operating temperatures for our MOE reaction with aluminum magnesium boride and zirconium diboride

Once the composition and operating temperature were found, we moved on to our following calculation, calculating the overall reaction potential and energy.

4.2.5 Calculating The Overall Reaction Energy & Potential

We began our following calculation, which surrounded the overall reaction needed to isolate Mn from MnO. To do this, it was essential to know that the end product had to be Mn and O₂. Since the reactant is only MnO, the overall reaction was easily found, and it was:



Knowing this, the overall reaction energy and potential were calculated. These two calculations were done through FactSage and a combination of FactSage and formulas. Our group took these steps to calculate the energy and potential:

1. Open up the “Reactions” program in FactSage
2. Input the above reaction into the program by selecting “Initial Conditions,” then click “Next”
3. Select “Liquids” for the product and make sure to choose the “SlagA” solution as “Immiscible” and click “Next”

4. In the next window on the bottom left corner, input the same temperature range, ensuring the desired operating temperature is within that range, and click “Calculate”
5. Tabulate the data of the Gibbs Energy trend and then click plot, changing the axis, to graph the Overall Reaction Energy Graph
6. Next, we used the Nernst Equation and the tabulated data to calculate the potential at our desired operational temperature.
 - a. Nernst Equation: $\Delta G_o * n * F = E_{cell}$
 - i. ΔG_o = the Gibbs energy
 - ii. n = the number of moles/displaced electrons
 - iii. F = Faraday’s constant
 - iv. E_{cell} = the overall reaction potential
7. Once we found Gibbs energy, we knew Faraday’s constant ($\approx 96485.3321 \frac{C}{mol}$) and the number of moles, which we can gather from the overall reaction, as 2
8. Thus we solved for the potential
9. To check this, return to the “Reactions” window, exchange the output from “Gibbs” to Potential, change the n to 2, and click Calculate
 - a. The results of the voltage will be the same
10. We then plotted the Potential graph the same way we plotted the Gibbs energy graph.

The results of following these steps for our test run with manganese MOE are shown below in the figures and tables.

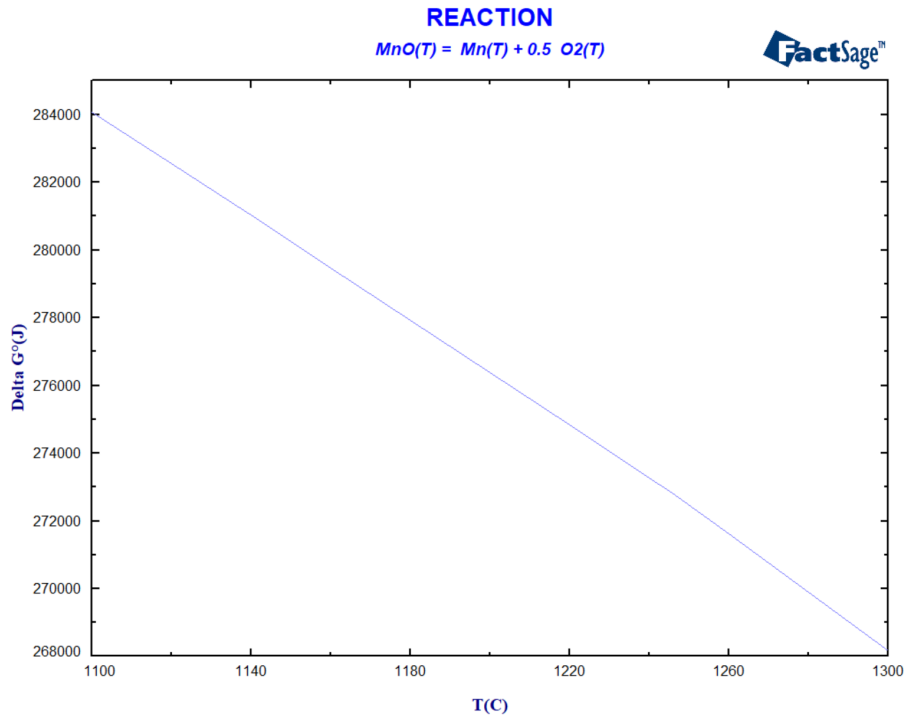


Figure 9: The Overall Reaction Energy Trend Graph from 1100 to 1300 °C. This graph is displayed as Temperature (in degrees Celsius) versus the change in Gibbs Energy (J).

OVERALL REACTION ENERGY	
Temperature (°C)	Gibbs Energy (J)
1100	284050.2
1120	282532.8
1138.85	281101.7
1140	281012.8
1160	279466.3
1180	277918.3
1200	276368.7
1220	274817.5
1240	273264.8
1245.85	272810.3
1260	271598.3
1280	269883.8
1300	268168

Table 4: The Overall Reaction Energy, with a temperature range from 1100°C To 1300°C and the corresponding change in Gibbs Energy for each temperature. The difference in Gibbs Energy of the desired Operating Temperature is highlighted at the bottom of the table.

<u>NERNST EQUATION</u>	<u>VOLTAGE REQUIREMENT</u>				
	<u>Temperature (oC)</u>	<u>Gibbs Energy [ΔG_o] (J)</u>	<u>Number Of Moles [n] (mol)</u>	<u>Farady's Constant [F] (C*mol⁻¹)</u>	<u>Voltage Requirement [Ecell] (V)</u>
$\Delta G_o = -n * F * E_{cell}$	1260	271598.3	2	96485.3321	-1.40745901
$\Delta G_o * (-n * F) = E_{cell}$					

Table 5: The Voltage Requirement is split into two tables. The first table shows the Nernst Equation and its rearranged form to calculate the voltage requirement of the electrolytic cell at the operating temperature. The second table shows the change in Gibbs Energy at 1260 °C, the number of moles or electrons transferred as 2, and the Faraday’s constant, all used to calculate the voltage requirement.

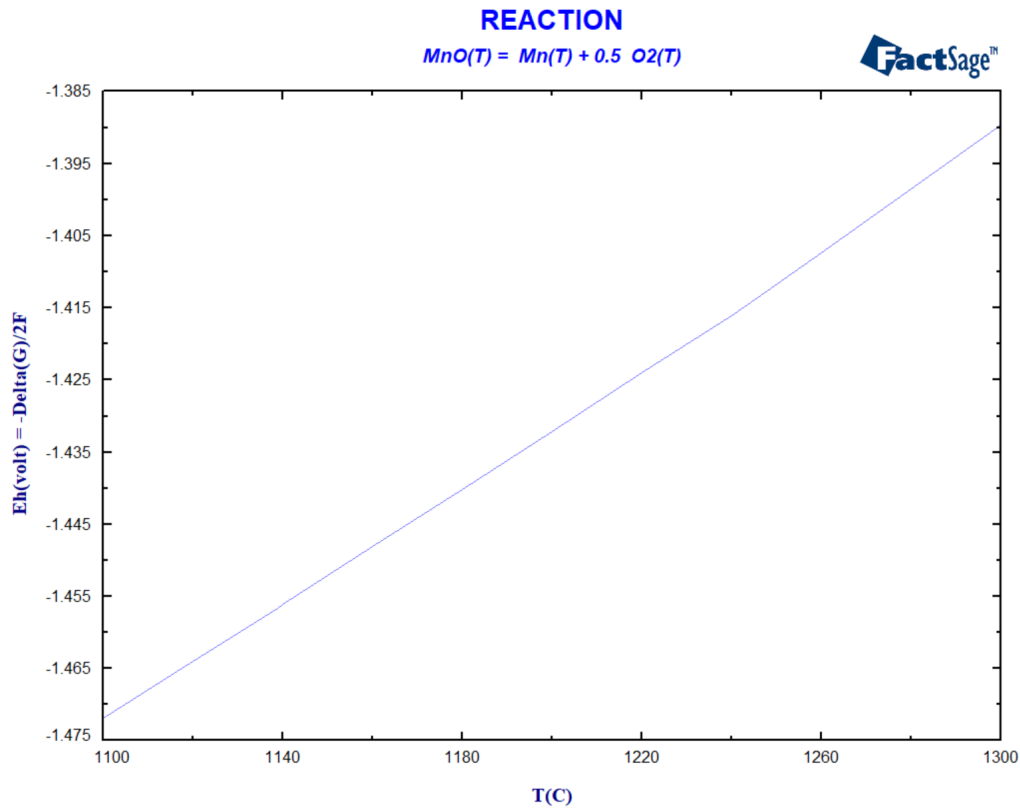
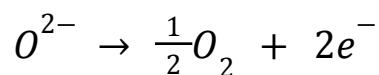


Figure 10: The Overall Reaction Potential Trend Graph from 1100 to 1300 °C. This graph is displayed as Temperature (in degrees Celsius) versus the Voltage Requirement (V).

This procedure was followed, in a similar fashion, for Aluminum Magnesium Boride and Zirconium Diboride.

4.2.6 Calculating The Half-Cell Reaction Energies & Potentials

To our group, these half-cell calculations were foreign and difficult to grasp. After extensive discussion with Professor Yu Zhong, Mr. Rui Wang, and Mr. Jize Zhang, our group concluded that this half-cell reaction energies and potentials were not a single value but a linear equation. Rather than referring to them as “half-cell,” we denoted one as cathodic reaction energy/potential and the other as anodic reaction energy/potential, such that we would be more specific to which side of the electrolytic cell we would be measuring our potential and energy. For our overall reaction regarding the synthesis of Manganese, we needed to separate the reaction into a half-reaction occurring at the cathode and a half-reaction at the anode. Upon further research and discussion, we came to the conclusion that the reaction occurring at the cathode was:



The reaction occurring at the anode would subsequently be:



Knowing the overall reaction, cathodic reaction, and anodic reaction we were able to proceed in our calculations. We first began by examining the overall reaction. From the “Reaction” Module on FactSage, the Gibbs Energy of the Overall Reaction from 1100 to 1300 °C was tabulated in a spreadsheet. Upon our research, we also remembered a formula involving Gibbs Energy that was very fruitful towards this calculation. The formula was:

$$\Delta G = \Delta H + T(\Delta S)$$

We compared this formula to the formula of a linear equation: $y = b + m(x)$. The change in Gibbs Energy (ΔG) was the independent variable (y), the change in Enthalpy (ΔH) was

the y-intercept (b), the difference in Entropy (ΔS) was the multiplier (m), and the Temperature (T) was the dependent variable. Knowing this, we extrapolated the data, used the slope and y-intercept formulas from Google Sheets, and got our Overall Reaction Energy Formula. Our next step was to calculate the Overall Reaction Potential Formula, which was quite simple after acquiring the energy formula. All that was needed was the Nernst Equation. Instead of Gibbs Energy being a value, it was a formula, and once the formula was simplified, we got our Overall Reaction Potential Formula. We then moved on to the Cathodic Reaction formulas. First, we focused on calculating the Cathodic Reaction Energy Formula. To do so, we needed to access a table in our research that provided us with the Standard Entropy and Enthalpy Change for our reaction. Once found, we set up the formula for our Cathodic Reaction Energy and plugged it into the Nernst Equation to get our Cathodic Reaction Potential formula. Finally, we could calculate the formulas for the Anodic side of the reaction, and it was done very simply. The Anodic Reaction Energy Formula was just the difference between the Overall Reaction and the Cathodic Reaction. Once that was calculated, the same was done with the overall and cathodic reactions to uncover the Anodic Reaction Potential Formula. We then plotted the Reaction Energies for the Overall, Cathodic, and Anodic reactions. We also did the same for the potential. The resulting calculations in the form of tables and graphs are shown below.

OVERALL REACTION ENERGY		OVERALL REACTION ENERGY FORMULA			
Temperature (oC)	Gibbs Energy (J)	Change In Entropy[Δs] (J/(mol*K))		Change In Enthalpy [ΔH] (J/mol)	
1100	284050.2	Formula	Value	Formula	Value
1120	282532.8	$\Delta s = \text{SLOPE}(C4:C16, B4:B16)$		$\Delta H = \text{INTERCEPT}(C4:C16, B4:B16)$	
1138.85	281101.7	-78.82671296		370883.398	
1140	281012.8	OVERALL REACTION ENERGY FORMULA			
1160	279466.3	$y = 370883.398 - 78.82671296 * x$			
1180	277918.3	$\Delta G_0 = 370883.398 - (78.82671296 * T)$			
1200	276368.7	OVERALL REACTION POTENTIAL FORMULA			
1220	274817.5	Nernst Equation	Number Of Moles [n] (mol)	Faraday's Constant [F] (C*mol ⁻¹)	
1240	273264.8	$\Delta G / (-n * F) = E$		2	
1245.85	272810.3	OVERALL REACTION POTENTIAL FORMULA			
1260	271598.3	$E_0 = -1.92196777 + (0.00040849 * T)$			
1280	269883.8				
1300	268168				

Table 6: The calculations made to obtain the Overall Reaction Energy and Potential formulas for the Manganese reaction.

CATHODIC REACTION ENERGY FORMULA		CATHODIC REACTION POTENTIAL FORMULA		
Change In Entropy[Δs1] (J)	Change In Enthalpy [ΔH1] (J)	Nernst Equation	Number Of Moles [n] (mol)	Faraday's Constant [F] (C*mol ⁻¹)
168.7	242600	$\Delta G / (-n * F) = E$		2
CATHODIC REACTION ENERGY FORMULA		CATHODIC REACTION POTENTIAL FORMULA		
$\Delta G_1 = 242600 - (168.7 * T)$		$E_1 = 1.25718591 - (8.74226148E-4 * T)$		

Table 7: The calculations made to obtain the Cathodic Reaction Energy and Potential formulas for the Manganese reaction.

ANODIC REACTION ENERGY FORMULA		ANODIC REACTION POTENTIAL FORMULA		
Formula		Nernst Equation	Number Of Moles [n] (mol)	Faraday's Constant [F] (C*mol ⁻¹)
$\Delta G_2 = \Delta G_0 - \Delta G_1$		$\Delta G / (-n * F) = E$		2
ANODIC REACTION ENERGY FORMULA		ANODIC REACTION POTENTIAL FORMULA		
$\Delta G_3 = 128283.398 + (89.8738287 * T)$		$E_1 = 0.66478186 - (4.65738298E-4 * T)$		

Table 8: The calculations made to obtain the Anodic Reaction Energy and Potential formulas for the Manganese reaction.

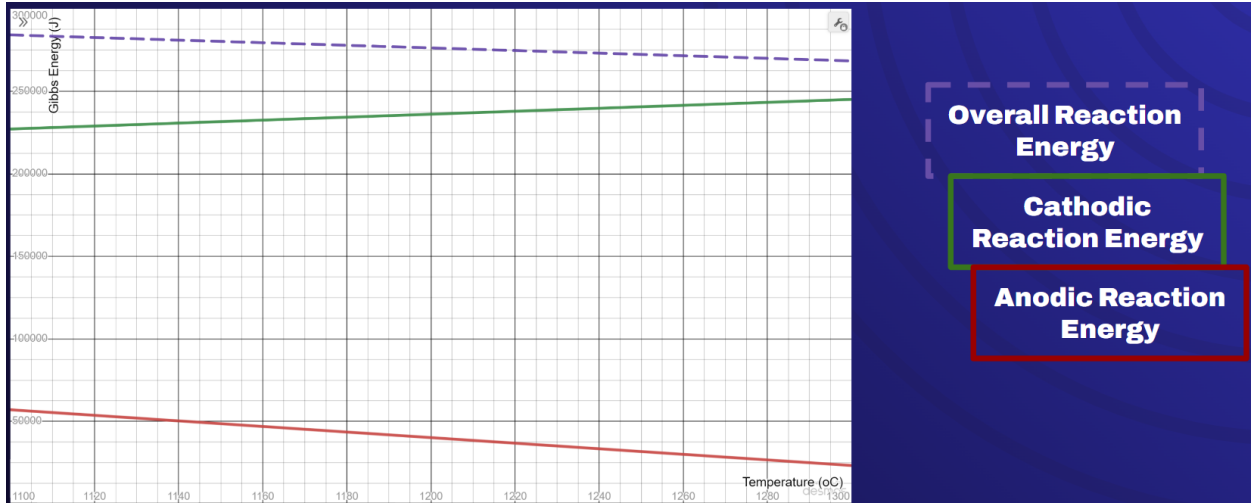


Figure 11: The Overall Reaction, Cathodic Reaction, and Anodic Reaction Energy Functions for the Manganese reaction graphed vs. Temperature.

Potentials Of Overall Reaction, Cathodic Reaction, & Anodic Reaction

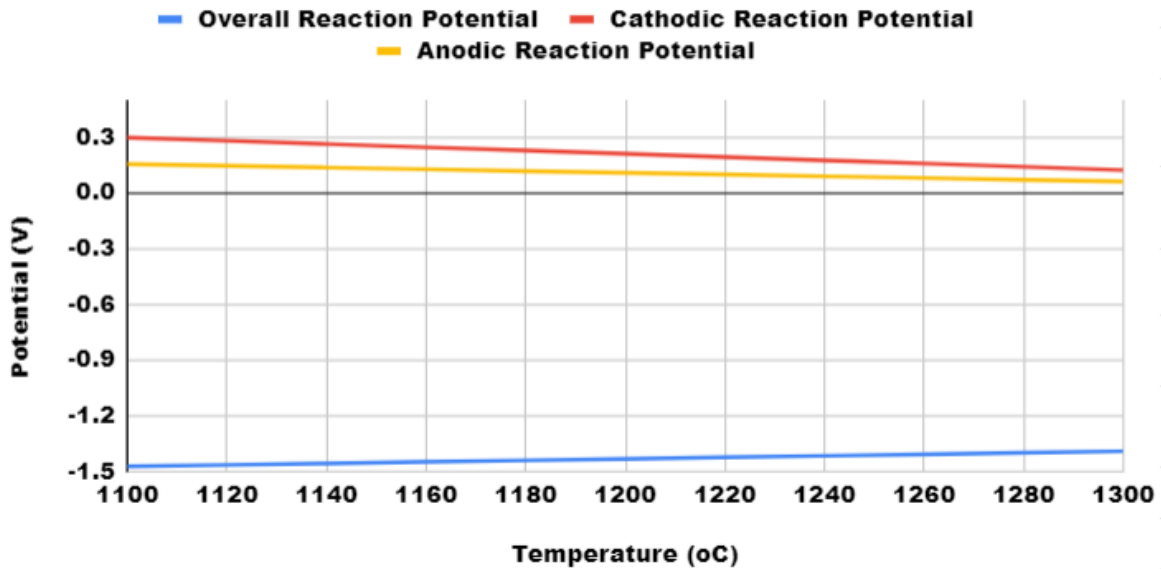


Figure 12: The Graph of the Overall Reaction, Cathodic Reaction, and Anodic Reaction Potential Functions for the Manganese reaction vs. Temperature.

The above steps for conducting this action item under the manganese molten oxide electrolysis reaction were identically followed for Aluminum Magnesium Boride and Zirconium Diboride.

4.2.7 Investigating The Mass Balance Of The Reaction

The calculation regarding Mass Balance required the electrolyte composition and the operating temperature. This was a calculation that required a very complex understanding. To resolve any confusion regarding this mass balance calculation, in the case of Mn MOE, we constructed an illustration to demonstrate the portrayal of the mass balance. This figure is shown below in *Figure 13*.

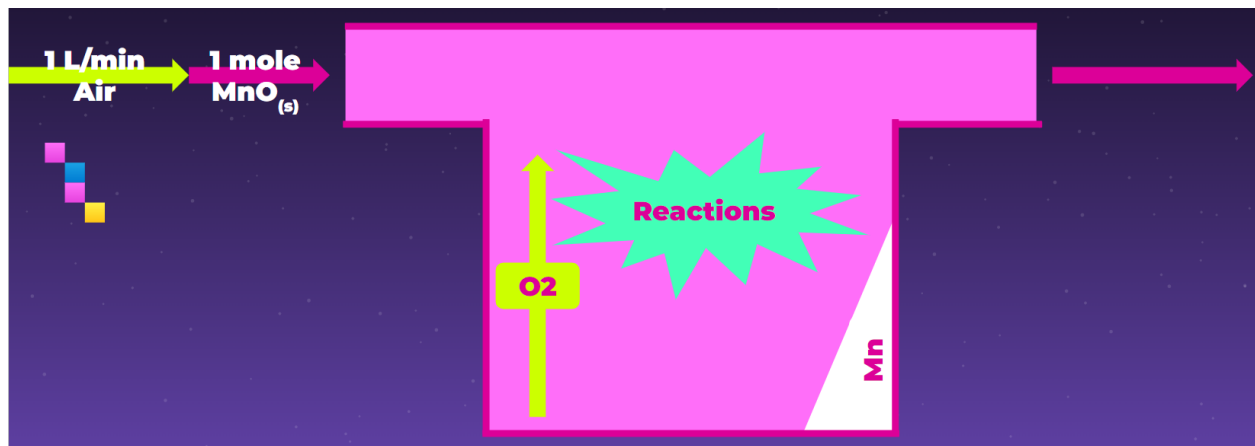


Figure 13: An illustration of what is occurring in the electrolytic cell. On the left-hand side, it shows 1 mole of solid-phase MnO being inserted into the cell alongside air at a rate of 1 liter/minute. Inside the cell (the U-shaped figure) is where the reactions occur, where ultimately, Manganese would subside to the bottom of the cell, and oxygen gas would be produced and rise to the top. All of the gasses, including oxygen gas, leave the system through the outlet shown on the right-hand side of the figure.

From the above figure and its description, we could better grasp what the mass balance provides and how to proceed with the calculations. We developed a procedure to calculate the Mn mass balance, and it appeared as follows:

1. Open FactSage and navigate to *Equilib* Module
2. Insert the corresponding moles to compounds of Composition Four and click “Next”

3. In the next window, select the appropriate phases (solid & ideal gasses), select Slag-A as “immiscible,” and change the temperature to 1260 °C, then press “Calculate”
4. In the Results window, record Mn's fugacity at this temperature in Google Spreadsheets
5. In Google Spreadsheets, construct a table consisting of the Mass Balance formula, designated air flow rate, total time, operating temperature, and fugacity of Mn
6. Calculate the fugacity rate per minute of Manganese using the following formula:

$$a. \hat{n} = \frac{P \cdot \hat{V}}{R \cdot T}$$

- i. \hat{n} is the fugacity rate of Mn [mol/min]
 - ii. P is the fugacity of Mn at 1260 °C [atm]
 - iii. \hat{V} is the airflow rate [L/min]
 - iv. R is the Universal Gas Constant
 - v. T is the Operating Temperature [°C]
7. Once we have calculated the fugacity rate per minute, we can determine the formula for the mass balance of Mn, which is as follows:

$$a. n_{Mn} = \hat{n} * t$$

- i. n_{Mn} is the manganese mass balance
 - ii. \hat{n} is the fugacity rate of Mn [mol/min]
 - iii. t is the time [min]
8. Upon determining the mass balance formula, we graphed the mass balance of Mn in a full day.

The results for the Mass Balance calculation for Mn MOE are shown below:

MASS BALANCE OF Mn							
Composition 4							
0.43858MnO - 0.413012SiO2 - 0.148408Al2O3							
Formula	Air Flow Rate [V_dot] (L/min)	Air Flow Rate (mol/min)	Total Time (t day in min)	Operational Temperature [T] (oC)	Operational Temperature [T] (K)	Fugacity of Mn @ Operational Temperature [P] (atm)	Fugacity Rate of Mn [n_dot] (mol/min)
$n_{Mn} = (n_{dot}) * (t)$	1	0.04464285714	1440	1260	1533.15	0.0010276	$n_{dot} = (P * V_{dot}) / (R * T)$ 0.000008168152042
Manganese Mass Balance Formula							
$n_{Mn} = (8.168152042E-6) * (t)$							

Table 9: The calculations made to obtain the Fugacity rates of Manganese over time for the Mass Balance of Mn.

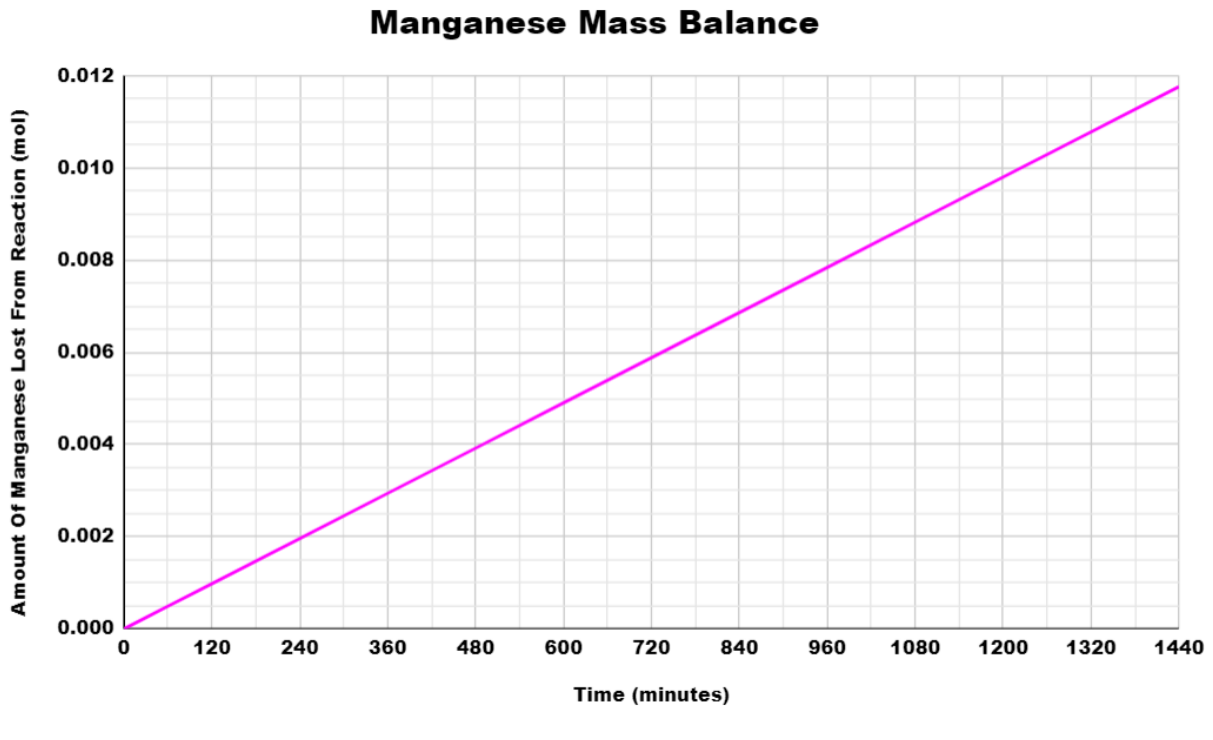


Figure 14: The total Mass Balance of Mn graphed in terms of Fugacity rate (atm/min) vs. time (min). The graph is mapped out over a full day in terms of minutes.

We conducted the same procedure for AlMgB₁₄ and ZrB₂ Mass balances. However, we had to consider the fugacity rate of multiple elements, as these borides were multi-element compounds. So, a few extra steps had to take place to ensure the completion of this calculation.

4.2.8 Investigating The Energy Balance Of The Reaction

There were two methods of calculating the energy balance of our overall reaction. The first method involved examining the reaction as a whole. We investigated energy balance concerning those two methods with our trial calculations with manganese molten oxide electrolysis. For the first method, this calculation was done through various steps with the assistance of FactSage. Here are the steps taken in conducting the calculation by examining the reaction as a whole:

1. We opened up FactSage. We navigated to the *Reaction Module*, where we imputed our overall reaction
2. We turned on “initial conditions” and then set the reactants to solids at 25 °C and the products to liquid (Mn) and gas (O₂) at 1260 °C, and then pressed “Next”
3. In the following window, we set our temperature to 1260 °C and pressed “Calculate” to yield thermodynamic properties about our reaction
 - a. Regarding energy balance, our focus was on Change in Gibbs Energy and Entropy Change
4. We recorded those two thermodynamic properties in Google Spreadsheets and plugged them into the Gibbs Energy formula
 - a. This formula was the formula for our Energy Balance
5. We then plotted this formula on a graph from 1100 °C to 1300 °C.

The results of this step are shown in the table and figure below:

ENERGY BALANCE		
<u>Formula</u>	<u>Gibbs Energy [ΔG] (J)</u>	<u>Entropy [Δs] (J/K)</u>
$\Delta H = \Delta G + (T * \Delta s)$	134285.9	169.834
ENERGY BALANCE FORMULA		
$\Delta H = 134285.9 + (169.834 * T)$		

Table 10: The calculations made to obtain the Energy Balance formula through the Gibbs Energy calculation in calculating the formula of Entropy Change for Mn MOE.

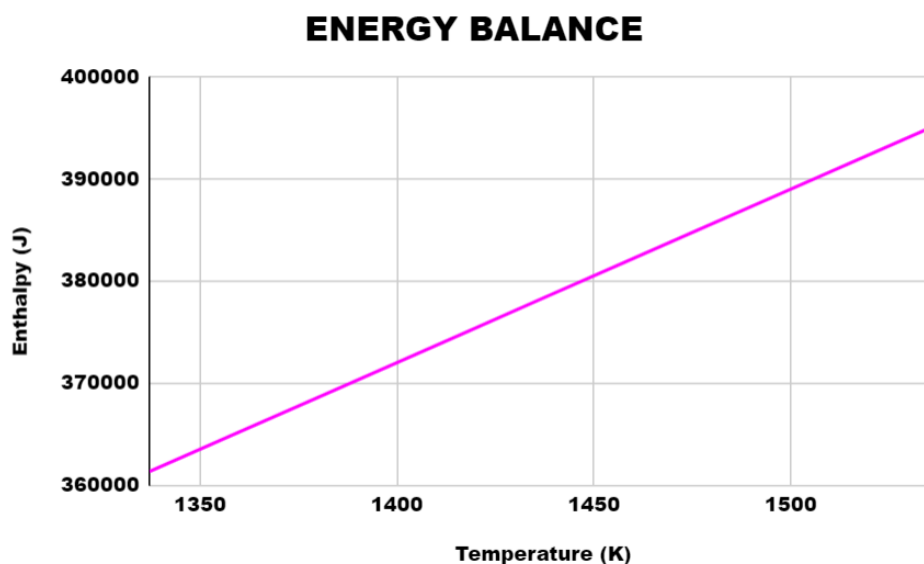


Figure 15: The total Energy Balance of Mn graphed in terms of enthalpy (kJ) vs. temperature (K).

The second method involved examining the reaction at different stages. The reaction stages included the reactants heating up and the reaction taking place. With the help of FactSage, this calculation was completed in a series of steps. The following steps were taken in conducting the computation by examining the entire reaction:

1. We opened up FactSage and navigated to the *Reaction Module*, where we inputted our overall reaction

2. We turned on “initial conditions” and then set the reactants to solids at 25 °C and the products to be the same as the reactants but at 1260 °C, and then pressed “Next”
3. In the following window, we set our temperature to 1260 °C and pressed “Calculate” to yield thermodynamic properties about our reaction
 - a. Our focus was on Change in Gibbs Energy and Entropy Change
4. We recorded those two thermodynamic properties in Google Spreadsheets and plugged them into the Gibbs Energy formula
 - a. This formula was the formula for our Energy Balance for when the reactants were heated up
5. We then cleared the menu window of the *Reactants* module and set up the overall reaction, and then pressed “Next”
 - a. However, this time our reactants (still solid) would be at the same temperature as our products—1260 °C
6. We repeated Steps 3 and 4 for the constraints of Step 5
7. We then plotted all of the formulas on a graph from the temperature range of 1100 °C to 1300 °C

The results of this step are shown in the table and figure below:

ENERGY BALANCE		
Enthalpy Change @ Room Temperature		
Formula	Gibbs Energy [ΔG_1] (J)	Entropy [Δs_1] (J/K)
$\Delta H_1 = \Delta G_1 + (T * \Delta s_1)$	-122346	109.864
$\Delta H_1 = -122346 + (109.864 * T)$		
Enthalpy Change @ Room Temperature		
Formula	Gibbs Energy [ΔG_2] (J)	Entropy [Δs_2] (J/K)
$\Delta H_2 = \Delta G_2 + (T * \Delta s_2)$	256631.9	59.97
$\Delta H_2 = 256631.9 + (59.97 * T)$		
Enthalpy Change @ Room Temperature		
Formula	Gibbs Energy [ΔG] (J)	Entropy [Δs] (J/K)
$\Delta H_0 = \Delta H_1 + \Delta H_2$	134285.9	169.834
ENERGY BALANCE FORMULA		
$\Delta H = 134285.9 + (169.834 * T)$		

Table 11: The calculations made to obtain the Energy Balance formulas through the Gibbs Energy calculation in calculating the formula of Entropy Change. These formulas are the formulas generated of the measured energy balance at each stage of the total reaction. This is for the Mn MOE reaction.

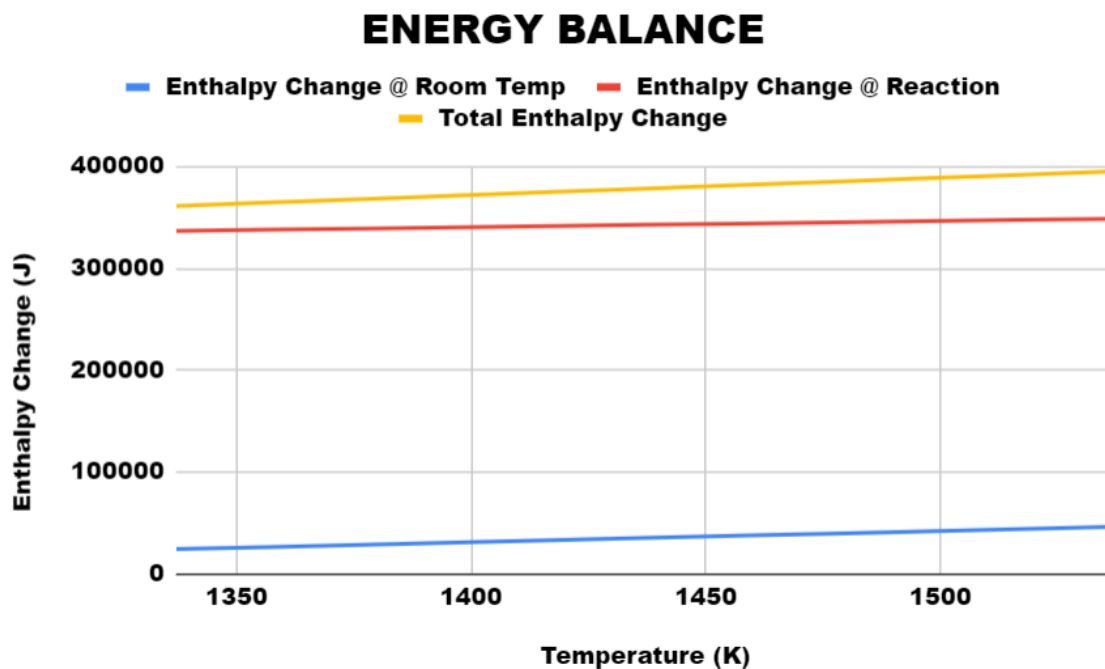


Figure 16: *The Energy Balances of Mn graphed in terms of enthalpy (kJ) vs. temperature (K). This shows the enthalpy changes at each stage of the reaction, as well as that for the total reaction.*

To ensure the calculations were correct, we compared the values of the Enthalpy Changes at each reaction stage to that of the total reaction and found that they matched. We similarly conducted this concerning AlMgB₁₄ and ZrB₂ MOE, with some alterations. One of those alterations in the aluminum magnesium boride results was that the product of the reaction remained solid, rather than in this situation where the product was liquid.

4.2.9 Calculating The Nominal Cathode-To-Anode Distance Of The Electrolytic Cell

The following data set to be procured concerned the nominal cathode-to-anode distance for the electrolytic cell of the specific reaction. For the sake of this methodology section and continuing with the same trend, we conducted this calculation for the Manganese Molten Oxide Electrolysis reaction. Before conducting the calculative process, one crucial selection had to be made. This selection was the selection of the anode and cathode material. Our research in the *3.0 Background Section* confirmed that our electrode material for this reaction would be graphite.

Now that the material was decided, we proceeded with the calculations of nominal cathode-to-anode distance. Before establishing the steps to calculate this distance, we had to examine the formula around said distance. This was the formula collected from our research $R = \frac{\rho^*D_{ac}}{Area}$, and it was explained in the *3.0 Background Section*. Once we had established the ordinance of this calculation, we postulated some steps to follow to calculate this distance. The steps are:

1. Calculate & record the Thermodynamic Properties of the Reaction. Those include

- a. Operating Temperature
- b. Change in Gibbs Energy
- c. Enthalpy Change
- d. Entropy Change
 - i. It can be derived from FactSage or through the Gibbs Energy Formula

2. Then, we focussed on calculating the Minimum Operating Voltage. This was done through a few steps of their own:

- a. The Heat Loss during Electrolysis was determined from this formula:

- i. $\Delta Q = \Delta S * T$

1. ΔQ is the heat loss during electrolysis
 2. ΔS is the enthalpy change
 3. T is the operating temperature

- b. Next, we calculated the Minimum Operating Voltage using the Nernst Equation. For the case of Manganese MOE, our “n” was 2

3. The Third Step was to calculate the Electrolysis Reaction Voltage, procured through this formula:

- a. $V_r = \frac{\Delta Q}{n * F}$

- i. The Heat Loss during Electrolysis was found during the Second Step

4. Afterward, we calculated the Voltage requirement for introducing Ore-Feedstock into the reaction at 25 °C. This was done in a two-mini-step process.

a. First, we determined the Enthalpy change for when the reactant of MnO heated up from 25 °C to 1260 °C.

b. Using this Enthalpy Change, we calculated the voltage using the formula

$$V_{feed} = \frac{\Delta H}{n * F}.$$

5. This Fifth Step was the final step in attaining the components of our Ohmic Drop (Step Six). In this step, we had to determine the Voltage for the Thermodynamic Losses of the reaction.

a. We assumed this Voltage to be Zero, as we assume that no thermodynamic losses occur throughout the reaction.

6. Step Six required us to calculate the Ohmic Drop

a. The Ohmic Drop was essentially the sum of all the Voltages calculated in the steps above

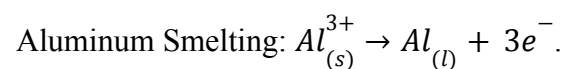
7. Once we completed that calculation, we used Ohm's Law to compare our distance formula to the Ohmic Drop. We proceeded to simplify based on this comparison.

a. The formula of Ohm's Law required us to examine the Current which we equated as the product of the Current Density and Area

8. Once all simplification was complete, we were left with this formula $V_{IR} = j * \rho * D_{ac}$. We made some assumptions to calculate our desired distance.

These assumptions are:

a. Current Density can be assumed to be $2 \frac{A}{cm^2}$, which is the same for



- b. Resistivity can be assumed to be $1 \text{ ohm} \cdot \text{cm}$ which is typical for Molten Salts.

9. Upon gathering all the necessary data, the Nominal Cathode-To-Anode Distance was calculated in terms of centimeters.

The results pertaining to Manganese Molten Oxide Electrolysis, as shown in the following table:

NOMINAL CATHODE TO ANODE DISTANCE							
Formula							
$R = (\rho * D_{ac}) / (\text{Area})$							
ρ	Resistivity ($\text{ohm} \cdot \text{cm}$)	R	Electrolyte (Ohms)	D_{ac}	Nominal Anode-To-Cathode Distance	Area	Area Between Anode & Cathode
Step Five: Calculating Voltage For Losses							
Assumption: 0							
Step Six: Calculating Ohmic Drop							
$V_{IR} = V_{feed} + V_r + V_{loss}$							
1.302543581							
Step Seven: Calculating The Anode-To-Cathode Distance							
$V_{IR} = I * R$							
$R = (\rho * D_{ac}) / (\text{Area})$							
$V_{IR} = I * ((\rho * D_{ac}) / (\text{Area}))$							
$I = j * \text{Area}$							
$V_{IR} = (j * \text{Area}) * ((\rho * D_{ac}) / (\text{Area}))$							
$V_{IR} = j * (\rho * D_{ac})$							
Step Three: Calculating Electrolysis Reaction Voltage							
Assumptions							
Current Density can be assumed to be 2 A/cm^2 , which is the same for Aluminum Smelting: $\text{Al}[3+] = 3e[-] + \text{Al}(l)$							
Resistivity can be assumed to be $1 \text{ ohm} \cdot \text{cm}$ which is typical for Molten Salts							
Voltage Drop From Reaction Ohmic Drop (V_{IR}) (V)							
1.302543581							
Current Density (j) (A/cm^2)							
2							
Resistivity (ρ) ($\text{ohm} \cdot \text{cm}$)							
1							
0.6807692793							
Step Four: Calculating Voltage For Introducing Ore Feedstock @ 25 oC							
Ore Feedstock MnO (s, 25 oC) To MnO (l, 1260 oC)							
Enthalpy Change $[\Delta H]$ (kJ/mol.Mn_l)							
119984.2							
Formula							
$V_{feed} = \Delta H / (n * F)$							
0.6217743018							

Table 12: The calculation process to obtain the Nominal Cathode-To-Anode Distance for the electrolytic cell containing the Mn MOE reaction.

The same steps were followed identically to calculate the distances for aluminum magnesium boride and zirconium diboride. The assumptions were the same throughout all calculations. However, the number of transferred electrons, amongst other measurements, would differ for each investigated boride.

4.2.10 Investigating The Faradaic & Energy Efficiency Of The Reaction

We subsequently evaluated the efficiency of our reaction after determining the notional cathode-to-anode distance. This was accomplished by combining previously calculated components from our process with the nominal cathode-to-anode distance. The first efficiency on which we concentrated was faradaic.

In this calculation, we did not need to calculate the faradaic efficiency. Instead, we were determining the potential amount of actual product produced based on a specific faradaic efficiency. The formula to conduct this exact calculation was $\eta_f = \frac{m}{m_o} * 100\%$ as described in *Section 3.0 Background*. Here were the steps we took to determine the amount of Manganese produced for our molten oxide electrolysis reaction based on the faradaic efficiency:

1. In the first step, we made an assumption. We assumed that the faradaic efficiency was 90%, as modern aluminum electrolysis cells operate at approximately 90% faradaic efficiency, so we assumed to apply the same efficiency to this manganese electrolysis cell.
 - a. This assumption was carried onto our boride calculations, as well.
2. In the second step, we calculated the theoretical mass of manganese produced in the MOE process. To do this, we used this formula $m = \frac{M*Q}{n*F}$, where M was the molar mass of Manganese, and Q was the charge.
 - a. To calculate the charge, we needed to use another formula. This formula was $Q = I * \Delta t = j * Area * \Delta t$.
 - i. We used the same assumption from our distance calculation for our Current Density.

- ii. We assumed the area to be under the conditions of 1 cm^2 .
 - iii. We also assumed that we operate our reaction over the scope of a day or 86400 seconds.
- b. Once our Charge was calculated, we calculated the theoretical mass of manganese produced in the MOE process simply by plugging in the missing variables.
3. In the third step, we use our formula for the faradaic efficiency to calculate the actual mass of manganese produced in the MOE process.

The following table shows the results of the actual mass of manganese produced under 90% faradaic efficiency in the Molten Oxide Electrolysis process:

FARADAIC EFFICIENCY (CURRENT EFFICIENCY)					
Formula					
$\eta_f = ((m) / (m_o)) * 100\%$					
η_f	Faradaic Efficiency	m	Actual Mass Produced (grams)	m_o	Theoretical Mass Produced (grams)
Step One: Developing Assumptions					
Assumption			Reasoning		
$\eta_f = 90\%$			Modern aluminum electrolysis cells operate at approximately 90% faradaic efficiency, so we can assume to apply the same efficiency to this manganese electrolysis cell		
Step Two: Calculating The Theoretical Mass Of Manganese Produced					
Formula					
$m = (M * Q) / (n * F)$					
Molar Mass [M] (g/mol-Mn)	54.938044	Number Of Tranferred Electrons [n] (mol-e/mol-Mn)	2	Faraday's Constant [F] (C/mol-e)	96485.3321
Charge [Q] (C/mol)					
$Q = I * \Delta t = (j * Area) * \Delta t$					
Current Density [j] (A/cm²)	2	Area [cm²]	1	Time [Δt] (s)	86400
172800					
Theoretical Mass [m] (gram)					
49.1955295					
Step Three: Calculating The Actual Mass Of Manganese Produced					
Formula					
$\eta_f = ((m) / (m_o)) * 100\%$					
Fradaic Efficiency [η_f] (%)	90	Theoretical Mass Produced [m_o] (g)	49.1955295		
44.27597655					

Table 13: The calculation process to obtain the Actual Produced Mass of Mn. This was done assuming the reaction occurred at a 90% faradaic efficiency.

The same approach was taken to calculate the actual mass of aluminum magnesium boride and zirconium diboride produced in their respective MOE reactions, which were assumed to operate at 90% faradaic efficiency. Throughout all calculations, the assumptions were the same. However, the number of electrons transported, among other data, would differ for each of the borides studied.

We then moved on to calculating the Energy efficiencies of our reactions. The formula for calculating this efficiency was $\eta_E = \frac{E_o}{E} * \eta_f$, where the parameters were previously explained in *Section 3.0 Background*. The assumed faradaic efficiency of 90% translated to this calculation, as seen in the following calculation steps:

1. Step One was developing that very assumption about the Faradaic Efficiency
2. Step Two was calculating the Theoretical Minimal Potential. This was done through the following formula: $E_o = V_{min} + V_r + V_{feed}$.
3. Step Three was the final step. In this step, the energy efficiency was calculated. However, first, the Actual Minimal Potential needed to be calculated.
 - a. The Actual Minimal Potential was calculated through this formula,

$$E = E_o + \frac{\Delta S * T}{n * F}$$
 - b. Once that was calculated, we used the energy efficiency formula to complete our calculation.

The following table shows the results of Energy efficiency for Manganese Molten Oxide Electrolysis:

ENERGY EFFICIENCY							
Formula							
$\eta_E = ((E_o) / (E)) * \eta_f$							
η_E	Energy Efficiency	E	Actual Minimal Potential (V)	E_o	Minimal Theoretical Potential (V)	η_f	Faradaic Efficiency
Step One: Developing Assumptions							
Assumption				Reasoning			
$\eta_f = 90\%$				Modern aluminum electrolysis cells operate at approximately 90% faradaic efficiency, so we can assume to apply the same efficiency to this electrolysis cell			
Step Two: Calculating The Minimal Theoretical Potential							
Formula							
$E_o = V_{min} + V_r + V_{feed}$							
Minimum Operating Voltage [V_min] (V)	1.40745901	Electrolysis Reaction Voltage [V_r] (V)	0.6807692793	Voltage For Introducing Ore Feedstock [V_feed] (V)	0.6217743018		
2.710002591							
Step Three: Calculating The Energy Efficiency							
Formula							
$\eta_E = ((E_o) / (E)) * \eta_f$							
Actual Minimal Potential							
$E = E_o + (T * \Delta S) / (2F)$							
Minimal Theoretical Potential [E_o] (V)	2.710002591	Operating Temperature [T] (K)	1533.15	Entropy Change [ΔS] (J/mol*K)	85.68535368	Faraday's Constant [F] (C/mol)	96485.3321
3.39077187							
79.92288171							

Table 14: The calculation process to obtain the Energy Efficiency of Mn. This was done assuming the reaction occurred at a 90% faradaic efficiency.

The same procedures were used to study aluminum magnesium boride and zirconium diboride's efficiency. Throughout all calculations, the assumptions were the same. However, the number of electrons transferred, among other data, would differ for each of the borides studied.

4.2.11 Endothermic Or Exothermic

The final calculation required for investigating the molten oxide electrolysis process was determining if the process was endothermic or exothermic. This was a very simple calculation. In the case of our trial calculations with Manganese MOE, we would examine the Energy Balance graph (Figure 15). If the slope of the energy balance graph was positive, the reaction would be endothermic. If the slope of the energy balance graph was negative, the reaction would be

exothermic. This designation of reaction type was conducted for the boride calculations based on the energy balance graphs generated from those reactions.

5.0 Results & Analysis

5.1 Aluminum Magnesium Boride

5.1.0 Pseudo-Binary Phase Diagram

We first started emulating isothermal sections based on temperature, similar to the manganese molten oxide electrolysis process we conducted as a test trial to familiarize us with the calculations. We started at 1100 °C. However, the slag-liquid region, the region we were targeting, was too small. We then moved on to 1200 °C and then 1300 °C, only to conclude that the slag-liquid region is too small to consider. Thus a pseudo-binary diagram was constructed.

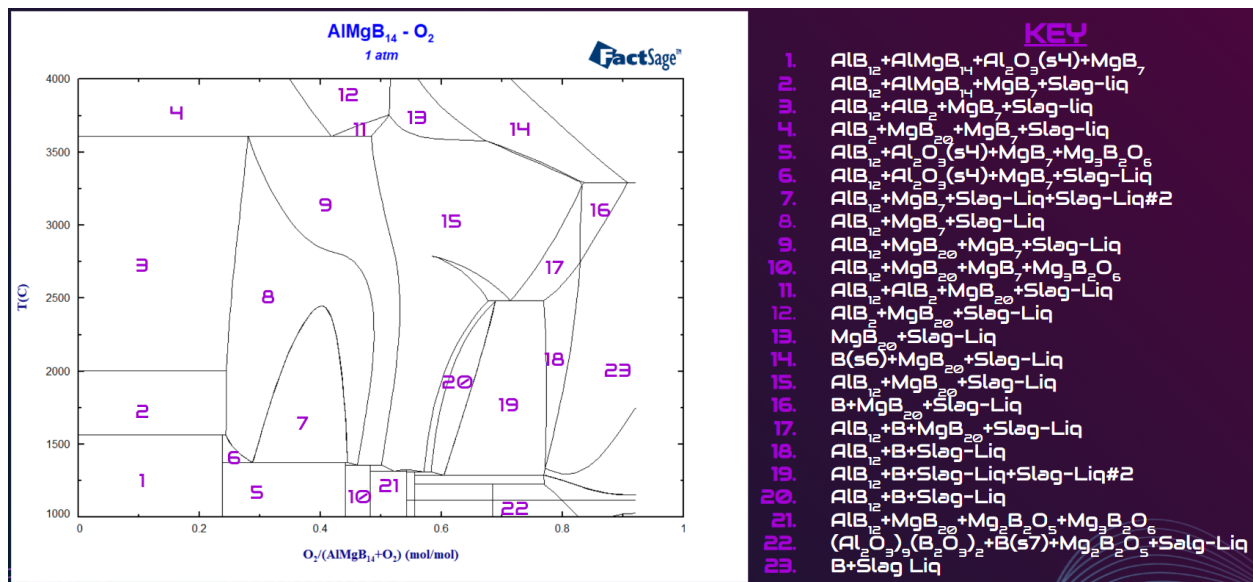


Figure 17: The Pseudo-Binary Phase Diagram Between $AlMgB_{14}$ and O_2 from a temperature range of 1000 °C to 4000 °C. The 23 most significant resulting compositions are shown and labeled with a key.

As shown in *Figure 17*, we graphed all possible compositions to obtain these products. As we read the graph from right to left, starting from the tail, we see that the Slag-Liquid gets compounds containing aluminum, magnesium, and boride added to it. These compounds include

AlB_{12} , MgB_7 , $AlMgB_{14}$, etc. Although this helped map out the products much better, it still needed to be determined which temperature to operate.

However, when looking at the pseudo-binary diagram, the bottom of the diagram, or more technically speaking, at the 1000 °C to 1500 °C, shows only solid compositions. This is not what we desire to obtain at any temperature. We had to take it further with this diagram and recalculate it at a more focused and suitable temperature range.

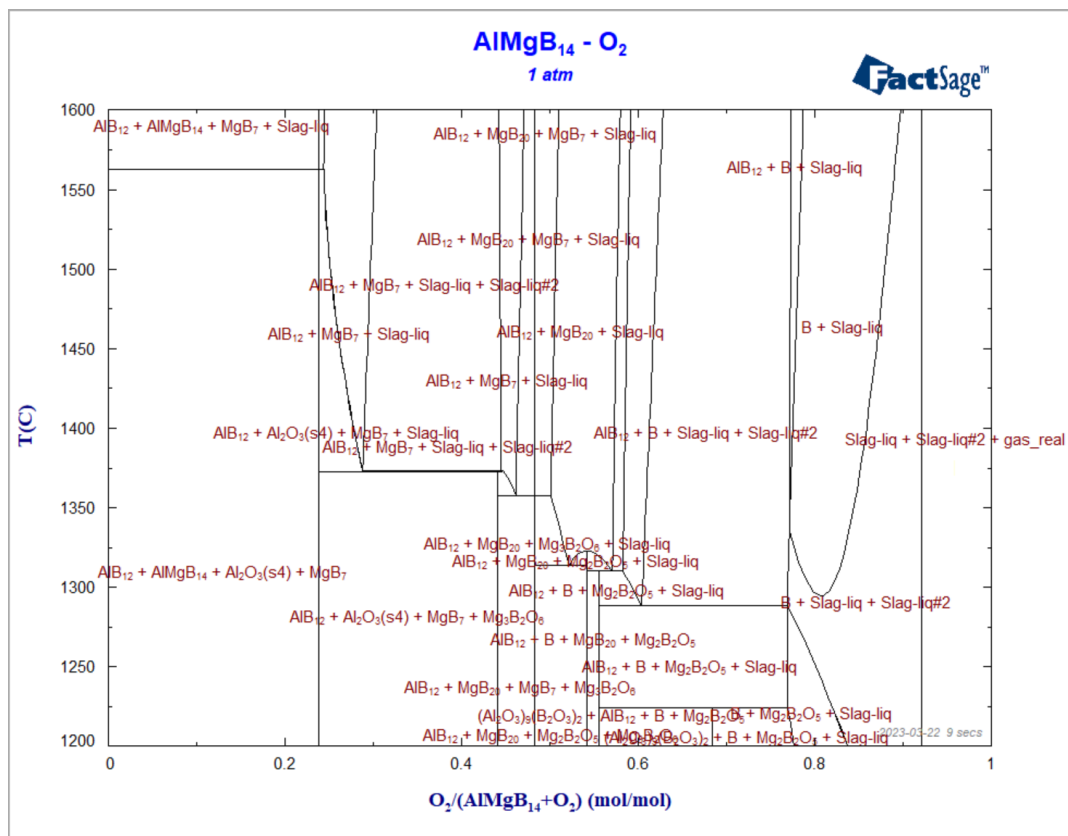


Figure 18: The Pseudo-Binary Phase Diagram Between $AlMgB_{14}$ and O_2 from a temperature range of 1200°C to 1600°C.

This range was from 1200 °C to 1600 °C, as seen in *Figure 18*. As previously explained, *Figure 8* shows the region between 1000 °C to 1500 °C, in some areas only containing solids; however, some sites just below the 1500 °C temperature line had Slag-liquid present. So the range needed to begin at a temperature suitable for that scenario. We first designated 1500 °C as the lower temperature range limit. Our upper limit was established to 2000 °C, as we noticed in

Figure 8, in the far left corner between 1000 °C and 2000 °C was where AlMgB_{14} was only present. We initially decided to observe the temperature of 1700 °C to be our operation temperature. However, we concluded that 1700 °C was not viable because the fugacity was too high. Thus we reexamined the range, such that the upper limit would be 1600 °C and our lower limit to be 1200 °C. When we analyzed this pseudo-binary phase diagram, we saw that after the 0.2-mole fraction of O_2 to $\text{AlMgB}_{14} + \text{O}_2$ solids, the only phase to form below approximately 1375 °C.

5.1.1 Isothermal Section

We decided to continue our calculations focusing on 1440 and 1600 °C because they were the best temperature from the pseudo-binary phase diagram in *Figure 18*. So our next step was constructing isothermal sections for both temperatures to select our seven focus compositions.

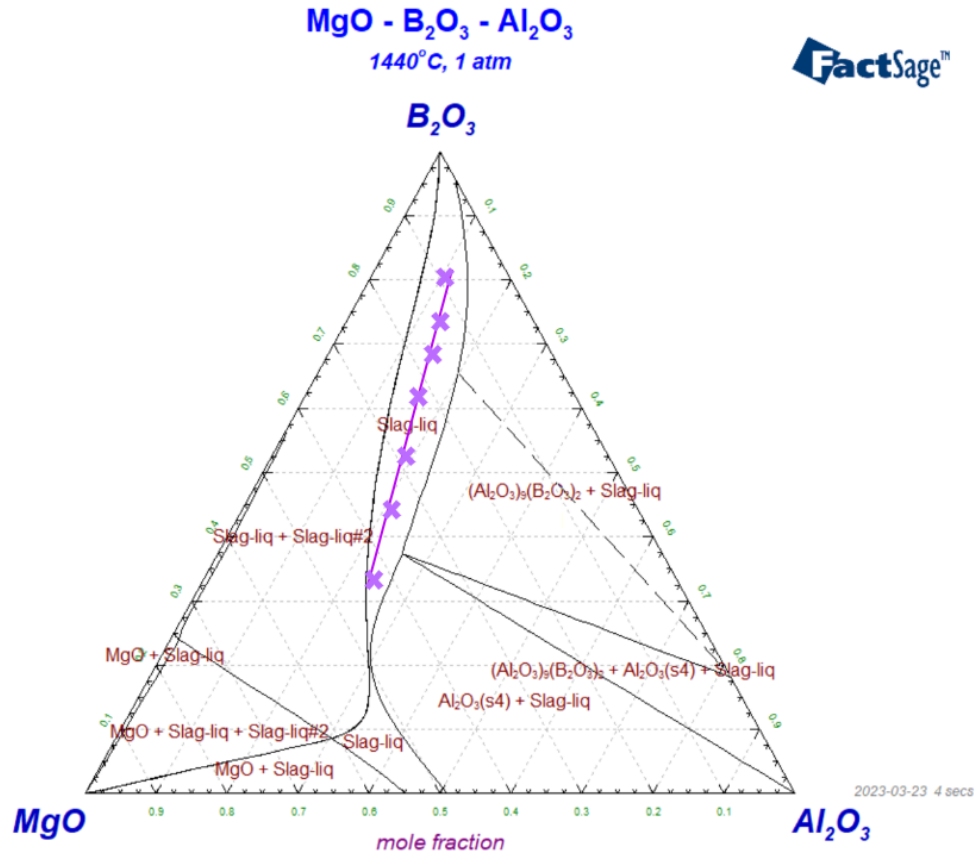


Figure 19: The Isothermal Section between B₂O₃, MgO, and Al₂O₃ at 1440 °C. The seven compositions we examine are the purple “x’s” in the Slag-liquid region.

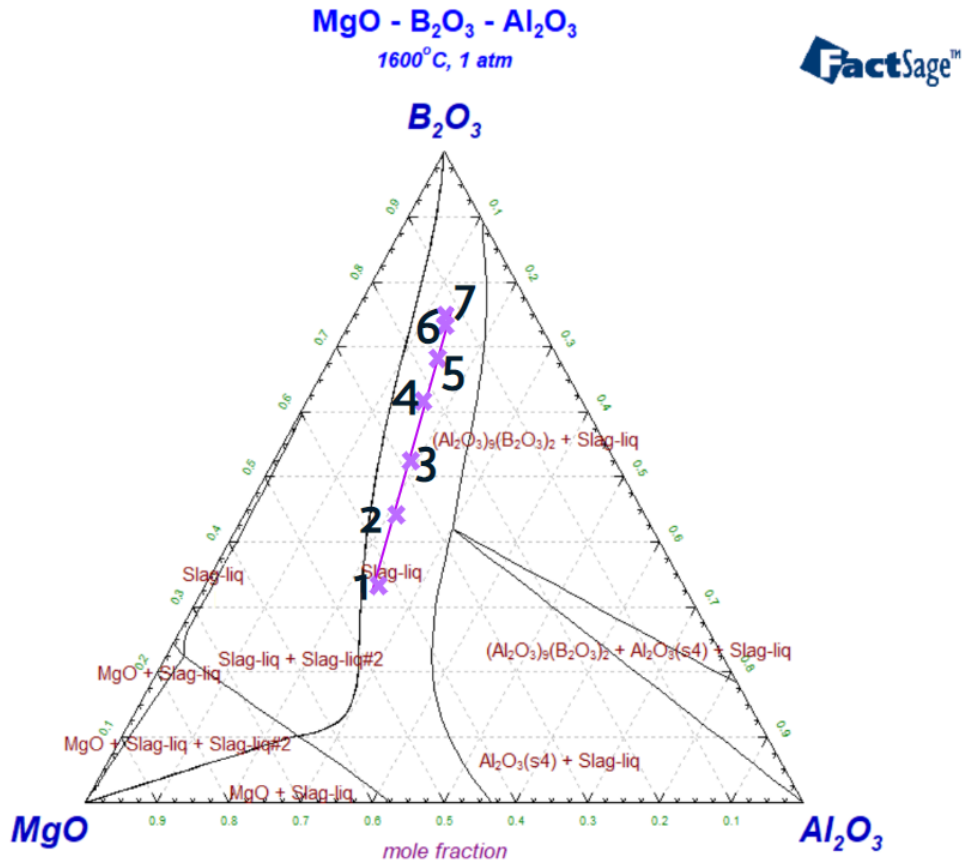


Figure 20: The Isothermal Section between B_2O_3 , MgO , and Al_2O_3 at $1600\text{ }^\circ\text{C}$. The purple “x’s” labeled one through seven are the same seven compositions consistent with the same region of $1440\text{ }^\circ\text{C}$.

Once we have gathered these seven compositions, we tabulate and graph the composition's vapor pressure, or fugacity, with the highest fugacity. The region of the isothermal section we are looking for is the Slag-liquid region, which appears at the center of the diagrams, as seen in *Figure 19* and *Figure 20*. This is because of the electrolyte reaction, in which we focus the yield on being liquid.

5.1.2 Vapor Pressure Trend Of The Seven Compositions

Once we mapped out the seven compositions, it came time to simulate and tabulate the fugacity of the composition with the highest fugacity. Our focus is the compound with the highest vaporization or vapor pressure. That means that during the reaction with electrolyte at temperature X, multiple formed compositions will experience vaporization.

In selecting our seven compositions, we found the mole fraction of each electrolyte compound, as the isothermal sections were mapped out in terms of mole fraction. We found each Al_2O_3 , B_2O_3 , and MgO mole fraction for each of the seven compositions, recorded them, and calculated the fugacities of the highest vapor pressure compound. Through the *Equilib* database on FactSage, we conducted this calculation for fugacity across a wide temperature range, as discussed in the *4.0 Methodology Section*. This temperature range was from 900 °C to 2000 °C in increments of 60 °C. Upon yielding the fugacity results across all temperatures of that range in the *Equilib* database. We found that it was B_2O_3 that had the highest vapor pressure of all other vaporizing compounds. Thus, we proceeded to record all of those fugacities from that temperature range and yielded the following table.

Table 15: Vapor Pressure/Fugacity Of Seven Compounds Of MgO-B₂O₃-Al₂O₃ Displaying Largest-Fugacity Compound (B₂O₃) From 900°C To 2000°C

As we can see from Table 15, the fugacity of B₂O₃ increases significantly as the temperature increases. To more easily see the trend across all seven compositions.

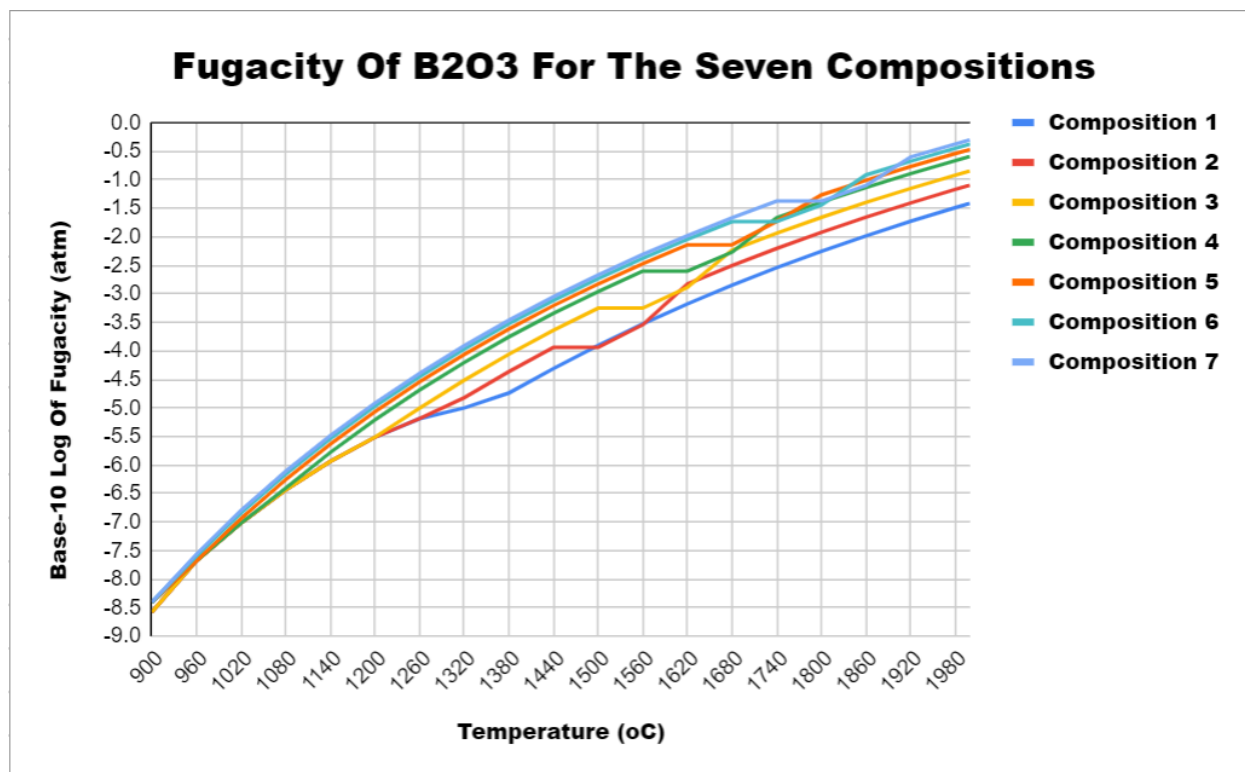


Figure 21: The Fugacity Trend of B₂O₃ from 900 to 2000 °C. This graph is displayed as Temperature (in degrees Celsius) versus the Base-10 Log of Fugacity in (atm).

We reconstructed the fugacity data into a Base-10 log for the data to be more readable and more linear, which made it easier to examine the fugacity trend of B₂O₃. Although we could see a trend in our fugacity, it was difficult to depict at this range, especially since our operating temperatures of focus were 1440 °C and 1600 °C, so another graph was constructed. This graph held both temperatures within the range, as shown below in Figure 22.

Fugacity Of B₂O₃ For The Seven Compositions (Focused)

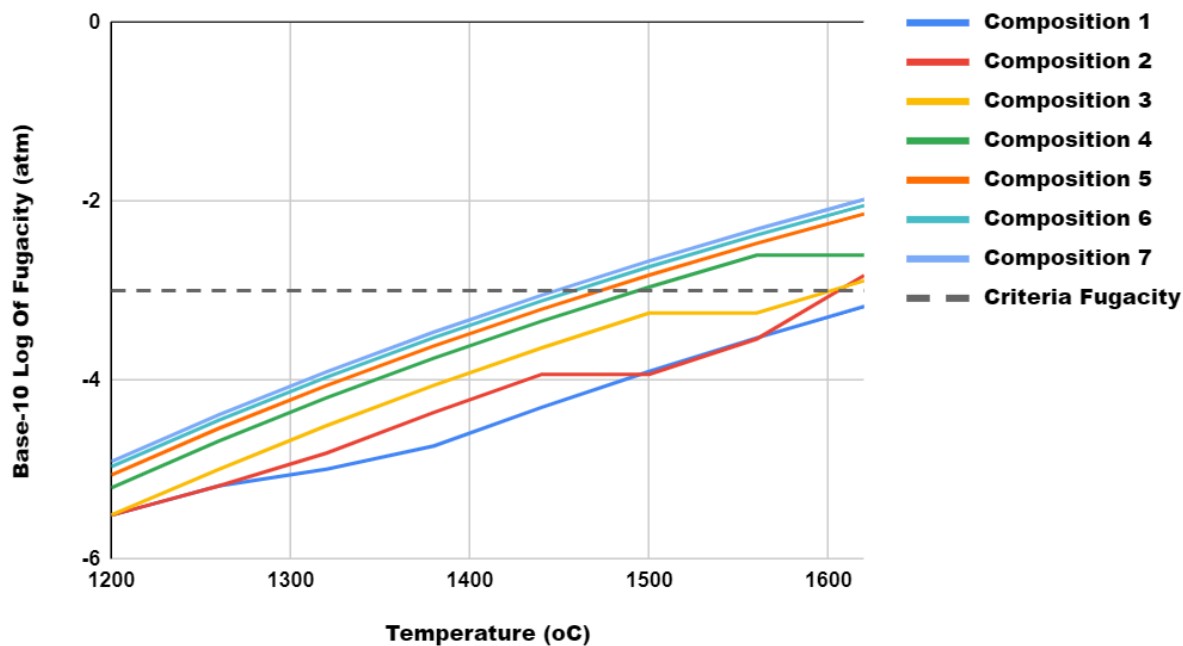


Figure 22: The “focused” Graph of the Fugacity Trend of B₂O₃ from 1200 to 1600 °C. This graph is displayed as Temperature (in degrees Celsius) versus the Base-10 Log of Fugacity in (atm).

In *Figure 22*, we see a “focused” version of the graph from *Figure 21*, which displays the Base-10 logarithm of the fugacity of B₂O₃ from 1200 °C to 1600 °C. Here we can see the trend at 1440 °C and 1600 °C. We also introduced a new line. This line was denoted as the criteria fugacity: the fugacity that we should yield at a specific operating temperature. This criteria fugacity is 10⁻³ atm and put into Base-10 Log form, it is -3 (as $\log(10^{-3}) = -3$). So the fugacity trend should meet this dotted line present in *Figure 22*. This line begins crossing through the fugacity trends of each of the seven compositions, starting at approximately the temperature of mid-1400 °C. *Table 15* shows that this “mid-1400 °C” can more accurately be stated at 1440 °C, which was one of the two temperatures we were observing. The temperature of 1600 °C has the fugacity to hit the criterion for compositions six and seven. However, all others

see a higher fugacity of B_2O_3 than this criterium. This information was something to be considered when deciding between 1440 °C and 1600 °C.

5.1.3 Viscosity Trend Of The Seven Compositions

Using the viscosity module of FactSage, the viscosity of the seven compositions can be found. The viscosity of each composition at temperatures ranging from 900 to 2000 °C was calculated, with the results shown in the table below.

Temp.	1	2	3	4	5	6	7
900	106.325	107.403	110.805	114.718	119.345	125.454	131.331
1000	40.933	41.323	42.591	44.042	45.78	48.115	50.572
1100	18.114	18.278	18.824	19.444	20.194	21.214	22.346
1200	8.957	9.034	9.297	9.594	9.956	10.452	11.022
1300	4.845	4.885	5.024	5.18	5.372	5.634	5.944
1400	2.821	2.844	2.923	3.011	3.12	3.27	3.45
1500	1.746	1.76	1.808	1.861	1.927	2.018	2.128
1600	1.138	1.147	1.178	1.211	1.253	1.312	1.382
1700	0.774	0.781	0.801	0.823	0.852	0.89	0.938
1800	0.547	0.551	0.566	0.581	0.601	0.628	0.661
1900	0.399	0.402	0.413	0.423	0.437	0.457	0.481
2000	0.299	0.302	0.309	0.317	0.328	0.342	0.359

Table 16: Raw data of the viscosity of selected compositions at various temperatures.

The results from *Table 16* show the different viscosities of each composition. Composition 1 had the lowest viscosity at 1.138 poise at 1600 °C, while Composition 7 had the highest viscosity at 1.382 at 1600 °C. The viscosity increased linearly from composition one up to composition 7. The difference in viscosities between the compositions remained consistent across all temperatures. As composition seven contains the highest percentage of B_2O_3 and composition 1 contains the lowest, it can be deduced that adding B_2O_3 increases the viscosity of

the composition. Since viscosity is inversely proportional to the reaction rate, a composition with a lower mole fraction of B_2O_3 should be selected (compositions 1-4) to achieve the highest efficiency MOE reaction possible. The tabulated data were then plotted using Microsoft Excel, producing the graphs below.

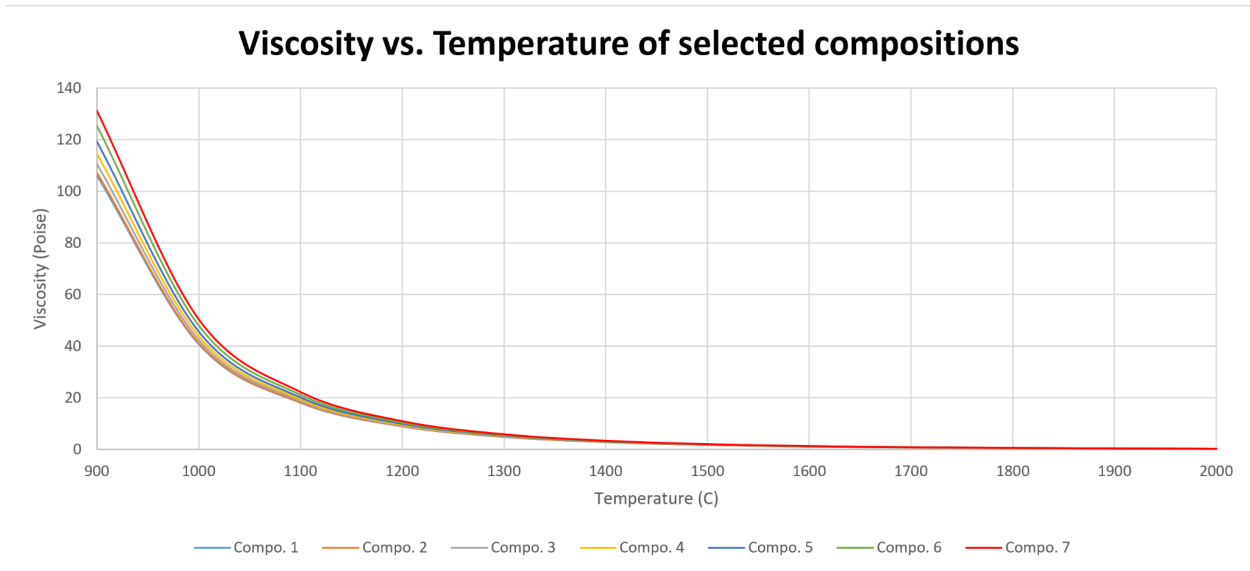


Figure 23: Graph of viscosity vs. temperature of selected compositions from 900 to 2000 °C

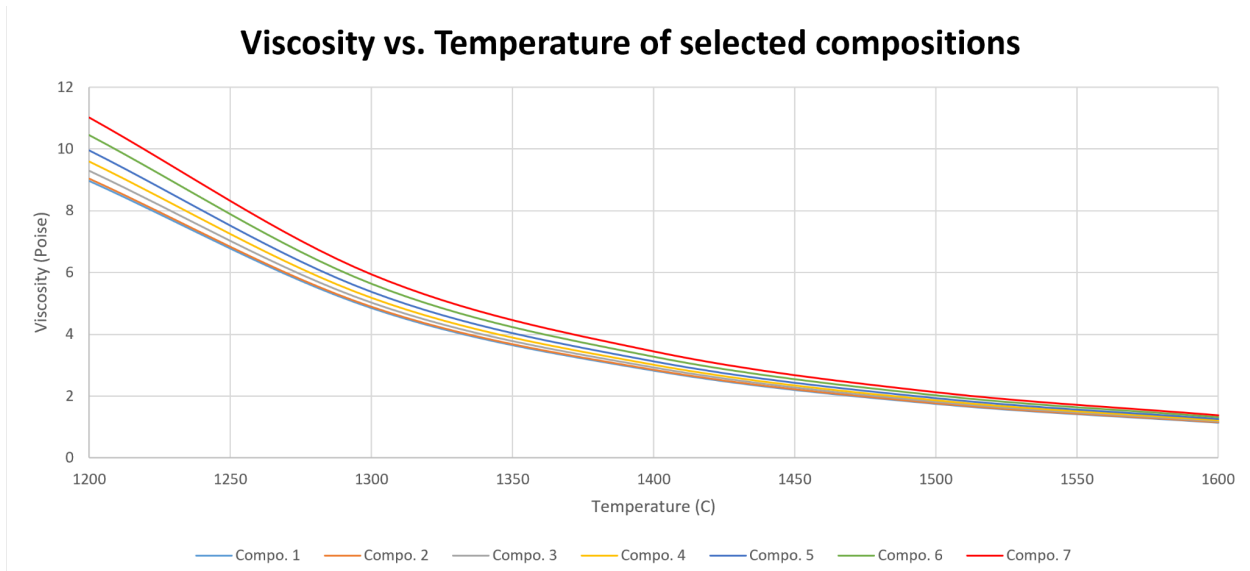


Figure 24: Graph of viscosity vs. temperature of selected compositions from 1200 to 1600 °C

The graphs above clearly show the relationship between viscosity and temperature. As the temperature increases, the viscosity of the compositions decreases exponentially. The exponential curve is most visible in *Figure 23*. This is because higher temperatures increase the speed and energy of the fluid molecules, causing them to move more freely and overcome intermolecular forces that may impede flow. The viscosities of all seven compositions change concerning temperature identically. This similarity can be seen in *Figure 24*, which shows how the shape of the viscosity vs. temperature curves shape the same between all compositions.

5.1.4 Deciding The Desired Composition & Operating Temperature

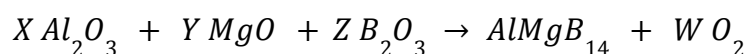
From the Results and Analysis *Subsections 5.2.0 to 5.2.3*, we concluded that our composition of focus was Composition 4, where the electrolyte was: **0.61547** B₂O₃ – **0.221198** MgO – **0.163332** Al₂O₃.

We also concluded that we would operate our reaction at a temperature of **1600 °C** rather than 1440 °C. The compositions created as a result of the reaction at 1600 °C, seen in *Figure 18*, show all liquid phases present; on the other hand, for the temperature of 1440 °C, we saw solids present, which is not ideal for the solution we are searching for. We then observed the fugacity at these temperatures. The fugacity of B₂O₃ at 1440 °C was $4.54 \cdot 10^{-4}$ atm, whereas this same fugacity at 1600 °C was between $2.49 \cdot 10^{-3}$ and $5.37 \cdot 10^{-3}$ atm. However, the fugacity at 1600 °C was more significant than the criterium fugacity, so we must consider the mass balance discussed in the *6.0 Conclusion* section of the paper.

Now that we found our composition and operating temperature, we moved on to our following calculation, calculating the overall reaction potential and energy.

5.1.5 Overall Reaction Energy & Potential

As stated in the *4.0 Methodology* section, to calculate the Overall Reaction Energy and Potential, we needed to do so via FactSage. This was done by inserting the overall reaction into the *Reaction* database of FactSage. But first, we needed to determine what our overall reaction was. This was done through logical and decisive thinking. We knew that our desired product was $AlMgB_{14}$ and that our reactants were the compounds of the electrolyte: Al_2O_3 , B_2O_3 , and MgO . Our product of Aluminum Magnesium Boride must only pertain to one mole to get the reaction down to its simplest form. Thus we have one mole of Al, one mole of Mg, and fourteen moles of B in our product. From our reactants, however, at the base of one mole per compound, we have two moles of Aluminum, one mole of Magnesium, and two moles of Boron. We first sorted out the products and reactants of the overall reaction:



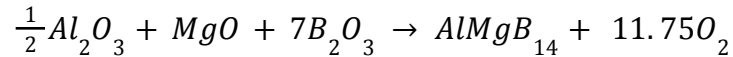
From writing out this formula, we determined that another end product, aside from our desired boride, would be Oxygen gas. But, like the moles of our reactants, we were unaware of how many moles of oxygen gas would be produced. By simple logic, we determined that we would have one mole of MgO ($Y = 1$), as there is only one mole of Mg in the boride. We also chose seven moles of B_2O_3 , as there are fourteen moles of boron in the boride product and only two moles of boron in the boron-based oxide ($Z = 14 / 2 = 7$). Finally, we determined the moles of Al_2O_3 to be 0.5, as we knew that our boride product only consisted of one mole of aluminum, whereas we had two moles of aluminum in our reactant ($X = \frac{1}{2}$). Now that our reactants were sorted out, we needed to determine the total moles of Oxygen gas (O_2) to balance the reaction. This was done by simple algebra, summing the total oxygen moles in the reaction. This calculation is shown below:

$$(n_O)_{prod} = (n_O)_{Al_2O_3} + (n_O)_{B_2O_3} + (n_O)_{MgO} = 3X + 3Z + Y$$

$$(n_O)_{prod} = 3 * \frac{1}{2} + 3 * 7 + 1 * 1 = 1.5 + 21 + 1 = 23.5$$

$$W = 0.5 * (n_O)_{prod} = 0.5 * 23.5 = 11.75$$

After all of the calculations, we determined our overall reaction to be:



Once we found this reaction, we could move onto calculating our overall reaction energy and potential. As mentioned above, this can be done through the *Reactants* module of FactSage. Inputting the reactants, products, and their respective moles, we initiated a simulation of the reaction at the temperature range that nested the operation temperature of 1600 °C. This simulation gave us thermodynamic properties, including the change in Gibbs Energy. This change in Gibbs energy is what we need to determine the overall reaction energy. Using the plotting function of this module, we extrapolated the following graph:

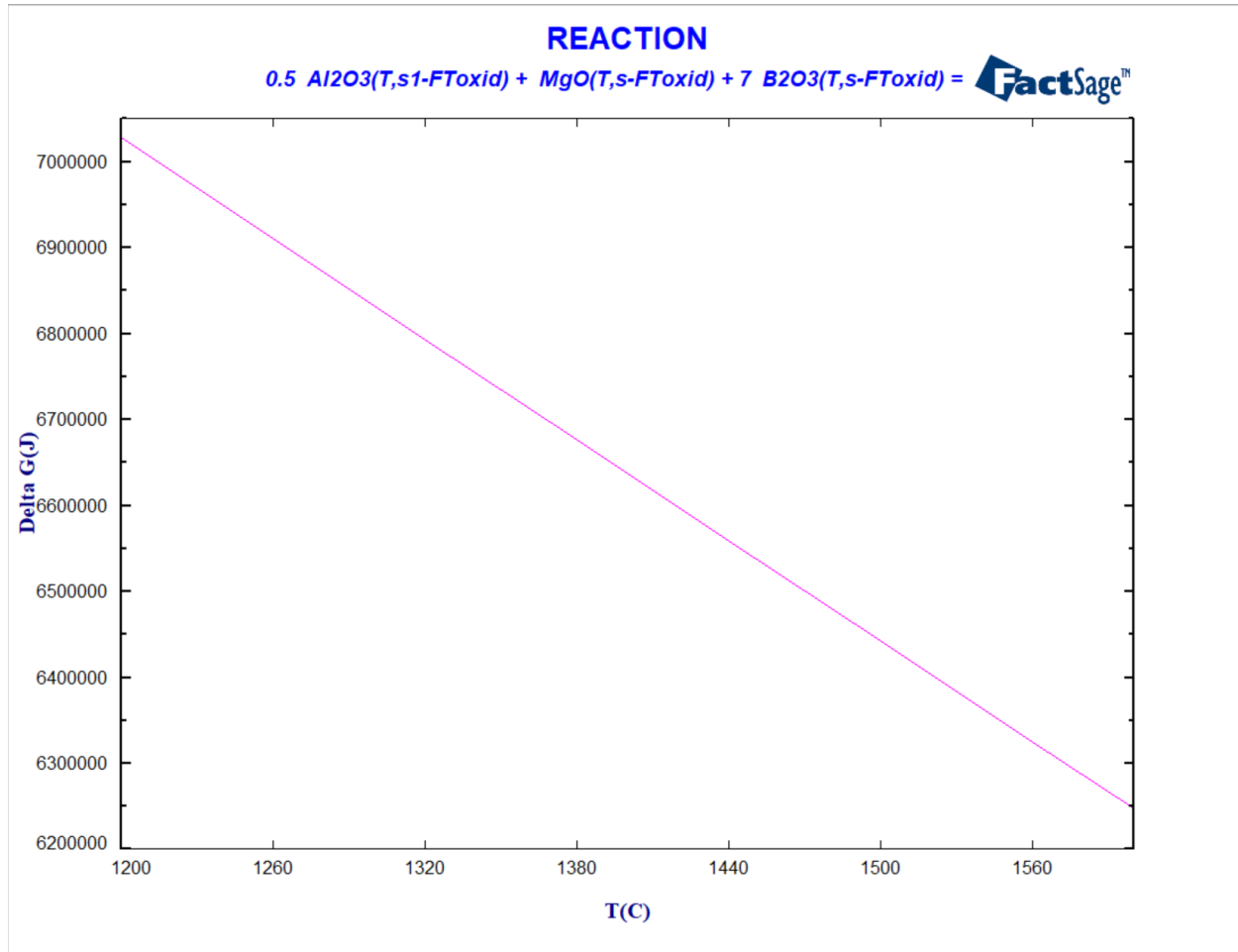


Figure 25: The Overall Reaction Energy Trend Graph from 1200 to 1600 °C. This graph is displayed as Temperature (in degrees Celsius) versus the change in Gibbs Energy (J).

From this graph data, we also extrapolated the change in Gibbs energy with the corresponding temperatures from the range presented in *Figure 24*. We focused our tabulation on highlighting the change in Gibbs Energy at our operating temperature of 1600 °C. *Table 17*, below, shows this tabulation and concentration at the desired operating temperature.

<u>OVERALL REACTION ENERGY</u>	
<u>Temperature (oC)</u>	<u>Gibbs Energy (J)</u>
1200	7028306.1
1260	6910353.1
1320	6792711.3
1380	6675356.3
1440	6558266
1500	6441420.2
1560	6324800.1
1600	6247170.2

Table 17: The Overall Reaction Energy, with a temperature range from 1200°C To 1600°C and the corresponding change in Gibbs Energy for each temperature. The difference in Gibbs Energy of the desired Operating Temperature is highlighted at the bottom of the table.

As clearly stated in the above table, we recorded our change in Gibbs Energy at our desired operating temperature. The energy value is **6247170.2 Joules** or **6247.1702 kJ**. Using this energy value, we can proceed with overall reaction potential calculations using this energy value through FactSage and Google Spreadsheets.

Now that we have this change in Gibbs free energy, we can calculate this potential, or voltage of this reaction, through the Nernst Equation, described previously in the *4.0 Methodology* section. Google Spreadsheets allowed for this calculation to run more smoothly and efficiently. Using this software, we created a table for calculating the potential at 1600 °C. Below is this table, denoted as *Table 18*.

<u>NERNST EQUATION</u>		<u>VOLTAGE REQUIREMENT</u>				
$\Delta G_o = (n * F)^{-1} * E_{cell}$		<u>Temperature</u> (oC)	<u>Gibbs Energy</u> [ΔG_o] (J)	<u>Number Of</u> <u>Moles [n]</u> (mol)	<u>Farady's</u> <u>Constant [F]</u> (C*mol ⁻¹)	<u>Voltage</u> <u>Requirement</u> [E _{cell}] (V)
$\Delta G_o * (n * F) = E_{cell}$		1600	6247170.2	47	96485.3321	1.377603331

Table 18: The Voltage Requirement is split into two tables. The first table shows the Nernst Equation and its rearranged form to calculate the voltage requirement of the electrolytic cell at the operating temperature. The second table shows the change in Gibbs Energy at 1600 °C, the number of moles or electrons transferred as 47, and the Faraday's constant, all used to calculate the voltage requirement.

The number of transferred electrons (a.k.a number of moles), denoted in the Nernst Equation as “n,” was calculated based on the oxygen gas product of the overall reaction. We knew there were 11.75 moles of O₂. This meant that there were 23.5 moles of the element O. As discovered in our Manganese Oxide trial calculation, we found that per every oxygen atom, we would have two total electrons transferred in these reactions. So for this boride reaction, the total number of transferred electrons was 47 moles (=23.5*2). Knowing that inserting into our table, we calculated that our required potential to operate this reaction at 1600 °C was approximately **1.378 Volts**. This could be double-checked and proven correct through FactSage’s *Reaction* module in the same process of calculating the change in Gibbs energy. However, in the Results drop-down menu, we can alter the results to show this potential by inserting our “n”-value and calculating. Once doing this, we recalculated our potentials from the same range as when we graphed our Overall Reaction Energy. *Figure 26* shows the result of this action, which is shown below.

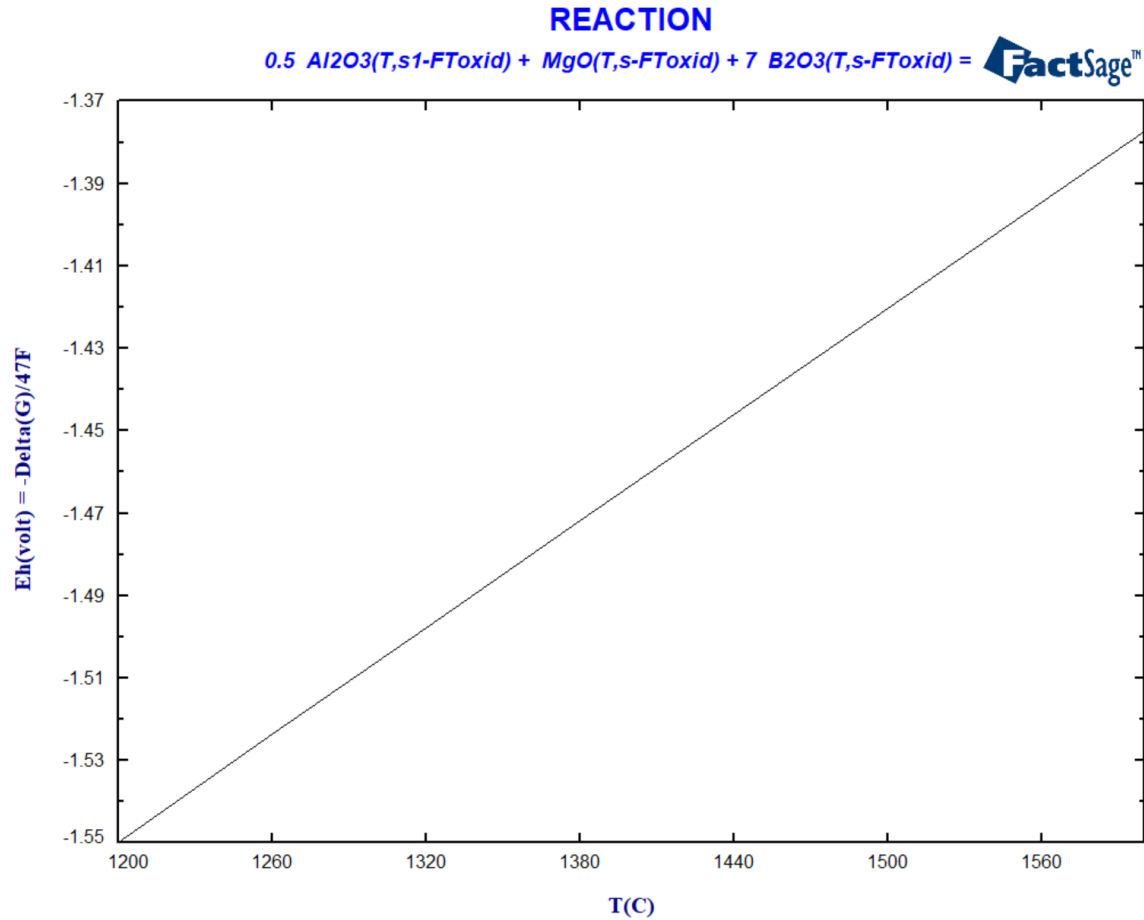


Figure 26: The Overall Reaction Potential Trend Graph from 1200 to 1600 °C. This graph is displayed as Temperature (in degrees Celsius) versus the Voltage Requirement (V).

Once all the overall reaction calculations about energy and potential were calculated, we determined our subsequent finding regarding the half-cell components of energy and potential.

5.1.6 Half-Cell Reaction Energy & Potential

Using the similar tabulated data to *Table 3* above, our first step was constructing a formula based on the tabulation for the overall reaction energy and potential. That is how we obtained the half-cell reaction energy and potential. These half-cell characteristics were not to be calculated as a singular value; instead, they were to be calculated as a function of Temperature.

In our first step, we conducted our calculations of overall reaction energy and potential formulas, as shown in the following table:

OVERALL REACTION ENERGY					
Temperature (oC)	Gibbs Energy (J)				
900	7623782.1				
960	7503808.8				
1020	7384313.4				
1080	7265255				
1140	7146596.8				
1200	7028306.1				
1260	6910353.1				
1320	6792711.3				
1380	6675356.3				
1440	6558266				
1500	6441420.2				
1560	6324800.1				
1620	6208388.5				
1680	6092169.6				
1740	5976128.6				
1800	5860252.2				
1860	5744529.4				
1920	5628949.8				
1980	5513503.9				
2000	5475050				

GIBBS ENERGY FORMULA			
$\Delta G = \Delta H - (T * \Delta s)$			
$y = b + (m * x)$			
$\Delta G = y$	$\Delta H = b$	$T = x$	$\Delta s = m$

OVERALL REACTION ENERGY FORMULA			
Change In Entropy[Δs] (J/(mol*K))		Change In Enthalpy [ΔH] (J/mol)	
Formula	Value	Formula	Value
$\Delta s =$ SLOPE(C4:C16,B4:B16)	-1950.971755	$\Delta H =$ INTERCEPT(C4:C16,B4:B16)	9371723.597
OVERALL REACTION ENERGY FORMULA			
$y = 9371723.597 - 1950.971755 * x$			
$\Delta G_0 = 9371723.597 - (1950.971755 * T)$			

OVERALL REACTION POTENTIAL FORMULA		
Nernst Equation	Number Of Moles [n] (mol)	Faraday's Constant [F] (C*mol ⁻¹)
$\Delta G / (n * F) = E$	47	96485.3321
OVERALL REACTION POTENTIAL FORMULA		
$E_0 = -2.066618522 + (4.302212204 * 10^{-4} * T)$		

Table 19: The calculations made to obtain the Overall Reaction Energy and Potential formulas for the $AlMgB_{14}$ reaction.

We could construct the overall reaction energy function using the Gibbs Energy formula in Table 19. We could emulate that formula to that of a linear formula, where each linear component is shown. Using the function capabilities of Google Spreadsheets, we found the Enthalpy and Entropy changes, which would be plugged in, and the overall reaction energy equation would be calculated. This equation is $\Delta G_0 = 9371723.597 - (1950.971755 * T)$. We could calculate the Overall Reaction Potential function. This function came to be $E_0 = -2.066618522 + (4.302212204 * 10^{-4} * T)$.

Once the overall reaction functions were found, we could move on to our half-cell reactions. However, we first needed to define the half-cell reactions. Half-cell reactions are the portions of the overall cell reaction that occur at the cathode and anode of an electrolytic cell. We denoted these “portions” as the cathodic and anodic reactions to help distinguish between them.

After consulting Mr. Rui Wang, Mr. Jize Zhang, Professor Yu Zhong, and some sources, we concluded that our cathodic reaction revolved around the oxygen generated from the overall reaction. Thus, we also concluded that the anodic reaction revolved around the aluminum magnesium boride. In more technical terms, we established the cathodic and anodic reactions to $23.5\text{O}^{2-} \rightarrow 11.75\text{O}_2 + 47\text{e}^-$ and $\text{AlMgB}_{14} + 47\text{e}^- \rightarrow \text{Al} + \text{Mg} + 7\text{B}_2$, respectively. This is true as adding the two reactions together constructs the overall reaction.

Upon defining the cathodic and anodic reactions, we continued to find the energy and potential functions of the cathodic and anodic reactions. We consulted the resources mentioned in the previous paragraph once again and decided to start with the cathodic side of the calculations. In this exact consultation, we derived our Entropy Change and Enthalpy Change. Our cathodic reaction energy formula was found using the same Gibbs Energy formula. We then proceeded similarly to that of the overall reaction potential function and found our cathodic reaction potential function.

CATHODIC REACTION ENERGY FORMULA		CATHODIC REACTION POTENTIAL FORMULA		
Change In Entropy [ΔS_1] (J/K)	Change In Enthalpy [ΔH_1] (J/mol)	Nernst Equation	Number Of Moles [n] (mol)	Faraday's Constant [F] ($\text{C}^*\text{mol}^{-1}$)
980.9	1.57E+07	$\Delta G / (-n * F) = E$	47	96485.3321
CATHODIC REACTION ENERGY FORMULA		CATHODIC REACTION POTENTIAL FORMULA		
$\Delta G_1 = 15676000 + (980.9 * T)$		$E_1 = -3.4568147 - (0.0002163 * T)$		

Table 20: The calculations made to obtain the Cathodic Reaction Energy and Potential formulas for the AlMgB_{14} reaction.

The Cathodic Reaction energy formula was found to be $\Delta G_1 = 1.5676 * 10^7 + (980.9 * T)$.

The Cathodic Reaction potential formula was found to be $\Delta E = -3.4568147 - (0.000213 * T)$.

The final step was to determine the anodic reaction functions for energy and potential. This was a simple step. As previously stated, the overall reaction is just the sum of the cathodic

and anodic reactions. This same relation translates to the reaction energy functions. The overall reaction energy formula was just the sum of the cathodic reaction energy formula and anodic reaction energy formula. At this stage, the anodic reaction energy formula was unknown but easily calculated by getting the difference between the overall and cathodic reaction energy formulas. We then calculated the anodic reaction potential formula through the Nernst equation, as seen in *Table 21* below.

ANODIC REACTION ENERGY FORMULA		
Formula		
$\Delta G_2 = \Delta G_0 - \Delta G_1$		
ANODIC REACTION ENERGY FORMULA		
$\Delta G_2 = -6304276.402 - (2931.871755 * T)$		
ANODIC REACTION POTENTIAL FORMULA		
Nernst Equation	Number Of Moles [n] (mol)	Faraday's Constant [F] ($C * mol^{-1} * s^{-1}$)
$\Delta G / (-n * F) = E$	47	96485.3321
ANODIC REACTION POTENTIAL FORMULA		
$E_2 = 1.390196184 + (6.465257334E-4 * T)$		

Table 21: The calculations made to obtain the Anodic Reaction Energy and Potential formulas for the $AlMgB_{14}$ reaction.

We then postulated that it would be best to illustrate these energies and voltages through graphing. This would best show the trends through the temperature range and compare the overall, cathodic, and anodic reactions.

Energies Of Overall Reaction, Cathodic Reaction, and Anodic Reaction

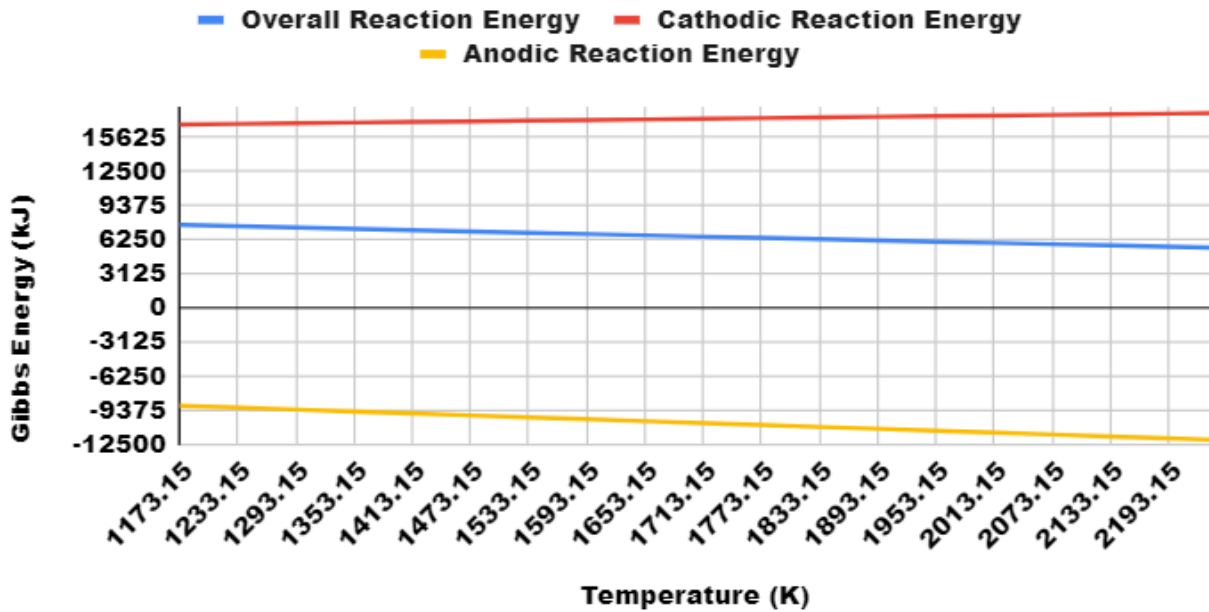


Figure 27: The Graph of the Overall Reaction, Cathodic Reaction, and Anodic Reaction Energy Functions for the $AlMgB_{14}$ reaction.

Potentials Of Overall Reaction, Cathodic Reaction, & Anodic Reaction

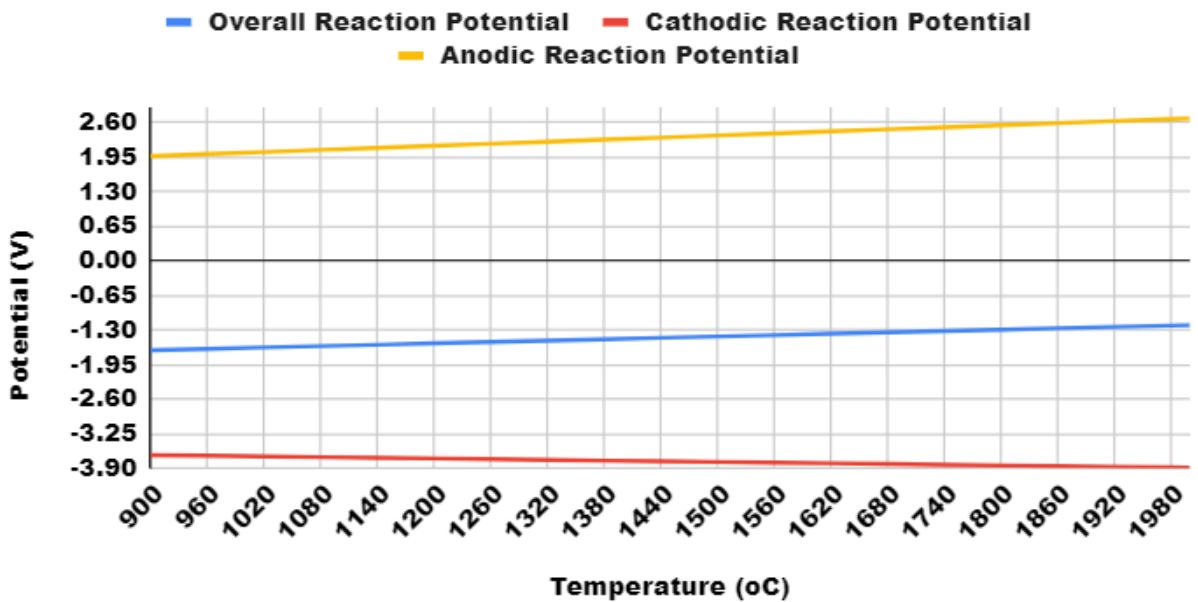


Figure 28: The Graph of the Overall Reaction, Cathodic Reaction, and Anodic Reaction Potential Functions for the $AlMgB_{14}$ reaction.

5.1.7 Mass Balance

The following calculation that was conducted was Mass Balance. This calculation would help us evaluate the reaction in terms of the compound that experiences some evaporation at the operating temperature of 1600 °C. Our focus on the compounds would pertain to those containing the elements of Boron, Magnesium, and Aluminum. These three elements are essential as they are the elemental makeup of our desired product, AlMgB₁₄. We examined the trend of this evaporation over time, as we mean for the reaction to occur for an expanded amount of time. To do this, we emulate the same process shown for the MnO MOE process in the 4.0 Methodology section. However, for Aluminum Magnesium Boride MOE, we have to consider more than one element, so three graphs must be made for the fugacity trend over time of Aluminum, Magnesium, and Boron over time.

MASS BALANCE OF ALL COMPOUNDS											
Composition 4											
0.61547B2O3 - 0.221198MgO - 0.163332Al2O3											
BORON COMPOUNDS				MAGNESIUM COMPOUNDS				ALUMINUM COMPOUNDS			
Compound	Fugacity Rate Of Compound	# Of Moles Of Boron	Fugacity Rate Of Boron	Compound	Fugacity Rate Of Compound	# Of Moles Of Boron	Fugacity Rate Of Boron	Compound	Fugacity Rate Of Compound	# Of Moles Of Boron	Fugacity Rate Of Boron
B2O3	4.18E-03	2	8.36E-03	Mg	2.11E-08	1	2.11E-08	AlBO2	2.26E-08	1	2.26E-08
BO2	1.23E-05	1	1.23E-05	MgO	1.28E-11	1	1.28E-11	AlO	2.43E-12	1	2.43E-12
BO	8.24E-06	1	8.24E-06	Mg2	7.93E-20	2	1.59E-19	Al	5.71E-13	1	5.71E-13
(BO)2	2.03E-06	2	4.06E-06					Al2O	8.96E-16	2	1.79E-15
AlBO2	2.26E-08	1	2.26E-08					Al2O2	2.65E-16	2	5.31E-16
B2O	1.41E-13	2	2.82E-13					Al2O3	7.35E-20	2	1.47E-19
B	2.26E-14	1	2.26E-14					Al2	1.89E-25	2	3.79E-25
B2	1.32E-25	2	2.64E-25					AlO2	8.96E-16	1	8.96E-16
NET BORON FUGACITY RATE (per minute)				NET MAGNESIUM FUGACITY RATE (per minute)				NET ALUMINUM FUGACITY RATE (per minute)			
5.97E-05				1.50E-10				1.61E-10			
Total Boron Lost Over A Day= 5.97E-05 * t				Total Magnesium Lost Over A Day= 1.50E-10 * t				Total Aluminum Lost Over A Day= 1.61E-10 * t			

Table 22: The calculations made to obtain the Fugacity rate of Boron, Magnesium, and Aluminum over time for the Mass Balance calculation of AlMgB₁₄.

We used Composition Four to conduct the calculation seen in Table 22 and examined all of the fugacities of each compound with a Boron atom, Magnesium atom, or Aluminum atom involved. Then, after tabulating this, we constructed our equations for the net fugacity of each element over time and constructed the following graphs:

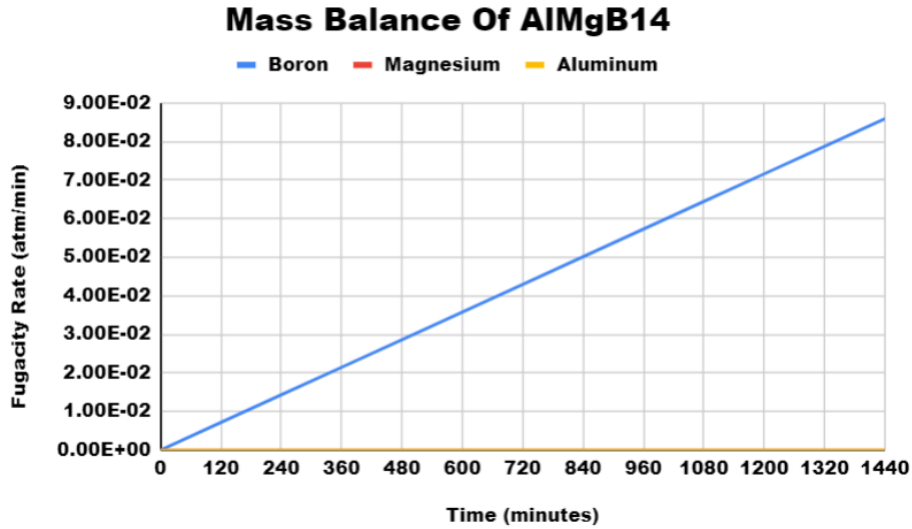


Figure 29: The total Mass Balance of AlMgB₁₄, graphed in terms of Fugacity rate (atm/min) vs. time (min). The graph is mapped out over a full day in terms of minutes.

As seen in *Figure 29*, the element with the highest fugacity rate is Boron, as evidenced by the B₂O₃ observation in the Vapor Pressure Trend calculations. This graph shows exactly how much boron, magnesium, and aluminum are vaporized over a day when operating at 1600 °C. However, it was difficult to see the trend of magnesium and aluminum, so we constructed a separate graph, below, to better see the mass balance in regards to those two elements.

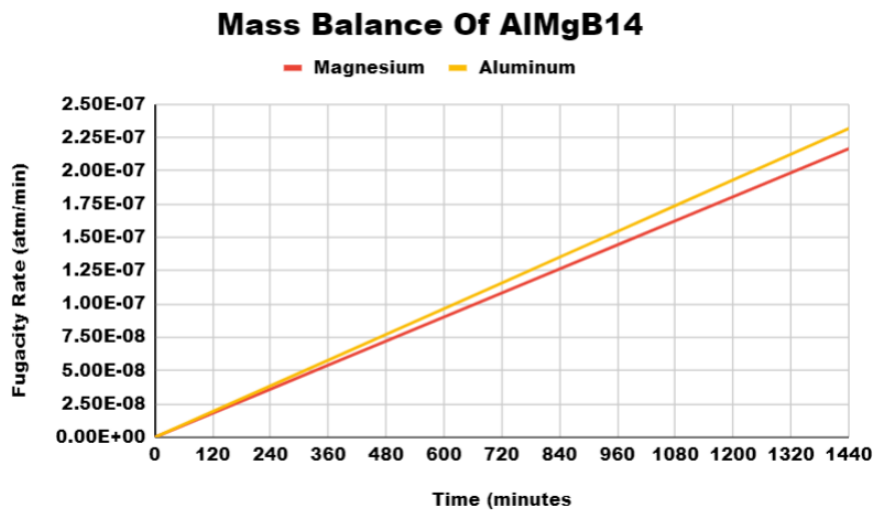


Figure 30: *The partial Mass Balance of $AlMgB_{14}$, graphed in terms of Fugacity rate (atm/min) vs. time (min). The graph is mapped out over a full day in terms of minutes. This graph only contains the trend of magnesium and aluminum.*

As seen through the fugacity rate range, or range of the y-axis, of *Figure 30*, the rate is extremely small with a range from 10^{-8} to 10^{-7} . Whereas this range, from *Figure 29*, is between values of the 10^{-2} range. This confirms that the mass lost from the reaction of aluminum- and magnesium-based products were almost negligible in comparison to the boron counterparts. This mapping of the mass balance allowed us to examine the trend and see exactly the parameters in which we would lose amounts of our desired product over a day of time.

5.1.8 Energy Balance

We, then, wanted to examine the trend of the energy balance that would occur over a range of temperatures. The energy balance of a process can also tell us about the amount of energy required to start the reaction as well as the quantity of energy that can be extracted from the reaction for useful uses. Understanding a reaction's energy balance is critical for forecasting and controlling chemical reactions in a wide range of industrial, environmental, and biological applications.

As mentioned in the *4.0 Methodology* section, there were two methods of calculating the energy balance of our overall reaction. The first method involved examining the reaction as a whole. The *4.0 Methodology* section shows the example test calculation process for Manganese Molten Oxide Electrolysis. We mimicked the procedure for this method with some alterations. Like our test calculations, we set the original temperatures of our reactants to 25 °C, the room temperature. However this time, our products have an operating temperature of 1600 °C. All of the inputs for this calculation can be seen below, as well as the results from these inputs:

Non-Isothermal Non-Standard State Reaction:						
$0.5 \text{ Al}_2\text{O}_3 + \text{MgO} + 7 \text{ B}_2\text{O}_3 = \text{AlMgB}_{14} + 11.75 \text{ O}_2$ <p style="text-align: center;"> <small>(25C,s4-FToxid) (25C,s-FToxid) (25C,s-FToxid) (1600C,s-FTlite) (1600C,g-FactPS)</small> </p>						
Delta H(J)	Delta G(J)	Delta Vol(litre)	Delta S(J/K)	Delta Cp(J/K)	Delta A(J)	Delta A (J)
11331724.8	4128593.6	1.8061E+03	3483.898	398.319	3945595.3	

Table 23: The Results Window from FactSage's Reaction Module for the Total Reaction.

As seen in the above table, at room temperature, these reactants are in the solid phase. This is the standard norm that the reaction was to be initiated. At 1600 °C, our boride product would still be solid. We were given the Entropy and Gibbs energy changes in this total reaction. These thermodynamic properties were necessary to conduct our next step in the calculation, as mentioned in the *4.0 Methodology* section. The third step was to derive the formula for enthalpy change, which was done using the thermodynamic calculations gathered in *Table 24*.

ENERGY BALANCE @ 1600 oC		
Formula	Gibbs Energy [ΔG] (J)	Entropy [Δs] (J/K)
$\Delta H = \Delta G + (T * \Delta s)$	4128593.6	3483.898
ENERGY BALANCE FORMULA		
$\Delta H = 4128593.6 + (3483.898 * T)$		

Table 24: The calculations made to obtain the Energy Balance formula through the Gibbs Energy calculation in calculating the formula of Entropy Change for AlMgB_{14} MOE.

As seen in the above table, we extrapolated the FactSage data, and through Google Spreadsheets, we tabulated and calculated the formula for our Energy Balance of the entire reaction. This formula is $\Delta H = 4128593.6 + (3483.898 * T)$. From this formula, we moved onto our final step and graphed the linear formula to map out our energy balance from a temperature range of 900 to 2000 °C.

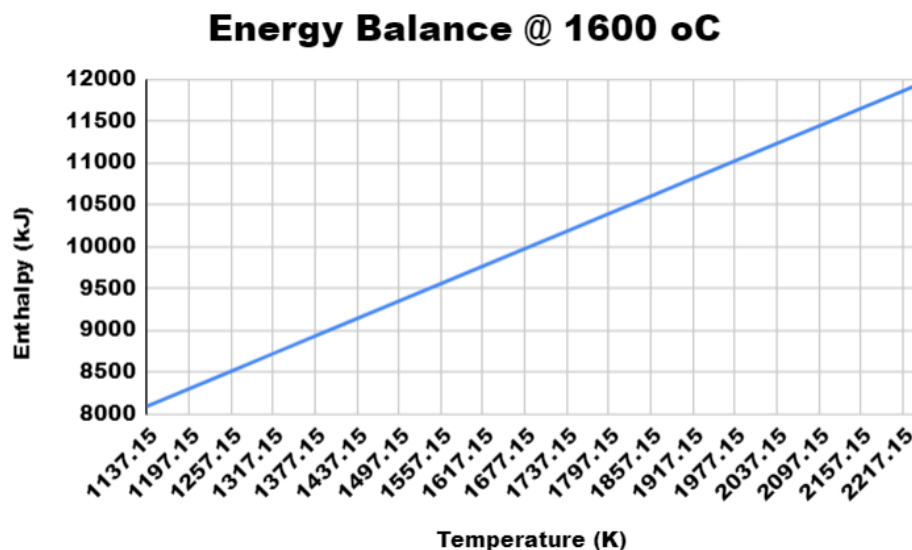


Figure 31: The total Energy Balance of $AlMgB_{14}$, graphed in terms of enthalpy (kJ) vs. temperature (K).

The second method for our reaction was a bit more lengthy. To begin we set our conditions and reaction through the *Reaction* module, however unlike the first way, we had it in such a way that the total reaction was analyzed in parts. The first part of the reaction analyzed was for when the reactants changed from room temperature to our operating temperature.

Non-Isothermal Non-Standard State Reaction:										
0.5 Al ₂ O ₃ (25C,s-FToxid)	+	MgO (25C,s-FToxid)	+	7 B ₂ O ₃ (25C,s-FToxid)	=	0.5 Al ₂ O ₃ (1600C,liq-FToxid)	+	MgO (1600C,liq-FToxid)	+	7 B ₂ O ₃ (1600C,liq-FToxid)
Delta H(J)	Delta G(J)	Delta Vol(litre)	Delta S(J/K)	Delta Cp(J/K)	Delta A(J)	Delta A (J)				
1769632.6	-2391552.6	0.0000E+00	1859.924	511.576	-2391552.6					

Table 25: The Results Window from FactSage's Reaction Module for the Reactants heating up.

As seen in the above table, the reactants in both methods were operating at the same initial conditions. In this stage, we calculate the thermodynamic properties of our reactants changing from room temperature to our operating temperature. In this temperature change of the reactants, we were given the Entropy change and Gibbs energy change, just like in the first method. The third step was to derive the formula for enthalpy change for the instance when the reactants are heated up. Web extrapolated the FactSage data, tabulated the results, and derived the formula for

our overall reaction's energy balance using Google Spreadsheets. This formula is $\Delta H = -2391552.6 + (1859.924 * T)$. We then repeated the same calculations similar to that of the total reaction of Method One, however, this time our reactants were placed at 1600 °C instead of room temperature.

Isothermal Non-Standard State Reaction:						
$0.5 \text{ Al}_2\text{O}_3 + \text{MgO} + 7 \text{ B}_2\text{O}_3 = \text{AlMgB}_4 + 11.75 \text{ O}_2$ <p style="text-align: center;"> <small>(1600C,liq-FToxid) (1600C,liq-FToxid) (1600C,liq-FToxid) (1600C,s-FTlite) (1600C,g-FactPS)</small> </p>						
Delta H(J)	Delta G(J)	Delta Vol(litre)	Delta S(J/K)	Delta Cp(J/K)	Delta A(J)	Delta A (J)
9562092.2	6520146.2	1.8061E+03	1623.974	-113.257	6337147.9	

Table 26: The Results Window from FactSage's Reaction Module for the Reaction after the reactants were heated up.

As seen in *Table 26*, the reactants and products are placed in the same temperature condition. In this stage, we calculated the thermodynamic properties of our reaction from the heated temperature to the products being formed. The next step was to derive the formula for enthalpy change for the instance when the reactants are heated up. We extrapolated the FactSage data, tabulated the results, and derived the formula for our overall reaction's energy balance using Google Spreadsheets. This formula is $\Delta H = 6520146.2 + (1623.974 * T)$. When simulating both instances of the total reaction all required thermodynamic calculations were tabulated in Google Spreadsheets, as seen below in *Table 27*.

ENERGY BALANCE @ 1600 oC		
Enthalpy Change @ Room Temperature		
<u>Formula</u>	<u>Gibbs Energy</u> [ΔG1] (J)	<u>Entropy</u> [Δs1] (J/K)
$\Delta H1 = \Delta G1 + (T * \Delta s1)$	-2032386.4	1768.259
$\Delta H1 = -2032386.4 + (1768.259 * T)$		
Enthalpy Change @ Reaction		
<u>Formula</u>	<u>Gibbs Energy</u> [ΔG2] (J)	<u>Entropy</u> [Δs2] (J/K)
$\Delta H2 = \Delta G2 + (T * \Delta s2)$	6780813.7	1634.751
$\Delta H2 = 6780813.7 + (1634.751 * T)$		
Total Enthalpy Change		
<u>Formula</u>	<u>Gibbs Energy</u> [ΔG] (J)	<u>Entropy [Δs]</u> (J/K)
$\Delta H0 = \Delta H1 + \Delta H1$	4748427.3	3403.01
ENERGY BALANCE FORMULA		
$\Delta H = 474827.3 + (3403.01 * T)$		

Table 27: The calculations made to obtain the Energy Balance formulas through the Gibbs Energy calculation in calculating the formula of Entropy Change. These formulas are the formulas generated of the measured energy balance at each stage of the total reaction. This is for the AlMgB₁₄ MOE reaction.

After conducting the above calculations, we, then, proceeded to our final step and graphed the linear formula to map out our energy balance from a temperature range of 900 to 2000 °C.

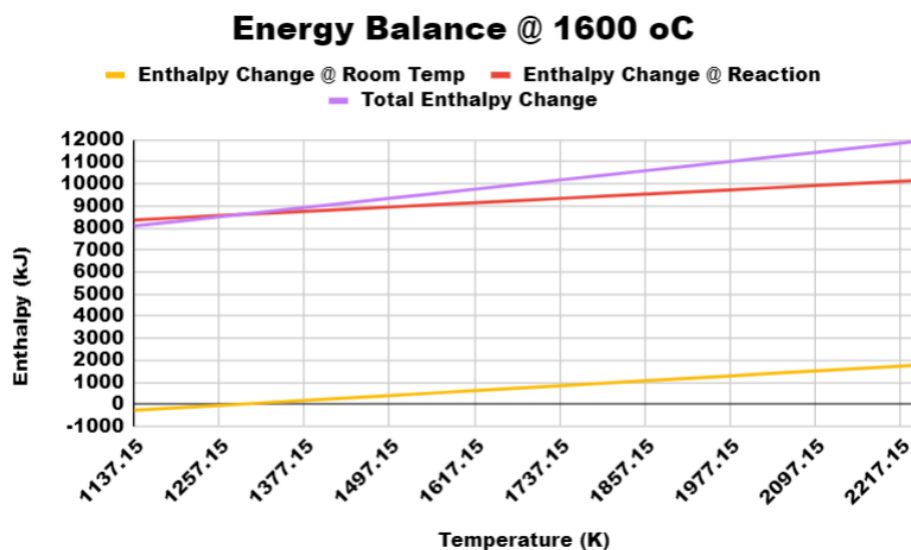


Figure 32: *The Energy Balances of $AlMgB_{14}$, graphed in terms of enthalpy (kJ) vs. temperature (K). This shows the enthalpy changes at each stage of the reaction, as well as that for the total reaction.*

After conducting our analysis of both methods, we saw that both methods yield the same overall reaction energy balance. Our thorough examination of these energy balance methods revealed that the energy balance formula indicated that a large amount of energy is needed for the reaction to proceed, consistent with the reaction occurring at a high temperature of 1600 oC. This knowledge can help with response conditions design and optimization and system behavior prediction under various temperature and energy input situations.

5.1.9 Nominal Cathode-To-Anode Distance

Our following results regarded the nominal cathode-to-anode distance for this particular reaction and electrolytic cell. To begin our pursuit of this distance value.

We first needed to determine the material for both the cathode and the anode for our electrolytic cell. By melting the oxide and running an electric current through it, a technique known as molten oxide electrolysis can separate metals from their oxides. This process causes the metal ions to be reduced to their elemental form at the cathode. The anode and cathode materials must be chosen carefully for the process to be effective and efficient. Graphite is the ideal material to use in molten oxide electrolysis for both the anode and cathode in this regard. Graphite's superior electrical conductivity enables effective electron transmission between the electrodes and the electrolyte, making it one of the best materials for the anode and cathode in molten oxide electrolysis. Graphite is an excellent material for molten oxide electrolysis because it has good resistance to corrosion and erosion in high-temperature conditions. Graphite can effectively transfer heat and tolerate high temperatures without degrading because of its low

melting point and excellent thermal conductivity. According to numerous investigations, graphite is a suitable material for use in molten oxide electrolysis. For instance, a study used graphite as both the anode and the cathode to electrolyze molten $\text{Li}_2\text{O-LiCl}$. The findings revealed that graphite had excellent electrochemical performance and stability with slight oxidation or degradation over an extended period of operation (Ahn et al., 2019). Similar to the previous work, graphite was employed as the anode in an additional investigation to electrolyze molten MgCl_2 . The findings revealed that graphite had high current efficiency and maintained performance throughout the experiment (Kuramoto et al., 2018).

Once we designated graphite as our electrode material, we calculated the nominal distance between our cathode and electrode. As explained in Sections 3.0 *Background* and 4.0 *Methodology*, many parameters must be found before calculating this distance. We completed this calculation in a seven-step calculation process.

NOMINAL CATHODE TO ANODE DISTANCE						Step Five: Calculating Voltage For Losses					
Formula						Assumption:					
$R = (\rho * D_{ac}) / (\text{Area})$						0					
ρ	Resistivity (ohm * cm)	R	Electrolyte (Ohm)	D_{ac}	Nominal Anode-To-Cathode Distance	Area	Area Between Anode & Cathode	Step Six: Calculating Ohmic Drop			
Step One: Mapping Out Energies Of Overall Reaction						$V_{IR} = V_{feed} + V_r + V_{loss}$					
Operation Temperature [T] (K)	Gibbs Energy [ΔG] (kJ/mol-Mn)	Enthalpy Change [ΔH] (kJ/mol-Mn)	Entropy Change Formula			Entropy Change [ΔS] (kJ/mol-Mn*K)		1.294363537			
1873.15	4115272.1	11316513.6	$\Delta S = -(\Delta G - \Delta H) / T$			3477.56		Step Seven: Calculating The Anode-To-Cathode Distance			
Step Two: Calculating Minimum Operation Voltage						$V_{IR} = I * R$					
Heat Loss During Electrolysis						$R = (\rho * D_{ac}) / (\text{Area})$					
$\Delta Q = \Delta S * T$						$V_{IR} = I * (\rho * D_{ac}) / (\text{Area})$					
6513991.514						$I = j * \text{Area}$					
Minimum Voltage						$V_{IR} = (j * \text{Area}) * ((\rho * D_{ac}) / (\text{Area}))$					
$V_{min} = \Delta G / (n * F)$						$V_{IR} = j * (\rho * D_{ac})$					
Number Of Transferred Electrons [n] (mol)	47	Faraday's Constant [F] (C/mol)	96485.3321	0.9074848886							
Step Three: Calculating Electrolysis Reaction Voltage						Assumptions					
$V_r = \Delta Q / (n * F)$						Current Density can be assumed to be 2 A/cm ² , which is the same for Aluminum Smelting: $\text{Al}^{3+} + 3e^- \rightarrow \text{Al}(l)$			Resistivity can be assumed to be 1 ohm*cm which is typical for Molten Salts		
1.4364418						Voltage Drop From Reaction Ohmic Drop [V_IR] (V)	1.294363537	Current Density [j] (A / cm ²)	2	Resistivity [ρ] (ohm * cm)	1
Step Four: Calculating Voltage For Introducing Ore Feedstock @ 25 oC						0.6471817686					
Ore Feedstock $\text{MgO} \cdot \text{Al}_2\text{O}_3 \cdot \text{B}_2\text{O}_3$ (s, 25 oC) To $\text{MgO} \cdot \text{Al}_2\text{O}_3 \cdot \text{B}_2\text{O}_3$ (l, 1260 oC)											
Enthalpy Change [ΔH] (kJ/mol-Mn_l)	1754421.4	Formula	$V_{feed} = \Delta H / (n * F)$	0.3868786486							

Table 28: The calculation process to obtain the Nominal Cathode-To-Anode Distance for the electrolytic cell containing the AlMgB_{14} MOE reaction.

As shown in Table 28, we had to work backward to obtain our desired distance. We started with

our formula: $R = \frac{\rho * D_{ac}}{\text{Area}}$, and worked backward to obtain our missing information. From this formula, all we know is the resistivity (ρ), so we had to work backward to find everything else.

To do so, it was important to realize that Ohm's Law ($V = I * R$) was a crucial piece of information in furthering this process. We had to calculate the net voltage, or ohmic drop, in order to be able to proceed with our distance formula. In order to calculate this ohmic drop, we had to find each of the partial-voltage components of this reaction. This was where we proceeded with our first voltage calculation: the minimal operation voltage. To do this, we first had to determine the heat lost during the electrolysis. To do this, we used FactSage to extrapolate thermodynamic characteristics, see Step One of *Table 28*. We found the necessary entropy change to be $3477.56 \frac{kJ}{mol-Mn*K}$. This characteristic was used to calculate the net heat loss via the formula $\Delta Q = \frac{\Delta S}{T}$. Substituting the values we needed, our $\Delta Q = 6513991.514 \frac{kJ}{mol-Mn}$.

Now that we had established all calculations regarding thermodynamic properties, we found the first two voltage components necessary to find our ohmic drop. Our minimum operating voltage was **0.9074848886 Volts**, and our electrolysis reaction voltage was **1.4364418 Volts**. We then determined the last two voltage components: the voltage requirement for introducing ore-feedstock at room temperature and the voltage from the reaction losses. To calculate the feedstock voltage, we needed to conduct another thermodynamic calculation for enthalpy change. As seen in *Table 28*, in Step Four, this enthalpy change was used to find our voltage which was **0.3868786486 Volts**. For our final voltage, the voltage for thermal losses in the reaction, we assumed there were no losses in our reaction. Hence the corresponding voltage would be assumed to be **0 Volts**. Our sixth step in the calculation was to find our ohmic drop, which was just the sum of all of the voltage components, and our ohmic drop came to be **1.294363537 Volts**. In our final step, we used the distance formula and ohmic drop formula (ohm's law) to find our distance by substituting our distance formula for the resistance. We also found that a valuable formula for current that helps us navigate to the distance was $I = j * Area$

, where j was the current density. Once the substitution and simplification of this formula were completed, we ended up with this as our formula: $V_{IR} = j * \rho * D_{ac}$. Afterward, we made two assumptions on the unknowns (resistivity and current density). For our current density, we assumed it to be $2 \frac{A}{cm^2}$, which is the same for Aluminum Smelting: $Al_{(s)}^{3+} \rightarrow Al_{(l)} + 3e^-$. For our resistivity, we assumed it to be $1 \text{ ohm} * \text{cm}$, which is typical for Molten Salts. Upon gathering everything, we used the formula application from Google Spreadsheets, and, as seen in *Table 28*, we calculated our nominal cathode-to-anode distance to be **0.6471817686 centimeters**. As we saw from our test calculations with Manganese MOE, this distance was approximately the same as our target reaction of Aluminum Magnesium Boride.

5.1.10 Faradaic Efficiency

Once the nominal cathode-to-anode distance was calculated, we moved on to calculating the efficiency of our reaction. This was done using the components we calculated from our process with the nominal cathode-to-anode distance. The first efficiency we focused on was faradaic.

When we were proceeding with our faradaic efficiency findings, we were not calculating this efficiency. Rather we would assume the reaction parameter of this efficiency and calculate the actual mass that would be produced from this reaction under the conditions of X-% faradaic efficiency. Below, in *Table 29*, are the steps taken and the specific calculations needed to find this produced mass of Aluminum Magnesium Boride.

FARADAIC EFFICIENCY (CURRENT EFFICIENCY)					
Formula					
$\eta_f = ((m) / (m_o)) * 100\%$					
η_f	Faradaic Efficiency	m	Actual Mass Produced (grams)	m_o	Theoretical Mass Produced (grams)
Step One: Developing Assumptions					
Assumption			Reasoning		
$\eta_f = 90\%$			Modern aluminum electrolysis cells operate at approximately 90% faradaic efficiency, so we can assume to apply the same efficiency to this electrolysis cell		
Step Two: Calculating The Theoretical Mass Of Aluminum Magnesium Boride Produced					
Formula					
$m = (M * Q) / (n * F)$					
Molar Mass [M] (g/mol-Mn)	202.640539	Number Of Tranferred Electrons [n] (mol-e/mol-Mn)	47	Faraday's Constant [F] (C/mol-e)	96485.3321
Charge [Q] (C/mol)					
$Q = I * \Delta t = (j * Area) * \Delta t$					
Current Density [j] (A/cm ²)	2	Area [cm ²]	1	Time [Δt] (s)	86400
172800					
Theoretical Mass [m] (gram)					
7.72166429					
Step Three: Calculating The Actual Mass Of Manganese Produced					
Formula					
$\eta_f = ((m) / (m_o)) * 100\%$					
Faradaic Efficiency [η_f] (%)	90	Theoretical Mass Produced [m_o] (g)	7.72166429		
6.949497861					

Table 29: The calculation process to obtain the Actual Produced Mass of $AlMgB_{14}$. This was done assuming that the reaction occurs at 90% faradaic efficiency.

The formula for faradaic efficiency is as follows: $\eta_f = \frac{m}{m_o} * 100\%$. Just like we did with the Manganese molten oxide electrolysis test calculations, we made the same assumption that our faradaic efficiency be 90% for the electrolysis reaction. This assumption was made on the basis that modern aluminum electrolysis cells operate at approximately 90% faradaic efficiency, so we can assume to apply the same efficiency to this electrolysis cell.

Our next step was to calculate the theoretical mass produced or m . This mass produced, whether theoretical or actual, was the mass produced of Aluminum Magnesium Boride. To calculate the theoretical mass produced, we used this formula: $m = \frac{M*Q}{n*F}$. We knew the number of electrons transferred and Faraday's constant to be 47 and 96485.3321, respectively. We found

the molar mass of AlMgB_{14} (M) by researching periodic tables and simple algebra. The molar mass of this compound is just the sum of the molar mass of one mole of aluminum, one mole of magnesium, and fourteen moles of boron. This calculation can be seen below:

$$M = M_{Al} + M_{Mg} + 14 * M_B = 26.981539 + 24.305 + 14 * 10.811 = 202.640539 \frac{g}{mol}$$

Our next missing component to this formula was the charge, Q, which we found through this formula: $Q = I * \Delta t$ or also $Q = j * Area * \Delta t$. We knew j, the current density, from our previous calculation—the nominal cathode-to-anode distance, that we assumed to be $2 \frac{A}{cm^2}$. The area and change in time (Δt) were assumed under the basis that the area was, $1 cm^2$ and the change in time was measured over one full day or 86400 seconds as we assumed the reaction to take an entire day. The charge we calculated came to be $172800 \frac{C}{mol}$.

Once we found everything we needed, the theoretical mass produced of aluminum magnesium boride was simply calculated through Google Spreadsheets, and it came to be **7.72166429 grams**. As seen in *Table 15*, we moved to the final step and calculated our actual mass of AlMgB_{14} produced, which was **6.949497861 grams**.

Comparing the same calculations conducted with our test run with manganese, we found our theoretical and actual mass produced of manganese to be 49.1955295 grams and 44.27597655 grams, respectively. We observed that our mass produced, both theoretical and actual, was significantly low for our boride calculation versus our manganese calculation. This occurrence will be discussed in the following section: *6.0 Conclusion*, on why this occurrence takes place and what that means for the reaction.

5.1.11 Energy Efficiency

Likewise with faradaic efficiency, our energy efficiency calculation was derived from previous characteristics. However, unlike in our faradaic efficiency, we calculate our energy efficiency. This calculation is shown below in a step-by-step structure.

ENERGY EFFICIENCY							
Formula							
$\eta_E = ((E_o) / (E)) * \eta_f$							
η_E	Energy Efficiency	E	Actual Minimal Potential (V)	E_o	Minimal Theoretical Potential (V)	η_f	Faradaic Efficiency
Step One: Developing Assumptions							
Assumption			Reasoning				
$\eta_f = 90\%$			Modern aluminum electrolysis cells operate at approximately 90% faradaic efficiency, so we can assume to apply the same efficiency to this manganese electrolysis cell				
Step Two: Calculating The Minimal Theoretical Potential							
Formula							
$E_o = V_{min} + V_r + V_{feed}$							
Minimum Operating Voltage [V_min] (V)	0.9074848886	Electrolysis Reaction Voltage [V_r] (V)	1.4364418	Voltage For Introducing Ore Feedstock [V_feed] (V)	0.3868786486		
2.730805337							
Step Three: Calculating The Energy Efficiency							
Formula							
$\eta_E = ((E_o) / (E)) * \eta_f$							
Actual Minimal Potential							
$E = E_o + (T * \Delta S) / (4F)$							
Minimal Theoretical Potential [E_o] (V)	2.730805337	Operating Temperature [T] (K)	1873.15	Entropy Change [ΔS] (J/mol*K)	3477.56	Faraday's Constant [F] (C/mol)	96485.3321
4.167247137							
58.977179							

Table 30: The calculation process to obtain the Energy Efficiency of $AlMgB_{14}$. This was done assuming that the reaction occurs at 90% faradaic efficiency.

This calculation process was split into three steps. In the first step, we established the assumption. This was the same assumption about faradaic efficiency; that the faradaic efficiency would be assumed to be at 90% for our $AlMgB_{14}$ MOE process. Next, we employed picking apart the energy efficiency formula, as seen in *Table 30*. This moved us to the second step, calculating the minimal theoretical potential. This potential value is the sum of the minimum operating voltage, electrolysis reaction voltage, and voltage required to introduce ore-feedstock. This summation yields us a minimum theoretical voltage of **2.730805337 Volts**. Our third step

involved us calculating the actual minimal potential. This was done through a formula presented in a previous study: $E = E_o + \frac{T*\Delta S}{n*F}$, which we stated in the *4.0 Methodology* section. We found E_o , and we knew n and F from previous calculations. We also knew the entropy change and our operating temperature, so calculating E was simple. From our calculation, the actual minimum voltage was **4.167247137 Volts**. Now that we gathered all the required information, the energy efficiency was calculated to be **58.977179%**. Compared to our test calculations with manganese, whose energy efficiency was 79.92288171%, our calculated energy efficiency was far less. This was because our potential for our boride reaction was much greater than the theoretical counterpart compared to the manganese moe process calculations. The reasoning behind this is shown in the following section: *6.0 Conclusion*.

5.1.12 Endothermic Or Exothermic

The final calculation required for investigating the molten oxide electrolysis process of Aluminum Magnesium Boride was determining if the process was endothermic or exothermic. This was a straightforward calculation, as evident from *Figure 31*, where the slope of the energy balance is positive. Hence the reaction would be endothermic.

5.2 Zirconium Diboride

After completing the above calculations for Aluminum Magnesium Boride, we transition to our investigation of producing Zirconium Diboride (ZrB_2) through the molten oxide electrolysis process.

5.2.0 Pseudo Binary Phase Diagram

As we did with our Aluminum Magnesium Boride investigation, our first calculation focused on the pseudo-binary phase diagram. Mapping out this graph would lay the groundwork for making decisions for our experiment that would alter the remaining results.

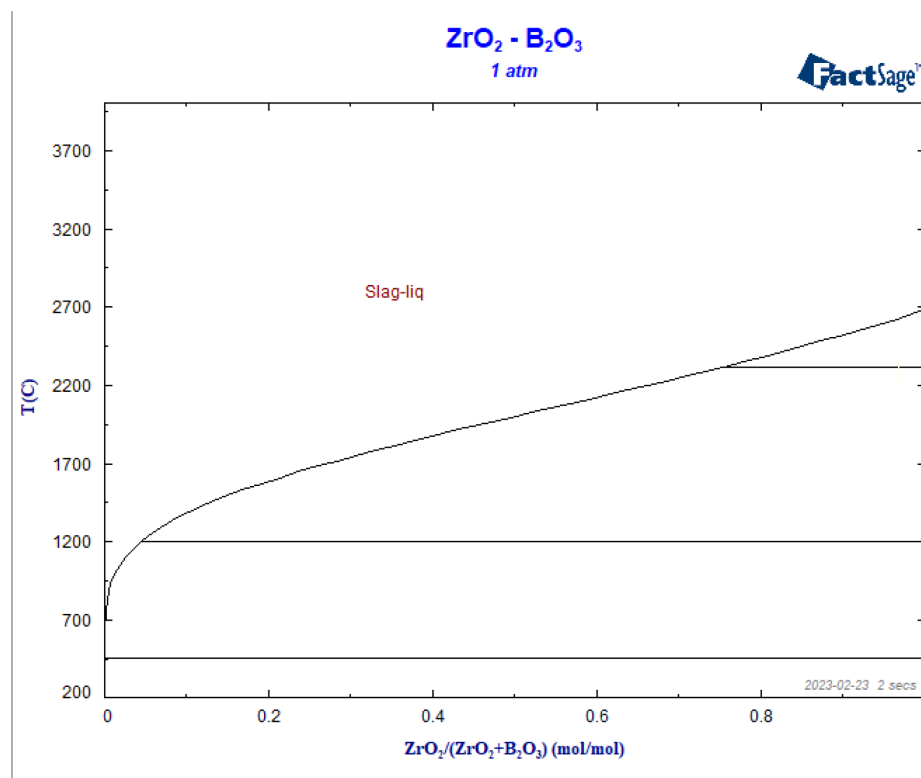


Figure 33: The Pseudo-Binary Phase Diagram Between ZrB_2 and O_2 from a temperature range of 200 °C to 4000 °C.

The construction and analysis of the pseudo-binary phase diagram, shown in *Figure 33*, between zirconium diboride (ZrB_2) and oxygen gas (O_2) from the x-axis of moles of ZrO_2 /the moles of $\text{ZrO}_2+\text{B}_2\text{O}_3$, was delivered to determine the most optimal operating temperature for the electrolysis of ZrB_2 via molten oxide electrolysis.

The pseudo-binary diagram, performed at temperatures ranging from 200 to 4000 degrees Celsius, demonstrated that the slag-liquid region, our target region, occurs only at extremely high temperatures. It was discovered that the slag liquid was present only at around 2700 °C, which is much higher and unusual. This temperature range implies that producing ZrB_2 via molten oxide electrolysis using ZrO_2 and B_2O_3 as electrolytes will necessitate a significant energy input and specialized equipment, which can be expensive and unfeasible.

Furthermore, the pseudo-binary phase diagram revealed that the appearance of only slag-liquid is feasible, but only if the amount of ZrO_2 in the combination is considerably low—less than 20%, to be precise. The subsequent inquiry was required to precisely determine the application of our investigation and subsequent investigation to other computations; accordingly, we developed a series of isothermal sections, as shown in the following subsection.

5.2.1 Isothermal Section

As we discovered from developing our pseudo-binary phase diagram, we constructed three isothermal sections at the following temperature conditions: 1200 °C, 1500 °C, and 2200 °C. We conducted this step to determine the amount of zirconium dioxide needed for this reaction and the feasibility of producing zirconium diboride through the MOE process.

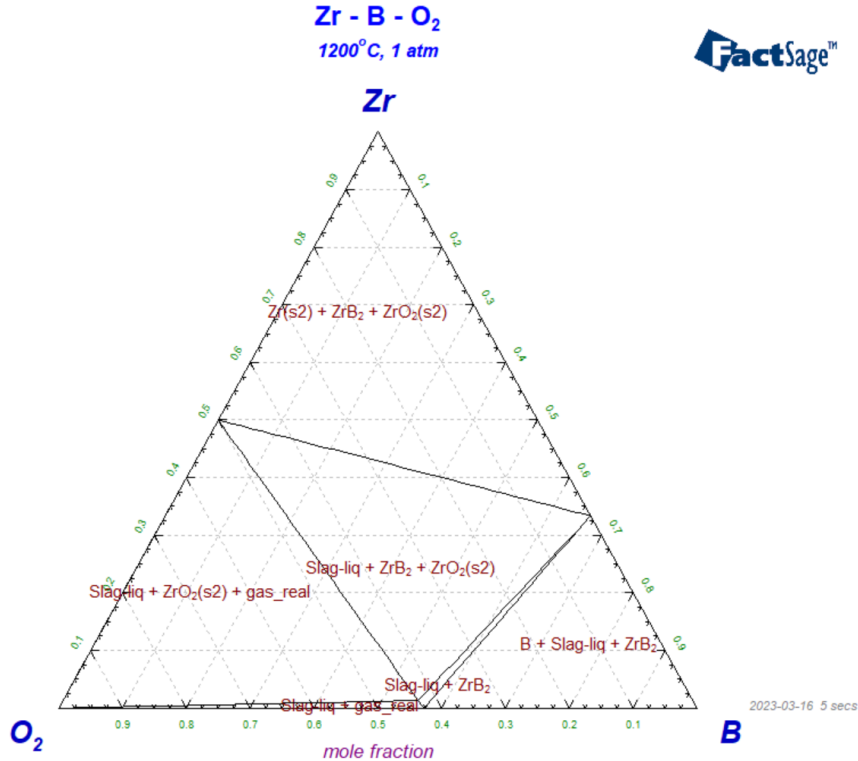


Figure 34: The Isothermal Section between Zr, B, and O₂ at 1200 °C.

Mentioned in the previous subsection and *Figure 33*, we evaluated the pseudo-binary phase diagram and determined that the lowest possible temperature we could examine via the isothermal section was 1200 °C. As mentioned in previous sections, our desired composition is the slag-liquid when analyzing an isothermal section. We see regions that have slag liquid. However, solids are also formed with this slag in many regions, which we do not want as our yield. However, towards the bottom of this diagram, a region appeared where slag-liquid and real gas were present. This was something to look into further. However, the results yield negative from looking at the mole fraction of Zirconium in this region. We position Zirconium at the top vertices of the isothermal section. To determine the mole fraction of zirconium at a particular point in the graph, we must use the side with the vertices of O₂ and Zr (opposite to B). In order to

read the mole fraction of Zirconium for this diagram, we follow this side, where the mole fraction increases from the O_2 vertices to the Zr vertices. Our region of interest, the Slag-liquid + gas_real region, appears towards the bottom of the diagram. We examined the mole fraction of zirconium, and drawing a line to that Zr- O_2 side, we found that this mole fraction is meager, far below 0.1 to be exact. That was impractical for our reaction yield, so we increased the temperature to 1500 °C.

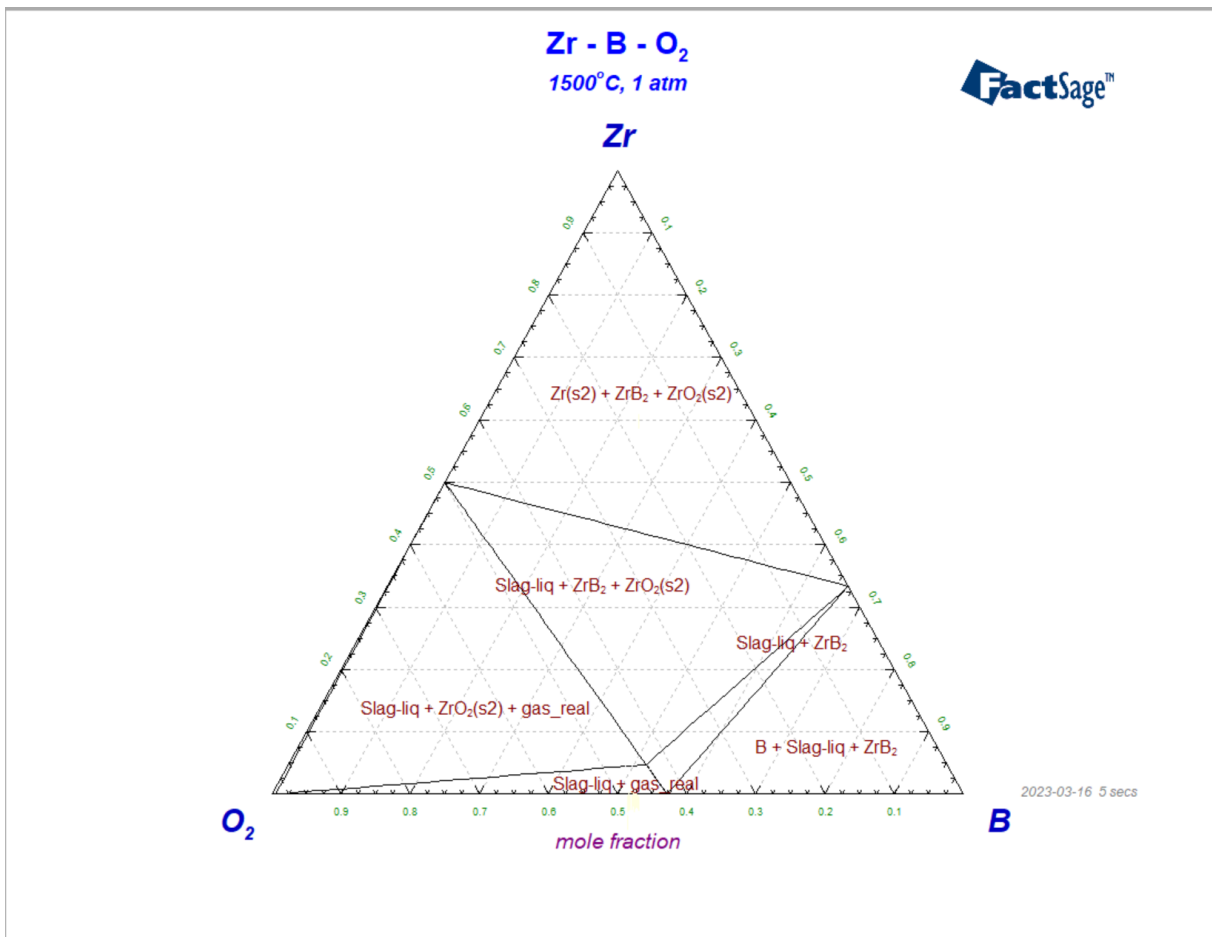


Figure 35: The Isothermal Section between Zr, B, and O_2 at 1500 °C.

We then re-established our isothermal section under the temperature of 1500 °C. We followed the same navigation for the isothermal section at 1200 °C and located the slag-liquid region without any solids (slag-liquid + gas_real). Compared to the diagram of *Figure 34*, *Figure*

35 showed this region to be much more significant, as more of the solution would liquefy as the temperature increased. Although this inherent “increase” occurred, it was not enough. The yield from that region with the maximum zirconium mole fraction was approximately 0.5, which was still too low for us to proceed with other calculations. So we changed our temperature of the isothermal section to a more drastic temperature of 2200 °C.

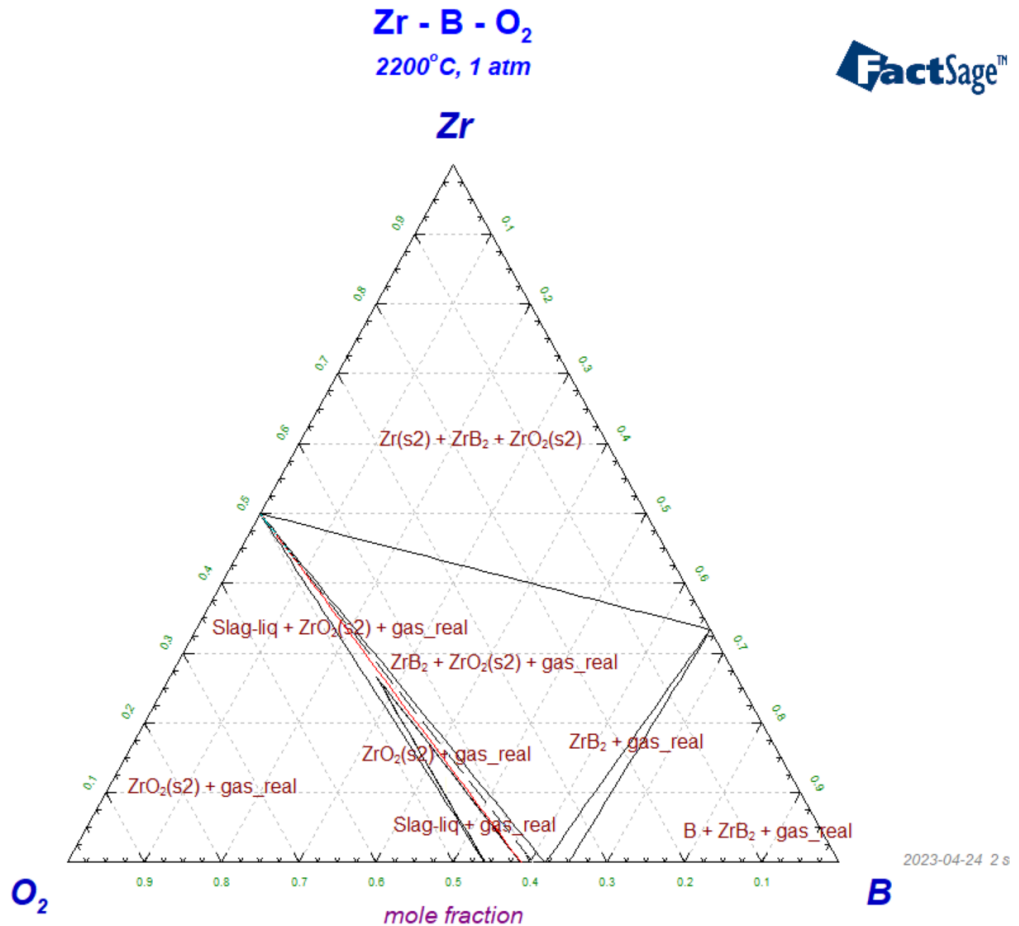


Figure 36: The Isothermal Section between Zr, B, and O₂ at 2200 °C.

From *Figure 36*, we saw a more drastic change in the appearance of the Slag-Liquid. However, we deemed the reaction still unfeasible because the mole fraction was still low for Zirconium, and increasing the operation temperature any further would be illogical for creating an environmentally sound and commercialized method for producing zirconium diboride through

molten oxide electrolysis. More of this will be discussed in the subsequent section: 6.0

Conclusion.

6.0 Conclusions

6.1 Aluminum Magnesium Boride

We reached several conclusions after studying the findings and calculations of the attempt to generate AlMgB_{14} by molten oxide electrolysis (MOE).

We could not produce pure AlMgB_{14} borides via MOE. This was derived from the energy balance calculation. However, the process will not create pure borides. Alternate techniques for manufacturing AlMgB_{14} must be investigated.

Second, our group discovered that increasing the operating temperature from 1400°C to 1600°C to accommodate a more liquid solution decreased the flow rate, which must be factored into the mass balance calculation.

Third, while composition four was optimal since it was the middle composition of the seven seen, the actual mass of Aluminum Magnesium Boride produced was discovered to be poor, resulting in low energy efficiency. As a result, additional compositional modification is required to increase aluminum magnesium boride production. Those modifications consisted of decreasing the flow rate of air into the system.

Fourth, our group analyzed the nominal cathode-to-anode distance and discovered it deviates from the typical distance in an aluminum electrolysis cell, which is about 4.5 centimeters. This distinction is due to practical constraints caused by periodic anode-cathode shorting, material and temperature control limitations, and bubble formation and residency at the anode, which prevents a return reaction with the aluminum product. As a result, more testing is required to find the ideal cathode-to-anode distance for the MOE of AlMgB_{14} .

In conclusion, based on the facts and analysis presented, commercial production of AlMgB₁₄ by MOE is not viable. The findings, however, provide valuable insights and direction for future research to improve process efficiency and optimize AlMgB₁₄ production. More testing is required to find the ideal operating conditions, composition, and cathode-to-anode distance for commercial production of AlMgB₁₄ via Molten Oxide Electrolysis. Our group continued investigation from this conclusion and pursued the possibility of a revolutionary approach to producing Aluminum Magnesium Boride through Molten Oxide Electrolysis. This investigation is shown in the next section: *7.0 A New Approach*.

6.2 Zirconium DiBoride

Based on the results and analyses presented in section *5.0 Results & Analysis*, we determined that producing zirconium diboride by molten oxide electrolysis (MOE) was not viable due to zirconium's very poor solubility in the electrolyte. The data from the pseudo-binary and ternary phase diagrams corroborated this conclusion.

The pseudo-binary phase diagram revealed that the slag-liquid zone, the electrolysis target region, only appeared at extremely high temperatures, around 2700 °C. Creating zirconium diboride through MOE with ZrO₂ and B₂O₃ as electrolytes would require substantial energy and specialized equipment, both prohibitively expensive. Furthermore, the diagram demonstrated that only slag-liquid might emerge if the proportion of ZrO₂ in the electrolyte mixture was relatively low, less than 20%.

The ternary phase diagrams performed at 1200 °C, 1500 °C, and 2200 °C corroborated the conclusion that zirconium solubility in the electrolyte is very low. The diagrams revealed that the

region containing just slag-liquid was limited and that solids formed in many regions, which was not desired for yield. Despite slag-liquid and actual gas, the mole percentage of zirconium at that moment was exceedingly low, far below 0.1. Even at 2200 °C, the mole fraction of zirconium in the slag-liquid region remained low, indicating that increasing the operating temperature further would not result in a practical and environmentally sound method of producing zirconium diboride via Molten Oxide Electrolysis.

Another reason for the infeasibility of this production process for ZrB_2 , was that the zirconium portion of the electrolyte— ZrO_2 —has an extremely high melting temperature. By mixing this compound with B_2O_3 to form the desired electrolyte, only a very limited amount of ZrO_2 could dissolve in the liquid.

In conclusion, due to the very low solubility of zirconium in the electrolyte, as well as the high melting temperature of ZrO_2 , it was determined that MOE was not a viable approach for generating zirconium diboride. This finding was backed by the scientific and professional examination of the results and the factual information presented. It is recommended that other methods for commercializing zirconium diboride production be investigated.

7.0 A New Approach Proposed

7.1 Introducing A Hydrogen Flux

Following the conclusion concerning aluminum magnesium boride, our group examined the prospect of a revolutionary way to manufacture this boride by molten oxide electrolysis. The potential of introducing a hydrogen flux linked with the molten oxide electrolysis reaction was investigated in this study.

7.1.0 The Benefits Of Introducing A Hydrogen Flux Into A Molten Oxide

Electrolysis Reaction

Before proceeding with our calculations regarding this approach, we researched the potential benefits of introducing a hydrogen flux into a molten oxide electrolysis reaction. This research would help us develop the process and conditions of introducing a hydrogen flux into our reaction.

Adding a hydrogen flux to a molten oxide electrolysis reaction has various advantages that can improve efficiency and cost-effectiveness. One key advantage is that the voltage and energy input necessary for the reaction are reduced. According to a 2019 study, introducing a hydrogen flux into titanium dioxide molten oxide electrolysis reduced the necessary voltage by up to 50%, significantly reducing energy input (Zhang et al., 2019). This reduction in energy input can result in significant cost savings and make the process more economically viable.

The hydrogen gas combines with the oxygen ions in the molten oxide, producing heat and raising the reaction temperature. Another advantage of including a hydrogen flux is that the

reaction becomes exothermic, increasing energy efficiency. As described in a 2020 study on the influence of hydrogen on the molten oxide electrolysis of iron ore, this exothermic action can reduce the overall energy required to support the operation (Wang et al., 2020). The exothermic features of the reaction can also contribute to a reduction in the needed operating temperature, increasing the process's energy efficiency.

Aside from these advantages, adding a hydrogen flux can increase the purity and yield of the desired product. Adding hydrogen to aluminum oxide molten oxide electrolysis increased the quality of the final aluminum product by eliminating contaminants such as silicon and iron (Liu et al., 2020). The scientists credit this improvement to the hydrogen gas's decrease of oxide ions, which reduces contaminants.

Introducing a hydrogen flux into a molten oxide electrolysis reaction provides various advantages that can improve efficiency and cost-effectiveness. These advantages include lower voltage and energy input, increased energy efficiency, and higher product purity and yield. Several studies have shown that using hydrogen gas as a reductant is effective, and it holds promise for improving molten oxide electrolysis technology in various industrial applications.

7.1.1 The Ramifications Of Introducing A Hydrogen Flux Into A MOE Reaction

Although adding a hydrogen flow to a molten oxide electrolysis operation offers various advantages, some potential consequences must be considered. One significant difficulty is the safety risks raised by using hydrogen gas. Hydrogen gas is highly explosive and combustible; mishandling or leaking can endanger lives. As a result, it is critical to ensure that the hydrogen input is appropriately managed and kept below acceptable levels. According to the same 2020

study by Wang's group, the hydrogen intake must be less than 4% to eliminate safety issues and provide effective reaction management (Wang et al., 2020).

Another potential ramification is the effect of hydrogen on reactor and other equipment corrosion. Hydrogen gas can accelerate corrosion, especially in high-temperature conditions, resulting in equipment failure and safety issues. As a result, it is critical to ensure that the reactor and accompanying equipment are correctly designed and built to withstand the potentially corrosive effects of hydrogen gas. The use of corrosion-resistant materials, such as ceramics and graphite, can help alleviate the impacts of hydrogen on equipment corrosion, according to the same 2019 study by Zhang's group (Zhang et al., 2019).

Aside from these problems, the addition of a hydrogen flux can have an impact on the overall environmental sustainability of the process. Hydrogen gas is often produced using fossil fuels such as natural gas or coal, which can result in greenhouse gas emissions and contribute to climate change. As a result, it is critical to evaluate the environmental impact of the hydrogen manufacturing process and investigate alternate methods of producing hydrogen gas, such as water electrolysis, using renewable energy sources.

While introducing a hydrogen flux into a molten oxide electrolysis operation provides some advantages, some potential consequences must be considered. Some of the critical difficulties that must be addressed to ensure the safe and sustainable use of hydrogen in the molten oxide electrolysis process are safety concerns, equipment corrosion, and environmental sustainability.

7.2 Pairing Molten Oxide Electrolysis With A Hydrogen Flux To Produce Aluminum Magnesium Boride

Now that we knew the capabilities and constraints of introducing a hydrogen flux into our production of aluminum magnesium boride prior to beginning the molten oxide electrolysis process, we began mapping out the calculations. These calculations were performed in a series of steps shown below in the following subsections.

7.2.0 Calculating The Individual Moles Of The Elements & Moles Of Oxygen Gas

The first step was to set up the reaction framework which was completed by determining the moles of aluminum, magnesium, and boron from the moles of Al_2O_3 , MgO , and B_2O_3 , respectively.

The composition of the electrolyte was consistent with the one chosen for our project results, which was Composition Four. The electrolyte formation of this composition was $\text{Al}_2\text{O}_3\text{-MgO-B}_2\text{O}_3$. The total moles of Al_2O_3 was **0.163332**. The total moles of MgO were **0.221198**. The total moles of B_2O_3 was **0.61547**. B_2O_3 was the component with the most concentration in Composition Four.

The next step taken was isolating the elements consistent with our reaction products: AlMgB_{14} and O_2 . Those isolated elements of the boride include aluminum, magnesium, and boron. These three elements were the first to receive our attention for calculating each of their respective moles. These calculations were done through Google Spreadsheets by use of the formula application of this program. These calculations are shown below:

Moles Of Composition		Moles Of Elements	
Al₂O₃	0.163332	Al	0.183643
MgO	0.221198	Mg	0.124352
B₂O₃	0.61547	B	0.692005
		O₂	0.718912

Table 31: The calculations made to obtain individual amounts of moles for the elements of AlMgB₁₄.

This was done through a formula that was respective to each of the elements. For aluminum, the formula we used was $X_{Al} = \frac{2 * X_{Al_2O_3}}{2 * X_{Al_2O_3} + X_{MgO} + 2 * X_{B_2O_3}}$; for magnesium, we used was $X_{Mg} = \frac{X_{MgO}}{2 * X_{Al_2O_3} + X_{MgO} + 2 * X_{B_2O_3}}$; for boron, the formula we used was $X_B = \frac{2 * X_{B_2O_3}}{2 * X_{Al_2O_3} + X_{MgO} + 2 * X_{B_2O_3}}$. X_{Al} , X_{Mg} , and X_B were the moles of aluminum, magnesium, and boron. $X_{Al_2O_3}$, X_{MgO} , and $X_{B_2O_3}$ were the moles of Al₂O₃, MgO, and B₂O₃. The basis of this formula was, for example, the moles of aluminum were calculated by dividing the two times the moles of Al₂O₃ by the total moles of aluminum, magnesium, and boron. The reason for us multiplying the moles of Al₂O₃ and B₂O₃ by two was that, for every mole of those compounds, there were two moles of aluminum and boron. Each was calculated and we ended up with approximately **0.183643** moles of Aluminum, **0.124352** moles of Magnesium, and **0.692005** moles of Boron.

Next, we had to calculate the moles of oxygen gas that would be present in our electrolyte composition. This calculation is shown above in Table 31. To conduct this step, we needed to construct another formula to derive the moles of oxygen gas. This formula was:

$$X_{O_2} = \frac{1}{2} * X_O = \frac{3}{2} X_{Al} + X_{Mg} + \frac{3}{2} X_B$$

The reason for this formula's 1.5 multipliers on the moles of aluminum and moles of boron was because, for the compounds of Al_2O_3 and B_2O_3 , there are three moles of oxygen per two moles of aluminum/boron. This summation was not, however, the total moles of oxygen gas. Instead, it was the moles for the element oxygen. To get the total moles of oxygen gas, we just multiply that summation by 0.5, as there are two moles of oxygen in oxygen gas. From this formula, we calculated the moles of oxygen gas to be approximately **0.718912** moles.

7.2.1 Calculating The Moles Of The Individual Products Of The Reaction & Oxygen Partial Pressures For Different Amounts Of Oxygen Gas Present

The next phase of establishing this new approach was to determine the amount of the individual product created from the reaction in the measurement of moles. We calculated the moles of aluminum, magnesium, and boron for that purpose. To determine the moles of the products, we simulated the reaction through FactSage. Using the *Equilib* module from FactSage, we imputed the elements involved—aluminum, magnesium, and boron—and their respective moles. This is present in *Table 20*, which shows the menu window prior to calculating reaction results. However, different from the elements associated with AlMgB_{14} , the O_2 component of the FactSage input was represented as a range. This range was from 0 moles to 0.718912 moles of Oxygen gas. We conducted this calculation like so because we were introducing hydrogen gas into the reaction. If we introduced a hydrogen flux into the reaction, the hydrogen gas would mix with the oxygen gas, essentially forming water. What this does is practically eliminate the formation of any residual oxides from our desired compound. So, this calculation simulates what products would emerge if we introduced certain moles of Hydrogen gas (or removed moles of

oxygen gas). If no hydrogen gas were introduced, we would have 0.718912 moles of O_2 . We simulated introducing hydrogen gas (or removal of oxygen gas) until we speculate that we conduct the reaction at 0 moles of O_2 .

The screenshot shows the FactSage 8.0 Equilib menu window. The window title is "Equilib - Menu: last system". The "Reactants (4)" field contains the text "0.183643 Al + 0.124352 Mg + 0.692005 B + <A> O2". The "Products" section is divided into "Compound species" and "Solution phases". Under "Compound species", there are radio buttons for "gas", "aqueous", "pure liquids", and "pure solids", with "gas" selected. The counts are 21 for gas, 0 for aqueous, 0 for pure liquids, and 45 for pure solids. A "Target" section shows "Estimate T(K): 1000" and "Quantity(mol): 0". The "Solution phases" table has columns for "*", "+", "Base-Phase", and "Full Name". The selected row is "I FToxid-SLAGA A-Slag-liq all oxides + S". The "Final Conditions" table has columns for "<A>", "", "T(C)", "P(atm)", and "Product H(J)". The values are 18912, 0.0359456, 1600, 1, and 21 calculations. The "Equilibrium" section has radio buttons for "normal", "normal + transitions", "transitions only", and "open", with "normal" selected. A "Calculate >>" button is visible.

Table 32: The menu window to the FactSage calculations for oxygen partial pressure, moles of Slag #1, moles of Slag #2, total moles of AlB_2 , total moles of MgB_2 , total moles of Al_2O_3 , total moles of MgB_7 , total moles of AlB_{12} , total moles of B, and total moles of $AlMgB_{14}$ for each specific mole-amount of O_2 . Each of the constraints selected is shown in this table.

Once we calculate the products of the reactions, we see twenty-one calculations similar to Table 33 below. One area of focus from each calculation includes the fugacity of O_2 , which we would use for graphing the Oxygen Partial Pressure. The other areas of focus include moles of

Slag-Liquid #1, the moles of Slag-Liquid #2, and the moles of the apparent solids produced for the conditions of the amount of oxygen present in each of the twenty-one calculations.

```

T = 1600 C
P = 1 atm
V = 0 dm3

STREAM CONSTITUENTS      AMOUNT/mol
Al      1.8364E-01
Mg      1.2435E-01
B       6.9200E-01
O2      2.1567E-01

PHASE: gas_real
EQUIL AMOUNT      MOLE FRACTION      FUGACITY
mol              atm
Mg      V  0.0000E+00      9.6152E-01      1.9556E-02
(BO)2   V  0.0000E+00      2.3237E-02      4.7262E-04
AlBO2   V  0.0000E+00      7.0277E-03      1.4294E-04
BO      V  0.0000E+00      6.1814E-03      1.2572E-04
B2O3    V  0.0000E+00      1.5271E-03      3.1061E-05
Al      V  0.0000E+00      3.6480E-04      7.4198E-06
Al2O    V  0.0000E+00      8.9976E-05      1.8300E-06
B2O     V  0.0000E+00      5.0653E-05      1.0202E-06
Mg2     V  0.0000E+00      3.3366E-06      6.7864E-08
B       V  0.0000E+00      5.3296E-07      1.0840E-08
BO2     V  0.0000E+00      2.9436E-07      5.9871E-09
AlO     V  0.0000E+00      4.9562E-08      1.0080E-09
MgO     V  0.0000E+00      1.8541E-08      3.7712E-10
Al2O2   V  0.0000E+00      2.2367E-09      4.5492E-11
Al2     V  0.0000E+00      1.5706E-09      3.1944E-11
O       V  0.0000E+00      3.4459E-11      7.0087E-13
B2      V  0.0000E+00      1.4894E-12      3.0293E-14
AlO2    V  0.0000E+00      5.8131E-16      1.1823E-17
O2      V  0.0000E+00      4.3667E-16      8.8849E-18
Al2O3   V  0.0000E+00      1.9742E-17      4.0153E-19
O3      V  0.0000E+00      3.7225E-32      7.5768E-34
TOTAL:  0.0000E+00      1.0000E+00      2.0339E-02
PHASE: Slag-liq#1
mol              MOLE FRACTION      ACTIVITY
Al2O3    6.5990E-02      2.9396E-01      1.0389E-01
MgO      1.2277E-01      5.4688E-01      3.9560E-02
B2O3     3.5728E-02      1.5916E-01      3.1114E-03
TOTAL:   2.2449E-01      1.0000E+00      1.0000E+00
Site fraction of sublattice constituents:
Al      0.40459      Stoichiometry calculated
Mg      0.37635
B       0.21906
-----
O       1.0000      Stoichiometry calculated
System component      Amount/mol      Amount/gram      Mole fraction      Mass fraction
Al      0.13198      3.5610      0.17501      0.25141
Mg      0.12277      2.9839      0.16279      0.21067
O       0.42792      6.8465      0.56744      0.48338
B       7.1457E-02      0.77252      9.4755E-02      5.4542E-02
PHASE: Slag-liq#2
mol              MOLE FRACTION      ACTIVITY
Al2O3    2.4875E-05      1.1314E-02      1.0389E-01
MgO      1.5849E-03      7.2085E-01      3.9560E-02
B2O3     5.8887E-04      2.6784E-01      3.1114E-03
TOTAL:   2.1986E-03      1.0000E+00      1.0000E+00
Site fraction of sublattice constituents:
Al      1.7690E-02      Stoichiometry calculated
Mg      0.56354
B       0.41877
-----
O       1.0000      Stoichiometry calculated
System component      Amount/mol      Amount/gram      Mole fraction      Mass fraction
Al      4.9750E-05      1.3423E-03      7.9747E-03      1.2497E-02
Mg      1.5849E-03      3.8520E-02      0.25405      0.35863
O       3.4261E-03      5.4816E-02      0.54919      0.51034
B       1.1777E-03      1.2733E-02      0.18879      0.11854
mol              ACTIVITY
AlB12_beta_tetragonal(s)  5.1614E-02      1.0000E+00
B_beta_rhombohedral_h(s)  0.0000E+00      7.9297E-01
E_diamond_A4(s3)         0.0000E+00      7.9246E-01

```

Table 33: The results window of the FactSage calculations for oxygen partial pressure, moles of Slag #1, moles of Slag #2, total moles of AlB_2 , total moles of MgB_2 , total moles of Al_2O_3 , total moles of MgB_7 , total moles of AlB_{12} , total moles of B, and total moles of $AlMgB_{14}$ for each specific mole-amount of O_2 . This particular example is for when we had 0.2157 moles of O_2 .

Each of the desired results from the twenty-one FactSage Calculations was tabulated in Google Spreadsheets through the association of the corresponding moles of Oxygen Gas present as the reactant. This tabulation is shown below in Table 34.

Mole Of O_2	O_2 Partial Pressure (atm)	Moles Of Slag #1	Moles Of Slag #2	Total Moles Of AlB_2	Total Moles Of MgB_2	Total Moles Of Al_2O_3	Total Moles Of MgB_7	Total Moles Of AlB_{12}	Total Moles Of B	Total Moles Of $AlMgB_{14}$
0.0000	0.000E+00	0.000E+00	0.000E+00	1.760E-01	1.168E-01	0.000E+00				7.602E-03
0.0359	6.669E-21	0.000E+00	0.000E+00	1.185E-01	1.072E-01	2.396E-02				1.719E-02
0.0719	6.669E-21	0.000E+00	0.000E+00	6.1016E-02	9.758E-02	4.793E-02				2.677E-02
0.1078	6.669E-21	0.000E+00	0.000E+00	3.5026E-03	8.799E-02	7.189E-02	0.000E+00	0.000E+00		3.636E-02
0.1438	4.293E-20	1.3698E-01	0.000E+00	0.000E+00	0.000E+00	0.000E+00	3.193E-02	3.113E-03		3.074E-02
0.1797	2.950E-18	1.8353E-01	0.000E+00				2.879E-02	3.832E-02		0.000E+00
0.2157	8.885E-18	2.245E-01	2.199E-03				0.000E+00	5.161E-02		
0.2516	2.370E-17	2.507E-01	0.000E+00					4.793E-02		
0.2876	3.785E-17	2.746E-01	0.000E+00					4.424E-02		
0.3235	5.135E-17	2.986E-01	0.000E+00					4.055E-02		
0.3595	6.467E-17	3.225E-01	0.000E+00					3.687E-02		
0.3954	7.784E-17	3.465E-01	0.000E+00					3.318E-02		
0.4313	9.068E-17	3.705E-01	0.000E+00					2.949E-02		
0.4673	1.030E-16	3.944E-01	0.000E+00					2.581E-02		
0.5032	1.145E-16	4.184E-01	0.000E+00					2.212E-02		
0.5392	1.253E-16	4.424E-01	0.000E+00					1.843E-02		
0.5751	1.351E-16	4.663E-01	0.000E+00					1.475E-02		
0.6111	1.441E-16	4.903E-01	0.000E+00					1.106E-02	0.000E+00	
0.6470	1.501E-16	5.143E-01	0.000E+00					2.655E-03	6.135E-02	
0.6830	1.601E-16	5.382E-01	0.000E+00					0.000E+00	4.793E-02	
0.7189	8.740E-09	5.622E-01	0.000E+00					0.000E+00	0.000E+00	

Table 34: The FactSage calculations for oxygen partial pressure, moles of Slag #1, moles of Slag #2, total moles of AlB_2 , total moles of MgB_2 , total moles of Al_2O_3 , total moles of MgB_7 , total moles of AlB_{12} , total moles of B, and total moles of $AlMgB_{14}$ for each specific mole-amount of O_2 .

Table 34 shows these twenty-one calculations derived from FactSage. Each of these calculations was performed from the scenario where we had no oxygen present to where we had all of our oxygen present, with a mole increment of approximately 0.0359. The partial pressure of oxygen from these calculations typically ranges from 10^{-21} to 10^{-16} . The moles of Slag-liquid #2 mostly appeared to be zero throughout the entire scope of the calculation. This holds from Slag-liquid #1 appeared to be zero from 0 moles to 0.1078 moles. Now examining the solids produced throughout the range of Oxygen gas, we saw that the solids produced were AlB_2 ,

MgB₂, Al₂O₃, MgB₇, AlB₁₂, B, and AlMgB₁₄. Upon collecting all the data for what solids appear for a specific amount of moles of O₂, we also placed zeros at the start (if it did not already start when zero moles O₂) and end to signify the appearance and disappearance of the solid solution based on the thermodynamic alterations taking place. The most prominent solid we saw throughout this calculation process was AlB₁₂. The least prominent were MgB₇ and B. Our desired product of AlMgB₁₄ appeared to be present when we had **0 moles** of O₂ in our reaction to when we had **0.1438 moles** of O₂ present.

7.2.2 Calculating The Mole Fractions Of The Individual Products Of The Reaction For Different Amounts Of Oxygen Gas Present

Our next step in this thorough analysis of the potential new approach was determining the mole fractions of all involved parties. These “parties” were the O₂ and all products yielded from the reaction calculations from *Table 34*.

This calculation was done through Google Spreadsheets with the assistance of the formula apparatus. The Mole fraction of the oxygen gas was calculated by using this formula:

$$N_{O_2} = \frac{X_{O_2}}{1+X_{O_2}}$$

In this above equation N_{O_2} was the mole fraction of oxygen and X_{O_2} was the number of moles for oxygen gas. $1 + X_{O_2}$ represented the total yield of oxygen gas, hence the formula of mole fraction. This calculation attributed 0 moles of O₂ to 0.718912 moles of O₂. Our range for mole fraction was, thus, from **0** to approximately **0.418**. The mole fraction of the products was simply calculated by dividing the mole of a singular product by the sum moles of all products created

(solids and slag). We calculated the mole fraction of all of the solids and the combined mole fraction of the slag-liquid product, as evident in *Table 35*, below.

Mole Fraction Of O ₂	Mole Fraction Of AlB ₂	Mole Fraction Of MgB ₂	Mole Fraction Of Al ₂ O ₃	Mole Fraction Of MgB ₇	Mole Fraction Of AlB ₁₂	Mole Fraction Of B	Mole Fraction Of AlMgB ₁₄	Mole Fraction Slag-Liquid
0.000	0.5860	0.3887	0.0000				0.0253	0.0000
0.035	0.4442	0.4016	0.0898				0.0644	0.0000
0.067	0.2615	0.4183	0.2054				0.1148	0.0000
0.097	0.0175	0.4405	0.3599	0.0000	0.0000		0.1820	0.0000
0.126	0.0000	0.0000	0.0000	0.1575	0.0154		0.1516	0.6756
0.152				0.1149	0.1529		0.0000	0.7322
0.177				0.0000	0.1855			0.8145
0.201					0.1605			0.8395
0.223					0.1388			0.8612
0.244					0.1196			0.8804
0.264					0.1026			0.8974
0.283					0.0874			0.9126
0.301					0.0737			0.9263
0.318					0.0614			0.9386
0.335					0.0502			0.9498
0.350					0.0400			0.9600
0.365					0.0307			0.9693
0.379					0.0221	0.0000		0.9779
0.393					0.0046	0.1061		0.8893
0.406					0.0000	0.0818		0.9182
0.418						0.0000		1.0000

Table 35: The calculations for the mole fractions of the products—AlB₂, MgB₂, Al₂O₃, MgB₇, AlB₁₂, B, AlMgB₁₄, and the Slag-Liquid—for each specific mole fraction of O₂.

From the solids, we noticed from our calculation that the composition seemed to appear from some amount of oxygen and dissipate after some other. To follow this exact trend we introduced a zero mole fraction for when many of the solids were introduced and for when they dissipated as a product. However, some of the solids (AlB₂, MgB₂, Al₂O₃, and AlMgB₁₄) were already present when we had no amount of oxygen gas present in the reaction. To better visualize the trend of the products, we constructed the following graph.

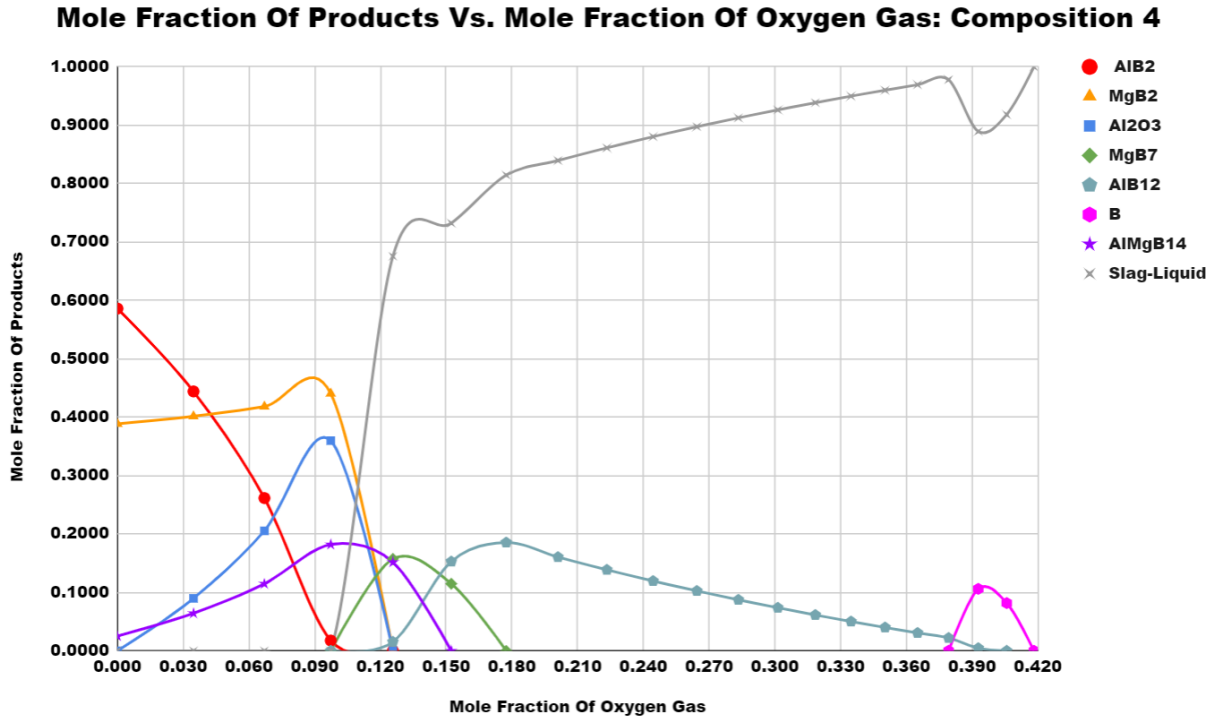


Figure 37: The Mole Fraction Data from Table 35 graphed out in a Mole Fraction Of Oxygen Vs. Mole Fraction Of Products relation.

From *Figure 37*, we saw that our target product, AlMgB₁₄, only appeared when there was no oxygen present to when we had approximately an oxygen gas mole fraction of **0.150**. The peak amount of AlMgB₁₄ appeared around the **0.105**-mole fraction of oxygen gas. This information will be helpful for later calculation when deciding when we stop introducing hydrogen and begin our MOE process. The next step was mapping out the hydrogen flux for our reaction.

7.2.3 Mapping Out The Hydrogen Flux

To better understand the introduction of a hydrogen flux into our reaction, we illustrated the appearance of the general process. This figure is shown below in *Figure 38*.

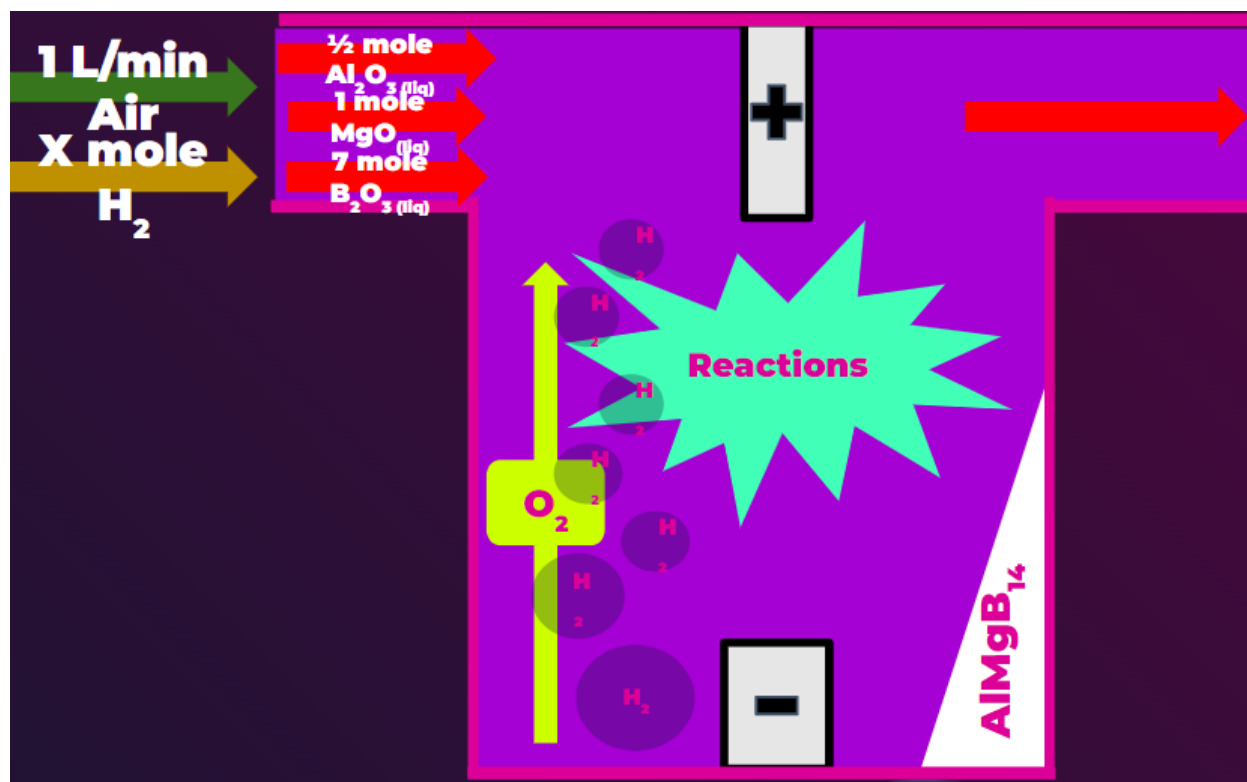


Figure 38: Illustration of the Reaction System with the Introduction of Hydrogen Gas (the brown arrow) entering the reaction.

This setup was very similar to our original reaction, except for the hydrogen gas input. As seen in the above illustration, when introducing the unknown amount of hydrogen gas, we get evaporating bubbles that are the hydrogen gas as well as oxygen gas, and they exit through the outlet of the reaction. That which remains pertaining to oxygen and hydrogen is water, which was attributed to the formation of a purer aluminum magnesium boride, with a lesser probability of the formation of oxides.

Upon our increased understanding of this hydrogen flux, we proceeded to map out the potential hydrogen flux required by our reaction parameters. This was done through the combination of the FactSage *Equilib* module and Google Spreadsheets. First, we conducted the FactSage calculations by filling in the menu window as shown below in *Table 36*.

The screenshot shows the FactSage Equilib software interface. The window title is "Equilib - Menu: last system". The menu bar includes "File", "Units", "Parameters", and "Help". The main window displays the following sections:

- Reactants (3):** A text box containing the chemical formula: $\langle A \rangle \text{ Ar} + \langle 1E-6A \rangle \text{ O}_2 + \langle 1-A \rangle \text{ H}_2$.
- Products:**
 - Compound species:** Radio buttons for "gas", "ideal", "real", "aqueous", "pure liquids", and "pure solids". "real" is selected. The count for "real" is 10, and for others is 0. Total species: 10.
 - Solution phases:** A table with columns "Base-Phase" and "Full Name".
 - Legend:** A "Show" button with radio buttons for "all" (selected) and "selected". Species and solutions counts are 0.
- Final Conditions:** A table with columns for "<A>", "", "T(C)", "P(atm)", and "Product H(J)". The values are: "<A>: .81", ": .01", "T(C): 1600", "P(atm): 1". There are "10 steps" and "21 calculations".
- Equilibrium:** Radio buttons for "normal" (selected), "normal + transitions", "transitions only", and "open". A "Calculate >>" button is present.

The status bar at the bottom left shows "FactSage 8.0".

Table 36: The menu window to the FactSage calculations for determining the moles of Hydrogen Gas that will satisfy the Oxygen Partial Pressure conditions of our unchanged reaction.

The $\langle A \rangle$, or Alpha for the moles of argon, oxygen, and hydrogen gas, signified a mole range that the database could calculate based on. The Alpha in this situation signifies the amount of argon, which translates to calculating the oxygen amount and H_2 amount. We believed the $\langle 1-A \rangle$ value would be the hydrogen gas percentage. Once we realized that, we started experimenting with the possible values of Alpha. We knew that the limits of this value had to be between 0 and 1 to emulate the percentage. The constraint we followed was that the oxygen partial pressure from the results had to be in the same range as the oxygen partial pressures of the changing moles of oxygen presented in Table 34. After careful examination, we proceeded with

the Alpha range of 0.8 to 1.0 with increments of 0.01, which produced 21 results, such as the one below.

```

T = 1600 C
P = 1 atm
V = 153.75 dm3

STREAM CONSTITUENTS          AMOUNT/mol
Ar          9.6000E-01
O2          9.6000E-07
H2          4.0000E-02

EQUIL AMOUNT      MOLE FRACTION      FUGACITY
mol              atm
PHASE: gas_real
Ar          V  9.6000E-01      9.5994E-01      9.6013E-01
H2          V  3.9934E-02      3.9931E-02      3.9939E-02
H           V  1.2844E-04      1.2843E-04      1.2845E-04
H2O         V  1.9195E-06      1.9194E-06      1.9196E-06
OH          V  4.8980E-10      4.8977E-10      4.8987E-10
O           V  1.1635E-12      1.1635E-12      1.1637E-12
O2          V  2.4490E-17      2.4489E-17      2.4493E-17
HOO         V  1.5994E-20      1.5993E-20      1.5996E-20
HOOH        TV 1.1414E-20      1.1413E-20      1.1416E-20
O3          V  3.4670E-33      3.4668E-33      3.4680E-33
TOTAL:      1.0001E+00      1.0000E+00      1.0000E+00
System component  Amount/mol      Amount/gram      Mole fraction      Mass fraction
Ar               0.96000        38.350           0.92308            0.99790
O                1.9200E-06     3.0719E-05      1.8462E-06        7.9933E-07
H                8.0000E-02     8.0635E-02      7.6923E-02        2.0982E-03
*****
Cp          H          S          G          V
J.K-1       J          J.K-1       J          dm3
*****
2.15343E+01  3.34047E+04  1.94074E+02  -3.30125E+05  1.53747E+02
*****
Cp          H          S          G
J.K-1       J          J.K-1       J
gas_real    2.15343E+01  3.34047E+04  1.94074E+02  -3.30125E+05

Cut-off limit for gaseous fractions/phase activities = 1.00E-70

Data on 1 product species identified with "T" have been extrapolated outside their valid temperature range
10 product species identified with "V" are modeled with an equation of state

Databases: FTSalt 8.0, FToxid 8.0, FTlite 8.0, FactPS 8.0
Data Search options: exclude gas ions; organic CxHy.. X(max) = 2; min soln cpts = 2
Final conditions: <A> = .8 1 .01, T(C) = 1600, P(atm) = 1

```

Table 37: The results window of the FactSage calculations for determining the moles of Hydrogen Gas that will satisfy the Oxygen Partial Pressure conditions of our unchanged reaction. This range of percent of Argon goes from 80% to 100%. This particular example is for when we had 96% of Argon.

The data from these twenty-one calculations, specifically the oxygen partial pressure, was tabulated in Google Spreadsheets, as shown below:

<u>Percent Of Argon (/100%)</u>	<u>Percent Of Hydrogen (/100%)</u>	<u>Oxygen Partial Pressure [atm]</u>	<u>Base-10 Log Of Oxygen Partial Pressure [atm]</u>
0.80	0.20	1.53E-17	-16.81400481
0.81	0.19	1.67E-17	-16.77668581
0.82	0.18	1.83E-17	-16.73788128
0.83	0.17	2.01E-17	-16.69743099
0.84	0.16	2.21E-17	-16.65517561
0.85	0.15	2.45E-17	-16.61095802
0.86	0.14	1.60E-18	-17.79520196
0.87	0.13	1.90E-18	-17.72076665
0.88	0.12	2.28E-18	-17.64128489
0.89	0.11	2.78E-18	-17.55586148
0.90	0.10	3.44E-18	-17.46334057
0.91	0.09	4.34E-18	-17.36219017
0.92	0.08	5.62E-18	-17.25034097
0.93	0.07	7.50E-18	-17.12490399
0.94	0.06	1.04E-17	-16.98163242
0.95	0.05	1.53E-17	-16.81400481
0.96	0.04	2.45E-17	-16.61095802
0.97	0.03	4.45E-17	-16.35187428
0.98	0.02	1.02E-16	-15.99046412
0.99	0.01	4.18E-16	-15.37880294
1.00	0.00	8.89E-07	-6.050941941

Table 38: The tabulation of the results window of the FactSage calculations for determining the moles of Hydrogen Gas that will satisfy the Oxygen Partial Pressure conditions of our unchanged reaction. This range of percent of Argon goes from 80% to 100%. In this table, we presented the percent of Argon (/100) and the corresponding percent of Hydrogen Gas (/100), alongside the oxygen partial pressure for each particular instance and the Base-10 logarithmic calculation of that pressure.

One of the calculations provided by Table 38 was determining the hydrogen gas percentage from the argon percentage with the $\langle A \rangle$ and $\langle 1-A \rangle$ relation of the two components presented earlier. The other calculation required us to convert our recorded oxygen partial pressures to a base-10 logarithmic variation to linearize the relation. This made mapping out our hydrogen flux easier, as seen in Figure 39, and allowed us to proceed to the placement of hydrogen gas influx and initiate the molten oxide electrolysis process.

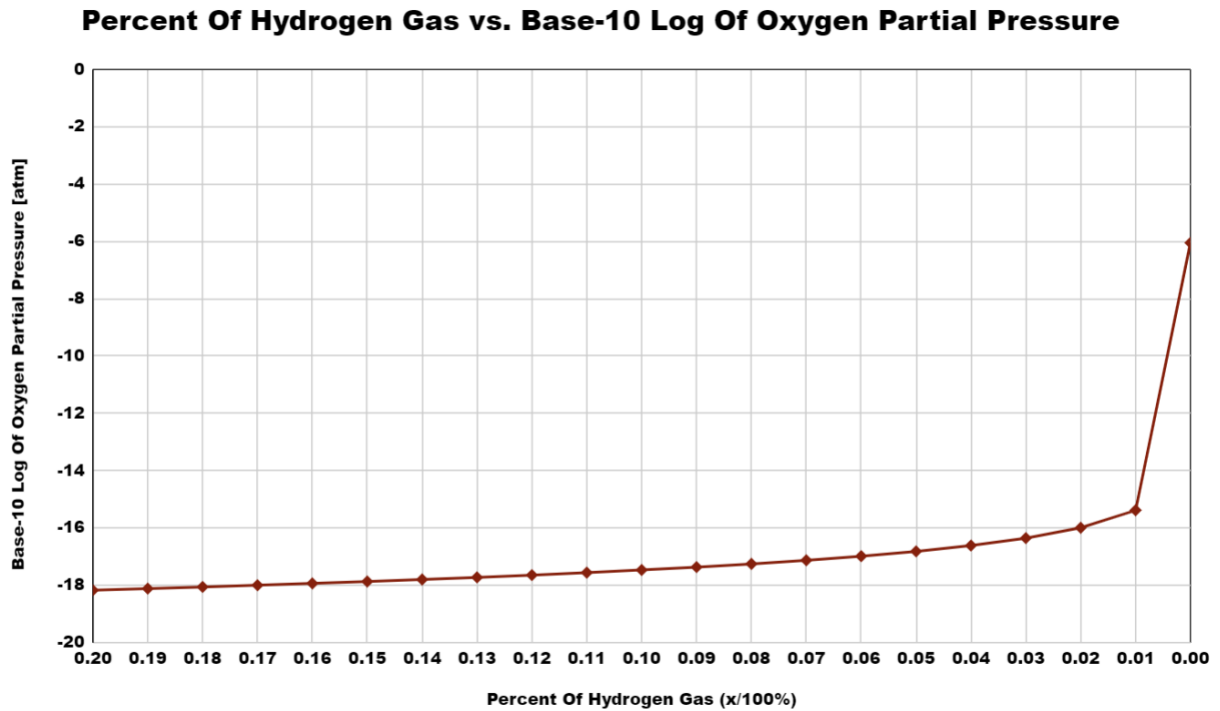


Figure 39: The data from Table 38 graphed out in a Hydrogen Percent vs. Base-10 Log Of Partial Pressure distribution.

7.2.4 Deciding Where To Begin MOE After Flux Is Introduced Into Reaction

In deciding where to introduce the hydrogen flux and where to introduce our molten oxide electrolysis, we had to combine the information of oxygen partial pressure, mole fractions of the products, and the percent of hydrogen. For that to be done, we first had to align the oxygen partial pressures derived in *Table 34* and relate them to hydrogen percentage based on the oxygen partial pressures we derived in *Table 38*. This comparison was conducted in Google Spreadsheets with the formation of the following table:

<u>Mole Fraction Of O₂</u>	<u>Base-10 Log Of O₂ Partial Pressure [No Hydrogen] (atm)</u>	<u>Percent Of Hydrogen (%)</u>	<u>Base-10 Log Of O₂ Partial Pressure [Hydrogen-Argon Introduction] (atm)</u>
0.000	0.00000	20	-18.16793
0.035	-20.17597	19	-18.11257
0.067	-20.17597	18	-18.05494
0.097	-20.17597	17	-17.99482
0.126	-19.36727	16	-17.93167
0.152	-17.53025	15	-17.86531
0.177	-17.05135	14	-17.79520
0.201	-16.62523	13	-17.72077
0.223	-16.42192	12	-17.64128
0.244	-16.28946	11	-17.55586
0.264	-16.18928	10	-17.46334
0.283	-16.10877	9	-17.36219
0.301	-16.04249	8	-17.25034
0.318	-15.98733	7	-17.12490
0.335	-15.94108	6	-16.98163
0.350	-15.90219	5	-16.81400
0.365	-15.86925	4	-16.61096
0.379	-15.84125	3	-16.35187
0.393	-15.82362	2	-15.99046
0.406	-15.79561	1	-15.37880
0.418	-8.05848	0	-6.05094

Table 39: The tabulation of the combination of our previous results from Table 33 and Table 37. This table shows the range of our oxygen partial pressure when we alter the oxygen gas's mole fraction (disregarding H₂) in base-10 logarithmic form. It also shows the hydrogen percentage from 0 to 20% and the corresponding oxygen partial pressure (regarding H₂) in base-10 logarithmic format.

From this combined data we see that the range of hydrogen-based oxygen partial pressure practically nests within our reaction-based oxygen partial pressure. With this knowledge we were adequately able to proceed to our next step, which was overlaying all of the data regarding the products, oxygen partial pressure, and percentage of hydrogen gas into a single graph, as shown below:

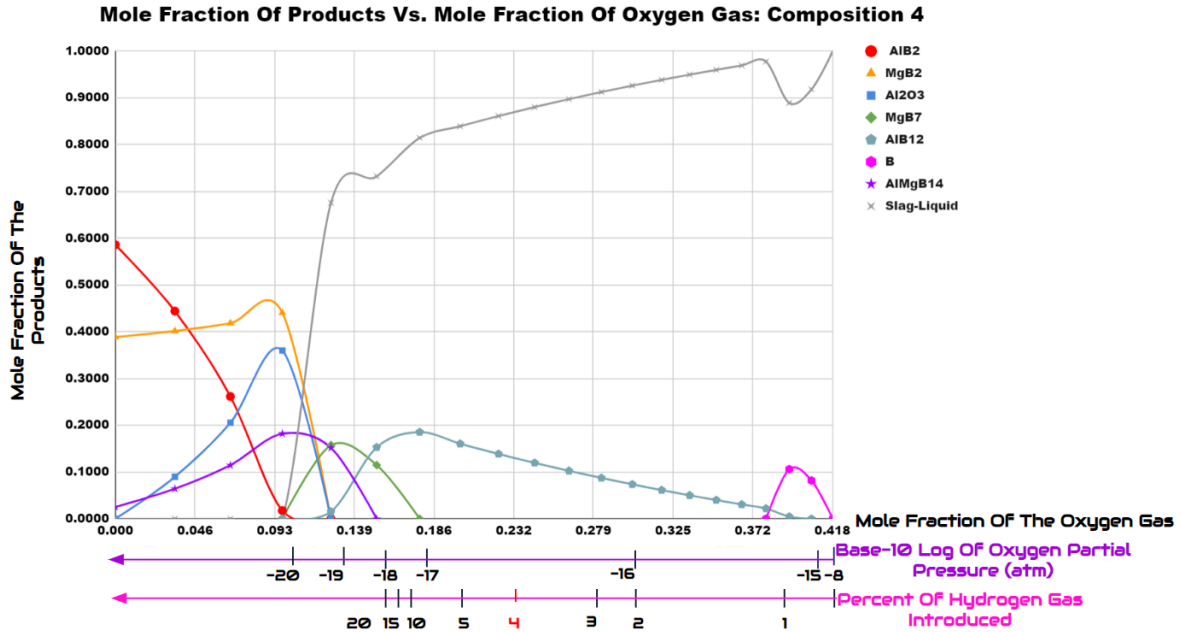


Figure 40: The graph of the accumulated data from the reaction products, oxygen partial pressure, and percent of hydrogen gas introduced.

The purple x-axis shows the base-10 logarithmic approximation of the oxygen partial pressures at the specific locations of the reaction taking place. The pink axis shows the percent of hydrogen gas introduced, and when vertically tracing above that axis, it shows that from introducing X% of hydrogen, Y is the yield of the reaction at that point. The 4% of this axis is highlighted in red as it is the safety limit to ensure the reaction is stabilized and will not explode.

Knowing all this, we proceeded to our final steps in determining the placement of hydrogen gas influx and molten oxide electrolysis. However, one other important piece of information had to be considered. As previously mentioned, “The peak amount of AlMgB₁₄ appeared around the 0.105-mole fraction of oxygen gas.” From our original project objectives, we were to develop the conditions of a MOE reaction to produce pure aluminum magnesium boride. That goal was to produce as much of the boride as possible in its purest state. This “side goal” of producing the maximum amount of this boride and the observed approximate peak amount of AlMgB₁₄ produced would be our end goal for this reaction. Alternatively, put more

simply, we must stop our reaction when we hit the maximum possible yield of aluminum magnesium boride. We also wanted to start our reaction with the hydrogen gas influx and continue it until we reach the near origin or our borides formation. From then we would use the molten oxide electrolysis method to conduct the rest of this reaction until we reach the maximum threshold of this produced boride. We mapped out this very process on top of the graph from *Figure 40*, to show at which points the specific reactions are initiated and terminated. This mapping is shown below:

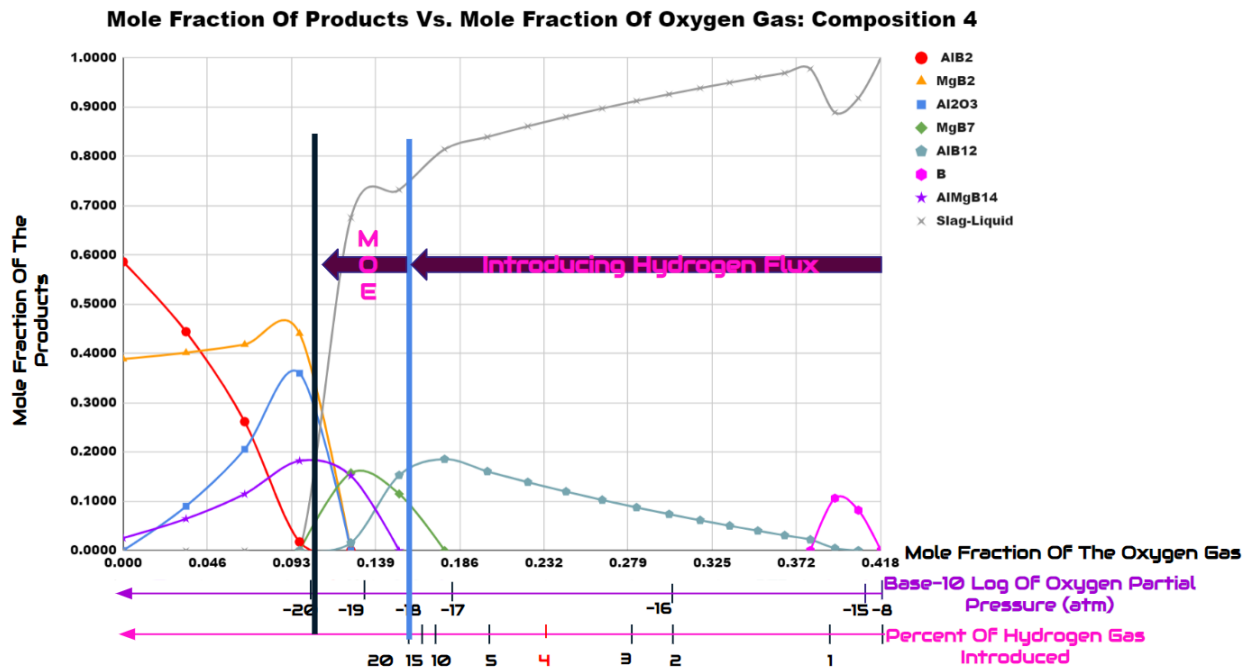


Figure 41: The graph from *Figure 40* with labels of where the hydrogen gas influx would begin and end and where the MOE reaction would begin and end.

The hydrogen gas influx would be introduced at approximately 20%, as shown by the light blue in *Figure 41*. Although this is atypical, theoretically, if the reaction system is exceptionally well maintained, the percentage of hydrogen gas influx could be increased beyond 4% without the implications of damage occurring. From then on, we would proceed with the

MOE reaction until we reach the yield where the maximum amount of our boride is produced. The location is approximately between the mole fraction of **0.093** and **0.139** for O₂.

7.2.5 How Much Energy Is Saved With The Introduction Of Our Hydrogen Flux

To recap, our initial reaction is endothermic, meaning it absorbs energy. Our previous *5.0 Results & Analysis* calculations show the very high energy required to conduct our reaction. The introduction of hydrogen gas would potentially decrease the energy requirement due to the element's exothermic properties. Our group explored this postulation to see how much energy we would save. However, we first needed the exact points at which our reaction begins and ends at each stage. We discussed this in the previous subsection. Hydrogen gas would reduce the oxygen gas mole fraction from **0.418** to **0.152**. The **0.152** mole-fraction of the O₂ location is where the AlMgB₁₄ would dissipate from the products, so we would initiate our MOE process. The end of this process is known to occur at the specific range of 0.093 and 0.139. However, for this calculation, we need to make sure of this endpoint. We know we want to end our reaction where we receive the maximum yield. The calculations to get this location are shown below:

<u>Upper & Lower Limit Of Mole Fraction Of O₂</u>	<u>Upper & Lower Limit Of Mole Of O₂</u>	<u>Mole Of O₂</u>	<u>Total Moles Of AlMgB₁₄</u>	<u>Maximum Boride Yield Mole Fraction Of O₂</u>
0.093	0.1025358324	0.1025358324	3.49E-02	0.1170257299
0.139	0.1614401858	0.1055358324	3.57E-02	
		0.1085358324	3.65E-02	
		0.1115358324	3.76E-02	
		0.1145358324	3.89E-02	
		0.1175358324	4.03E-02	
		0.1205358324	4.16E-02	
		0.1235358324	4.29E-02	
		0.1265358324	4.42E-02	
		0.1295358324	4.56E-02	
		0.1325358324	4.68E-02	
		0.1355358324	4.42E-02	
		0.1385358324	4.11E-02	
		0.1415358324	3.74E-02	
		0.1445358324	2.84E-02	
		0.1475358324	1.91E-02	
		0.1505358324	9.81E-03	
		0.1535358324	5.07E-04	
		0.1565358324	0.00E+00	
		0.1595358324	0.00E+00	
		0.1625358324	0.00E+00	

Table 40: The tabulation for the mole fraction O₂ required to obtain the maximum yield of AlMgB₁₄.

Simulating the same calculations for determining the solids and moles of solids produced over a changing mole of O₂, we obtained the total moles of AlMgB₁₄ from our range of mole

fraction. First, we had to turn the upper and lower limit of our desired mole fraction range into moles of O₂. This was done through the following formula:

$$X_{O_2} = \frac{N_{O_2}}{1-N_{O_2}}$$

Once we obtained the moles of our limits, we set the necessary increments to perform twenty-one calculations. We tabulated those results and then used the moles of oxygen gas that produced the maximum boride yield as the designated end point of our overall reaction process. This mole value was then converted into a mole fraction, and we obtained the endpoint of our MOE reaction to be approximately the oxygen gas mole fraction of **0.117**.

Now we could move on to obtaining the amount of energy saved. This calculation was done using the *Equilib* module on FactSage and was tabulated and equated through Google Spreadsheets. First, we had to calculate the corresponding moles of oxygen gas for our respective points of interest (designated in mole fraction of oxygen gas). This was performed in Google Spreadsheets, as shown below:

<u>Points Of Interest</u>	<u>Mole Fraction Of O₂ Associated With Point</u>	<u>Moles Of O₂ Associated With Point</u>
Where Hydrogen Gas Was Introduced	0.418237	0.718911942
Where MOE Process Was Introduced	0.152347	0.179728000

Table 41: The calculation for the moles O₂ at the three points of interest that would assist in attaining the amount of energy saved.

From *Table 41*, we saw that introducing hydrogen gas flux decreased the oxygen required for our MOE reaction by about **0.539 moles**, approximately **75%** of the total amount of oxygen required without hydrogen. This meant there would be a high likelihood that pure aluminum magnesium boride would be produced and that the energy may be significantly decreased for the MOE portion of the boride production.

The next phase of the calculation required FactSage. In FactSage, we performed three calculations about those above points of interest and their respective mole fraction. Our focus is the change in Gibbs energy, which tells us the energy required to perform the MOE reaction at the temperature of 1600 °C and in correspondence with the specific moles of oxygen required (i.e., 0.719 and 0.180 moles of O₂). Using these thermodynamic values the amount of energy saved was calculated using these thermodynamic values, as shown in *Table 41* below.

<u>Points Of Interest</u>	<u>Mole Fraction Of O₂ Associated With Point</u>	<u>Moles Of O₂ Associated With Point</u>	<u>Energy Required [kJ] To Conduct MOE Reaction If The Amount Of O₂ Present Is...</u>	<u>Total Amount Of Energy Saved [kJ]</u>
Where Hydrogen Gas Was Introduced	0.418237	0.718911942	-843.00	552.08
Where MOE Process Was Introduced	0.152347	0.179728000	-290.92	

Table 42: *The calculation for the amount of energy saved.*

The total energy we could save from this procedure would be approximately **552.08 kJ**. This meant that by introducing an Hydrogen Gas Flux into the reaction, the amount of energy usage to conduct the reaction—and produce the maximum yield of AlMgB₁₄—would be reduced by approximately **65.49%**. This process would be significantly beneficial for the production of aluminum magnesium boride in future commercial practices.

8.0 Future Recommendations

8.1 General Recommendations

Throughout the course of this project, several obstacles were encountered and had to be taken care of. In understanding the problems we faced, a future group can learn how to avoid them. FactSage is a program that has aided tremendously in capturing data and relaying information, however, people who are unfamiliar with the program, or the logistics of Molten Oxide Electrolysis, can run into problems quickly. This section of recommendations will deal with general recommended knowledge one should have beforehand and with specific recommendations when navigating FactSage and the like.

8.1.0 Literature Knowledge

Before embarking on this journey, it was evident that our team did not contain all of the knowledge regarding chemistry, physical metallurgy, thermodynamics, and the like. This was dealt with by conducting literature reviews. It was so successful in elucidating the process of MOE and what actually happens inside the smeltery, that we recommend future groups to continue to expand their knowledge. Even if one is not privy to a certain subject, it could very well be literature that answers questions you may encounter down the road. A series of information was gathered on intricate details of processes, reactions, variables and constants, and more. It was only during the readings that we understood there was a lot to fit in.

The literature we decided to focus on were scientific peer-reviewed articles, published books, video tutorials, PowerPoint instructions, patents, and more. Our recommendation would

be to implement a storage unit dedicated to sources that have been acquired. Organizing the folder by source type, relevance, and other techniques has helped us in tracking our sources and creating a visual road map.

Some recommendations on where to acquire sources include the WPI George C. Gordon Library, Google Scholar, JSTOR, and other similar databases. Some of our sources also came from material manufacturing websites and tutorials. The benefit in collecting sources from different locations is primarily the wide variety of choices. Some databases may only subscribe to a collection of articles and journals whereas a website might be a focused narrative that enlightens other literature.

8.1.1 Division of Roles

Once the project starts taking form either by the acquisition of sources or knowledge regarding MOE, it is essential to be sharing experience and information. We knew that if only one person was dedicated to FactSage and another to gathering sources, not everyone would have the same insight into the project. Therefore, it was core in the foundation of undertaking this project that we split roles, and times when these roles would be switched.

Firstly, we worked in accordance with each WPI quarter denoted as a term. The first term we all focused on compiling a grand list of sources and dividing it into categories of work related material. Once compiled we set roles of creating presentations and documents that would analyze the sources together and post different findings. Another role was to circulate who was producing FactSage calculation, and we established a biweekly system that would last the entire term.

The second term involved the advancement of the FactSage findings into practical terms and into the boride realm. With this, we dedicated longer periods of work and cycling between

who is on FactSage, who is creating and compiling all the figures and calculations, and who is assessing and writing down results. The periods we chose lasted until the end of the third term.

The last term was focused on each team member to focus on their strengths and roles they felt most comfortable with throughout the project. Secondly, the roles were divided once more with the completion of the poster and this report. This was our approach at handling the division of labor throughout the project and it proved to be successful as each one of us are confident in the use of FactSage and the details of the MOE process.

8.1.2 Experimenting With FactSage

Although one may learn a lot from literature, we actually comprehended and retained the knowledge acquired through practical application. Once we delved into FactSage, we were able to compute, visualize, and even predict what would occur in a given reaction at given variables. Being the main program used to complete this project, we recommend a healthy introduction of experimenting with FactSage, as the program constitutes many different operations that can be held, as well as different formulations and tabulations for different thermodynamic principals are acquired.

The same principle applies to any program one may use, or methodology one may take. Acclimating to new things may not be comfortable, but it is after experimenting and toiling with it that one acquires more understanding of it. This was evident with the various different modules offered by FactSage and with the layers of different windows and features in each. In the specific recommendations we give, we discuss the main modules and features used so that although its knowledge is vast, we highlight which features help obtain this information.

8.2 Specific Recommendations

Understanding the immense amount of information regarding MOE and FactSage may cause one to panic and be confused regarding their approach. In this section, we will discuss our specific approach to understanding the main uses of FactSage and the connection to the MOE process.

8.2.0 Equilibrium Module

The first step we undertook was to familiarize ourselves with the “Equilib” module in FactSage. It is this module that accesses the databases for solutions and compounds, as well as allows for multiphase and multicomponent calculations. It also turned out to be the main module used throughout the entire project, as the other two modules of Viscosity and Phase Diagram, carried over calculation from this Equilib module.

The *Equilib* module – Regular Features

- *Equilib* calculates the conditions for multiphase, multicomponent equilibria, with a wide variety of tabular and graphical output modes, under a large range of constraints.
- *Equilib* accesses both compound and solution databases.

Table of contents

Section 1	Table of Contents
Section 2	Opening the Equilib Module
Section 3	From stoichiometric reactions to complex equilibria
Section 4	Simple equilibrium case ($Mg+3Cu_2O+2Fe_3C+Ar$)
Section 5	Additional output using the LIST window
Section 6	HELP with right mouse button
Section 7	Constant volume calculation (Si_4 decomposition)
Section 8	Constant pressure in steps ($MgO+Si$)
Section 9	Non-ideal gas (boiling point of water)

(continued)



Equilib 1.1

www.factsage.com

Figure 42: *The regular features that come within the Equilib module of FactSage.*

In the figure above, a range of simple cases and complex calculations are present within the first training module provided by FactSage. Even the regular features already present an immense amount of information.

The *Equilib* module

Table of contents (continued)

Section 10	<u>Adiabatic combustion, use of the «A» parameter (CH₄ + O₂)</u>
Section 11	<u>Fixed activity calculation (FeS under O₂ partial pressure)</u>
Section 12	<u>Setting up an ideal liquid and adding activity coefficients</u> A part of the Cu-Cr System
Section 13	<u>Standard equilibrium: aqueous solution</u> Leaching arsenic-bearing copper concentrate
Section 14	<u>Standard equilibrium: non-ideal solution Fe-Mn-Si-C</u>
Section 15	<u>Adding slag: An explanation on SlagA, SlagB, Slag?</u>
Section 16	<u>Standard case: Desulphurisation of steel adding CaSi</u>
Section 17	<u>Standard case: Pitzer aqueous with NaCl</u>
Section 18	<u>Heterogeneous equilibria and the phase rule</u>
Section 19	<u>Compound species selection - <i>FactSage</i> 6.4</u>



Equilib 1.2

www.factsage.com

Figure 43: *The regular features that come within the Equilib module of FactSage (cont.).*

The continuation of this list highlights all of the important aspects that relate to MOE. Within the process, the metals and oxides that are melted remain in the liquid phase. However, depending on the operating temperature selected for the given compositions, some material may heat up so much that it transitions to the gas phase. These gasses escape, causing heat loss which alters the energy required and output relating to the specification of the material whether it was induced from the anode, or deposited on the cathode.

Sections 16 and 19 above are core concepts to understand in order to properly select a proper slag and composition to plot onto the Phase Diagram, which ultimately can be translated in the Viscosity module. Doing so in this order and assessing each acquired result allowed for the

maximal understanding of the reaction of the compounds, the products, energy balances, and efficiency level.

8.2.1 Utilize Online Tutorials and Forums

FactSage is a well developed software that has a large database on understanding the intricate intercalculational processes that it can handle. Sometimes knowing all of that information may not be viable. Instead, it is important to understand the MOE process and look up on FactSage any key terms that may have to do with MOE. Surely, we were able to bypass a lot of different tutorials and sources that otherwise were irrelevant to the completion of our project. We reasoned that understanding the fundamental actions and reactions of MOE, and whether FactSage can simulate or clarify the process was much easier than learning everything under the sun about FactSage.

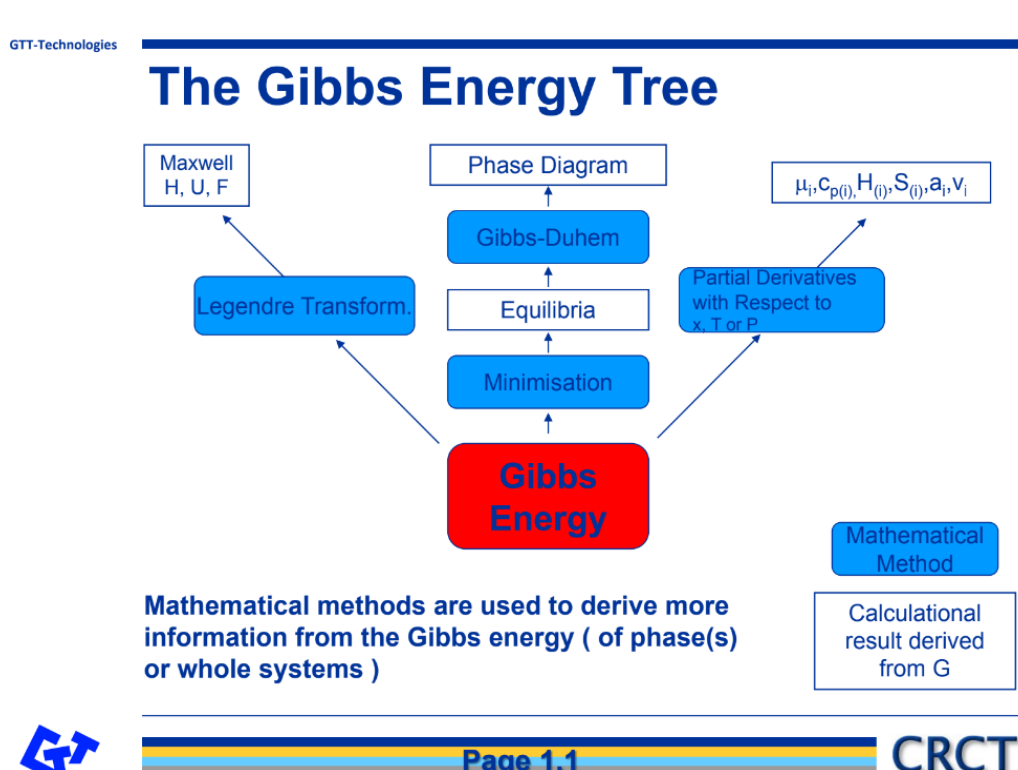


Figure 44: *Mathematical tree delineating the flowchart of FactSage computation.*

Coming across this article, the biggest piece of information was that FactSage, specifically within the Equilib, Viscosity, and Phase Diagram module, uses Gibbs Energy to presume and calculate other variables that are given. Gibbs Energy correlates to many variables and processes, thus eliminating many doubts on what variables should be assigned and which should be filled in via calculation and also elucidating which thermodynamic calculations to use.

1. Utilizing FactSage (FToxid, FSstel databases and modules) calculate:

- a) Melting points (electrolyte + Mn product)
- b) Vapor pressure (electrolyte + Mn product)
- c) Viscosity (electrolyte)
- d) Half-cell and overall cell reaction
- e) Minimum decomposition voltage along with overall and half cell reactions
- f) Pseudo-binary composition-temperature phase diagrams for MnO-electrolyte
- g) Equilibrium product Mn impurity concentrations (Si, Al, Mg, Ca)
- h) Heat required to be removed/added to maintain isothermal electrolysis (taking into account reactants are initially at room temperature and the overall electrolysis reaction)

2. Utilizing info from the report and your FactSage calculations estimate:

- a) Voltage balance
- b) Energy balance
- c) Mass balance
- d) Nominal Anode-Cathode distance
- e) Faradaic efficiency
- f) Energy efficiency
- g) Specific energy (MWh/t)
- h) Cathode current density (A/m^2)
- i) Productivity ($kg/h/m^2$)
- j) Cell capacity (kg/h)

3. Compare your FactSage calculations with what is reported by Winand et al.

Figure 45: *A bullet list of calculations the company Saint Gobain takes interest in Manganese in regards to MOE.*

The calculations listed above come from a list sent by Saint Gobain in which Manganese was the primary metal studied, mentioned earlier in the report. Each and every calculation contains all of the needed variables and required information regarding MOE. Comparing the calculations from the simulation of FactSage to the actual acquired numbers of the Winand experiment, it is guaranteed that your understanding of MOE will increase. It turns out that values are accurately compiled in FactSage. These steps are the same that were taken with borides, and the process was much easier after running trial and error on Manganese calculations.

8.2.2 Directed Experimentation

With these pieces of information, it sets as a guideline for one's experimentation and learning of FactSage, not to restrict the experimenting but to aid in understanding and visualizing the simulation to the practical reality. The final recommendation we want to state is the optimization in selected compositions. It is evident that FactSage allows for many reactions to take place, sometimes even ones that may not actualize in reality.

Again, in no way do we want to limit the expansive nature of FactSage, we want to elucidate where we stumbled and how we have learned to adapt. From certain reactions and compositions that one may input, certain outcomes may prove to be trivial. Not all scenarios will result in the desired outcomes. And it is from trial and error that we recommend experimenting with compositions and different initial values. After gathering information, notice certain trends that are exhibited by different compositions.

In this way, you increase the optimization of selecting the oxides that provide the most efficient and realistic reactions. However, sometimes it may not be so clear as to which oxide over another should be chosen. In this way, our recommendation really is to limit the random plugging and checking, and focus on logical and chemically sound compositions that previous literature expounds upon. Also, focus on connecting each oxide with benefits that relate to industrial applications. Engaging in a multi-perspective view of the project this way enables a better understanding of the process abstractly and practically.

References

- Abdelrahman, M., Elsamny, M. M., Abd El-Ghany, M. A., & Kandil, U. F. (2021). A comprehensive review on metal borides: Synthesis, properties, and applications. *Journal of Alloys and Compounds*, 875, 159849. <https://doi.org/10.1016/j.jallcom.2021.159849>.
- Ahn, J., Kim, H., & Kim, H. (2019). Electrochemical properties of graphite anodes and cathodes for lithium-ion batteries in molten Li₂O-LiCl. *Journal of Alloys and Compounds*, 782, 1122-1127.
- Allanore, A., Yin, L., & Sadoway, D. R. (2013). A new anode material for oxygen evolution in molten oxide electrolysis. *Nature*, 497(7449), 353–356. <https://doi.org/10.1038/nature12134>.
- Allanore, A. (2014). Features and Challenges of Molten Oxide Electrolytes for Metal Extraction. *Journal of The Electrochemical Society*, 162(1). <https://doi.org/10.1149/2.0451501jes>.
- American Elements. (2017, June 13). *Aluminum Magnesium Boride*. American Elements. <https://www.americanelements.com/aluminum-magnesium-boride>.
- Bhabha Atomic Research Centre. *Production of Zirconium diboride (ZrB₂) powder and Fabrication of high-density ZrB₂ shapes*. Government of India Department of Atomic Energy. https://www.barc.gov.in/technologies/zirconium_diboride/index.html.
- Boston Metal. (2023, March 15). *Molten Oxide Electrolysis for steel decarbonization*. Boston

Metal. <https://www.bostonmetal.com/transforming-metal-production/>.

Chaput, K. J., Lee, C., & Thomas, S. (2019). Boride-based ceramics: Synthesis, properties and applications. *Journal of Materials Science*, 54(9), 7249-7271.

Corrosionpedia. *Current Efficiency*. Corrosionpedia.

<https://www.corrosionpedia.com/definition/355/current-efficiency#:~:text=Current%20efficiency%20describes%20the%20efficiency>.

Evans, J. W. (2003). Metal production: Electrometallurgy. *Encyclopedia of Materials: Science and Technology*, 1–12. <https://doi.org/10.1016/b0-08-043152-6/01888-x>.

fxSolver. *Paschen's Law*. fxSolver.

<https://www.fxsolver.com/browse/formulas/Paschen%27s+Law>.

Gao, Y., Zeng, L., & Zhang, H. (2020). Progress in research on biomedical applications of borides. *Journal of Materials Science & Technology*, 40, 1-10.

<https://doi.org/10.1016/j.jmst.2019.08.035>.

Gomes, J. M. & Uchida, K. (1973, November 27). Electrolytic Preparation Of Titanium Zirconium Diborides Using A Molten, Sodium Salt Electrolyte.

Government of India Department of Atomic Research. Bhabha Atomic Research Centre.

Production of Zirconium diboride (ZRB2) powder and Fabrication of high density zrb2 shapes. https://www.barc.gov.in/technologies/zirconium_diboride/index.html.

- Gupta, A., Singh, D., & Jain, P. (2019). Molten oxide electrolysis: A promising technology for the synthesis of borides. *Journal of Alloys and Compounds*, 800, 174-183.
doi:10.1016/j.jallcom.2019.05.358.
- Hine, F. (1985). *Electrode Processes and Electrochemical Engineering*. New York: Plenum Press.
- Huang, S., Wu, J., Wang, Z., & Zhang, Y. (2019). Electrochemical Extraction of Zirconium from Zirconium Oxide Using Molten Salt Electrolysis. *Journal of Sustainable Metallurgy*, 5(1), 76-83. <https://doi.org/10.1007/s40831-018-0209-9>.
- Huda, M. N., Ali, J., & Amin, R. (2019). Boride-based materials for thermoelectric applications: A review. *Renewable and Sustainable Energy Reviews*, 103, 468-483.
<https://doi.org/10.1016/j.rser.2018.12.033>.
- Jarrett, N. (1987). United States Extractive Metallurgy – The 80's and Beyond. *Metall. Trans. B*, vol. 18B, no. 6, pp. 289–313.
- Kanitkar, A., Ghosh, S., & Singh, J. P. (2021). Mechanical properties of zirconium diboride synthesized by spark plasma sintering. *Journal of Materials Research and Technology*, 10, 1822-1832.
- Kellner, J. D. (1975, April 29). Process For Electrodepositing Titanium DiBoride From Fused Salts.
- Kjølseth, C., Bakken, E., Grande, T., Wiik, K., & Dahl, J. (2019). Electrochemical reduction of zirconia to produce nanostructured zirconium diboride in molten calcium chloride. *Journal of The Electrochemical Society*, 166(6), D123-D131. doi:10.1149/2.0561906jes.
- Kumar, A., Yadav, S., Bhattacharya, J., & Kim, H. S. (2018). Efficient metal recovery from electronic waste by a novel electrochemical process. *Waste Management*, 76, 290-298.

<https://doi.org/10.1016/j.wasman.2018.03.041>.

Kuramoto, K., Ishikawa, H., & Okada, T. (2018). Electrolysis of MgCl₂ in Graphite Anode. *ECS Transactions*, 85(13), 61-67.

Lee, D., Kim, D. Y., Kim, H. J., Kim, D. Y., & Kim, K. H. (2019). Tribological performance of boride coatings in automotive engine components: A review. *Journal of Mechanical Science and Technology*, 33, 4991-5015. <https://doi.org/10.1007/s12206-019-0935-5>.

Li, M., Huang, X., Yang, X., Zhu, C., Ma, Y., & Wang, Z. (2020). The corrosion behavior of TiB₂-coated carbon steel in chloride and sulfate solutions. *Journal of Materials Science: Materials in Electronics*, 31(10), 7324-7334.

Li, Y., Zhang, L., Wu, Y., Chen, G., Li, J., & Li, X. (2017). Molten Oxide Electrolysis for the Extraction of Titanium and Other Reactive Metals. *Metallurgical and Materials Transactions B*, 48(5), 2949-2956. <https://doi.org/10.1007/s11663-017-1034-2>.

Liu, X., Huang, L., Xue, Q., & Zhao, B. (2020). Effects of Hydrogen Gas on Molten Oxide Electrolysis of Aluminum Oxide. *Metallurgical and Materials Transactions B*, 51(6), 3186-3193. <https://doi.org/10.1007/s11663-020-01956-7>.

Malyshev, V., Gab, A., Shakhnin, D., Popescu, A.-M., Constantin, V., & Olteanu, M. (2009).

HIGH TEMPERATURE ELECTROCHEMICAL SYNTHESIS OF MOLYBDENUM,
TUNGSTEN AND CHROMIUM BORIDES FROM HALIDE-OXIDE MELTS.

ACADEMIA ROMÂNĂ, 55(4), 233–238.

Mathew, P., George, J., Mathews, S. T., & Kurian, P. J. (2019). Experimental verification of modified Paschen's Law in DC glow discharge Argon Plasma. *AIP Advances*, 9(2),

025215. <https://doi.org/10.1063/1.5086246>.

Miroshnichenko, I., Fayeulle, S., & Dubois, J. L. (2021). ZrB₂ production by molten oxide

electrolysis. *Journal of Materials Science*, 56(12), 7674-7687.

<https://doi.org/10.1007/s10853-021-05845-0>.

Morita, K., Arita, R., & Kobayashi, H. (2020). Molten oxide electrolysis for sustainable metals extraction. *Nature Reviews Materials*, 5(7), 523-537.

<https://doi.org/10.1038/s41578-020-0202-6>.

Nakanishi, Brad, and Elizabeth Murphy. "Chemical Metallurgy." *Boron*, vol. 3, no. 19, 15 May 2015.

Nies, N. P. (1960). Preparation of Boron by Fused Salt Electrolysis. *Journal Of The*

Electrochemical Society, 107(10), 817–820.

Norton Company. (1955, July 18). Electrolytic extraction of pure metal from its carbide.

Paul, F., Theopold, K., & Langley, R. (2020, September 8). 23.4: *Electrometallurgy*. Chemistry

LibreTexts. [https://chem.libretexts.org/Courses/University_of_Missouri/MU%3A_133_0H_\(Keller\)/23%3A_Metals_and_Metallurgy/23.4%3A_Electrometallurgy#:~:text=Sodium%2C%20aluminum%2C%20and%20magnesium%20are,in%20the%20purification%20of%20copper](https://chem.libretexts.org/Courses/University_of_Missouri/MU%3A_133_0H_(Keller)/23%3A_Metals_and_Metallurgy/23.4%3A_Electrometallurgy#:~:text=Sodium%2C%20aluminum%2C%20and%20magnesium%20are,in%20the%20purification%20of%20copper).

Prasad, S. (2016). Entropic Heat Effects In Aluminum Electrolysis Cells With Inert Anode.

Metall. Mater. Trans. B, vol. 47, no. 2, pp. 1274–1279.

Royal Society Of Chemistry. *Manganese*. Periodic Table.

<https://www.rsc.org/periodic-table/element/25/manganese>.

Sindebad, S. J. (1956, April 10). Production Of Metal Borides By Fused Salt Electrolysis.

Sridhar, V., Kumar, V. R., & Anthonysamy, S. (2015). Molten oxide electrolysis—a route for synthesis of ceramic borides. *Journal of the American Ceramic Society*, 98(4), 945-959.

Svendsen, A., & Westlund, E. (2021, March 18). *Big Blue Technologies developing*

carbothermal reduction technology for magnesium metal production. *Light Metal Age*

Magazine. [https://www.lightmetalage.com/news/industry-news/magnesium/big-blue-](https://www.lightmetalage.com/news/industry-news/magnesium/big-blue-Technologies-developing-carbothermal-reduction-technology-for-magnesium-metal-production/)

[Technologies-developing-carbothermal-reduction-technology-for-magnesium-metal-production/](https://www.lightmetalage.com/news/industry-news/magnesium/big-blue-Technologies-developing-carbothermal-reduction-technology-for-magnesium-metal-production/).

Trunnano. *Aluminum Magnesium Boride BAM AlMgB14 Powder*. Boride Powder.

<https://www.nanotrunk.com/ternary-boron-alloy-powder-bam-aluminum-magnesium-boride-almgbl4-powder-p00270p1.html>.

Urquhart, James. (2020, January 27). *Greener, Cleaner Steel*. *Chemistry World*.

<https://www.chemistryworld.com/news/greener-cleaner-steel-/6155.article>.

Wang, D., Wu, Q., & Zhang, Y. (2020). Effect of Hydrogen on the Molten Oxide Electrolysis of Iron Ore. *Metallurgical and Materials Transactions B*, 51(4), 1879-1887.

<https://doi.org/10.1007/s11663-020-01862-z>.

Wang, Q., Gao, S., Xing, X., Wang, Y., Li, H., Ma, W., & Zhang, L. (2021). Research progress

on surface modification of steel with metal borides. *Surface Engineering*, 37, 1-17.

<https://doi.org/10.1080/02670844.2020.1820808>.

Wang, Z., Chen, J., Wang, J., & Li, J. (2018). Progress and challenges of metal boride materials in electronics. *Journal of Materials Science & Technology*, 34, 2211-2219.

<https://doi.org/10.1016/j.jmst.2018.05.018>.

Wang, Z., Huang, J., Yang, J., He, M., & He, X. (2020). Mechanical and thermal properties of transition metal borides: A review. *Journal of Alloys and Compounds*, 846, 156369.

<https://doi.org/10.1016/j.jallcom.2020.156369>.

Wei, W., Han, Y., Xu, H., & Sun, Z. (2019). Molten oxide electrolysis for sustainable metals production: A review. *Applied Energy*, 240, 717-732.

<https://doi.org/10.1016/j.apenergy.2019.02.080>.

Wills, B. A., & Finch, J. A. (2016). Introduction. *Wills' Mineral Processing Technology*, 1-27.

<https://doi.org/10.1016/b978-0-08-097053-0.00001-7>.

Winard, R., Fontana, A., Segers, L., Hannaert, P., & Lacave, J. (1977). Molten salt electrolysis in metal production. *The Institution Of Mining And Metallurgy*, 42-50.

Zhang, X., Yu, H., & Feng, Y. (2017). Synthesis of transition metal borides: A review. *Progress in Materials Science*, 88, 467-498. <https://doi.org/10.1016/j.pmatsci.2017.06.003>.

Zhang, Y., Li, Z., Li, W., Li, Y., Yang, L., Liu, W., & Li, X. (2017). Electrochemical Extraction of Molybdenum from Spent Hydrotreating Catalysts Using Molten Oxide Electrolysis. *Industrial & Engineering Chemistry Research*, 56(10), 2617-2625.

<https://doi.org/10.1021/acs.iecr.6b04853>.

Zhang, Y., Ma, S., Chen, J., & Wang, L. (2019). Reduction of Titanium Dioxide by Hydrogen in Molten Salt Electrolysis. *Metallurgical and Materials Transactions B*, 50(4), 1621-1628.

<https://doi.org/10.1007/s11663-019-01505-7>.

Appendix A: Manganese MOE

Figures

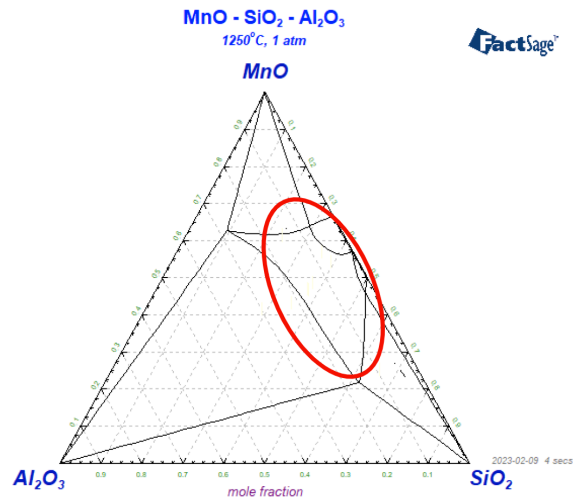


Figure 5: A base ternary phase diagram, which we graphed, of MnO, SiO₂, and Al₂O₃

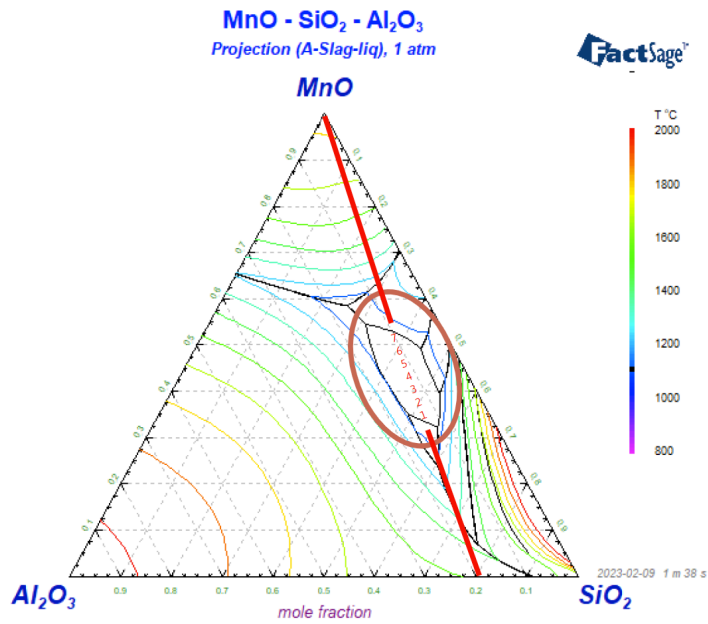


Figure 6: Liquidus projection we constructed of MnO, SiO₂, and Al₂O₃

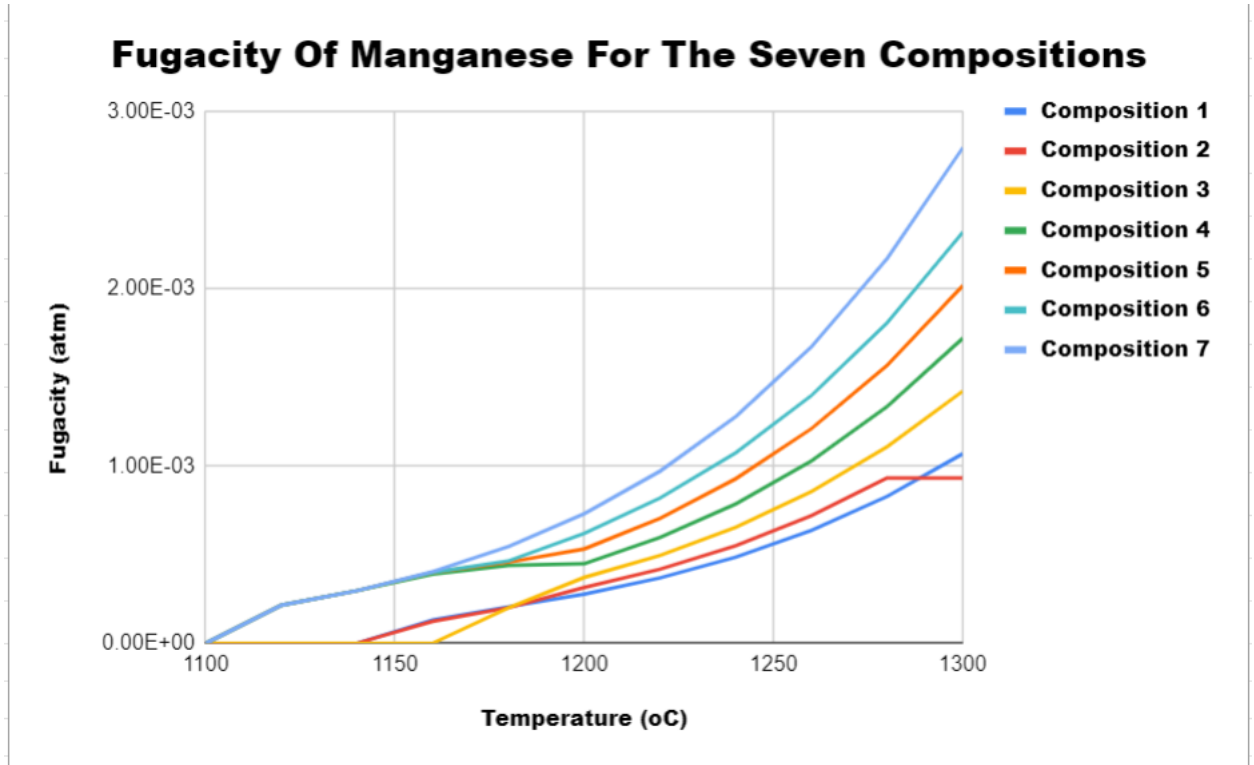


Figure 7: Fugacity Trend Of All Seven Compositions Of MnO-SiO₂-Al₂O₃ Graphed Out In A Temperature Vs. Fugacity Graph

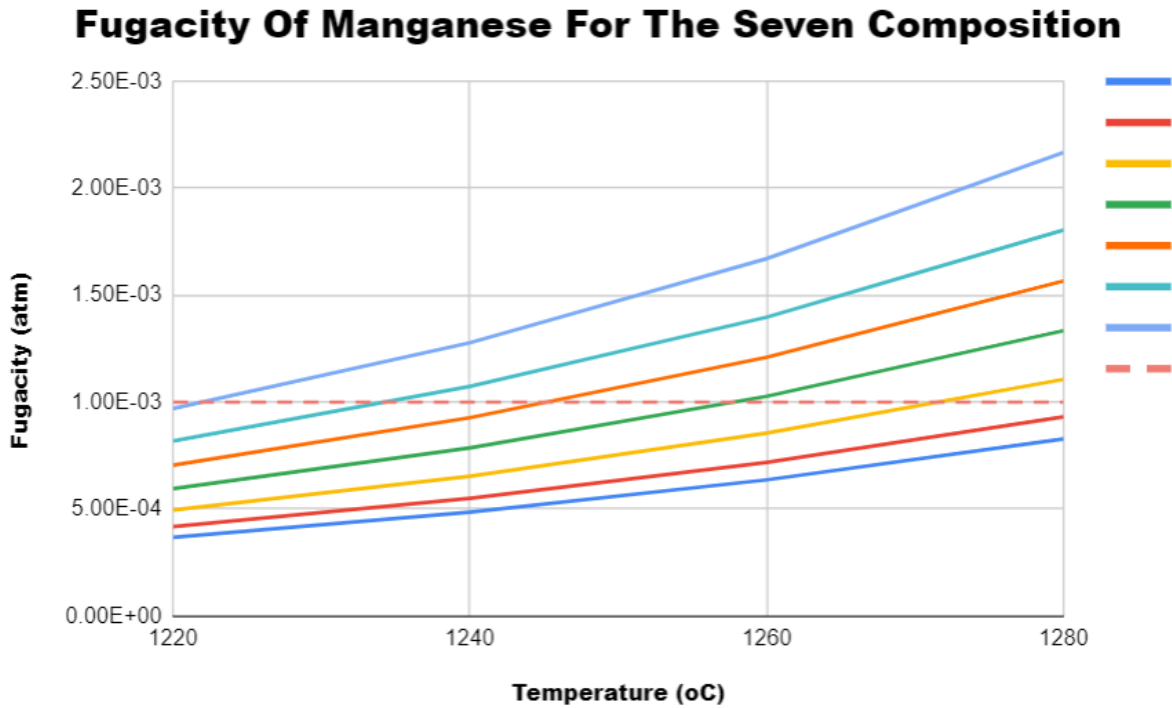


Figure 8: Focused Fugacity Trend Of All Seven Compositions Of MnO-SiO₂-Al₂O₃ Graphed Out In A Temperature Vs. Fugacity Graph. The Dotted Line Shows The Fugacity Value Of 10⁻³ atm.

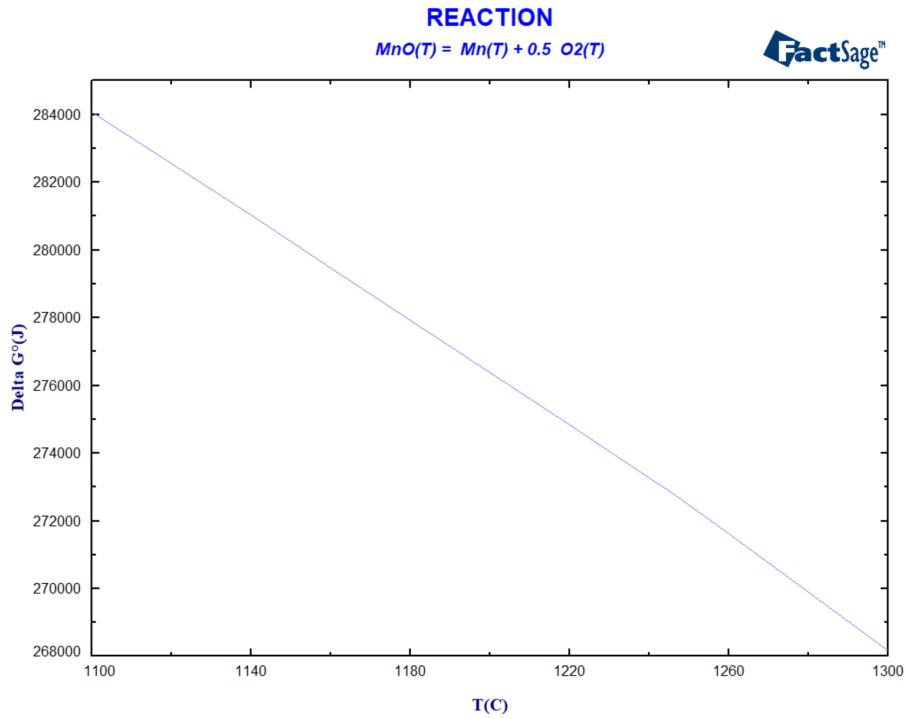


Figure 9: The Overall Reaction Energy Trend Graph from 1100 to 1300 °C. This graph is displayed as Temperature (in degrees Celsius) versus the change in Gibbs Energy (J).

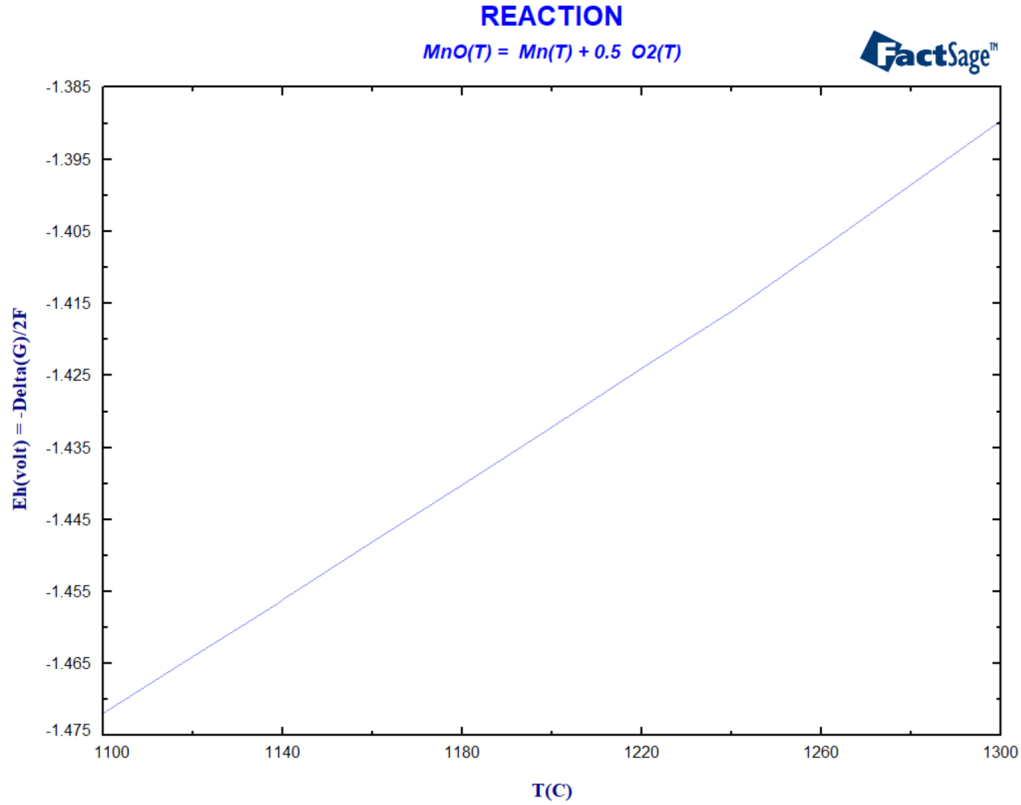


Figure 10: The Overall Reaction Potential Trend Graph from 1100 to 1300 °C. This graph is displayed as Temperature (in degrees Celsius) versus the Voltage Requirement (V).

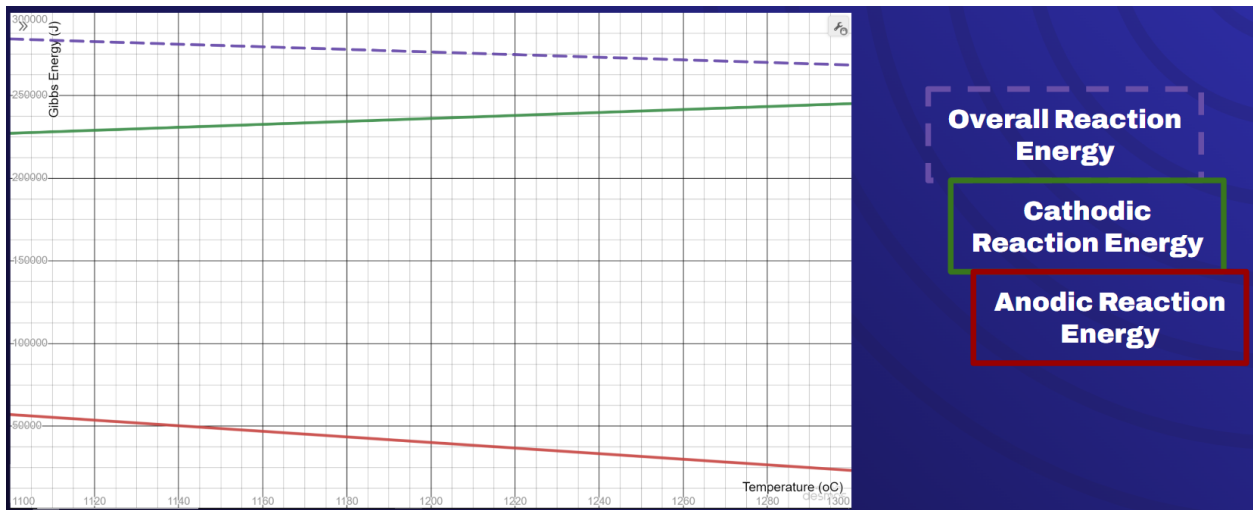


Figure 11: The Overall Reaction, Cathodic Reaction, and Anodic Reaction Energy Functions for the Manganese reaction graphed vs. Temperature.

Potentials Of Overall Reaction, Cathodic Reaction, & Anodic Reaction

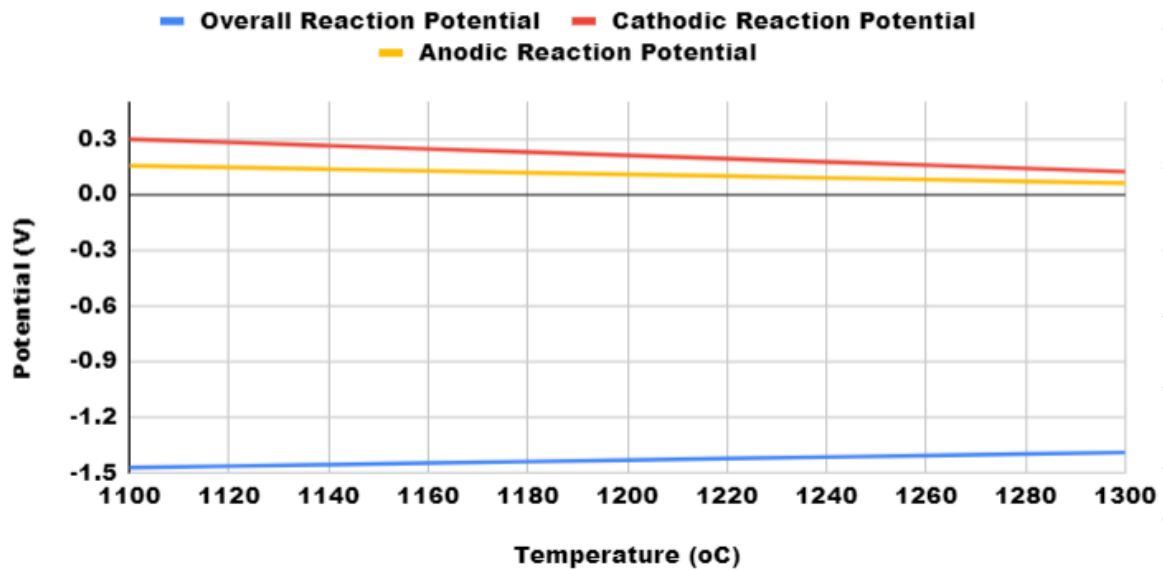


Figure 12: The Overall Reaction, Cathodic Reaction, and Anodic Reaction Potential Functions for the Manganese reaction vs. Temperature.

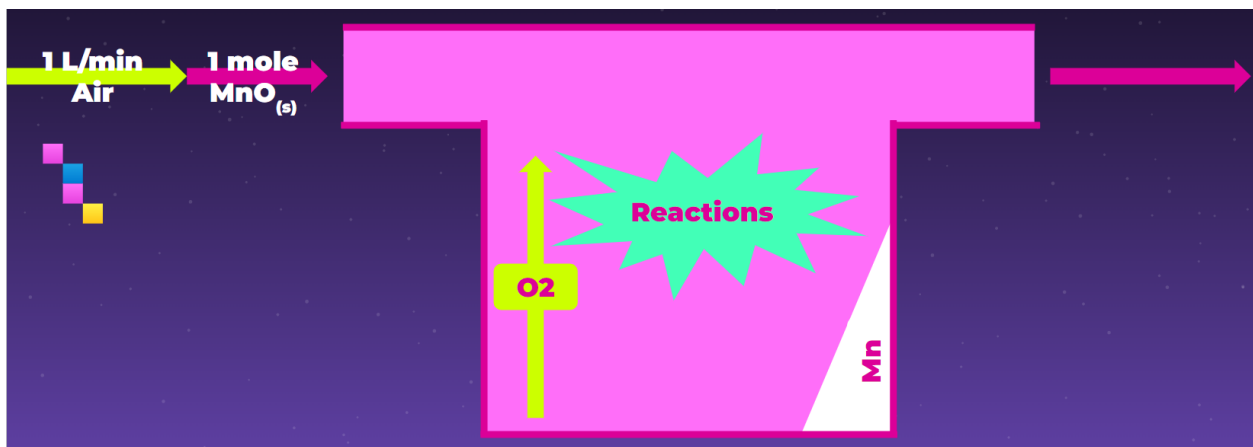


Figure 13: An illustration of what is occurring in the electrolytic cell. On the left-hand side, it shows 1 mole of solid-phase MnO being inserted into the cell alongside air at a rate of 1 liter/minute. Inside the cell (the t-shaped figure) is where the reactions occur; where ultimately, Manganese would subside to the bottom of the cell, and oxygen gas would be produced and rise to the top. All of the gasses, including oxygen gas, leave the system through the outlet shown on the right-hand side of the figure.

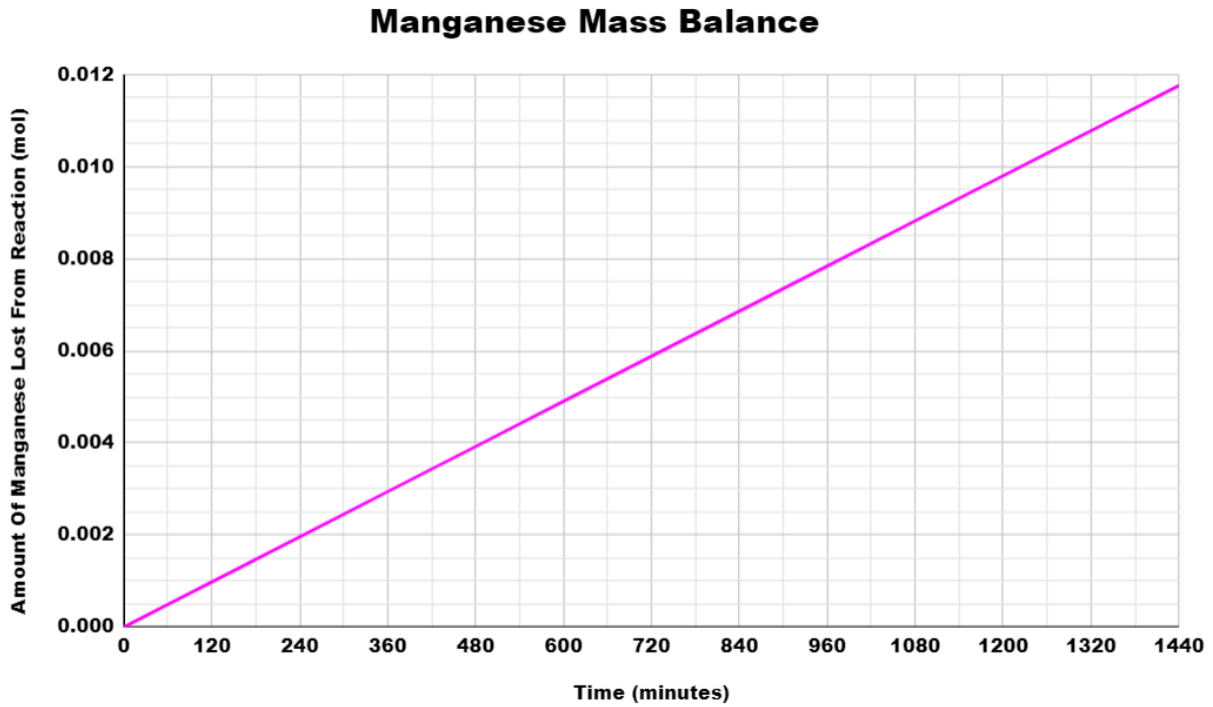


Figure 14: The total Mass Balance of Mn graphed in terms of Fugacity rate (atm/min) vs. time (min). The graph is mapped out over a full day in terms of minutes.

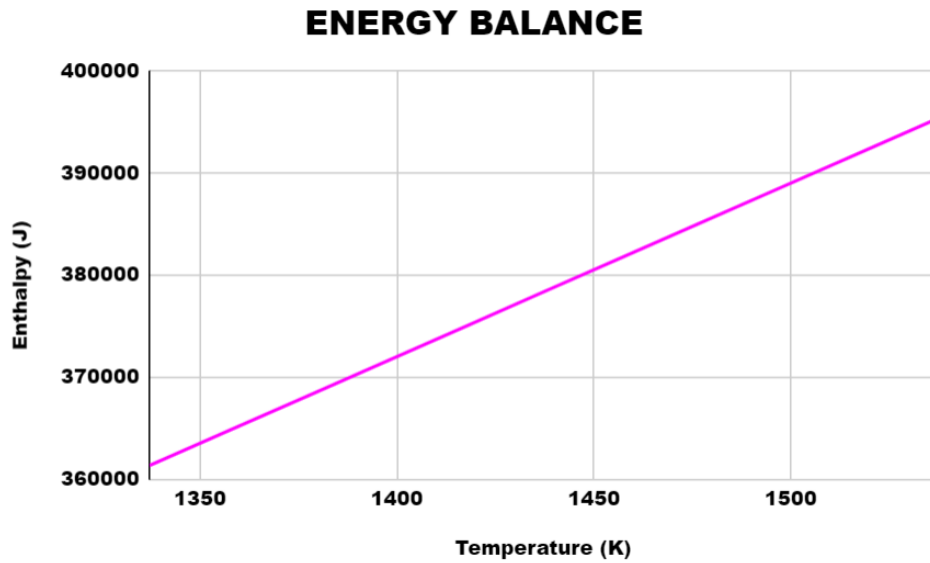


Figure 15: The total Energy Balance of Mn graphed in terms of enthalpy (kJ) vs. temperature (K).

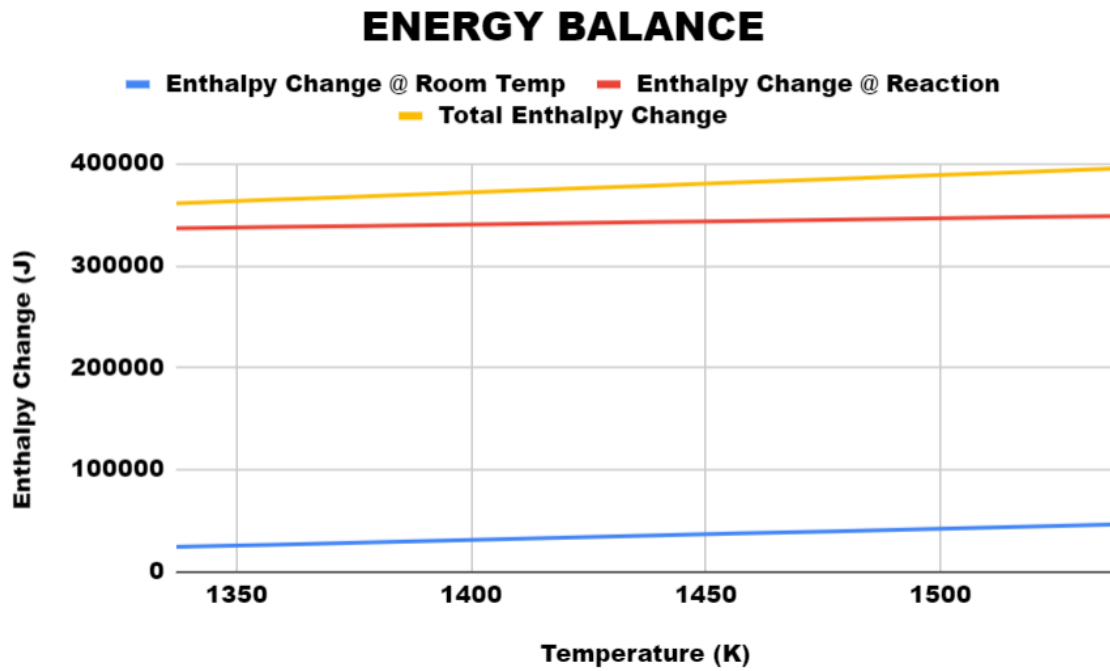


Figure 16: The Energy Balances of Mn graphed in terms of enthalpy (kJ) vs. temperature (K). This shows the enthalpy changes at each stage of the reaction, as well as that for the total reaction.

Tables

	Temperature	MnO	Al ₂ O ₃	SiO ₂
1	1154.74	0.345767	0.177504	0.476729
2	1163.3	0.378524	0.161125	0.46035
3	1174.49	0.403093	0.158733	0.438175
4	1179.57	0.43858	0.148408	0.413012
5	1179.34	0.468607	0.140813	0.390579
6	1175.43	0.493176	0.135948	0.370877
7	1159.2	0.528663	0.128096	0.343241

Table 1: Melting point and mole fractions of MnO, SiO₂, and Al₂O₃

VAPOR PRESSURE OF ALL POTENTIAL COMPOUNDS												
Composition	Electrolyte Compound Mole Fraction MnO: 0.XXX SiO ₂ : 0.XXX Al ₂ O ₃ : 0.XXX	Temperature (1100 to 1300 oC)										
		1100	1120	1140	1160	1180	1200	1220	1240	1260	1280	1300
Vapor Pressure or Fugacity (atm) of Manganese												
1	0.345767 0.476729 0.117504	3.37E-11	5.98E-11	1.04E-10	1.31E-04	2.06E-04	2.76E-04	3.68E-04	4.86E-04	6.36E-04	8.27E-04	1.07E-03
2	0.378534 0.46035 0.161125	3.37E-11	5.98E-11	1.04E-10	1.23E-04	2.00E-04	3.15E-04	4.18E-04	5.50E-04	7.18E-04	9.31E-04	1.20E-03
3	0.403093 0.438175 0.158733	3.69E-11	6.54E-11	1.14E-10	1.95E-10	2.00E-04	3.71E-04	4.94E-04	6.54E-04	8.55E-04	1.11E-03	1.42E-03
4	0.43858 0.413012 0.148408	1.64E-10	2.15E-04	2.96E-04	3.90E-04	4.39E-04	4.48E-04	5.96E-04	7.83E-04	1.03E-03	1.33E-03	1.72E-03
5	0.468607 0.390579 0.140813	1.64E-10	2.15E-04	2.96E-04	3.99E-04	4.57E-04	5.33E-04	7.05E-04	9.27E-04	1.21E-03	1.57E-03	2.02E-03
6	0.493176 0.370877 0.135948	1.64E-10	2.15E-04	2.96E-04	3.99E-04	4.64E-04	6.19E-04	8.18E-04	1.07E-03	1.40E-03	1.81E-03	2.32E-03
7	0.538663 0.343241 0.128096	1.64E-10	2.15E-04	2.96E-04	4.04E-04	5.45E-04	7.30E-04	9.70E-04	1.28E-03	1.67E-03	2.17E-03	2.79E-03

Table 2: Vapor Pressure/Fugacity Of Seven Compounds Of MnO-SiO₂-Al₂O₃ Displaying Largest-Fugacity Compound (Manganese) From 1100°C To 1300°C

Temp.	1	2	3	4	5	6	7
900	106.325	107.403	110.805	114.718	119.345	125.454	131.331
1000	40.933	41.323	42.591	44.042	45.78	48.115	50.572
1100	18.114	18.278	18.824	19.444	20.194	21.214	22.346
1200	8.957	9.034	9.297	9.594	9.956	10.452	11.022
1300	4.845	4.885	5.024	5.18	5.372	5.634	5.944
1400	2.821	2.844	2.923	3.011	3.12	3.27	3.45
1500	1.746	1.76	1.808	1.861	1.927	2.018	2.128
1600	1.138	1.147	1.178	1.211	1.253	1.312	1.382
1700	0.774	0.781	0.801	0.823	0.852	0.89	0.938
1800	0.547	0.551	0.566	0.581	0.601	0.628	0.661
1900	0.399	0.402	0.413	0.423	0.437	0.457	0.481
2000	0.299	0.302	0.309	0.317	0.328	0.342	0.359

Table 3: Raw data of the viscosity of selected compositions at a range of temperatures from the Mn MOE reaction.

OVERALL REACTION ENERGY	
Temperature (oC)	Gibbs Energy (J)
1100	284050.2
1120	282532.8
1138.85	281101.7
1140	281012.8
1160	279466.3
1180	277918.3
1200	276368.7
1220	274817.5
1240	273264.8
1245.85	272810.3
1260	271598.3
1280	269883.8
1300	268168

Table 4: The Table of the Overall Reaction Energy, with a temperature range from 1100°C To 1300°C and the corresponding change in Gibbs Energy for each temperature. The difference in Gibbs Energy of the desired Operating Temperature is highlighted at the bottom of the table.

NERNST EQUATION		VOLTAGE REQUIREMENT				
$\Delta G_0 = -n * F * E_{cell}$		Temperature (oC)	Gibbs Energy [ΔG_0] (J)	Number Of Moles [n] (mol)	Faraday's Constant [F] ($C * mol^{-1}$)	Voltage Requirement [Ecell] (V)
$\Delta G_0 * (-n * F) = E_{cell}$		1260	271598.3	2	96485.3321	-1.40745901

Table 5: The Voltage Requirement is split into two tables. The first table shows the Nernst Equation and its rearranged form to calculate the voltage requirement of the electrolytic cell at the operating temperature. The second table shows the change in Gibbs Energy at 1260 °C, the number of moles or electrons transferred as 2, and the Faraday's constant, all used to calculate the voltage requirement.

OVERALL REACTION ENERGY		OVERALL REACTION ENERGY FORMULA			
Temperature (oC)	Gibbs Energy (J)	Change In Entropy [Δs] (J/(mol*K))		Change In Enthalpy [ΔH] (J/mol)	
1100	284050.2	Formula	Value	Formula	Value
1120	282532.8	$\Delta s = \text{SLOPE}(C4:C16,B4:B16)$		$\Delta H = \text{INTERCEPT}(C4:C16,B4:B16)$	
1138.85	281101.7	-78.82671296		370883.398	
1140	281012.8	OVERALL REACTION ENERGY FORMULA			
1160	279466.3	$y = 370883.398 - 78.82671296 * x$			
1180	277918.3	$\Delta G_0 = 370883.398 - (78.82671296 * T)$			
1200	276368.7	OVERALL REACTION POTENTIAL FORMULA			
1220	274817.5	Nernst Equation	Number Of Moles [n] (mol)	Faraday's Constant [F] ($C * mol^{-1}$)	
1240	273264.8	$\Delta G = y$	$\Delta H = b$		
1245.85	272810.3	$T = x$	$\Delta s = m$		
1260	271598.3	$\Delta G / (-n * F) = E$		2	96485.3321
1280	269883.8	OVERALL REACTION POTENTIAL FORMULA			
1300	268168	$E_0 = -1.92196777 + (0.00040849 * T)$			

Table 6: The calculations made to obtain the Overall Reaction Energy and Potential formulas for the Manganese reaction.

CATHODIC REACTION ENERGY FORMULA		CATHODIC REACTION POTENTIAL FORMULA		
Change In Entropy [Δs] (J)	Change In Enthalpy [ΔH] (J)	Nernst Equation	Number Of Moles [n] (mol)	Faraday's Constant [F] ($C * mol^{-1}$)
168.7	242600	$\Delta G / (-n * F) = E$	2	96485.3321
CATHODIC REACTION ENERGY FORMULA		CATHODIC REACTION POTENTIAL FORMULA		
$\Delta G_1 = 242600 - (168.7 * T)$		$E_1 = 1.25718891 - (8.74226148E-4 * T)$		

Table 7: The calculations made to obtain the Cathodic Reaction Energy and Potential formulas for the Manganese reaction.

ANODIC REACTION ENERGY FORMULA		ANODIC REACTION POTENTIAL FORMULA		
Formula		Nernst Equation	Number Of Moles [n] (mol)	Faraday's Constant [F] (C ² mol ⁻¹)
$\Delta G_2 = \Delta G_0 - \Delta G_1$		$\Delta G / (-n * F) = E$	2	96485.3321
ANODIC REACTION ENERGY FORMULA		ANODIC REACTION POTENTIAL FORMULA		
$\Delta G_3 = 128283.398 + (89.8738287 * T)$		$E_1 = 0.66478186 - (4.65738298E-4 * T)$		

Table 8: The calculations made to obtain the Anodic Reaction Energy and Potential formulas for the Manganese reaction.

MASS BALANCE OF Mn							
Composition 4							
$0.43858MnO - 0.413012SiO_2 - 0.1484084I_2O_3$							
Formula	Air Flow Rate [V_dot] (L/min)	Air Flow Rate (mol/min)	Total Time (l day in min)	Operational Temperature [T] (oC)	Operational Temperature [T] (K)	Fugacity of Mn @ Operational Temperature [P] (atm)	Fugacity Rate of Mn [n_dot] (mol/min)
$n_{Mn} = (n_{dot}) * (t)$	1	0.04464285714	1440	1260	1533.15	0.0010276	$n_{dot} = (P * V_{dot}) / (R * T)$ 0.000008168152042
Manganese Mass Balance Formula							
$n_{Mn} = (8.168152042E-6) * (t)$							

Table 9: The calculations made to obtain the Fugacity rates of Manganese over time for the Mass Balance of Mn.

ENERGY BALANCE		
Formula	Gibbs Energy [ΔG] (J)	Entropy [Δs] (J/K)
$\Delta H = \Delta G + (T * \Delta s)$	134285.9	169.834
ENERGY BALANCE FORMULA		
$\Delta H = 134285.9 + (169.834 * T)$		

Table 10: The calculations made to obtain the Energy Balance formula through the Gibbs Energy calculation in calculating the formula of Entropy Change for Mn MOE.

ENERGY BALANCE		
Enthalpy Change @ Room Temperature		
Formula	Gibbs Energy [ΔG1] (J)	Entropy [Δs1] (J/K)
$\Delta H1 = \Delta G1 + (T * \Delta s1)$	-122346	109.864
$\Delta H1 = -122346 + (109.864 * T)$		
Enthalpy Change @ Room Temperature		
Formula	Gibbs Energy [ΔG2] (J)	Entropy [Δs2] (J/K)
$\Delta H2 = \Delta G2 + (T * \Delta s2)$	256631.9	59.97
$\Delta H2 = 256631.9 + (59.97 * T)$		
Enthalpy Change @ Room Temperature		
Formula	Gibbs Energy [ΔG] (J)	Entropy [Δs] (J/K)
$\Delta H0 = \Delta H1 + \Delta H1$	134285.9	169.834
ENERGY BALANCE FORMULA		
$\Delta H = 134285.9 + (169.834 * T)$		

Table 11: The calculations made to obtain the Energy Balance formulas through the Gibbs Energy calculation in calculating the formula of Entropy Change. These formulas are the formulas generated of the measured energy balance at each stage of the total reaction. This is for the Mn MOE reaction.

NOMINAL CATHODE TO ANODE DISTANCE												
Formula								Step Five: Calculating Voltage For Losses				
$R = (\rho * D_{ac}) / (\text{Area})$								Assumption:				
								0				
ρ	Resistivity (ohm * cm)	R	Electrolyte (Ohms)	D_ac	Nominal Anode-To-Cathode Distance	Area	Area Between Anode & Cathode	Step Six: Calculating Ohmic Drop				
Step One: Mapping Out Energies Of Overall Reaction								$V_{IR} = V_{feed} + V_r + V_{loss}$				
Operation Temperature [T] (K)	Gibbs Energy [ΔG] (kJ/mol-Mn)	Enthalpy Change [ΔH] (kJ/mol-Mn)	Entropy Change Formula			Entropy Change [ΔS] (kJ/mol-Mn*K)		1.302543581				
1533.15	271598.3	402966.8	$\Delta S = -(\Delta G - \Delta H) / T$			85.68535368		Step Seven: Calculating The Anode-To-Cathode Distance				
Step Two: Calculating Minimum Operation Voltage								$V_{IR} = I * R$				
Heat Loss During Electrolysis								$R = (\rho * D_{ac}) / (\text{Area})$				
$\Delta Q = \Delta S * T$								131368.5				
Minimum Voltage								$V_{IR} = I * ((\rho * D_{ac}) / (\text{Area}))$				
$V_{min} = \Delta G / (n * F)$								$I = j * \text{Area}$				
Number Of Transferred Electrons [n] (mol)	2	Faraday's Constant [F] (C/mol)	96485.3321	1.40745901		$V_{IR} = j * (\rho * D_{ac})$						
Step Three: Calculating Electrolysis Reaction Voltage								Assumptions				
$V_r = \Delta Q / (n * F)$								Current Density can be assumed to be 2 A/cm ² , which is the same for Aluminum Smelting: $Al[3+] = 3e[-] + Al(l)$				
0.6807692793								Resistivity can be assumed to be 1 ohm*cm which is typical for Molten Salts				
Voltage Drop From Reaction Ohmic Drop [V_IR] (V)								1.302543581	Current Density [j] (A / cm ²)	2	Resistivity [ρ] (ohm * cm)	1
Step Four: Calculating Voltage For Introducing Ore Feedstock @ 25 oC								0.6512717906				
Ore Feedstock MnO (s, 25 oC) To MnO (l, 1260 oC)												
Enthalpy Change [ΔH] (kJ/mol-Mn_l)	119984.2	Formula	$V_{feed} = \Delta H / (n * F)$			0.6217743018						

Table 12: The calculation process to obtain the Nominal Cathode-To-Anode Distance for the electrolytic cell containing the Mn MOE reaction.

FARADAIC EFFICIENCY (CURRENT EFFICIENCY)					
Formula					
$\eta_f = ((m) / (m_o)) * 100\%$					
η_f	Faradaic Efficiency	m	Actual Mass Produced (grams)	m_o	Theoretical Mass Produced (grams)
Step One: Developing Assumptions					
Assumption			Reasoning		
$\eta_f = 90\%$			Modern aluminum electrolysis cells operate at approximately 90% faradaic efficiency, so we can assume to apply the same efficiency to this manganese electrolysis cell		
Step Two: Calculating The Theoretical Mass Of Manganese Produced					
Formula					
$m = (M * Q) / (n * F)$					
Molar Mass [M] (g/mol-Mn)	54.938044	Number Of Tranferred Electrons [n] (mol-e/mol-Mn)	2	Faraday's Constant [F] (C/mol-e)	96485.3321
Charge [Q] (C/mol)					
$Q = I * \Delta t = (j * Area) * \Delta t$					
Current Density [j] (A/cm²)	2	Area [cm²]	1	Time [Δt] (s)	86400
172800					
Theoretical Mass [m] (gram)					
49.1955295					
Step Three: Calculating The Actual Mass Of Manganese Produced					
Formula					
$\eta_f = ((m) / (m_o)) * 100\%$					
Fradaic Efficiency [η_f] (%)	90	Theoretical Mass Produced [m_o] (g)	49.1955295		
44.27597655					

Table 13: The calculation process to obtain the Actual Produced Mass of Mn. This was done assuming the reaction occurred at a 90% faradaic efficiency.

ENERGY EFFICIENCY							
Formula							
$\eta_E = ((E_o) / (E)) * \eta_f$							
η_E	Energy Efficiency	E	Actual Minimal Potential (V)	E_o	Minimal Theoretical Potential (V)	η_f	Faradaic Efficiency
Step One: Developing Assumptions							
Assumption			Reasoning				
$\eta_f = 90\%$			Modern aluminum electrolysis cells operate at approximately 90% faradaic efficiency, so we can assume to apply the same efficiency to this electrolysis cell				
Step Two: Calculating The Minimal Theoretical Potential							
Formula							
$E_o = V_{min} + V_r + V_{feed}$							
Minimum Operating Voltage [V_min] (V)	1.40745901	Electrolysis Reaction Voltage [V_r] (V)	0.6807692793	Voltage For Introducing Ore Feedstock [V_feed] (V)	0.6217743018		
2.710002591							
Step Three: Calculating The Energy Efficiency							
Formula							
$\eta_E = ((E_o) / (E)) * \eta_f$							
Actual Minimal Potential							
$E = E_o + (T * \Delta S) / (2F)$							
Minimal Theoretical Potential [E_o] (V)	2.710002591	Operating Temperature [T] (K)	1533.15	Entropy Change [ΔS] (J/mol*K)	85.68535368	Faraday's Constant [F] (C/mol)	96485.3321
3.39077187							
79.92288171							

Table 14: The calculation process to obtain the Energy Efficiency of Mn. This was done assuming the reaction occurred at a 90% faradaic efficiency.

Appendix B: Aluminum Magnesium Boride MOE

Figures

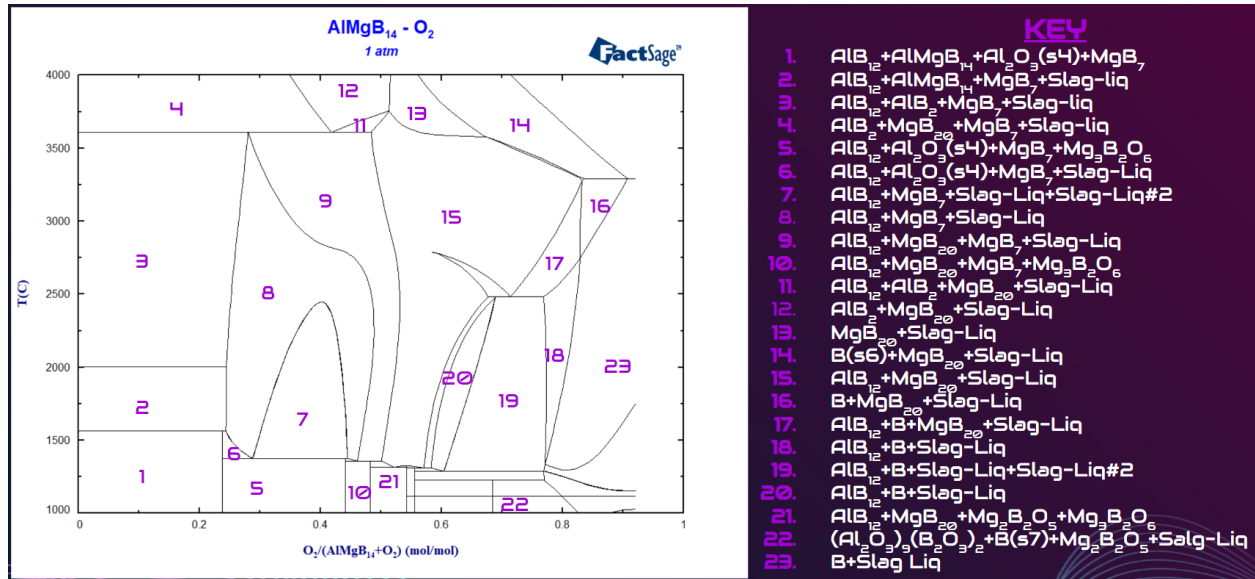


Figure 17: The Pseudo-Binary Phase Diagram Between AlMgB₁₄ and O₂ from a temperature range of 1000 °C to 4000 °C. The 23 most significant resulting compositions are shown and labeled with a key.

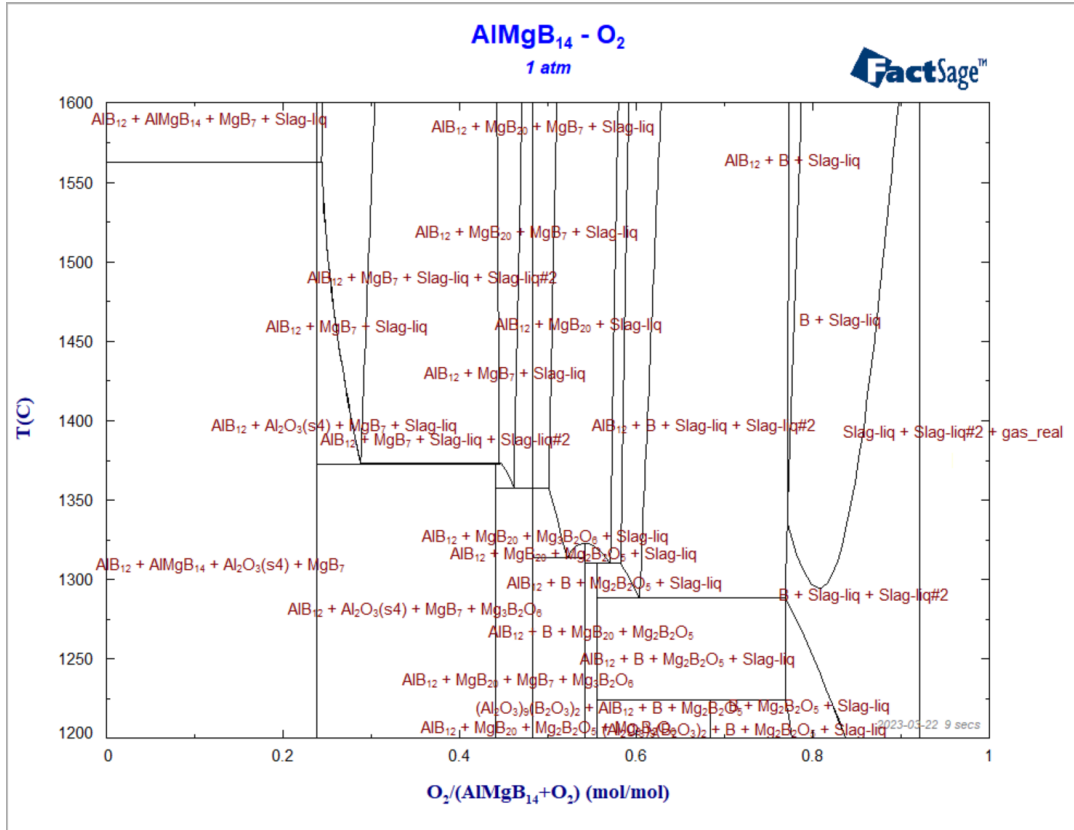


Figure 18: The Pseudo-Binary Phase Diagram Between AlMgB₁₄ and O₂ from a temperature range of 1200°C to 1600°C.

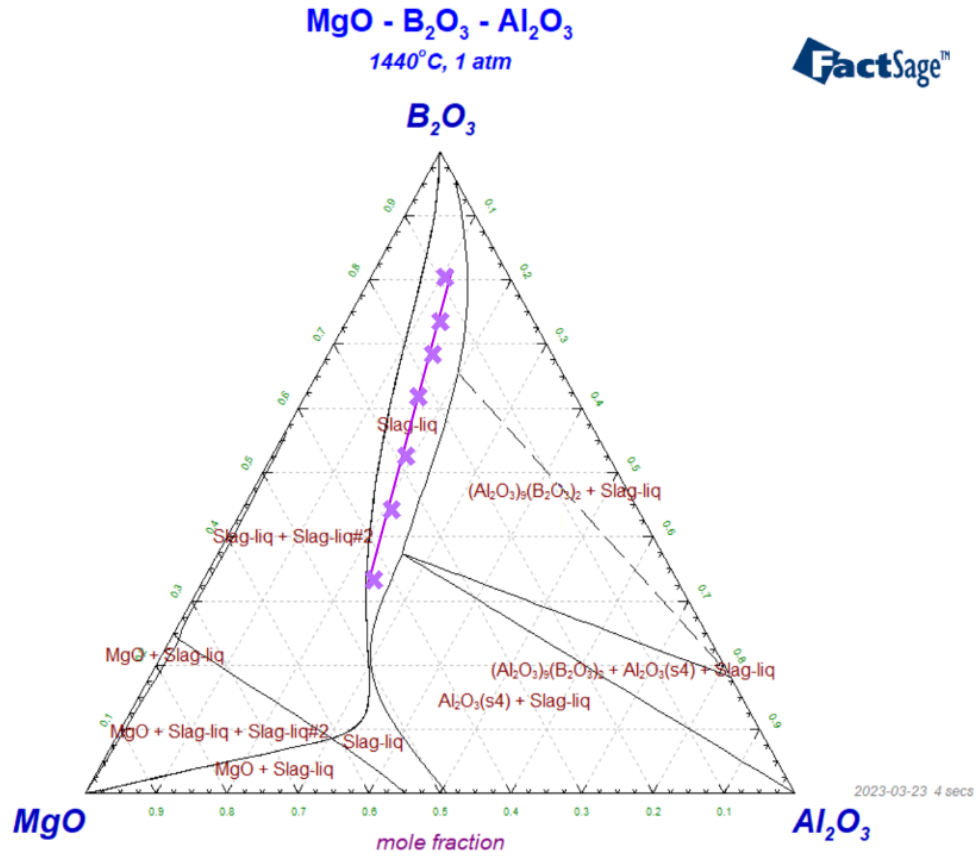


Figure 19: The Isothermal Section between B₂O₃, MgO, and Al₂O₃ at 1440 °C. The seven compositions we examine are the purple “x’s” in the Slag-liquid region.

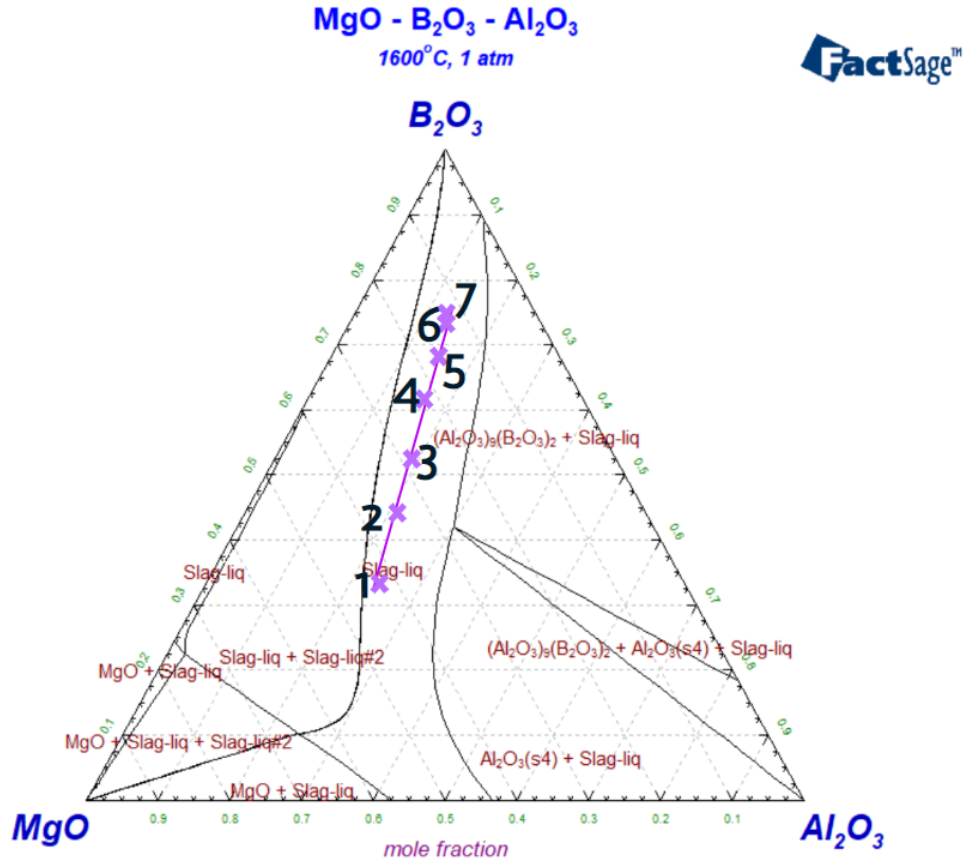


Figure 20: The Isothermal Section between B₂O₃, MgO, and Al₂O₃ at 1600 °C. The purple “x’s” labeled one through seven are the same seven compositions consistent with the same region of 1440 °C.

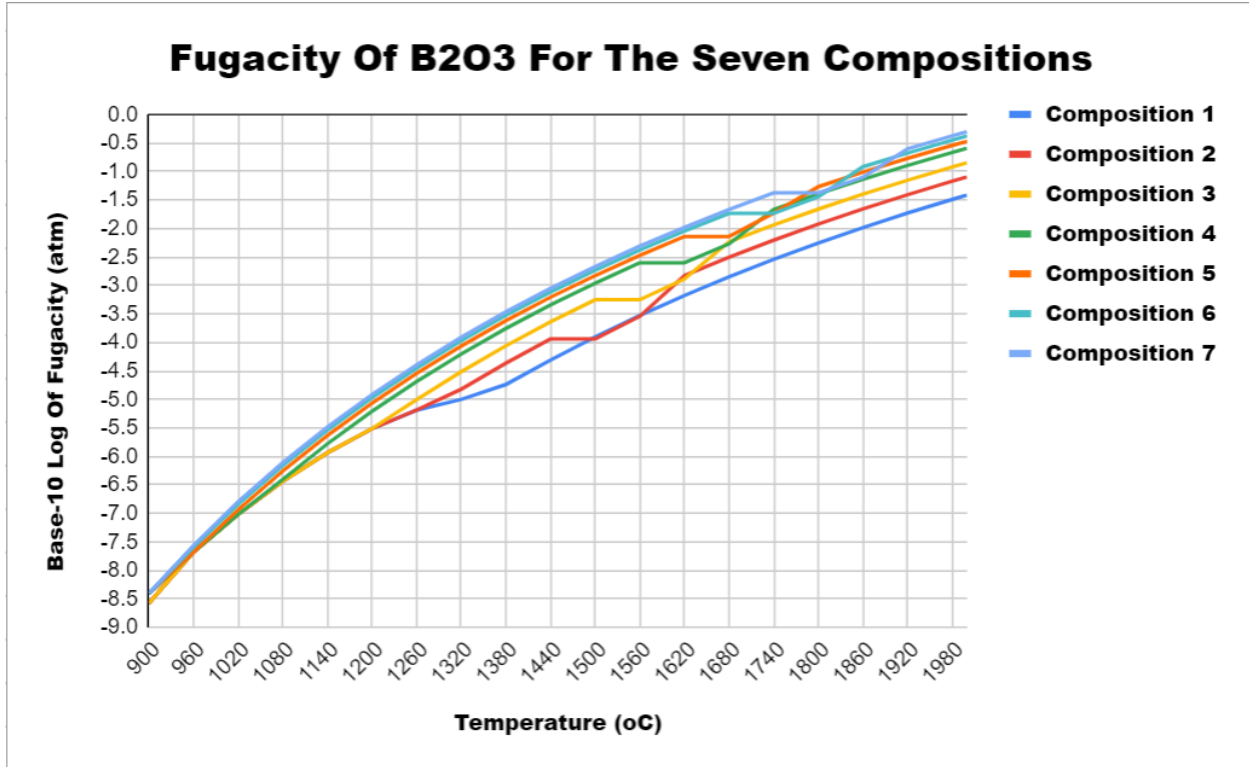


Figure 21: The Fugacity Trend of B₂O₃ from 900 to 2000 °C. This graph is displayed as Temperature (in degrees Celsius) versus the Base-10 Log of Fugacity in (atm).

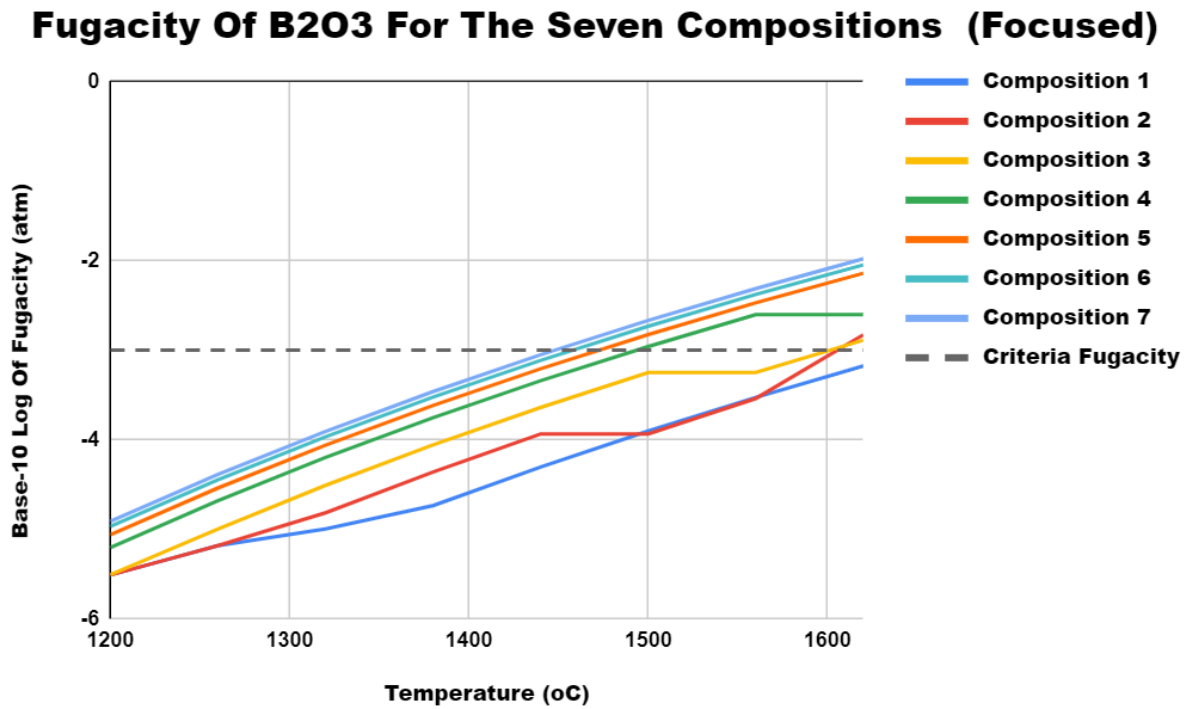


Figure 22: The “focused” Graph of the Fugacity Trend of B₂O₃ from 1200 to 16000 °C. This graph is displayed as Temperature (in degrees Celsius) versus the Base-10 Log of Fugacity in (atm).

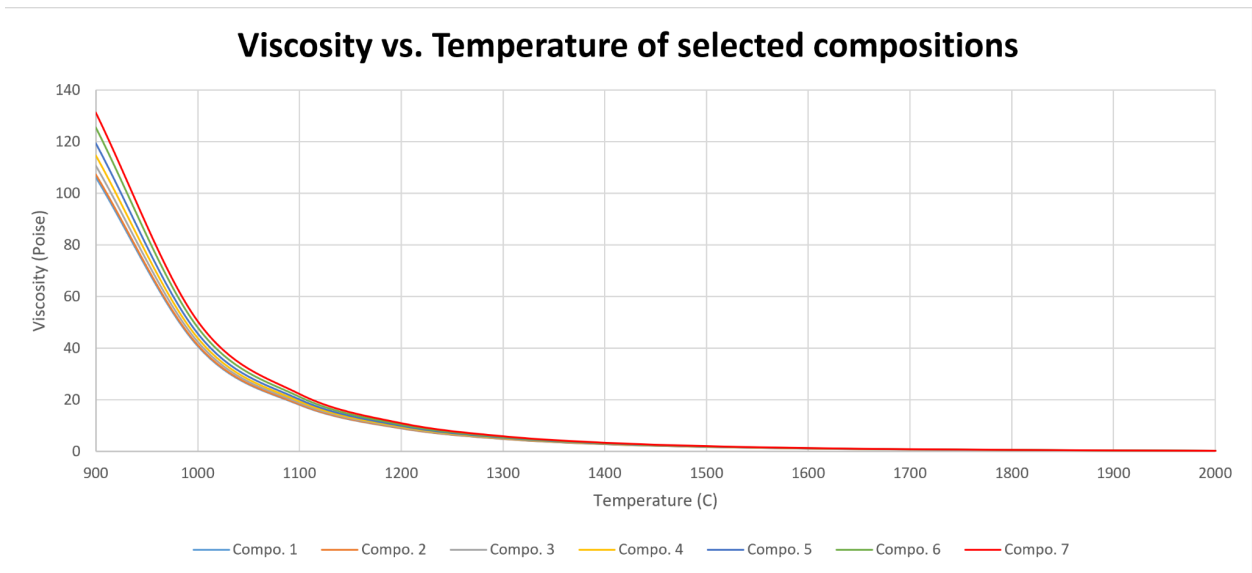


Figure 23: Graph of viscosity vs. temperature of selected compositions from 900 to 2000 °C

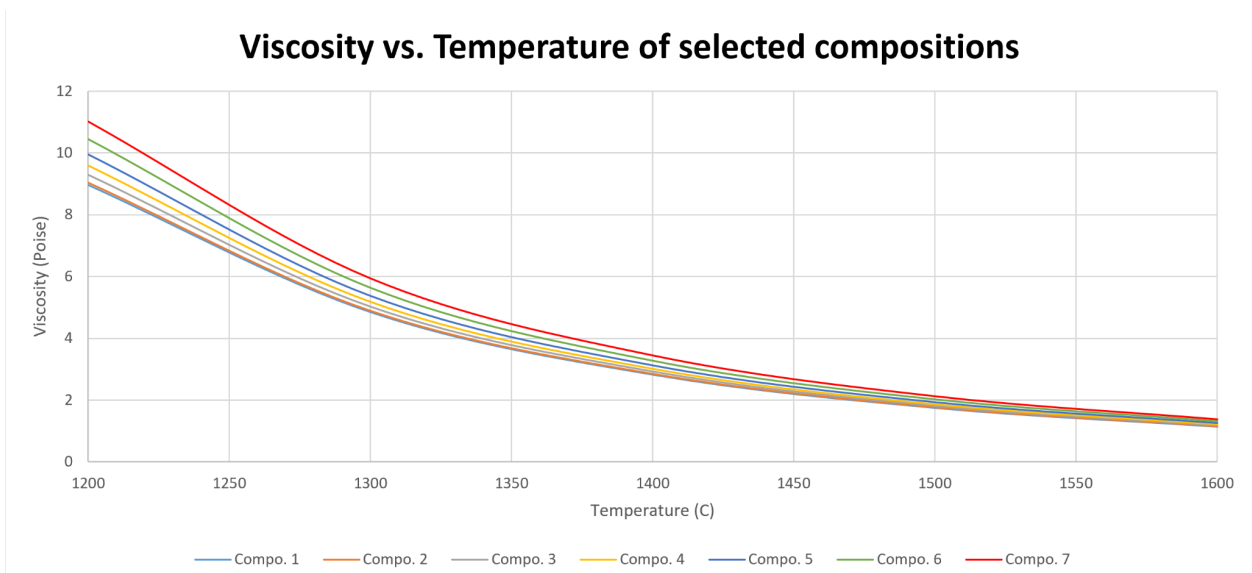


Figure 24: Graph of viscosity vs. temperature of selected compositions from 1200 to 1600 °C

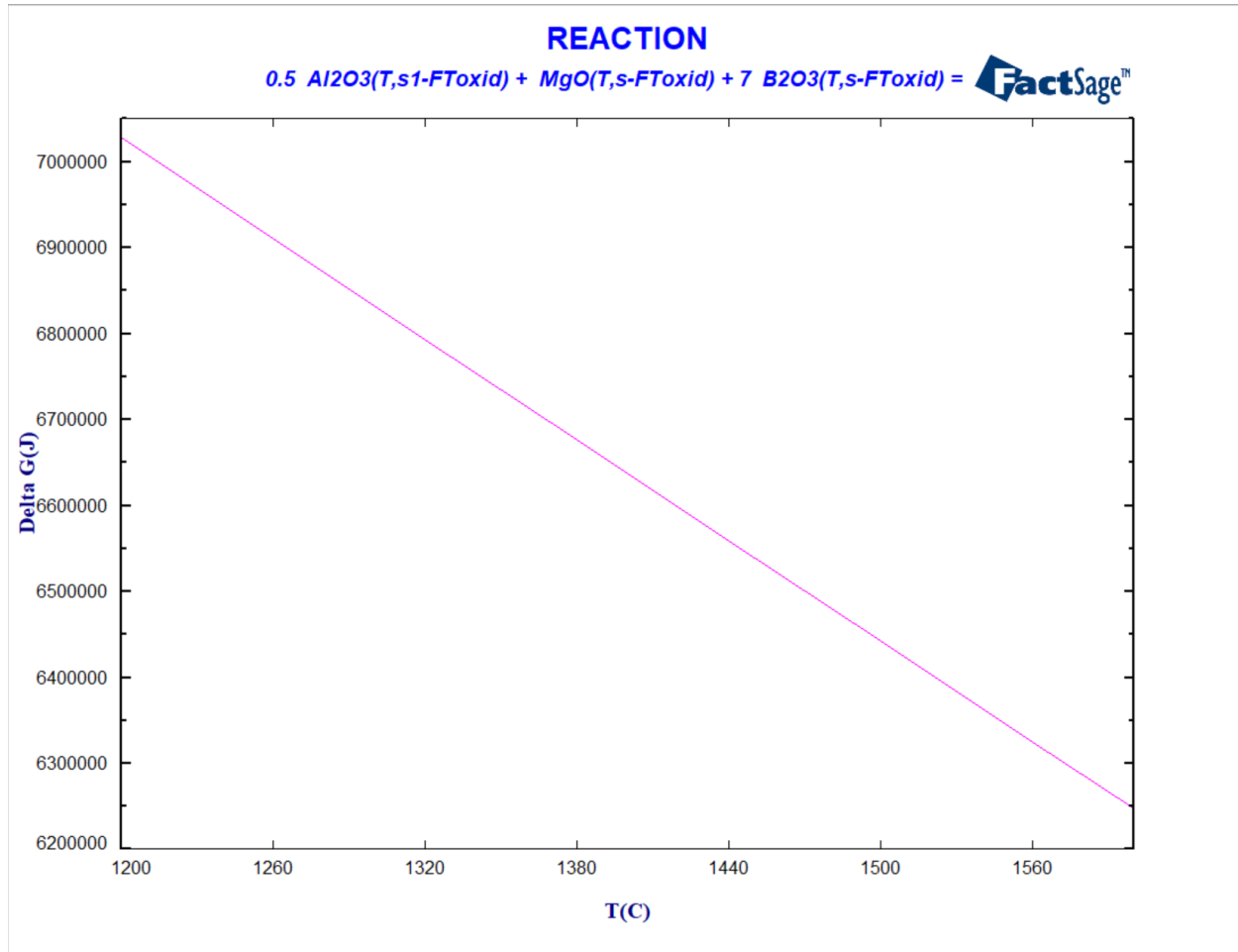


Figure 25: The Overall Reaction Energy Trend Graph from 1200 to 16000 °C. This graph is displayed as Temperature (in degrees Celsius) versus the change in Gibbs Energy (J).

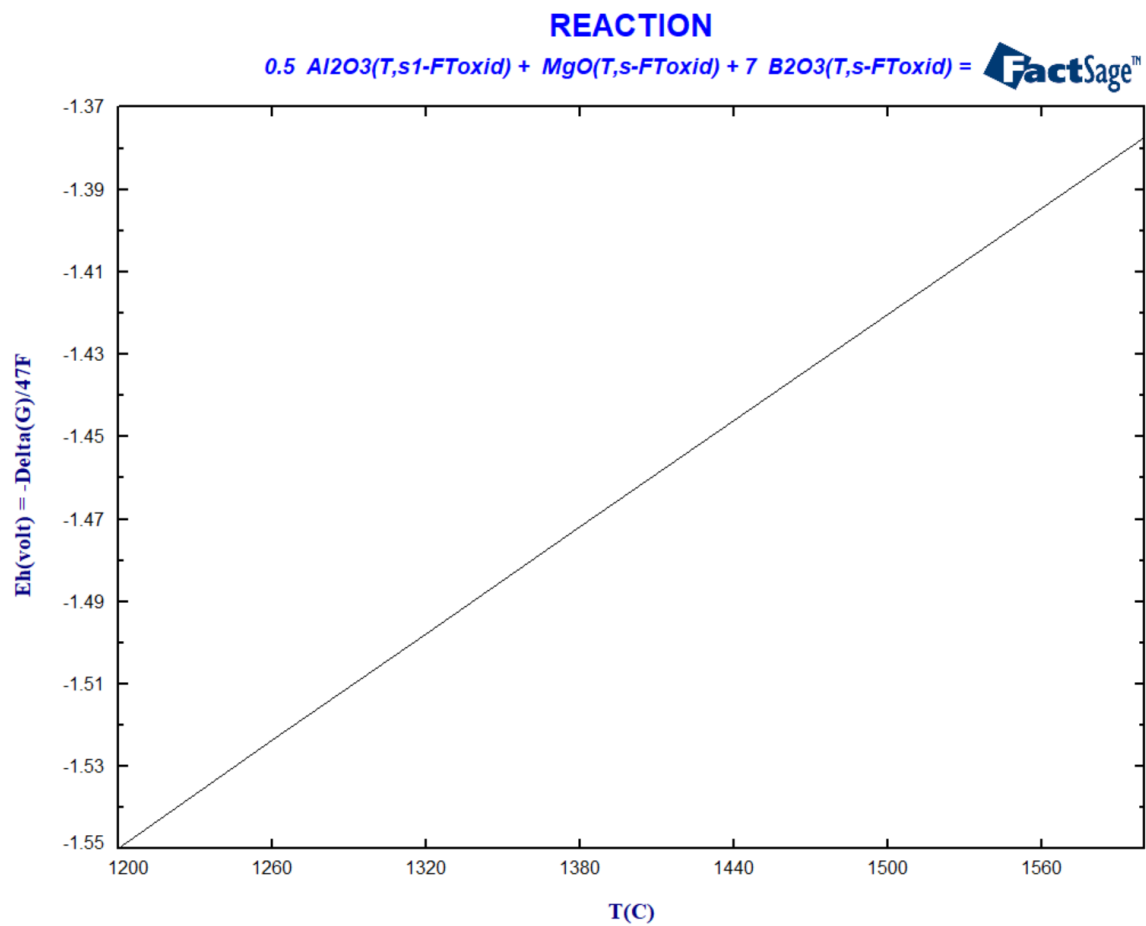


Figure 26: The Overall Reaction Potential Trend Graph from 1200 to 1600 °C. This graph is displayed as Temperature (in degrees Celsius) versus the Voltage Requirement (V).

Energies Of Overall Reaction, Cathodic Reaction, and Anodic Reaction

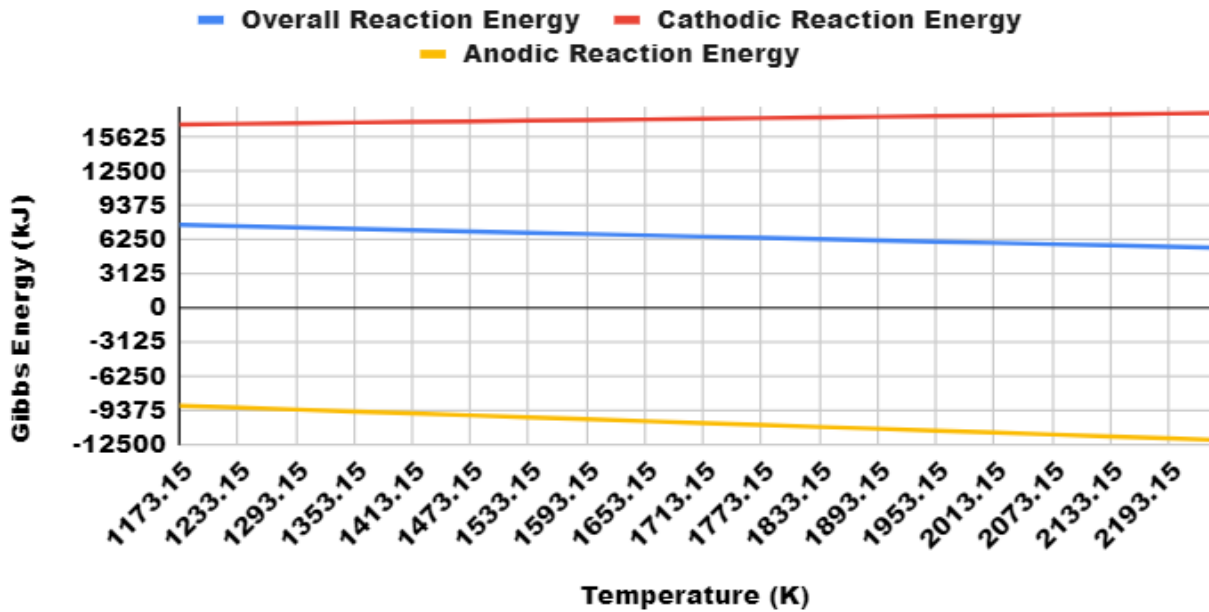


Figure 27: The Graph of the Overall Reaction, Cathodic Reaction, and Anodic Reaction Energy Functions for the $AlMgB_{14}$ reaction.

Potentials Of Overall Reaction, Cathodic Reaction, & Anodic Reaction

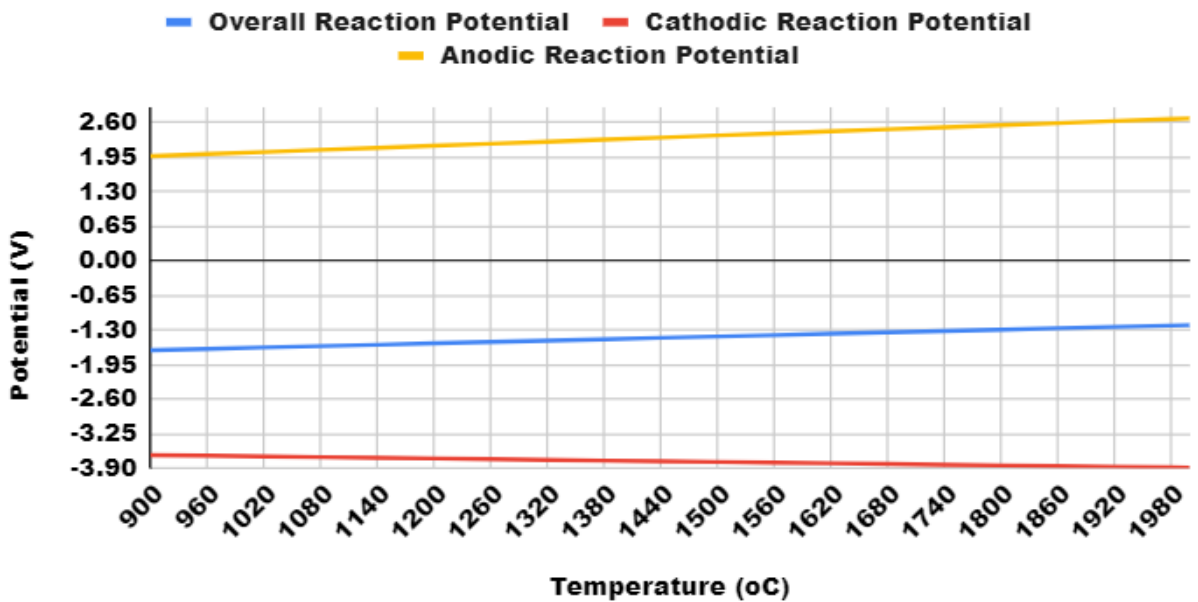


Figure 28: The Graph of the Overall Reaction, Cathodic Reaction, and Anodic Reaction Potential Functions for the $AlMgB_{14}$ reaction.

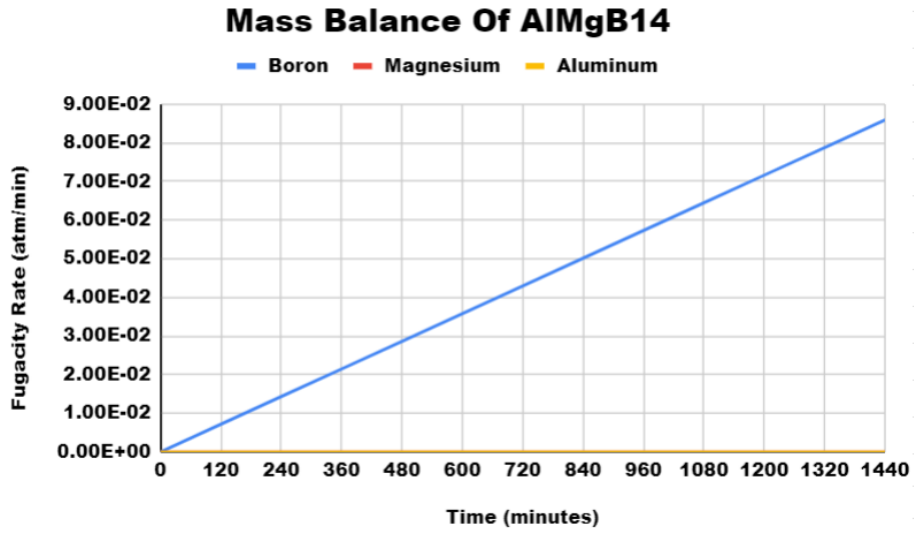


Figure 29: The total Mass Balance of AlMgB₁₄, graphed in terms of Fugacity rate (atm/min) vs. time (min). The graph is mapped out over a full day in terms of minutes.

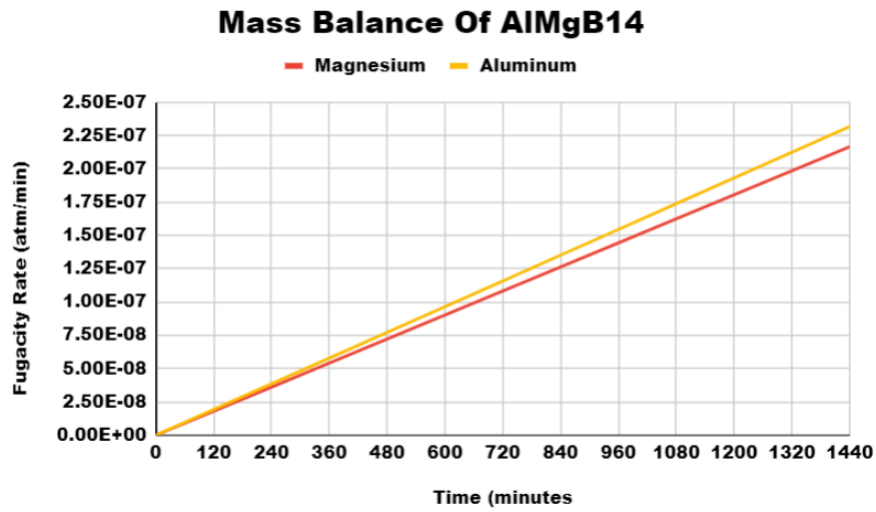


Figure 30: The partial Mass Balance of AlMgB₁₄, graphed in terms of Fugacity rate (atm/min) vs. time (min). The graph is mapped out over a full day in terms of minutes. This graph only contains the trend of magnesium and aluminum.

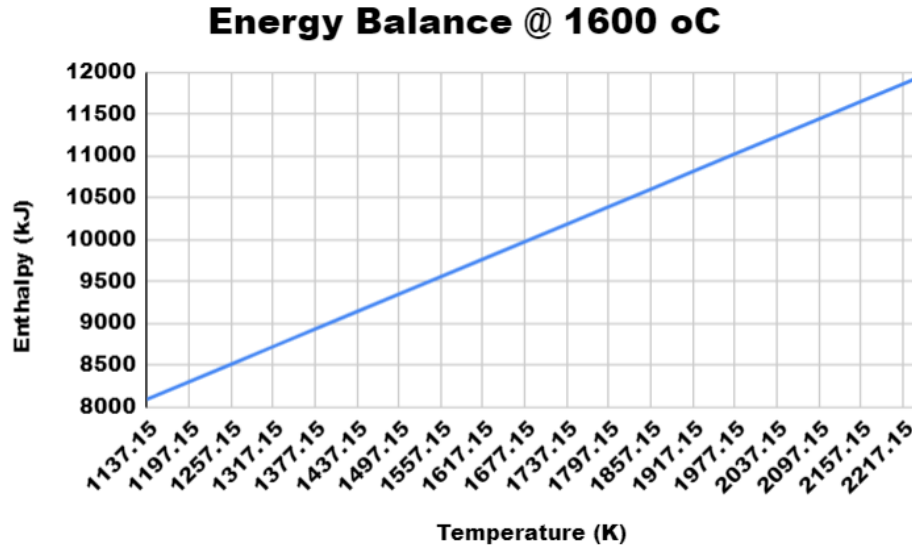


Figure 31: The total Energy Balance of AlMgB₁₄, graphed in terms of enthalpy (kJ) vs. temperature (K).

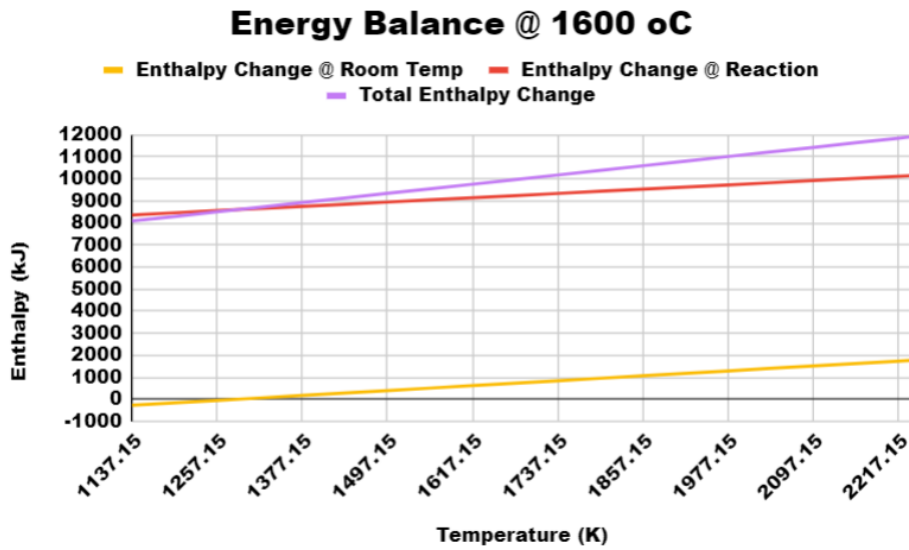


Figure 32: The Energy Balances of AlMgB₁₄, graphed in terms of enthalpy (kJ) vs. temperature (K). This shows the enthalpy changes at each stage of the reaction, as well as that for the total reaction.

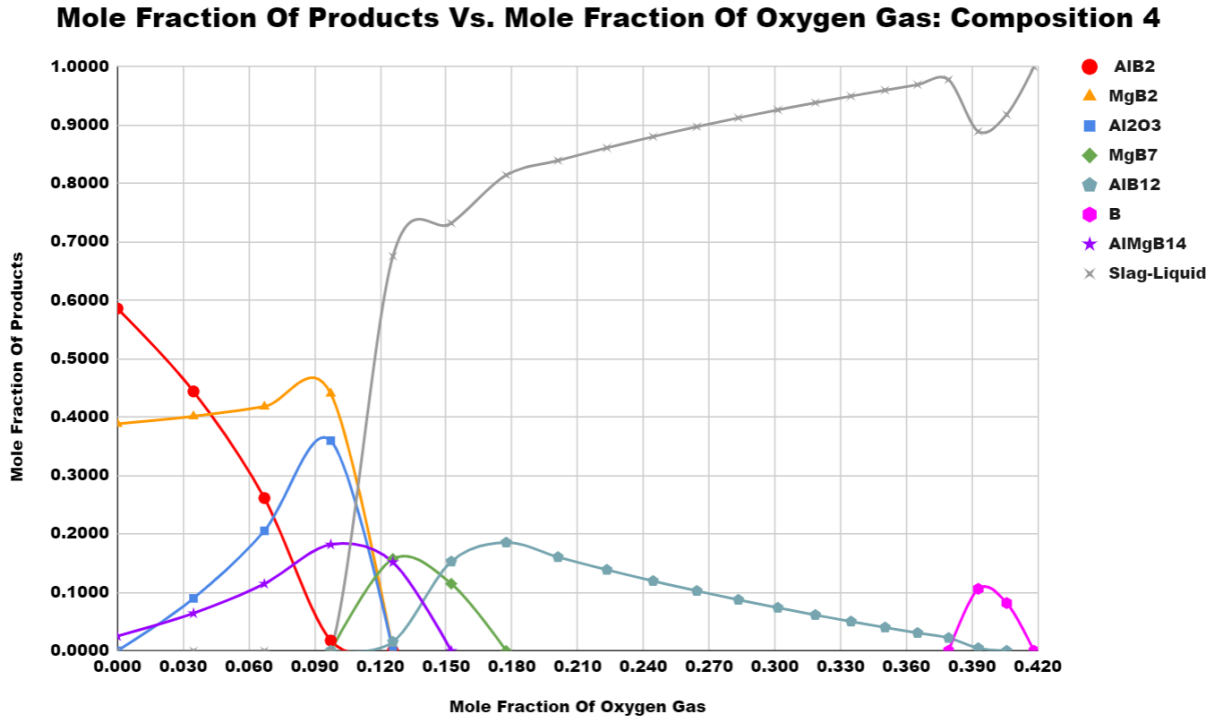


Figure 37: The Mole Fraction Data from Table 35 graphed out in a Mole Fraction Of Oxygen Vs. Mole Fraction Of Products relation.

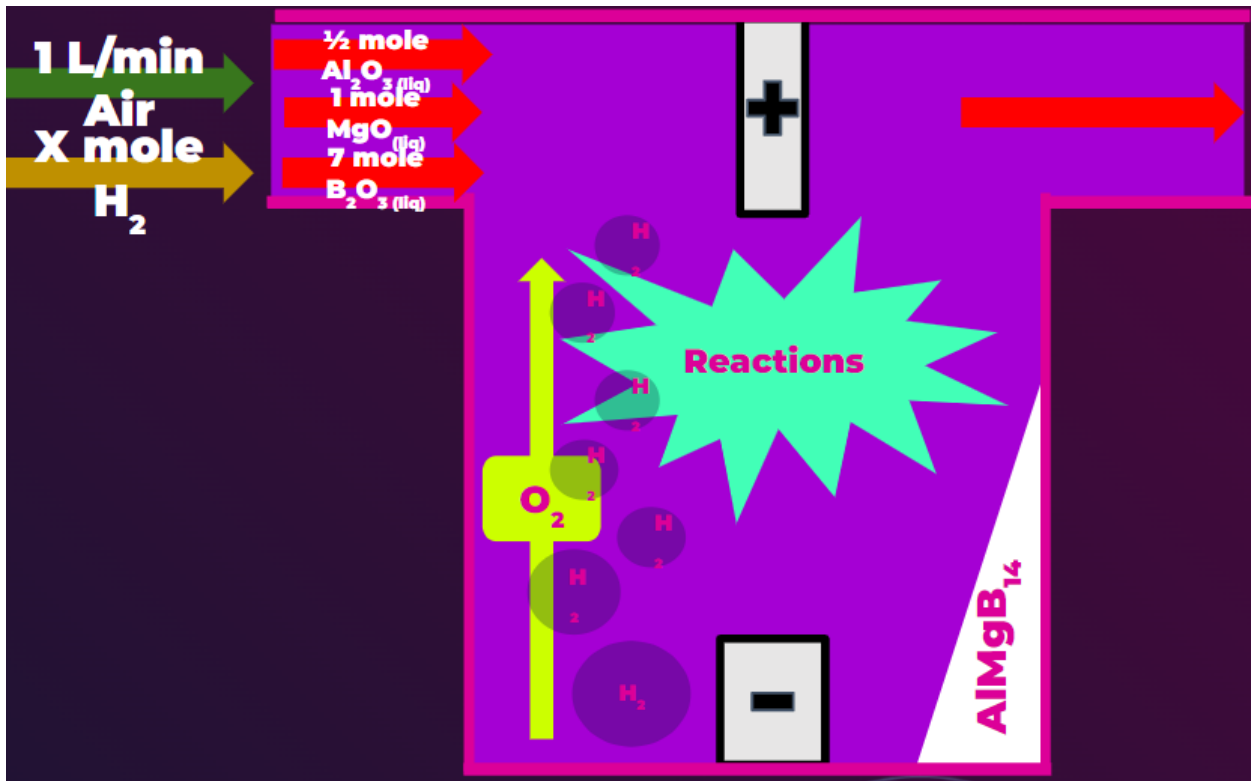


Figure 38: Illustration of the Reaction System with the Introduction of Hydrogen Gas (the brown arrow) entering the reaction.

Percent Of Hydrogen Gas vs. Base-10 Log Of Oxygen Partial Pressure

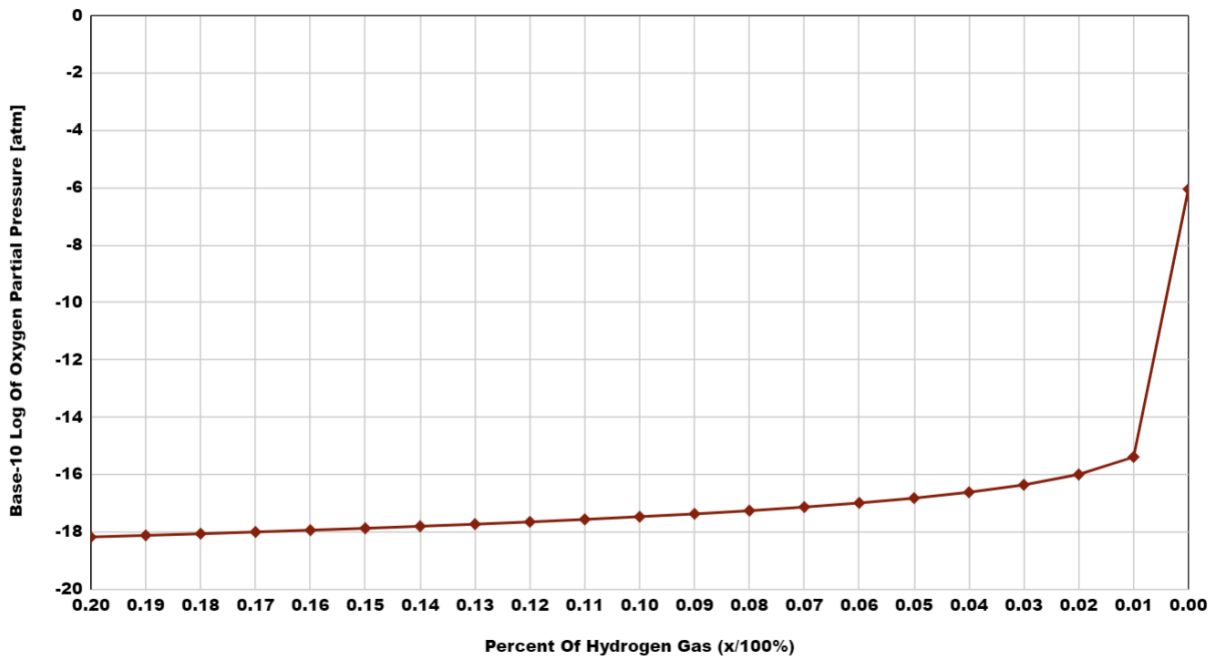


Figure 39: The data from Table 38 graphed out in a Hydrogen Percent vs. Base-10 Log Of Partial Pressure distribution.

Mole Fraction Of Products Vs. Mole Fraction Of Oxygen Gas: Composition 4

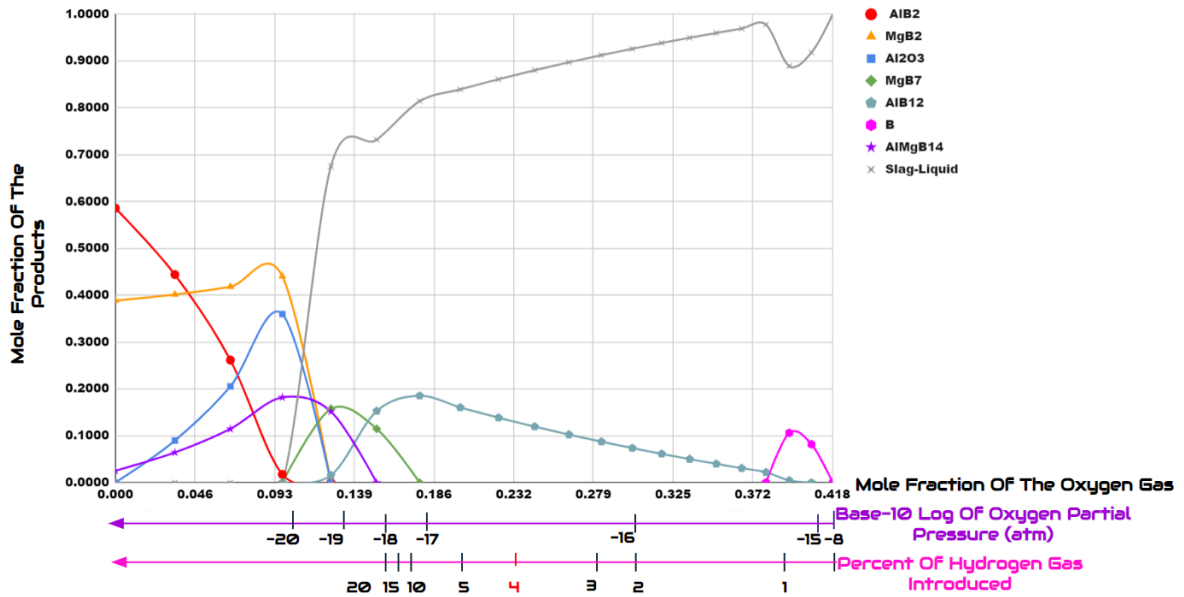


Figure 40: The graph of the accumulated data from the reaction products, oxygen partial pressure, and percent of hydrogen gas introduced.

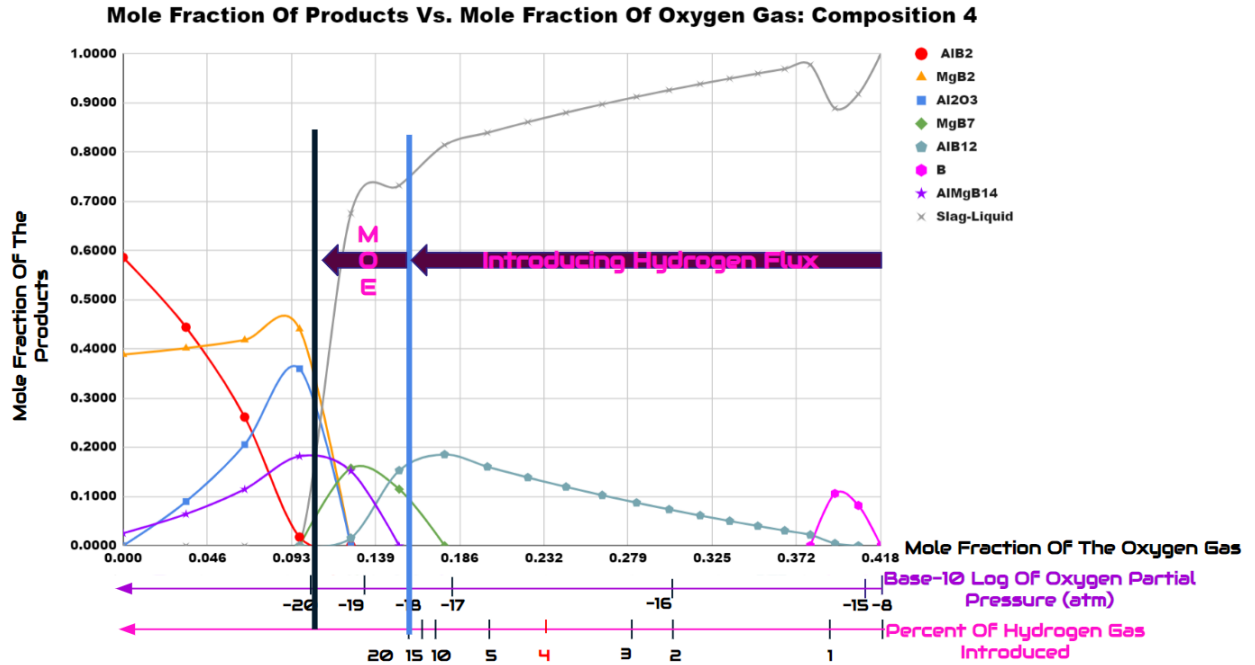


Figure 41: The graph from Figure 40 with labels of where the hydrogen gas influx would begin and end and where the MOE reaction would begin and end.

Temp.	1	2	3	4	5	6	7
900	106.325	107.403	110.805	114.718	119.345	125.454	131.331
1000	40.933	41.323	42.591	44.042	45.78	48.115	50.572
1100	18.114	18.278	18.824	19.444	20.194	21.214	22.346
1200	8.957	9.034	9.297	9.594	9.956	10.452	11.022
1300	4.845	4.885	5.024	5.18	5.372	5.634	5.944
1400	2.821	2.844	2.923	3.011	3.12	3.27	3.45
1500	1.746	1.76	1.808	1.861	1.927	2.018	2.128
1600	1.138	1.147	1.178	1.211	1.253	1.312	1.382
1700	0.774	0.781	0.801	0.823	0.852	0.89	0.938
1800	0.547	0.551	0.566	0.581	0.601	0.628	0.661
1900	0.399	0.402	0.413	0.423	0.437	0.457	0.481
2000	0.299	0.302	0.309	0.317	0.328	0.342	0.359

Table 16: Raw data of the viscosity of selected compositions at various temperatures.

<u>OVERALL REACTION ENERGY</u>	
<u>Temperature (oC)</u>	<u>Gibbs Energy (J)</u>
1200	7028306.1
1260	6910353.1
1320	6792711.3
1380	6675356.3
1440	6558266
1500	6441420.2
1560	6324800.1
1600	6247170.2

Table 17: The Overall Reaction Energy, with a temperature range from 1200°C To 1600°C and the corresponding change in Gibbs Energy for each temperature. The difference in Gibbs Energy of the desired Operating Temperature is highlighted at the bottom of the table.

<u>NERNST EQUATION</u>		<u>VOLTAGE REQUIREMENT</u>				
$\Delta G_o = (n * F)^{-1} * E_{cell}$		<u>Temperature</u> (oC)	<u>Gibbs Energy</u> [ΔG_o] (J)	<u>Number Of Moles [n]</u> (mol)	<u>Farady's Constant [F]</u> ($C * mol^{-1}$)	<u>Voltage Requirement</u> [E_{cell}] (V)
$\Delta G_o * (n * F) = E_{cell}$		1600	6247170.2	47	96485.3321	1.377603331

Table 18: The Voltage Requirement is split into two tables. The first table shows the Nernst Equation and its rearranged form to calculate the voltage requirement of the electrolytic cell at the operating temperature. The second table shows the change in Gibbs Energy at 1600 °C, the number of moles or electrons transferred as 47, and the Faraday's constant, all used to calculate the voltage requirement.

<u>OVERALL REACTION ENERGY</u>		<u>OVERALL REACTION ENERGY FORMULA</u>			
<u>Temperature</u> (oC)	<u>Gibbs Energy (J)</u>	<u>Change In Entropy [Δs] (J/(mol*K))</u>		<u>Change In Enthalpy [ΔH] (J/mol)</u>	
900	7623782.1	Formula	Value	Formula	Value
960	7503808.8	$\Delta s =$	-1950.971755	$\Delta H =$	9371723.597
1020	7384313.4	SLOPE(C4:C16,B4:B16) INTERCEPT(C4:C16,B4:B16)			
1080	7265255	<u>OVERALL REACTION ENERGY FORMULA</u>			
1140	7146596.8	$y = 9371723.597 - 1950.971755 * x$			
1200	7028306.1	$\Delta G_o = 9371723.597 - (1950.971755 * T)$			
1260	6910353.1	<u>OVERALL REACTION POTENTIAL FORMULA</u>			
1320	6792711.3	<u>GIBBS ENERGY FORMULA</u>		<u>Nernst Equation</u>	
1380	6675356.3	$\Delta G = \Delta H - (T * \Delta s)$		Number Of Moles [n] (mol)	
1440	6558266	$y = b + (m * x)$		Faraday's Constant [F] ($C * mol^{-1}$)	
1500	6441420.2	$\Delta G = y$	$\Delta H = b$	96485.3321	
1560	6324800.1	$T = x$	$\Delta s = m$	<u>OVERALL REACTION POTENTIAL FORMULA</u>	
1620	6208388.5	$E_o = -2.066618522 + (4.302212204E-04 * T)$			
1680	6092169.6	<u>CATHODIC REACTION ENERGY FORMULA</u>			
1740	5976128.6	<u>Change In Entropy [Δs] (J/K)</u>		<u>CATHODIC REACTION POTENTIAL FORMULA</u>	
1800	5860252.2	980.9		$\Delta G / (-n * F) = E$	
1860	5744529.4	<u>Change In Enthalpy [ΔH] (J/mol)</u>		Number Of Moles [n] (mol)	
1920	5628949.8	1.57E+07		47	
1980	5513503.9	$\Delta G_1 = 15676000 + (980.9 * T)$			
2000	5475050	$E_1 = -3.4568147 - (0.0002163 * T)$			

Table 19: The calculations made to obtain the Overall Reaction Energy and Potential formulas for the $AlMgB_{14}$ reaction.

<u>CATHODIC REACTION ENERGY FORMULA</u>		<u>CATHODIC REACTION POTENTIAL FORMULA</u>		
<u>Change In Entropy [Δs] (J/K)</u>	<u>Change In Enthalpy [ΔH] (J/mol)</u>	<u>Nernst Equation</u>	<u>Number Of Moles [n] (mol)</u>	<u>Faraday's Constant [F] ($C * mol^{-1}$)</u>
980.9	1.57E+07	$\Delta G / (-n * F) = E$	47	96485.3321
<u>CATHODIC REACTION ENERGY FORMULA</u>		<u>CATHODIC REACTION POTENTIAL FORMULA</u>		
$\Delta G_1 = 15676000 + (980.9 * T)$		$E_1 = -3.4568147 - (0.0002163 * T)$		

Table 20: The calculations made to obtain the Cathodic Reaction Energy and Potential formulas for the $AlMgB_{14}$ reaction.

ANODIC REACTION ENERGY FORMULA	ANODIC REACTION POTENTIAL FORMULA		
Formula	Nernst Equation	Number Of Moles [n] (mol)	Faraday's Constant [F] (C*mol ⁻¹)
$\Delta G_2 = \Delta G_0 - \Delta G_1$	$\Delta G / (-n * F) = E$	47	96485.3321
ANODIC REACTION ENERGY FORMULA	ANODIC REACTION POTENTIAL FORMULA		
$\Delta G_2 = -6304276.402 - (2931.871755 * T)$	$E_2 = 1.390196184 + (6.4652573334E-4 * T)$		

Table 21: The calculations made to obtain the Anodic Reaction Energy and Potential formulas for the AlMgB₁₄ reaction.

MASS BALANCE OF ALL COMPOUNDS											
Composition 4											
0.61547B2O3 - 0.221198MgO - 0.163332Al2O3											
BORON COMPOUNDS				MAGNESIUM COMPOUNDS				ALUMINUM COMPOUNDS			
Compound	Fugacity Rate Of Compound	# Of Moles Of Boron	Fugacity Rate Of Boron	Compound	Fugacity Rate Of Compound	# Of Moles Of Boron	Fugacity Rate Of Boron	Compound	Fugacity Rate Of Compound	# Of Moles Of Boron	Fugacity Rate Of Boron
B2O3	4.18E-03	2	8.36E-03	Mg	2.11E-08	1	2.11E-08	AlBO2	2.26E-08	1	2.26E-08
BO2	1.23E-05	1	1.23E-05	MgO	1.28E-11	1	1.28E-11	AlO	2.43E-12	1	2.43E-12
BO	8.24E-06	1	8.24E-06	Mg2	7.93E-20	2	1.59E-19	Al	5.71E-13	1	5.71E-13
(BO)2	2.03E-06	2	4.06E-06					Al2O	8.96E-16	2	1.79E-15
AlBO2	2.26E-08	1	2.26E-08					Al2O2	2.65E-16	2	5.31E-16
B2O	1.41E-13	2	2.82E-13					Al2O3	7.35E-20	2	1.47E-19
B	2.26E-14	1	2.26E-14					Al2	1.89E-25	2	3.79E-25
B2	1.32E-25	2	2.64E-25					AlO2	8.96E-16	1	8.96E-16
NET BORON FUGACITY RATE (per minute)				NET MAGNESIUM FUGACITY RATE (per minute)				NET ALUMINUM FUGACITY RATE (per minute)			
5.97E-05				1.50E-10				1.61E-10			
Total Boron Lost Over A Day= 5.97E-05 * t				Total Magnesium Lost Over A Day= 1.50E-10 * t				Total Aluminum Lost Over A Day= 1.61E-10 * t			

Table 22: The calculations made to obtain the Fugacity rate of Boron, Magnesium, and Aluminum over time for the Mass Balance calculation of AlMgB₁₄.

Non-Isothermal Non-Standard State Reaction:						
$0.5 \text{ Al}_2\text{O}_3 + \text{MgO} + 7 \text{ B}_2\text{O}_3 = \text{AlMgB}_{14} + 11.75 \text{ O}_2$ <p style="text-align: center;">(25C,s4-FToxid) (25C,s-FToxid) (25C,s-FToxid) (1600C,s-FTlite) (1600C,g-FactPS)</p>						
Delta H(J)	Delta G(J)	Delta Vol(litre)	Delta S(J/K)	Delta Cp(J/K)	Delta A(J)	Delta A (J)
11331724.8	4128593.6	1.8061E+03	3483.898	398.319	3945595.3	

Table 23: The Results Window from FactSage's Reaction Module for the Total Reaction.

ENERGY BALANCE @ 1600 oC		
Formula	Gibbs Energy [ΔG] (J)	Entropy [Δs] (J/K)
$\Delta H = \Delta G + (T * \Delta s)$	4128593.6	3483.898
ENERGY BALANCE FORMULA		
$\Delta H = 4128593.6 + (3483.898 * T)$		

Table 24: The calculations made to obtain the Energy Balance formula through the Gibbs Energy calculation in calculating the formula of Entropy Change for AlMgB₁₄ MOE.

Non-Isothermal Non-Standard State Reaction:						
$0.5 \text{ Al}_2\text{O}_3 + \text{MgO} + 7 \text{ B}_2\text{O}_3 = 0.5 \text{ Al}_2\text{O}_3 + \text{MgO} + 7 \text{ B}_2\text{O}_3$ <p style="text-align: center;"> <small>(25C,s4-FToxid) (25C,s-FToxid) (25C,s-FToxid) (1600C,liq-FToxid) (1600C,liq-FToxid) (1600C,liq-FToxid)</small> </p>						
Delta H(J)	Delta G(J)	Delta Vol[litre]	Delta S(J/K)	Delta Cp(J/K)	Delta A(J)	Delta A (J)
1769632.6	-2391552.6	0.0000E+00	1859.924	511.576	-2391552.6	

Table 25: The Results Window from FactSage's Reaction Module for the Reactants heating up.

Isothermal Non-Standard State Reaction:						
$0.5 \text{ Al}_2\text{O}_3 + \text{MgO} + 7 \text{ B}_2\text{O}_3 = \text{AlMgB}_{14} + 11.75 \text{ O}_2$ <p style="text-align: center;"> <small>(1600C,liq-FToxid) (1600C,liq-FToxid) (1600C,liq-FToxid) (1600C,s-FTlite) (1600C,g-FactPS)</small> </p>						
Delta H(J)	Delta G(J)	Delta Vol[litre]	Delta S(J/K)	Delta Cp(J/K)	Delta A(J)	Delta A (J)
9562092.2	6520146.2	1.8061E+03	1623.974	-113.257	6337147.9	

Table 26: The Results Window from FactSage's Reaction Module for the Reaction after the reactants were heated up.

ENERGY BALANCE @ 1600 oC		
Enthalpy Change @ Room Temperature		
Formula	Gibbs Energy [ΔG1] (J)	Entropy [Δs1] (J/K)
$\Delta H_1 = \Delta G_1 + (T * \Delta s_1)$	-2032386.4	1768.259
$\Delta H_1 = -2032386.4 + (1768.259 * T)$		
Enthalpy Change @ Reaction		
Formula	Gibbs Energy [ΔG2] (J)	Entropy [Δs2] (J/K)
$\Delta H_2 = \Delta G_2 + (T * \Delta s_2)$	6780813.7	1634.751
$\Delta H_2 = 6780813.7 + (1634.751 * T)$		
Total Enthalpy Change		
Formula	Gibbs Energy [ΔG] (J)	Entropy [Δs] (J/K)
$\Delta H_0 = \Delta H_1 + \Delta H_2$	4748427.3	3403.01
ENERGY BALANCE FORMULA		
$\Delta H = 474827.3 + (3403.01 * T)$		

Table 27: The calculations made to obtain the Energy Balance formulas through the Gibbs Energy calculation in calculating the formula of Entropy Change. These formulas are the formulas generated of the measured energy balance at each stage of the total reaction. This is for the AlMgB_{14} MOE reaction.

NOMINAL CATHODE TO ANODE DISTANCE									
Formula									
$R = (\rho * D_{ac}) / (\text{Area})$									
ρ	Resistivity (ohm * cm)	R	Electrolyte (Ohms)	D_{ac}	Nominal Anode-To-Cathode Distance	Area	Area Between Anode & Cathode		
Step One: Mapping Out Energies Of Overall Reaction									
Operation Temperature [T] (K)	Gibbs Energy [ΔG] (kJ/mol-Mn)	Enthalpy Change [ΔH] (kJ/mol-Mn)	Entropy Change Formula			Entropy Change [ΔS] (kJ/mol-Mn*K)			
1873.15	4115272.1	11316513.6	$\Delta S = -(\Delta G - \Delta H) / T$			3477.56			
Step Two: Calculating Minimum Operation Voltage									
Heat Loss During Electrolysis									
$\Delta Q = \Delta S * T$									
6513991.514									
Minimum Voltage									
$V_{min} = \Delta G / (n * F)$									
Number Of Transferred Electrons [n] (mol)	47	Faraday's Constant [F] (C/mol)	96485.3321			0.9074848886			
Step Three: Calculating Electrolysis Reaction Voltage									
$V_r = \Delta Q / (n * F)$									
1.4364418									
Step Four: Calculating Voltage For Introducing Ore Feedstock @ 25 oC									
Ore Feedstock MgO:Al2O3:B2O3 (s, 25 oC) To MgO:Al2O3:B2O3 (l, 1260 oC)									
Enthalpy Change [ΔH] (kJ/mol-Mn_D)	1754421.4	Formula	$V_{feed} = \Delta H / (n * F)$			0.3868786486			
Step Five: Calculating Voltage For Losses									
Assumption:									
0									
Step Six: Calculating Ohmic Drop									
$V_{IR} = V_{feed} + V_r + V_{loss}$									
1.294363537									
Step Seven: Calculating The Anode-To-Cathode Distance									
$V_{IR} = I * R$									
$R = (\rho * D_{ac}) / (\text{Area})$									
$V_{IR} = I * ((\rho * D_{ac}) / (\text{Area}))$									
$I = j * \text{Area}$									
$V_{IR} = (j * \text{Area}) * ((\rho * D_{ac}) / (\text{Area}))$									
$V_{IR} = j * (\rho * D_{ac})$									
Assumptions									
Current Density can be assumed to be 2 A/cm ² , which is the same for Aluminum Smelting: Al[3+] = 3e[-] + Al(l)					Resistivity can be assumed to be 1 ohm*cm which is typical for Molten Salts				
Voltage Drop From Reaction	1.294363537	Current Density [j] (A / cm ²)	2			Resistivity [ρ] (ohm * cm)	1		
Ohmic Drop [V_IR] (V)	0.6471817686								

Table 28: The calculation process to obtain the Nominal Cathode-To-Anode Distance for the electrolytic cell containing the AlMgB₁₄ MOE reaction.

FARADAIC EFFICIENCY (CURRENT EFFICIENCY)					
Formula					
$\eta_f = ((m) / (m_o)) * 100\%$					
η_f	Faradaic Efficiency	m	Actual Mass Produced (grams)	m_o	Theoretical Mass Produced (grams)
Step One: Developing Assumptions					
Assumption			Reasoning		
$\eta_f = 90\%$			Modern aluminum electrolysis cells operate at approximately 90% faradaic efficiency, so we can assume to apply the same efficiency to this electrolysis cell		
Step Two: Calculating The Theoretical Mass Of Aluminum Magnesium Boride Produced					
Formula					
$m = (M * Q) / (n * F)$					
Molar Mass [M] (g/mol-Mn)	202.640539	Number Of Transferred Electrons [n] (mol-e/mol-Mn)	47	Faraday's Constant [F] (C/mol-e)	96485.3321
Charge [Q] (C/mol)					
$Q = I * \Delta t = (j * \text{Area}) * \Delta t$					
Current Density [j] (A/cm ²)	2	Area [cm ²]	1	Time [Δt] (s)	86400
172800					
Theoretical Mass [m] (gram)					
7.72166429					
Step Three: Calculating The Actual Mass Of Manganese Produced					
Formula					
$\eta_f = ((m) / (m_o)) * 100\%$					
Faradaic Efficiency [η_f] (%)	90	Theoretical Mass Produced [m_o] (g)	7.72166429		
6.949497861					

Table 29: The calculation process to obtain the Actual Produced Mass of AlMgB₁₄. This was done assuming that the reaction occurs at 90% faradaic efficiency.

ENERGY EFFICIENCY							
Formula							
$\eta_E = ((E_o) / (E)) * \eta_f$							
η_E	Energy Efficiency	E	Actual Minimal Potential (V)	E_o	Minimal Theoretical Potential (V)	η_f	Faradaic Efficiency
Step One: Developing Assumptions							
Assumption			Reasoning				
$\eta_f = 90\%$			Modern aluminum electrolysis cells operate at approximately 90% faradaic efficiency, so we can assume to apply the same efficiency to this manganese electrolysis cell				
Step Two: Calculating The Minimal Theoretical Potential							
Formula							
$E_o = V_{min} + V_r + V_{feed}$							
Minimum Operating Voltage [V_min] (V)	0.9074848886	Electrolysis Reaction Voltage [V_r] (V)	1.4364418	Voltage For Introducing Ore Feedstock [V_feed] (V)	0.3868786486		
2.730805337							
Step Three: Calculating The Energy Efficiency							
Formula							
$\eta_E = ((E_o) / (E)) * \eta_f$							
Actual Minimal Potential							
$E = E_o + (T * \Delta S) / (47F)$							
Minimal Theoretical Potential [E_o] (V)	2.730805337	Operating Temperature [T] (K)	1873.15	Entropy Change [ΔS] (J/mol*K)	3477.56	Faraday's Constant [F] (C/mol)	96485.3321
4.167247137							
58.977179							

Table 30: The calculation process to obtain the Energy Efficiency of $AlMgB_{14}$. This was done assuming that the reaction occurs at 90% faradaic efficiency.

Moles Of Composition		Moles Of Elements	
Al₂O₃	0.163332	Al	0.183643
MgO	0.221198	Mg	0.124352
B₂O₃	0.61547	B	0.692005
		O₂	0.718912

Table 31: The calculations made to obtain individual amounts of moles for the elements of $AlMgB_{14}$.

Equilib - Menu: last system

File Units Parameters Help

T(C) P(atm) Energy(J) Quantity(mol) Vol(litre)

Reactants (4)

0.183643 Al + 0.124352 Mg + 0.692005 B + <A> O2

Products

Compound species

gas ideal real 21

aqueous 0

pure liquids 0

pure solids 45

* - custom selection species: 66

Target

- none -

Estimate T(K): 1000

Quantity(mol): 0

Solution phases

*	+	Base-Phase	Full Name
		FTsalt-B1	Rocksalt
I		FToxid-SLAGA	A-Slag-liq all oxides + S
		FToxid-SPINA	A-Spinel
		FToxid-MeO_A	A-Monoxide
		FTlite-Liqu	Liquid
		FTlite-A1	FCC-A1
		FTlite-A2	BCC-A2
		FTlite-A3	HCP-A3

Legend

I - immiscible 1

Show all selected

species: 6

solutions: 2

Custom Solutions

0 fixed activities

0 ideal solutions

Pseudonyms

apply

Volume data

assume molar volumes of solids and liquids = 0

include molar volume data and physical properties data

paraequilibrium & Gmin

Virtual species: 6

Total Species (max 5000) 72

Total Solutions (max 200) 2

Total Phases (max 1500) 48

Final Conditions

<A>		T(C)	P(atm)	Product H(J)
18912	0.0359456	1600	1	

10 steps Table

Equilibrium

normal normal + transitions

transitions only open

- no time limit -

FactSage 8.0

Table 32: The menu window to the FactSage calculations for oxygen partial pressure, moles of Slag #1, moles of Slag #2, total moles of AlB_2 , total moles of MgB_2 , total moles of Al_2O_3 , total moles of MgB_7 , total moles of AlB_{12} , total moles of B, and total moles of $AlMgB_{14}$ for each specific mole-amount of O_2 . Each of the constraints selected is shown in this table.

```

T = 1600 C
P = 1 atm
V = 0 dm3

STREAM CONSTITUENTS          AMOUNT/mol
Al          1.8364E-01
Mg          1.2435E-01
B           6.9200E-01
O2          2.1567E-01

                                EQUIL AMOUNT   MOLE FRACTION   FUGACITY
                                mol              atm
PHASE: gas_real
Mg          V  0.0000E+00   9.6152E-01   1.9556E-02
(BO)2       V  0.0000E+00   2.3237E-02   4.7262E-04
AlBO2       V  0.0000E+00   7.0277E-03   1.4294E-04
EO          V  0.0000E+00   6.1814E-03   1.2572E-04
B2O3        V  0.0000E+00   1.5271E-03   3.1061E-05
Al          V  0.0000E+00   3.6480E-04   7.4198E-06
Al2O        V  0.0000E+00   8.9976E-05   1.8300E-06
B2O         V  0.0000E+00   5.0653E-05   1.0302E-06
Mg2         V  0.0000E+00   3.2366E-06   6.7864E-08
B           V  0.0000E+00   5.3296E-07   1.0840E-08
BO2         V  0.0000E+00   2.9436E-07   5.9871E-09
AlO         V  0.0000E+00   4.9562E-08   1.0080E-09
MgO         V  0.0000E+00   1.8541E-08   3.7712E-10
Al2O2       V  0.0000E+00   2.2367E-09   4.5492E-11
Al2         V  0.0000E+00   1.5706E-09   3.1944E-11
O           V  0.0000E+00   3.4459E-11   7.0087E-13
B2          V  0.0000E+00   1.4894E-12   3.0293E-14
AlO2        V  0.0000E+00   5.8131E-16   1.1823E-17
O2          V  0.0000E+00   4.3667E-16   8.8849E-18
Al2O3       V  0.0000E+00   1.9742E-17   4.0153E-19
O3          V  0.0000E+00   3.7225E-32   7.5768E-34
TOTAL:      0.0000E+00   1.0000E+00   2.0339E-02
PHASE: Slag-liq#1
                                mol           MOLE FRACTION   ACTIVITY
Al2O3       6.5990E-02   2.9396E-01   1.0389E-01
MgO         1.2277E-01   5.4688E-01   3.9560E-02
B2O3        3.5728E-02   1.5916E-01   3.1114E-03
TOTAL:      2.2449E-01   1.0000E+00   1.0000E+00
  Site fraction of sublattice constituents:
  Al          0.40459           Stoichiometry calculated
  Mg          0.37635
  B           0.21906
-----
O            1.0000           Stoichiometry calculated
System component  Amount/mol   Amount/gram   Mole fraction   Mass fraction
Al            0.13198         3.5610         0.17501         0.25141
Mg            0.12277         2.9839         0.16279         0.21067
O             0.42792         6.8465         0.56744         0.48328
B             7.1457E-02       0.77252        9.4755E-02       5.4542E-02
PHASE: Slag-liq#2
                                mol           MOLE FRACTION   ACTIVITY
Al2O3       2.4875E-05   1.1314E-02   1.0389E-01
MgO         1.5849E-03   7.2085E-01   3.9560E-02
B2O3        5.8887E-04   2.6784E-01   3.1114E-03
TOTAL:      2.1986E-03   1.0000E+00   1.0000E+00
  Site fraction of sublattice constituents:
  Al          1.7690E-02       Stoichiometry calculated
  Mg          0.56354
  B           0.41877
-----
O            1.0000           Stoichiometry calculated
System component  Amount/mol   Amount/gram   Mole fraction   Mass fraction
Al            4.9750E-05         1.3423E-03       7.9747E-03       1.2497E-02
Mg            1.5849E-03         3.8520E-02       0.25405         0.35863
O             3.4261E-03         5.4816E-02       0.54919         0.51034
B             1.1777E-03         1.2732E-02       0.18879         0.11854
                                mol           ACTIVITY
AlB12_beta_tetragonal(s)  5.1614E-02   1.0000E+00
E_beta_rhombohedral_h(s)  0.0000E+00   7.9297E-01
E_diamond_A4(s3)          0.0000E+00   7.9246E-01

```

Table 33: The results window of the FactSage calculations for oxygen partial pressure, moles of Slag #1, moles of Slag #2, total moles of AlB_2 , total moles of MgB_2 , total moles of Al_2O_3 , total moles of MgB_2 , total moles of AlB_{12} , total moles of B, and total moles of $AlMgB_{14}$ for each specific mole-amount of O_2 . This particular example is for when we had 0.2157 moles of O_2 .

Mole Of O2	O2 Partial Pressure (atm)	Moles Of Slag #1	Moles Of Slag #2	Total Moles Of AlB2	Total Moles Of MgB2	Total Moles Of Al2O3	Total Moles Of MgB7	Total Moles Of AlB12	Total Moles Of B	Total Moles Of AlMgB14
0.0000	0.000E+00	0.000E+00	0.000E+00	1.760E-01	1.168E-01	0.000E+00				7.602E-03
0.0359	6.669E-21	0.0000E+00	0.0000E+00	1.185E-01	1.072E-01	2.396E-02				1.719E-02
0.0719	6.669E-21	0.0000E+00	0.0000E+00	6.1016E-02	9.758E-02	4.793E-02				2.677E-02
0.1078	6.669E-21	0.0000E+00	0.0000E+00	3.5026E-03	8.799E-02	7.189E-02	0.000E+00	0.000E+00		3.636E-02
0.1438	4.293E-20	1.3698E-01	0.0000E+00	0.0000E+00	0.000E+00	0.000E+00	3.193E-02	3.113E-03		3.074E-02
0.1797	2.950E-18	1.8353E-01	0.0000E+00				2.879E-02	3.832E-02		0.0000E+00
0.2157	8.885E-18	2.245E-01	2.199E-03				0.000E+00	5.161E-02		
0.2516	2.370E-17	2.507E-01	0.0000E+00					4.793E-02		
0.2876	3.785E-17	2.746E-01	0.0000E+00					4.424E-02		
0.3235	5.135E-17	2.986E-01	0.0000E+00					4.055E-02		
0.3595	6.467E-17	3.225E-01	0.0000E+00					3.687E-02		
0.3954	7.784E-17	3.465E-01	0.0000E+00					3.318E-02		
0.4313	9.068E-17	3.705E-01	0.0000E+00					2.949E-02		
0.4673	1.030E-16	3.944E-01	0.000E+00					2.581E-02		
0.5032	1.145E-16	4.184E-01	0.0000E+00					2.212E-02		
0.5392	1.253E-16	4.424E-01	0.0000E+00					1.843E-02		
0.5751	1.351E-16	4.663E-01	0.0000E+00					1.475E-02		
0.6111	1.441E-16	4.903E-01	0.0000E+00					1.106E-02	0.000E+00	
0.6470	1.501E-16	5.143E-01	0.0000E+00					2.655E-03	6.135E-02	
0.6830	1.601E-16	5.382E-01	0.0000E+00					0.000E+00	4.793E-02	
0.7189	8.740E-09	5.622E-01	0.0000E+00						0.000E+00	

Table 34: The FactSage calculations for oxygen partial pressure, moles of Slag #1, moles of Slag #2, total moles of AlB₂, total moles of MgB₂, total moles of Al₂O₃, total moles of MgB₇, total moles of AlB₁₂, total moles of B, and total moles of AlMgB₁₄ for each specific mole-amount of O₂.

Mole Fraction Of O2	Mole Fraction Of AlB2	Mole Fraction Of MgB2	Mole Fraction Of Al2O3	Mole Fraction Of MgB7	Mole Fraction Of AlB12	Mole Fraction Of B	Mole Fraction Of AlMgB14	Mole Fraction Slag-Liquid
0.000	0.5860	0.3887	0.0000				0.0253	0.0000
0.035	0.4442	0.4016	0.0898				0.0644	0.0000
0.067	0.2615	0.4183	0.2054				0.1148	0.0000
0.097	0.0175	0.4405	0.3599	0.0000	0.0000		0.1820	0.0000
0.126	0.0000	0.0000	0.0000	0.1575	0.0154		0.1516	0.6756
0.152				0.1149	0.1529		0.0000	0.7322
0.177				0.0000	0.1855			0.8145
0.201					0.1605			0.8395
0.223					0.1388			0.8612
0.244					0.1196			0.8804
0.264					0.1026			0.8974
0.283					0.0874			0.9126
0.301					0.0737			0.9263
0.318					0.0614			0.9386
0.335					0.0502			0.9498
0.350					0.0400			0.9600
0.365					0.0307			0.9693
0.379					0.0221	0.0000		0.9779
0.393					0.0046	0.1061		0.8893
0.406					0.0000	0.0818		0.9182
0.418						0.0000		1.0000

Table 35: The calculations for the mole fractions of the products—AlB₂, MgB₂, Al₂O₃, MgB₇, AlB₁₂, B, AlMgB₁₄, and the Slag-Liquid—for each specific mole fraction of O₂.

Equilib - Menu: last system

File Units Parameters Help

T(C) P(atm) Energy(J) Quantity(mol) Vol(litre)

Reactants (3)

<A> Ar + <1E-6A> O2 + <1-A> H2

Products

Compound species

gas ideal real 10

aqueous 0

pure liquids 0

pure solids 0

species: 10

Target

- none -

Estimate T(K): 1000

Quantity(mol): 0

Solution phases

*	+	Base-Phase	Full Name

Legend

Show all selected

species: 0

solutions: 0

Select

Custom Solutions

0 fixed activities

0 ideal solutions

Pseudonyms

apply Edit ...

Volume data

assume molar volumes of solids and liquids = 0

include molar volume data and physical properties data

paraequilibrium & Gmin edit

Virtual species: 0

Total Species (max 5000) 10

Total Solutions (max 200) 0

Total Phases (max 1500) 1

Final Conditions

<A>		T(C)	P(atm)	Product H(J)
.8	.01	1600	1	

10 steps Table

21 calculations

Equilibrium

normal normal + transitions

transitions only open

- no time limit -

Calculate >>

FactSage 8.0

Table 36: The menu window to the FactSage calculations for determining the moles of Hydrogen Gas that will satisfy the Oxygen Partial Pressure conditions of our unchanged reaction.

T = 1600 C
P = 1 atm
V = 153.75 dm3

```

STREAM CONSTITUENTS          AMOUNT/mol
Ar                            9.6000E-01
O2                             9.6000E-07
H2                             4.0000E-02

PHASE: gas_real
EQUIL AMOUNT   MOLE FRACTION   FUGACITY
mol            atm
Ar              V  9.6000E-01   9.5994E-01   9.6013E-01
H2              V  3.9934E-02   3.9931E-02   3.9939E-02
H               V  1.2844E-04   1.2843E-04   1.2845E-04
H2O             V  1.9195E-06   1.9194E-06   1.9196E-06
OH              V  4.8980E-10   4.8977E-10   4.8987E-10
O               V  1.1635E-12   1.1635E-12   1.1637E-12
O2              V  2.4490E-17   2.4489E-17   2.4493E-17
HOO             V  1.5994E-20   1.5993E-20   1.5996E-20
HOOH           TV  1.1414E-20   1.1413E-20   1.1416E-20
O3              V  3.4670E-33   3.4668E-33   3.4680E-33
TOTAL:          1.0001E+00   1.0000E+00   1.0000E+00
System component  Amount/mol   Amount/gram   Mole fraction   Mass fraction
Ar                0.96000    38.350        0.92308         0.99790
O                 1.9200E-06  3.0719E-05   1.8462E-06     7.9933E-07
H                 8.0000E-02  8.0635E-02   7.6923E-02     2.0982E-03
*****
Cp          H          S          G          V
J.K-1      J          J.K-1      J          dm3
*****
2.15343E+01  3.34047E+04  1.94074E+02  -3.30125E+05  1.53747E+02
*****
Cp          H          S          G
J.K-1      J          J.K-1      J
gas_real   2.15343E+01  3.34047E+04  1.94074E+02  -3.30125E+05

```

Cut-off limit for gaseous fractions/phase activities = 1.00E-70

Data on 1 product species identified with "T" have been extrapolated outside their valid temperature range

10 product species identified with "V" are modeled with an equation of state

Databases: FTsalt 8.0, FToxid 8.0, FTlite 8.0, FactPS 8.0

Data Search options: exclude gas ions; organic CxHy.. X(max) = 2; min soln cpts = 2

Final conditions: <A> = .8 1 .01, T(C) = 1600, P(atm) = 1

Table 37: The results window of the FactSage calculations for determining the moles of Hydrogen Gas that will satisfy the Oxygen Partial Pressure conditions of our unchanged reaction. This range of percent of Argon goes from 80% to 100%. This particular example is for when we had 96% of Argon.

<u>Percent Of Argon (/100%)</u>	<u>Percent Of Hydrogen (/100%)</u>	<u>Oxygen Partial Pressure [atm]</u>	<u>Base-10 Log Of Oxygen Partial Pressure [atm]</u>
0.80	0.20	1.53E-17	-16.81400481
0.81	0.19	1.67E-17	-16.77668581
0.82	0.18	1.83E-17	-16.73788128
0.83	0.17	2.01E-17	-16.69743099
0.84	0.16	2.21E-17	-16.65517561
0.85	0.15	2.45E-17	-16.61095802
0.86	0.14	1.60E-18	-17.79520196
0.87	0.13	1.90E-18	-17.72076665
0.88	0.12	2.28E-18	-17.64128489
0.89	0.11	2.78E-18	-17.55586148
0.90	0.10	3.44E-18	-17.46334057
0.91	0.09	4.34E-18	-17.36219017
0.92	0.08	5.62E-18	-17.25034097
0.93	0.07	7.50E-18	-17.12490399
0.94	0.06	1.04E-17	-16.98163242
0.95	0.05	1.53E-17	-16.81400481
0.96	0.04	2.45E-17	-16.61095802
0.97	0.03	4.45E-17	-16.35187428
0.98	0.02	1.02E-16	-15.99046412
0.99	0.01	4.18E-16	-15.37880294
1.00	0.00	8.89E-07	-6.050941941

Table 38: The tabulation of the results window of the FactSage calculations for determining the moles of Hydrogen Gas that will satisfy the Oxygen Partial Pressure conditions of our unchanged reaction. This range of percent of Argon goes from 80% to 100%. In this table, we presented the percent of Argon (/100) and the corresponding percent of Hydrogen Gas (/100), alongside the oxygen partial pressure for each particular instance and the Base-10 logarithmic calculation of that pressure.

<u>Mole Fraction Of O₂</u>	<u>Base-10 Log Of O₂ Partial Pressure [No Hydrogen] (atm)</u>	<u>Percent Of Hydrogen (%)</u>	<u>Base-10 Log Of O₂ Partial Pressure [Hydrogen-Argon Introduction] (atm)</u>
0.000	0.00000	20	-18.16793
0.035	-20.17597	19	-18.11257
0.067	-20.17597	18	-18.05494
0.097	-20.17597	17	-17.99482
0.126	-19.36727	16	-17.93167
0.152	-17.53025	15	-17.86531
0.177	-17.05135	14	-17.79520
0.201	-16.62523	13	-17.72077
0.223	-16.42192	12	-17.64128
0.244	-16.28946	11	-17.55586
0.264	-16.18928	10	-17.46334
0.283	-16.10877	9	-17.36219
0.301	-16.04249	8	-17.25034
0.318	-15.98733	7	-17.12490
0.335	-15.94108	6	-16.98163
0.350	-15.90219	5	-16.81400
0.365	-15.86925	4	-16.61096
0.379	-15.84125	3	-16.35187
0.393	-15.82362	2	-15.99046
0.406	-15.79561	1	-15.37880
0.418	-8.05848	0	-6.05094

Table 39: The tabulation of the combination of our previous results from Table 33 and Table 37. This table shows the range of our oxygen partial pressure when we alter the oxygen gas's mole fraction (disregarding H₂) in base-10 logarithmic form. It also shows the hydrogen percentage from 0 to 20% and the corresponding oxygen partial pressure (regarding H₂) in base-10 logarithmic format.

<u>Upper & Lower Limit Of Mole Fraction Of O₂</u>	<u>Upper & Lower Limit Of Mole Of O₂</u>	<u>Mole Of O₂</u>	<u>Total Moles Of AlMgB₁₄</u>	<u>Maximum Boride Yield Mole Fraction Of O₂</u>
0.093	0.1025358324	0.1025358324	3.49E-02	0.1170257299
0.139	0.1614401858	0.1055358324	3.57E-02	
		0.1085358324	3.65E-02	
		0.1115358324	3.76E-02	
		0.1145358324	3.89E-02	
		0.1175358324	4.03E-02	
		0.1205358324	4.16E-02	
		0.1235358324	4.29E-02	
		0.1265358324	4.42E-02	
		0.1295358324	4.56E-02	
		0.1325358324	4.68E-02	
		0.1355358324	4.42E-02	
		0.1385358324	4.11E-02	
		0.1415358324	3.74E-02	
		0.1445358324	2.84E-02	
		0.1475358324	1.91E-02	
		0.1505358324	9.81E-03	
		0.1535358324	5.07E-04	
		0.1565358324	0.00E+00	
		0.1595358324	0.00E+00	
		0.1625358324	0.00E+00	

Table 40: The tabulation for the mole fraction O₂ required to obtain the maximum yield of AlMgB₁₄.

<u>Points Of Interest</u>	<u>Mole Fraction Of O2 Associated With Point</u>	<u>Moles Of O2 Associated With Point</u>
Where Hydrogen Gas Was Introduced	0.418237	0.718911942
Where MOE Process Was Introduced	0.152347	0.179728000

Table 41: The calculation for the moles O_2 at the three points of interest that would assist in attaining the amount of energy saved.

<u>Points Of Interest</u>	<u>Mole Fraction Of O2 Associated With Point</u>	<u>Moles Of O2 Associated With Point</u>	<u>Energy Required [kJ] To Conduct MOE Reaction If The Amount Of O2 Present Is....</u>	<u>Total Ammount Of Energy Saved [kJ]</u>
Where Hydrogen Gas Was Introduced	0.418237	0.718911942	-843.00	552.08
Where MOE Process Was Introduced	0.152347	0.179728000	-290.92	

Table 42: The calculation for the amount of energy saved.

Appendix C: Zirconium Diboride MOE

Figures

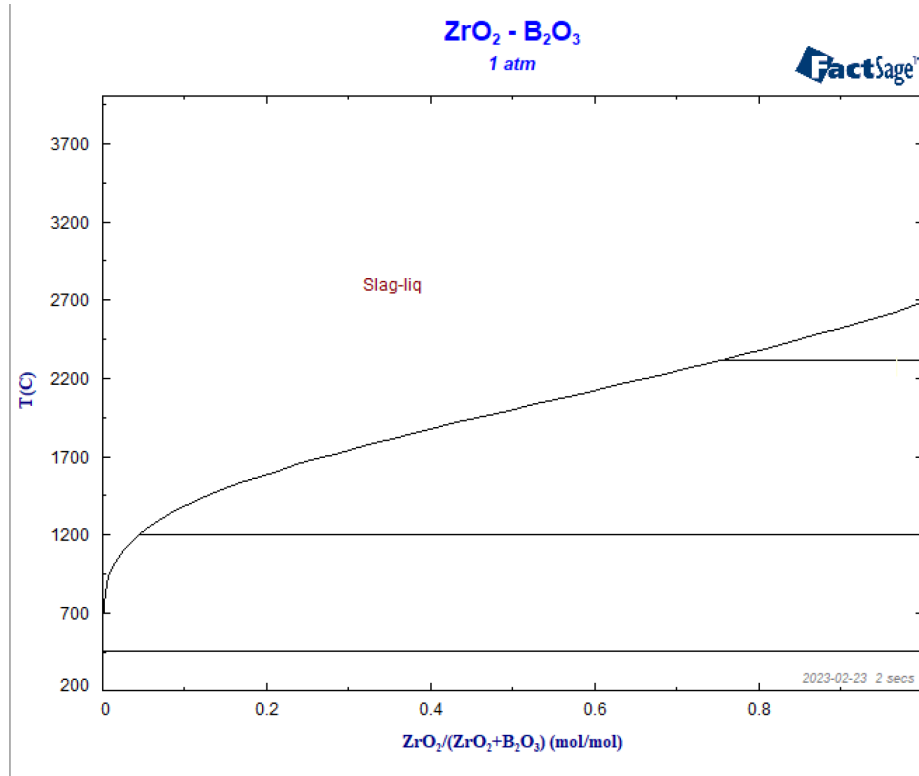


Figure 33: The Pseudo-Binary Phase Diagram Between ZrB₂ and O₂ from a temperature range of 200 °C to 4000 °C.

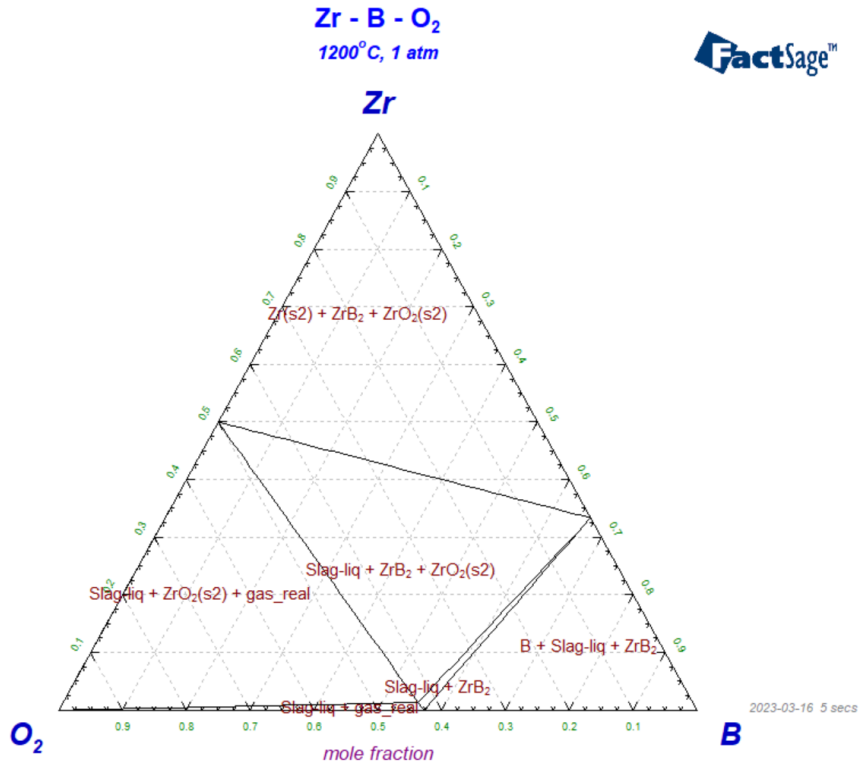


Figure 34: The Isothermal Section between Zr, B, and O₂ at 1200 °C.

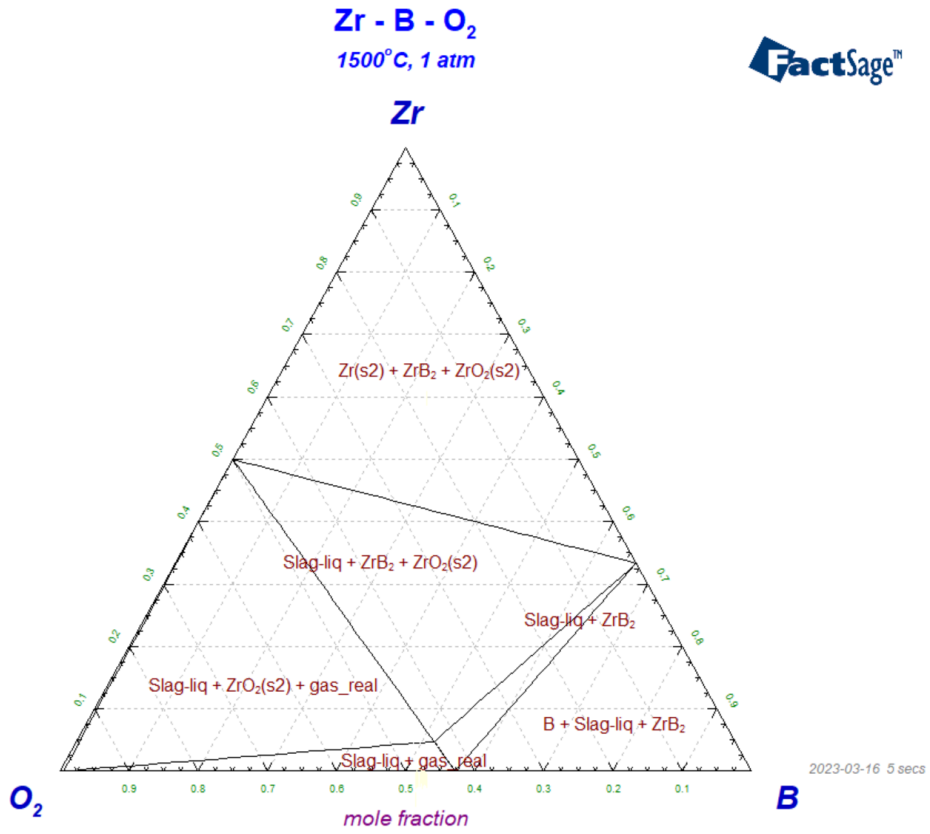


Figure 35: The Isothermal Section between Zr, B, and O₂ at 1500 °C.

Zr - B - O₂
2200°C, 1 atm

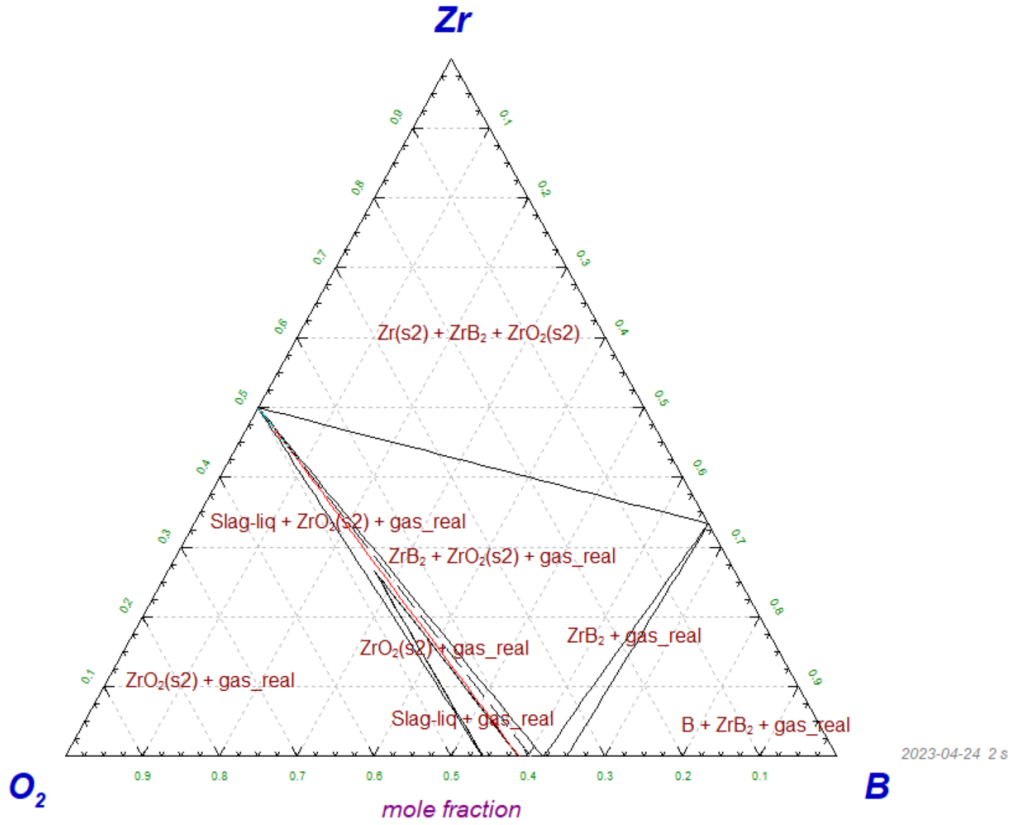


Figure 36: The Isothermal Section between Zr, B, and O₂ at 2200 °C.

Appendix D: Miscellaneous

Figures

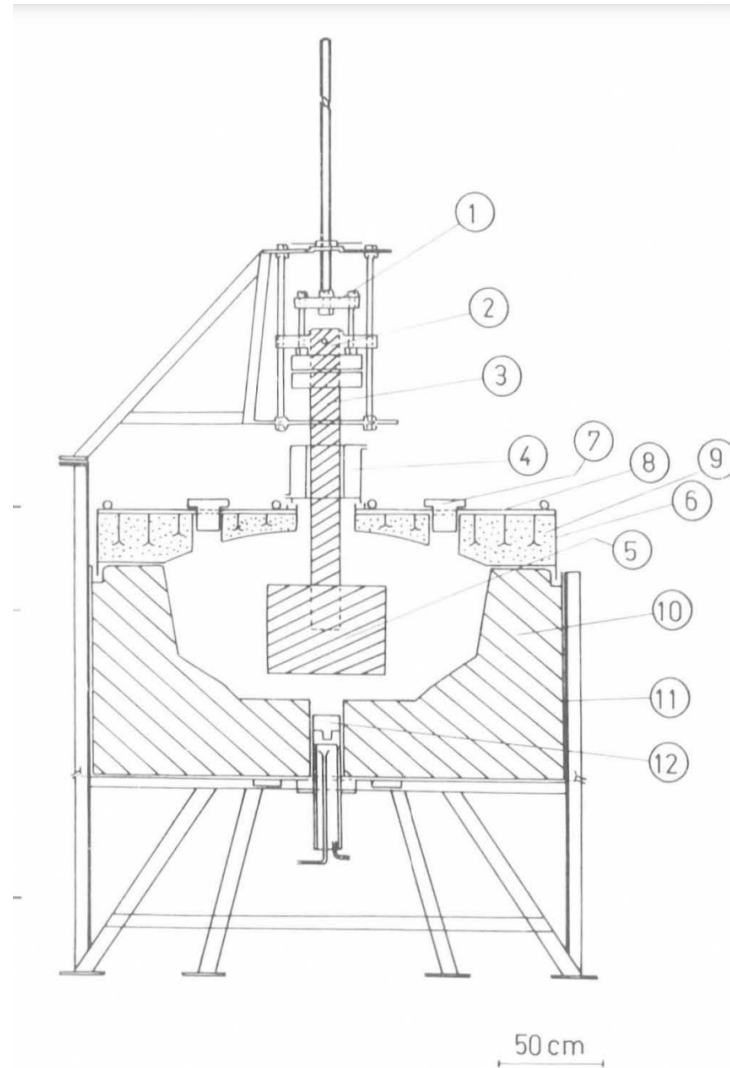


Figure 1: A diagram of an electrolytic cell. Point 1 is the position of the anode. Point 2 is where the anode is electrically connected. Point 3 is the graphite anode. Points 4 and 8 are the tanks in which the water is cooled. Point 5 is a graphite anode in the shape of a cylinder. Point 6 is the location of the cover that holds over the graphite cylinder. Point 7 is a refractory removable plug (there are 2). Points 9 and 10 are refractory lining (9 is concrete, and 10 is manganese). Point 11 is the external metal-based sheath of the system. Point 12 is the cathode (Winard et al., 1977).

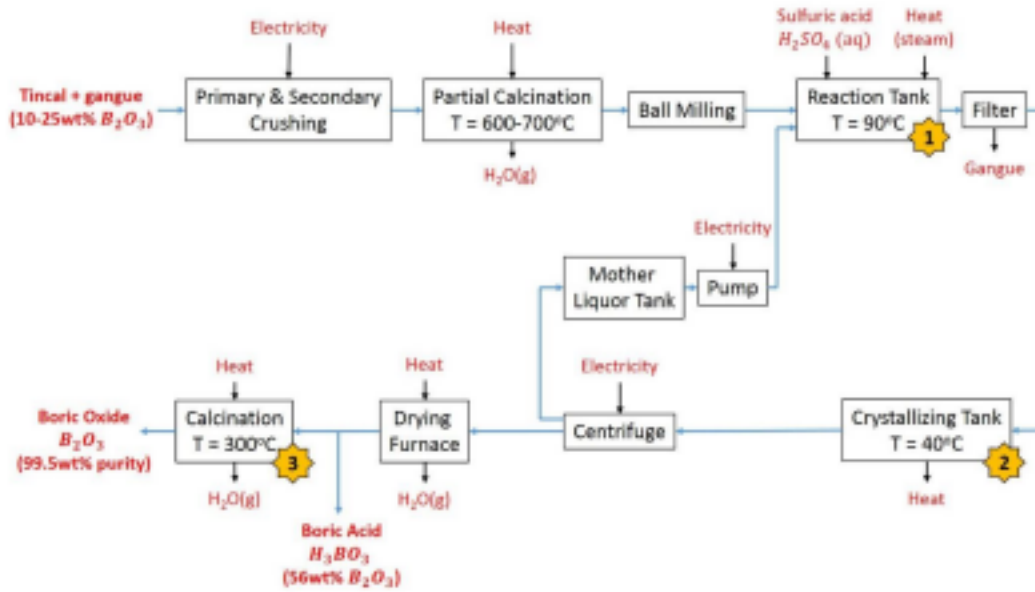


Figure 2: A process, shown by a flow chart, in which boron is isolated from a compound (Nakanishi & Murphy, 2015).

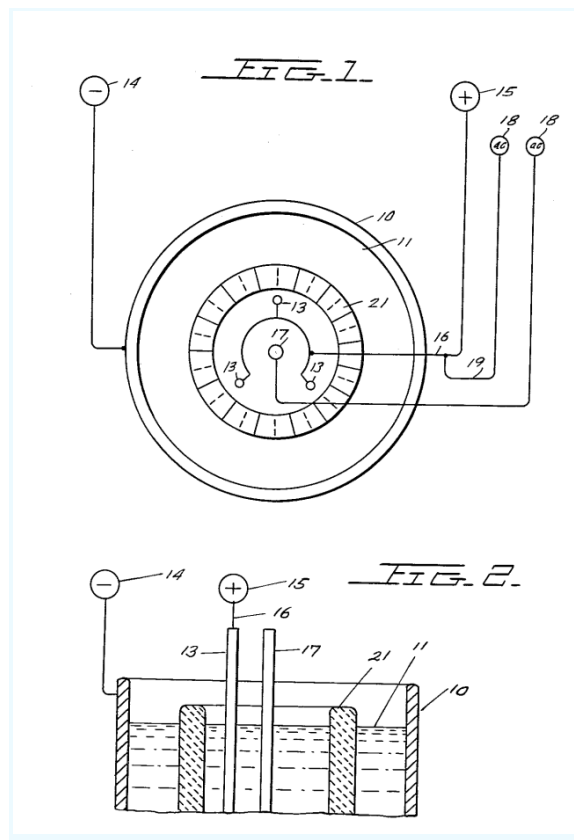


Figure 3: The invention of the mechanism responsible for housing and helping conduct the efficient and pure production of metal borides through fused salt electrolysis (Sindebad).

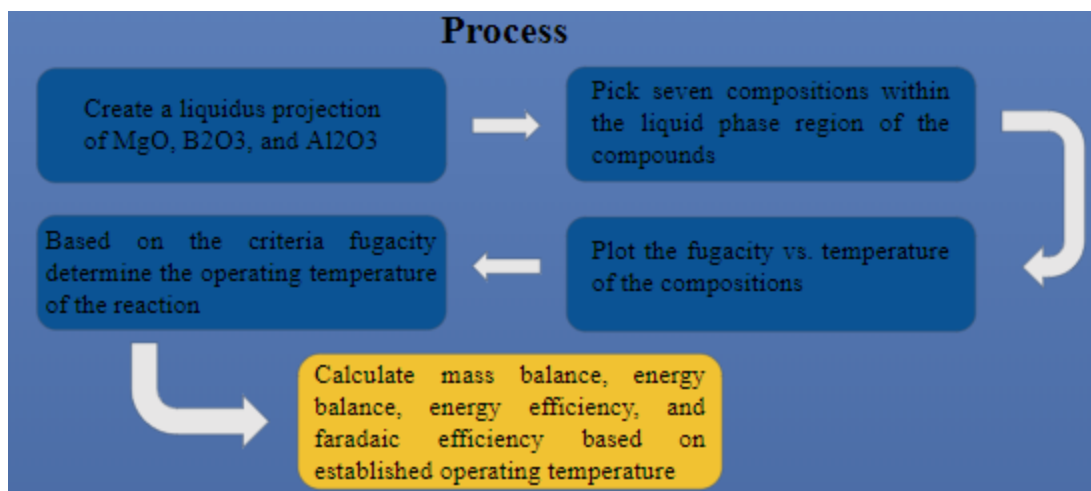


Figure 4: A summarized flowchart of the generalized process taken to ensure the completion of this project

The *Equilib* module – Regular Features

- *Equilib* calculates the conditions for multiphase, multicomponent equilibria, with a wide variety of tabular and graphical output modes, under a large range of constraints.
- *Equilib* accesses both compound and solution databases.

Table of contents

Section 1	Table of Contents
Section 2	Opening the Equilib Module
Section 3	From stoichiometric reactions to complex equilibria
Section 4	Simple equilibrium case (Mg+3Cu₂O+2Fe₃C+Ar)
Section 5	Additional output using the LIST window
Section 6	HELP with right mouse button
Section 7	Constant volume calculation (Si₄ decomposition)
Section 8	Constant pressure in steps (MgO+Si)
Section 9	Non-ideal gas (boiling point of water)

(continued)

The *Equilib* module

Table of contents (continued)

Section 10	<u>Adiabatic combustion, use of the «A» parameter (CH₄ + O₂)</u>
Section 11	<u>Fixed activity calculation (FeS under O₂ partial pressure)</u>
Section 12	<u>Setting up an ideal liquid and adding activity coefficients</u> A part of the Cu-Cr System
Section 13	<u>Standard equilibrium: aqueous solution</u> Leaching arsenic-bearing copper concentrate
Section 14	<u>Standard equilibrium: non-ideal solution Fe-Mn-Si-C</u>
Section 15	<u>Adding slag: An explanation on SlagA, SlagB, Slag?</u>
Section 16	<u>Standard case: Desulphurisation of steel adding CaSi</u>
Section 17	<u>Standard case: Pitzer aqueous with NaCl</u>
Section 18	<u>Heterogeneous equilibria and the phase rule</u>
Section 19	<u>Compound species selection - <i>FactSage</i> 6.4</u>

The *Equilib* module

Table of contents (continued)

Section 10	<u>Adiabatic combustion, use of the «A» parameter ($\text{CH}_4 + \text{O}_2$)</u>
Section 11	<u>Fixed activity calculation (FeS under O_2 partial pressure)</u>
Section 12	<u>Setting up an ideal liquid and adding activity coefficients</u> A part of the Cu-Cr System
Section 13	<u>Standard equilibrium: aqueous solution</u> Leaching arsenic-bearing copper concentrate
Section 14	<u>Standard equilibrium: non-ideal solution Fe-Mn-Si-C</u>
Section 15	<u>Adding slag: An explanation on SlagA, SlagB, Slag?</u>
Section 16	<u>Standard case: Desulphurisation of steel adding CaSi</u>
Section 17	<u>Standard case: Pitzer aqueous with NaCl</u>
Section 18	<u>Heterogeneous equilibria and the phase rule</u>
Section 19	<u>Compound species selection - <i>FactSage</i> 6.4</u>



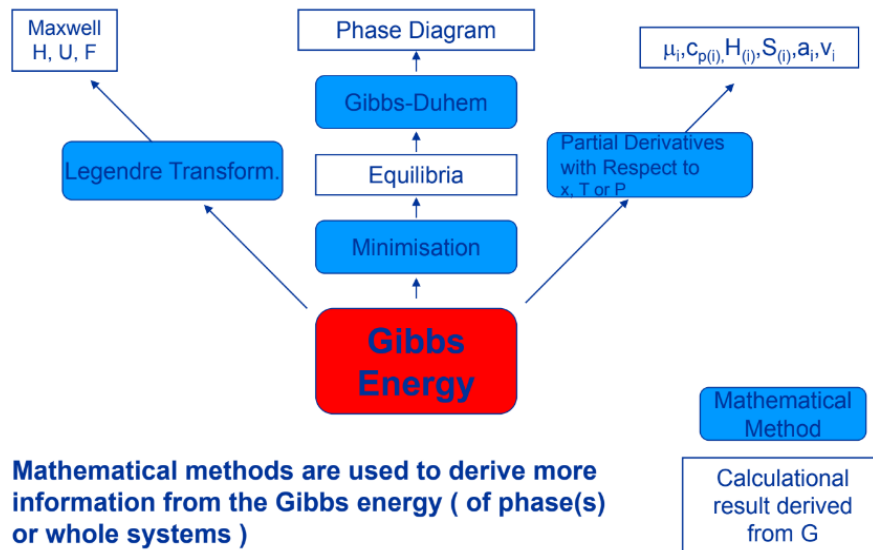
Equilib 1.2

www.factsage.com

Figure 43: The regular features that come within the Equilib module of FactSage (cont.).

GTT-Technologies

The Gibbs Energy Tree



Page 1.1

CRCT

Figure 44: Mathematical tree delineating the flowchart of FactSage computation.

1. Utilizing FactSage (FToxid, FSstel databases and modules) calculate:

- a) Melting points (electrolyte + Mn product)
- b) Vapor pressure (electrolyte + Mn product)
- c) Viscosity (electrolyte)
- d) Half-cell and overall cell reaction
- e) Minimum decomposition voltage along with overall and half cell reactions
- f) Pseudo-binary composition-temperature phase diagrams for MnO-electrolyte
- g) Equilibrium product Mn impurity concentrations (Si, Al, Mg, Ca)
- h) Heat required to be removed/added to maintain isothermal electrolysis (taking into account reactants are initially at room temperature and the overall electrolysis reaction)

2. Utilizing info from the report and your FactSage calculations estimate:

- a) Voltage balance
- b) Energy balance
- c) Mass balance
- d) Nominal Anode-Cathode distance
- e) Faradaic efficiency
- f) Energy efficiency
- g) Specific energy (MWh/t)
- h) Cathode current density (A/m^2)
- i) Productivity ($kg/h/m^2$)
- j) Cell capacity (kg/h)

3. Compare your FactSage calculations with what is reported by Winand et al.

Figure 45: A bullet list of calculations the company Saint Gobain takes interest in Manganese in regards to MOE.